Ir^{I}(η^4-diene) precatalyst activation:

Role of the base

Paven Kisten

Doctor of Philosophy

University of York

Université Toulouse III - Paul Sabatier

Chemistry

October 2023

Abstract

Transfer hydrogenation catalysts are important in the synthesis of fine chemicals. Previous work has shown that a base is often necessary to achieve high activities for the asymmetric hydrogenation of polar substrates. New mechanistic views for such systems have emerged to account for the activity of such systems in which the ligand does not actively participate in proton donation which nevertheless need a strong base for activity. In this work, the role of the base in the associated chemistry of [IrCl(COD)(L$_2$)] (L$_2$ = dppe, dppf, (*S*)-BINAP, P,S^{iPr}, P,S^{Bz}, P,S^{Ph}, P,S^{Cy}, (P,S^R = CpFe[1,2-C$_5$H$_3$(PPh$_2$)(CH$_2$S^R)]) systems was studied.

In the presence of an alkoxide with a β-hydrogen, two monohydride complexes of the form [IrH(C$_8$H$_{12}$)(dppe)] resulted from [IrCl(COD)(dppe)], which interconvert and this was supported by complementary DFT studies which gave a similar result. When no β-hydrogen was present on the base, two isomeric monohydride complexes were formed through COD deprotonation, [IrH(1-κ-4,5,6-η^3-C$_8$H$_{10}$)(dppe)]. DFT calculations were used to rationalize that the mechanism of interconversion proceeds *via* partial rotation of the cyclic C$_8$H$_{10}$ ligand. These model complexes were transformed by heating in the presence of KO^{t}Bu (or NaOMe) and isopropanol at 80 °C, to yield M[IrH$_4$(dppe)] (M = K, Na). Similar Ir^{III} products M[Ir(H)$_4$(L$_2$)] (L$_2$ = dppf, (*S*)-BINAP) were selectively generated from [IrCl(COD)(L$_2$)] and demonstrated that anionic tetrahydrido iridium complexes can be formed under catalytically relevant conditions.

Finally, the alkali metal-dependent hydrogenation activity of these complexes towards benzophenone was examined. The active catalyst, generated in situ from [IrCl(COD)]$_2$ and (P,S^R) under H$_2$ in the presence of a strong base was the solvated M[Ir(H)$_4$(P,S^R)] salt. Their activity increased, for all R derivatives, in the order Li < Na < K. On the other hand, the nature of the cation did not affect the *ee*. DFT calculations revealed that the rate-determining barrier corresponds to outer-sphere hydride transfer and that the enantio-discriminating interactions are largely unaffected by the cation but rather through π-π interactions. It was found that the model used to describe the alkali-metal cation coordination sphere in the DFT studies is critical for reproducing the experimental results.

Table of Contents

List of Tables

List of Figures

List of Schemes

List of Equations

Acknowledgements

The research presented in this thesis would not have been possible without the ideas, and encouragement and of my PhD supervisors Professor Rinaldo Poli, Professor Simon Duckett, Professor Jason Lynam and Dr. John Slattery. In addition, I would like to thank Dr. Eric Manoury for the help with synthetic aspects of my project, and Professor Agustí Lledós for the help with computational aspects of the project. It has been a pleasure to work with you all. I am lucky to have been able to learn from the best, where each discussion was intellectually stimulating, ranging from scientific discussions to popular culture. The sincerest thank you to you all.

To the members of CHyM, thank you for your support and making the days more exciting in the office and the lab. Thank you to Helena, Callum, Aminata, Vicky L. To the members of Team G in Toulouse for helping me settle into France and welcoming me with open arms. To the members at UAB, to Bernat, and Iker for being a great guide in Barcelona and helping me with Spanish. To the members of Tecnalia who helped me gain a host of new skills on my industrial placement in Vitoria-Gasteiz. Pablo for providing excellent support when needed.

Special thanks to the Postdocs and technical staff. Pete, Matt, and Vicky A in York for assistance in the laboratory, that helped me improve my technical competency. Agnés and Sandrine in Toulouse who helped me improve my synthetic skills dramatically, and provided constant support when trying to traverse the minefield that is French bureaucracy.

The members of the CCIMC network for organising all the network events. A special thanks to Agustin, Max, and Sara who I had met across the various placements of the network for their support. I would like to thank the friends I made during this PhD and beyond for their support. Consoling me at some difficult points, but also supporting me during the high points. Particularly the friends who I will collectively call Can('t)yon trip, Griffou-tang Clan, Jojo, and Sofia. I am truly thankful to have such a tremendous network of support. A special thanks to Tiago, The'M (Matty) and Steven who welcomed me into their family homes during the Festive period, when I was unable to travel home.

Finally, the deepest gratitude to both of my parents for their sustained support, but for whom none of this would be possible. For working tirelessly and making sacrifices to give me the best life possible. Helping me through my youth until now, to achieve my goals and instilling me with strength to get through all the changes in my life with relative ease. To my brother for his encouragement and guidance, and my extended family for their support.

Author's Declaration

I declare that this thesis is a presentation of original work, and I am the sole author. This work has not previously been presented for a degree or other qualification at this University or elsewhere. It is being simultaneously presented to the Graduate School of the University of Toulouse 3 as per the bilateral agreement. All sources are acknowledged as references.

Paven Kisten

Chapter 1:   Introduction

1.1 Catalysts and catalysis

1.1.1 Fundamental principles of catalysts

Over the past century, tremendous efforts have been made to improve the efficiency of organic synthetic methods. Earlier workers often used stoichiometric amounts of additives for organic transformations,[1,2] For example, the reduction of carbonyls using lithium reagents[3–5] at an industrial scale brings about vast amounts of waste, namely Al/Li salts.[6] The shift towards efficient catalysts mitigates this issue.

Catalysis works on the principle of providing an alternative kinetic pathway for a reaction to occur. Catalysts therefore provide for faster, operationally simple reactions, and most importantly can sometimes be recycled and reused.[7–9] This mitigates the issues traditionally associated with the use of stoichiometric additives. It is no surprise therefore that bio-based, organometallic homogenous and heterogeneous catalytic systems are commonly employed in industrial processes.[10,11] Through advances in computational methods, molecular architecture, and the push for more sustainable protocols, homogenous organometallic catalysts now reflect some of the most well-established systems in modern chemistry.[12]

A catalyst increases the rate of a chemical reaction by providing a lower energy pathway for the reaction. The kinetic parameters determine the rate of reaction, and thermodynamic parameters determine the equilibrium of a reaction. The latter can be expressed in terms of Gibbs Free Energy changes (ΔG) (**Equation 1-1**).

$$\Delta G = \Delta H - T\Delta S$$

Equation 1-1 Gibbs Free Energy equation. H represents the enthalpy, T temperature, S entropy and G is the Gibbs free energy

For a reaction to be thermodynamically feasible the overall change in Gibbs free energy between the reagents and final products must be negative, if this criterion is met a reaction could proceed. While the overall Gibbs free energy of a selected chemical transformation does not change with catalysis, a catalyst reduces the energy barriers associated with the formation of a product.

The catalytic cycle shown in **Figure 1-1** shows a simplistic view of the reaction between two substrates (A and B) to yield C. Several reactions may occur between the initial activation of the reagents and the formation of the final products, including the formation of different

transition states, off-loop species, and side reactions. In this case a transition state of A and B (AB) is formed on the reaction coordinate leading to the product C. The thermodynamic parameters involved in the formation of C are the equilibrium constant *K* that relates the concentration of the products and reactants (**Equation 1-2**).
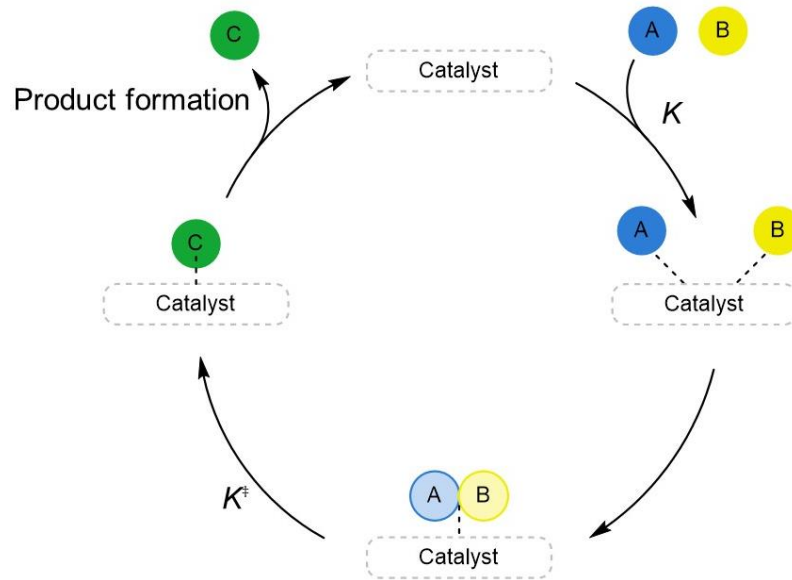
Figure 1-1. Catalytic Cycle for the formation of C from A and B. The equilibrium constant (*K*) and equilibrium constant for the transition state (*K*‡) for AB to C are indicated.

$$A + B \ \rightarrow \ C$$

$$K = \frac{[C]}{[A][B]}$$

$$A + B \ \rightarrow (AB)^{\ddagger} \rightarrow C$$
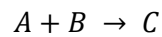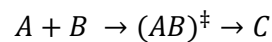
$$K^{\ddagger} = \frac{[C]}{[AB]}$$

Equation 1-2. Equilibrium expression for the reactions involving A and B to form C.

The equilibrium constant (*K*) is linked to the Gibbs Free energy of a reaction by **Equation 1-3** and for a reaction at equilibrium by **Equation 1-4**.

$$\Delta G = \ \Delta G^{o} + \ RT \ lnK$$

Equation 1-3. Calculation for the Gibbs free energy. ΔG^{o} is the standard Gibbs free energy (1 atm, 298 K, pH 7), R is the Ideal Gas constant, and *K* is the equilibrium constant.

$$\Delta G^o = -RT\ lnK$$

$$\Delta G^{\ddagger} = -RTlnK^{\ddagger}$$

Equation 1-4. Standard Gibbs Free energy for a reaction at equilibrium ($\Delta G = 0$), and the Gibbs energy of activation (below).

The Arrhenius equation (**Equation 1-5**) relates the reaction rate constant to the activation energy for a given reaction using a pre-exponential factor, which is used to represent collisions within the system. The value of the pre-exponential factor is determined experimentally using an Arrhenius plot where A is the exponential of the y-intercept.[13]

$$k = Ae^{\frac{-E_a}{RT}}$$

$$lnk = \frac{-E_a}{RT} + \ln A$$

Equation 1-5. Empirical (above) and linear (below) versions of the Arrhenius equation. E_a is defined as the minimum energy to activate the reactant molecules.

The Arrhenius equation relates to the Eyring equation (**Equation 1-6**), which is used to calculate the Gibbs energy of activation for a given reaction.

$$k = \frac{k_B}{h}e^{\frac{-G^{\ddagger}}{RT}}$$

Equation 1-6. The Eyring Equation relates to k to $\Delta G^{\ddagger}$ is the Gibbs energy of activation.

Using the Eyring equation, the rate of reaction can be linked to the rate constant at constant temperature for a reaction. This allows the activation energy for a reaction pathway to be determined and used as a method to validate catalyst efficiency.

1.1.2 Metrics of activity

The activity of a catalyst is evaluated by several different metrics. Catalysts that are applied to the same chemical reactions are often compared by their ability to reduce the activation energy associated with the process. The turnover frequency (TOF) is an important metric that determines the "speed" of a chemical reaction and is shown in **Equation 1-7**.

$$TOF = \frac{Number\ of\ cycles}{[c]t}$$

Equation 1-7. Turnover frequency for a catalyst, [c] is the concentration of catalyst, t is the time.

One of the most important metrics for determining catalyst efficiency is the rate-determining state which shapes the kinetics of the process. Interestingly, there is significant confusion in the community and it is often implied that each individual step in a reaction proceeds at the same rate as the other.[14,15] A lower energy barrier for a reaction is synonymous with a faster and more efficient turnover. The TOF is directly related to the activation energy of a system and determined by the resting state of the catalyst **Equation 1-8** shows the relationship between $\Delta G^{\ddagger}$ and TOF.[16]

$$TOF = \left(\frac{k_B T}{h}\right) e^{-\frac{\Delta G^{\ddagger}}{RT}}$$

Equation 1-8. Equation relating the TOF to the energy span of a catalytic cycle ($\Delta G^{\ddagger}$), k_b is the Boltzmann constant, *h* is Planck's constant.

From what has been discussed thus far, it is logical that catalysts that produce a higher TOF (and hence a lower $\Delta G^{\ddagger}$) would be selected for a given chemical transformation. However, for chemical transformations involving more than one tuneable functionality, it is important that the catalyst can selectively transform the starting material to a desired product. The turnover number (TON) a different metric used to evaluate catalysis efficiency, and is associated with the number of cycles the catalyst can pass before becoming deactivated. A large TON number is indicative of a stable long-lived catalyst.

$$TON = \frac{[substrate]}{[c]} \times \% \, yield \, of \, product$$

Equation 1-9. Equation for the TON of a catalyst. [c] is the concentration of the catalyst in the reaction.

Chemoselectivity is equally important for the generation of high-value products. For example, α,β-unsaturated carbonyl compounds have two unsaturated (carbonyl or alkene) sites that can undergo hydrogenation (**Figure 1-2**). If a catalyst is employed for hydrogenation, it is important that it can selectively hydrogenate a functional group to yield a desired product.[17]
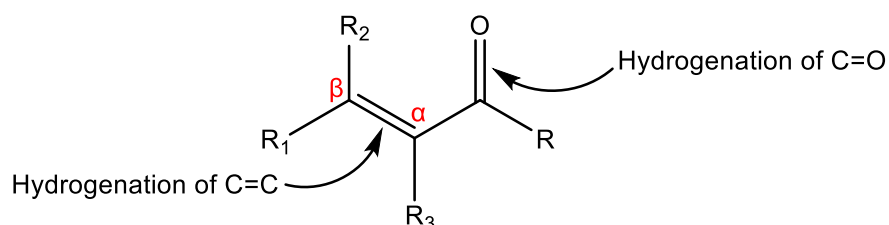
Figure 1-2. Possible sites of hydrogenation for an α,β-unsaturated carbonyl compound.

Achiral reagents are another group of chemicals that are targeted to access chiral products that are used in various applications. If the reaction is not enantioselective a mixture of

enantiomers is formed. From an environmental and toxicological standpoint this is not ideal. Hence, it is important to induce selectivity for these processes.[18–20] Catalysts can dictate the selectivity of a given reaction and induce selective transformations to yield a single enantiomer over the racemic mixture. A method of quantifying the enantioselectivity of a reaction is the enantiomeric excess (*ee*) (**Equation 1-10**).

$$Enantiomeric\ excess\ (ee) = \frac{[R] - [S]}{[R] + [S]} \times 100\ \%$$

Equation 1-10. Calculation for *ee*, where [R] and [S] represent the concentration of the respective enantiomer.

It is important to note that the ground state energies for an *R* or *S* enantiomer of a given substrate are identical, however, across the reaction coordinate in the presence of a chiral catalyst the enantio-determining transition states are different (**Figure 1-3**). The enantiomeric excess is dictated by differential activation parameters of those listed in **Equation 1-1**, leading to **Equation 1-11**.

$$\Delta\Delta G^{\ddagger} = \Delta\Delta H^{\ddagger} - T\Delta\Delta S^{\ddagger}$$

$$\frac{k_R}{k_S} = e^{\frac{-\Delta\Delta G^{\ddagger}}{RT}}$$

Equation 1-11. Relationship between the rate constants of the formation of two enantiomers and the relative Gibbs activation energy.
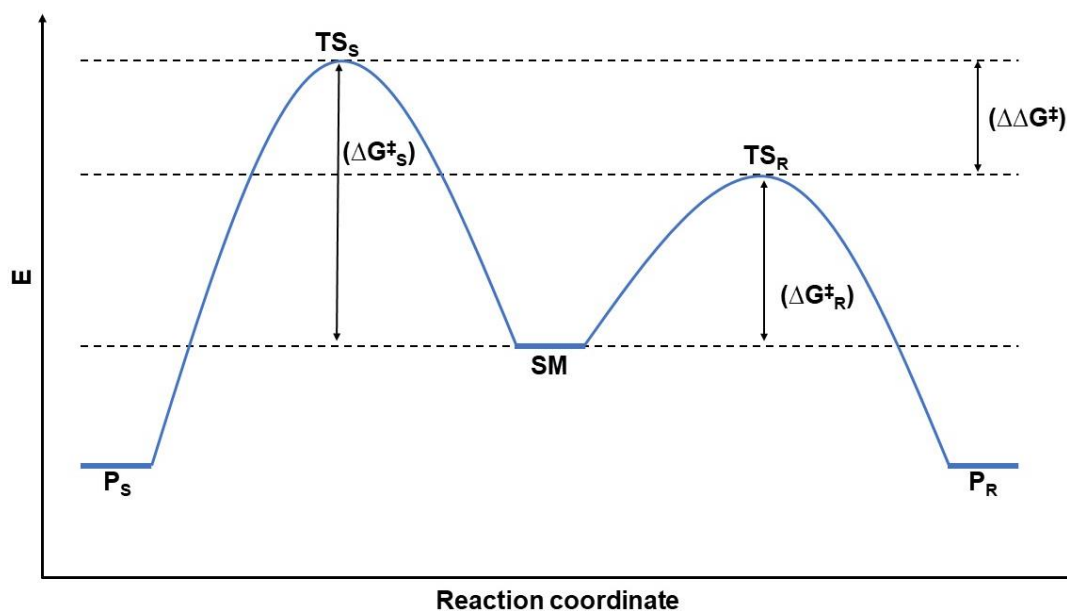
Figure 1-3. Reaction coordinate for an enantioselective reaction. $\Delta\Delta G^{\ddagger}$ is the difference in energy between the $\Delta G^{\ddagger}_R$ (pro-*R* transition state) and $\Delta G^{\ddagger}_S$ (pro-*S* transition state). P_S and P_R refer to the *S*- and *R*-products respectively. SM is the starting material.

An increase in the difference in energies for the pro-*R* and pro-*S* transition states results in a higher enantioselectivity. To design an efficient catalyst, it is therefore important to take all these metrics into account.

The one size fits all approach to catalysis is rarely adopted, and it is only by judicious and rational design that catalysts are implemented for a given chemical transformation.

1.2 Activation of dihydrogen (H₂)

Organometallic complexes have attracted a lot of attention in the development of hydrogenation catalysts because of their ability to form metal-hydrogen bonds in hydride complexes that facilitate catalysis. The splitting of dihydrogen under standard conditions is an energetically demanding transformation and requires an energy input of 103.9 kcal mol^{-1}.[21] Transition metals, however, can activate small molecules such as dihydrogen and dinitrogen under ambient conditions, bypassing the energy input required to split H_2 and yield transition metal hydrides.[22,23]

One of the first transition metal hydride complexes was an iron carbonyl complex, [(H)$_2$Fe(CO)$_4$], discovered by Hieber,[24,25] at this point the occurrence of the M-H bond was not fully understood, it was only later, when Wilkinson probed the existence of a Re-H bond through a series of spectroscopic experiments for Cp$_2$ReH,[26,27] that the transition metal-hydrogen bond was better understood.

The location of the hydride in the crystal structure of [Rh(H)(CO)(PPh$_3$)$_3$] prompted much speculation about metal hydrides, and how dihydrogen is activated, either as dihydride (M(H)$_2$) or as dihydrogen ligands (M-η^2-H$_2$) (**Figure 1-4**).[28,29]
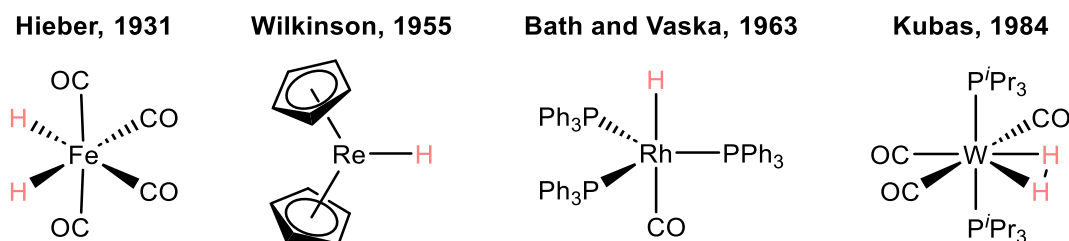
Figure 1-4. Some early reported transition metal hydride complexes, note the different coordination of H_2, as either (H)$_2$ or (H$_2$).

Seminal work by Vaska *et al.* on the addition of H_2 to [IrCl(CO)(PPh$_3$)$_2$] (termed Vaska's complex) at 298 K yields the corresponding dihydride complex ([Ir(H)$_2$Cl(CO)(PPh$_3$)$_2$]. The coordinatively unsaturated Ir^{I} species is formally oxidized to Ir^{III} upon hydrogenation (**Scheme 1-1**). This study demonstrated how small molecules are activated in the presence of an electron-rich transition metal at standard temperature. [30,31]
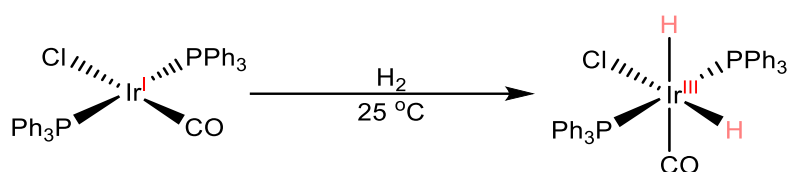
Scheme 1-1. Activation of Vaska's complex by H_2 addition to yield $[IrCl(H)_2(CO)(PPh_3)_2]$.

The splitting of H_2 is proposed to occur through an M-H σ interaction, with d-orbitals on the metal donating electron density to the $σ^*$ orbitals of the H_2 molecule. This interaction weakens the H-H bond and strengthens the M-H bond through subsequent back-bonding from the H_2 σ orbitals (**Figure 1-5**).[32,33]
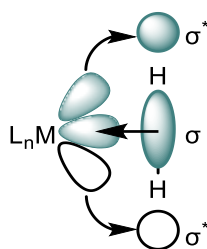
Figure 1-5. σ–only interactions between M and H_2. L represents a ligand.

The degree of back-bonding determines whether a dihydride or dihydrogen complex is formed. This was highlighted by Kubas with the synthesis and characterization of a tungsten dihydrogen complex ($[W(CO)_3(η^2-H_2)(P^iPr_3)_2]$), the dihydrogen molecule is highly labile in this case and a constant H_2 pressure is necessary to examine the complex as a $η^2-H_2$ isomer. Broadly speaking, less electron rich metal centres (for example cationic species) favour dihydrogen complexes, and more electron rich metal centres, hydride complexes.[34] Through advances in computational techniques, alongside advanced NMR, IR and crystallographic studies, metal hydrides are now routinely studied. The detection of transition metal hydrides and phosphines using spectroscopic techniques has helped elucidate several hydrogenation mechanisms in situ.[35–38]

Wilkinson's catalyst $[RhCl(PPh_3)_3]$, for example, is a precatalyst that is used in the hydrogenation of prochiral substituted olefins. In this case, the PPh_3 ligand dissociates in solution to yield an electron deficient 14 electron complex which is stabilized through solvation. H_2 is activated by the Rh^I complex to a Rh^{III} complex (**Scheme 1-2**).[39,40] The species $[RhCl(H)_2(PPh_3)_2]$ hydrogenates the olefin and is subsequently regenerated through H_2 splitting.
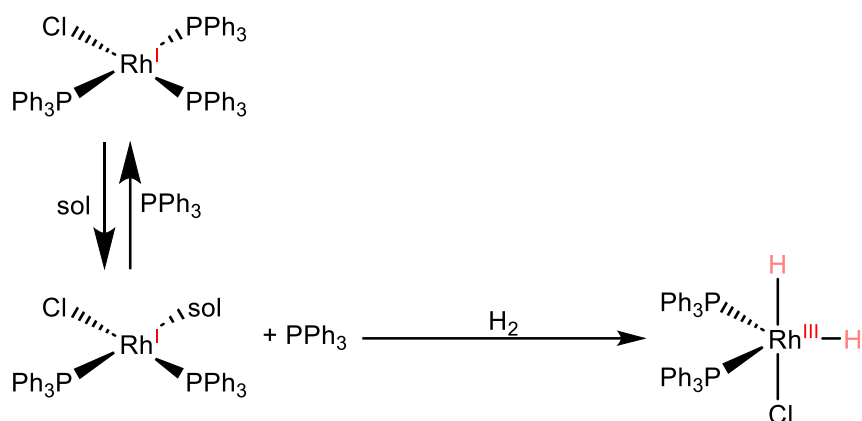
Scheme 1-2. Route to the formation of $[RhCl(H)_2(PPh_3)_3]$ used in the hydrogenation of olefins. Note that the triphenyl phosphine ligand readily dissociates to yield a coordinatively unsaturated $[RhCl(PPh_3)_2]$ complex.

Vaska's and Wilkinson's complexes yield dihydride species upon the addition of H_2, in both cases the metals are formally oxidised ($M^I \rightarrow M^{III}$ (M = Ir, Rh)). This phenomenon is termed as homolytic cleavage of H_2 and is observed with nucleophilic metals (**Scheme 1-3**).

Heterolytic cleavage   Homolytic cleavage
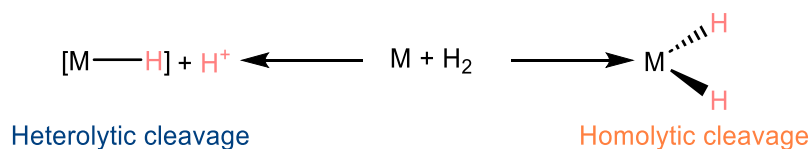
Scheme 1-3. Transition metal activation of dihydrogen through; (a) heterolytic cleavage and (b) homolytic cleavage.

Heterolytic cleavage of H_2 is an alternative activation mechanism that results in the polarization of dihydrogen to a hydride (H^-) and proton (H^+) ligand. The polarization of hydrogen results in ligation of the hydride to the metal. The proton is then susceptible to nucleophilic attack by an external base, ancillary ligand, or an anion.[41] Heterolytic cleavage, unlike homolytic cleavage, does not change the oxidation state of the metal, and is observed with several catalytic systems.[42,43]

1.2.1 Hydrogenation

From a practical standpoint the activation of H_2 is useful for hydrogenation catalysts to facilitate the hydrogenation of prochiral substrates. Several mechanisms have been studied and generally depict the hydrogenation occurring *via* H transfer from the transition metal centre to the unsaturated molecule.[44,45] These mechanisms are discussed later (**1.3**), however, a general scheme for the hydrogenation of a prochiral ketone is shown in **Scheme 1-4**.

The scheme shows the stepwise process of the catalytic cycle for the inner-sphere hydrogenation mechanism wherein the reagent binds to the metal centre and is subsequently hydrogenated. While using H_2 is a popular way to reduce these functional groups on an industrial level, an alternative process called transfer hydrogenation exists.
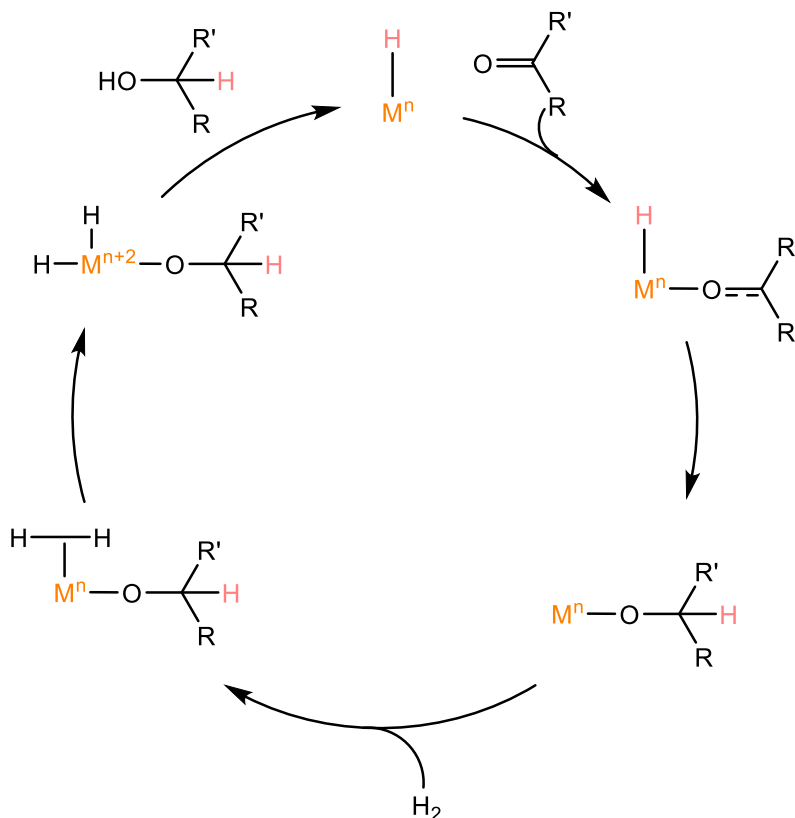
Scheme 1-4. Inner-sphere (redox) mechanism of hydrogenation of a prochiral ketone.

1.2.2 Transfer hydrogenation

Hydrogenation generally refers to the addition of pressurized H_2 gas to reduce a molecule, whereas transfer hydrogenation refers to the transfer of hydrogen atoms from a donor molecule to the substrate molecule without the direct application of H_2. Transfer hydrogenation reagents are typically alcohols where the α-hydrogen atom and hydroxyl hydrogen provide a source of hydrides and protons respectively (**Scheme 1-5**) and can also include reagents such as formic acid, hydrazine and dihydroanthracene.[35,46] Transfer hydrogenation provides the advantages of an operationally simple experimental setup, the reagents are typically inexpensive, and side-products can be easily separated from the reaction mixtures.[47,48] The reaction is driven forward by forming another alcohol upon hydrogenation of a ketone.
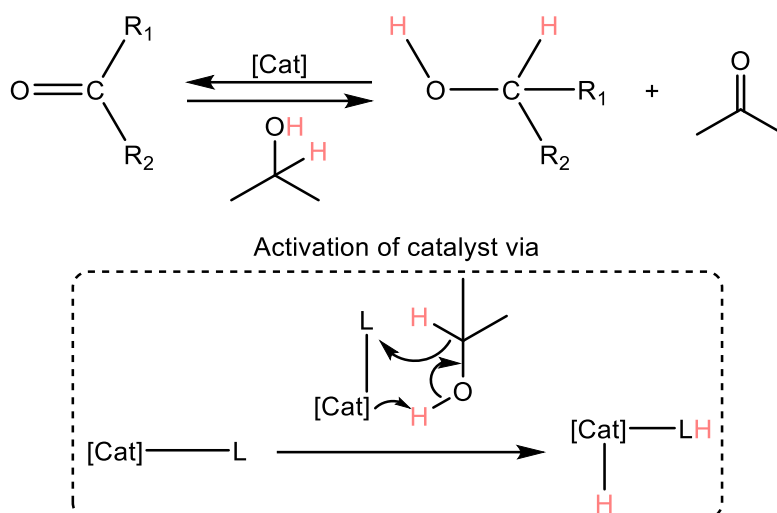
Scheme 1-5. General scheme for transfer hydrogenation using isopropanol as a transfer reagent. Acetone is lost as a by-product of the reaction.

[Ru(Cl)$_2${(*S*)-BINAP}{(*S*,*S*)-dpen}] (BINAP = 2,2′-bis(diphenylphosphino)-1,1′-binaphthyl; dpen = diphenylethylenediamine) (**Figure 1-6**) used for enantioselective hydrogenation of ketones can work *via* hydrogenation or transfer hydrogenation to yield chiral products. Over the course of the reaction the H atoms are split into a hydridic and protic components, which coordinate to the Ru and N atoms respectively.[45,49,50] This system operates through an outer-sphere mechanism, there is no substrate coordination to the metal centre and the reaction occurs outside of the coordination sphere of the metal.
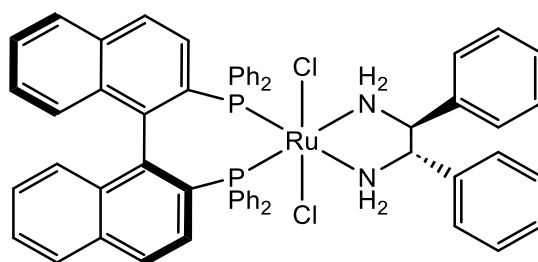
Figure 1-6. [Ru(Cl)$_2${(*S*)-BINAP}{(*S*,*S*)-dpen}] the precatalyst used for the asymmetric hydrogenation of ketones.[45,49,51]

1.3 Hydrogenation mechanisms

The optimization of substrate specific hydrogenation relies on an understanding of the reaction mechanism. The evaluation of reaction mechanisms is thus important to create robust catalytic systems. Hydrogenation mechanisms are broadly classed by the catalyst interaction with the substrate. This is often influenced by the ligand within the transition metal complex, which is discussed in later sections (**1.4**), however, this subchapter aims to give a brief overview on a selected few hydrogenation mechanisms (**Figure 1-7**), and ligands are discussed where applicable.

**Inner-sphere
Metal-ligand cooperativity (MLC)**

Inner-sphere dihydride

**Inner-sphere
Meerwein-Ponndorf-Verley (MPV)**

**Outer-sphere
Metal-ligand cooperativity (MLC)**

Cation-assisted
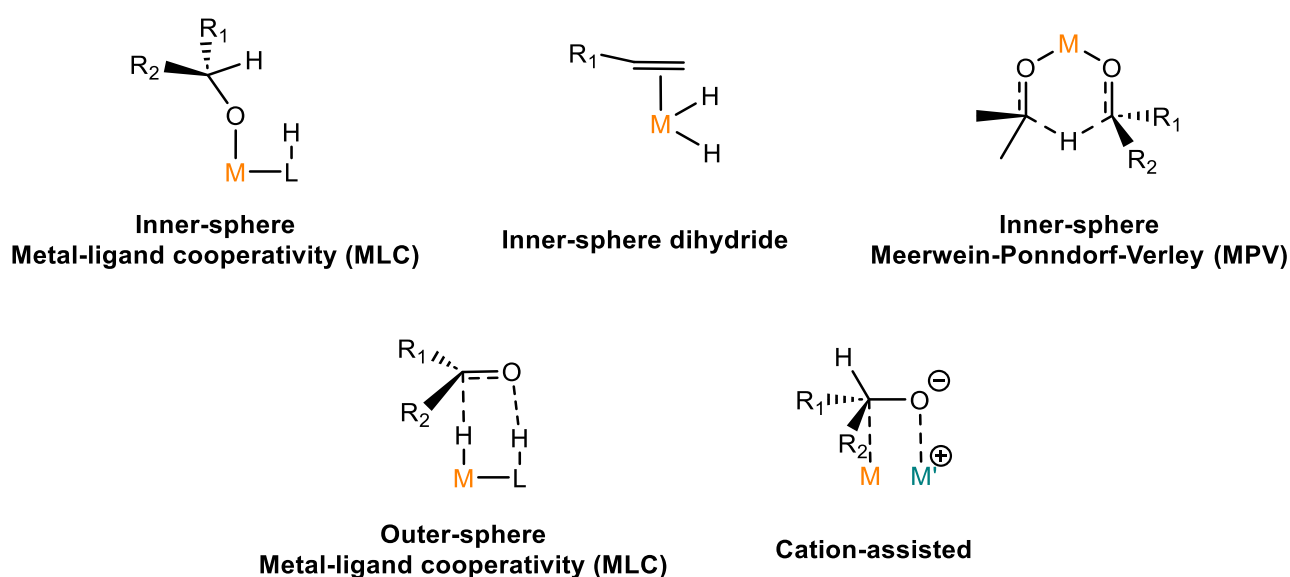
Figure 1-7. Representation of intermediates in hydrogenation reactions. Inner-sphere (top), and outer-sphere mechanisms (below) intermediates are shown.[46,52–55]

1.3.1 Substrate considerations

The enantioselective reduction of polar bonds including carbonyls and imines is an area of research that has made tremendous progress in the past decade owing to transition metal catalysts. The high value products obtained (chiral alcohols and amines) are of particular interest to the manufacture of fine chemicals and pharmaceuticals.[56–59]

C=O bonds for example are highly polarized, bind weakly to transition metal centres, and show weak H-bonding interactions. As a result of these parameters, catalytic systems can be designed to best optimise the hydrogenation. The substrate often influences the reaction mechanism based on the interaction with the coordination sphere of the complex.[60]

The directing effect observed for terpen-4-ol in the presence of Crabtree's catalyst ([Ir(COD)(PCy$_3$)(py)]) exemplifies how the directing effect of the substrate can influence reactivity and selectivity. The -OH group on the terpen-4-ol interacts within the metal coordination sphere to direct hydrogenation to occur on the face of the molecule bearing the -OH group (**Figure 1-8**).[61]
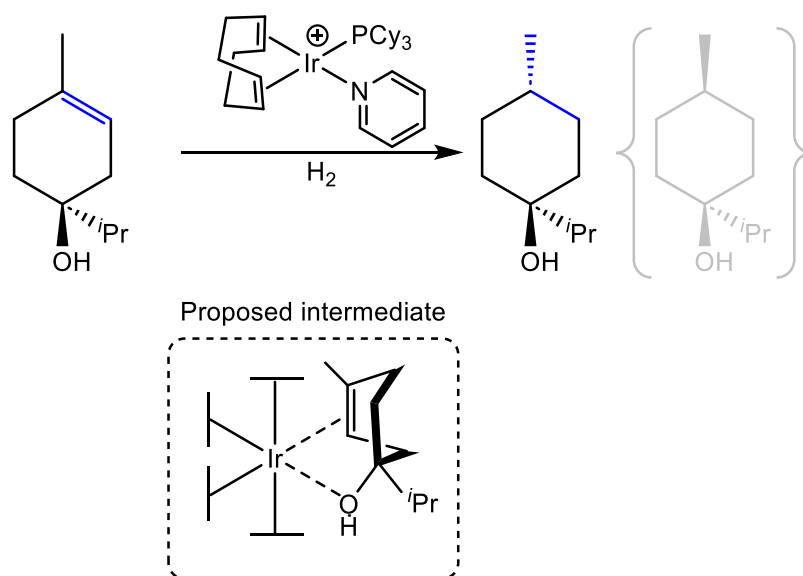
Figure 1-8. Selective hydrogenation of terpinen-4-ol.[61]

1.3.2 Inner-sphere mechanisms

The inner-sphere hydrogenation was briefly alluded to in **1.2.1**. This method of hydrogenation is characterized by substrate coordination to the metal centre, and the subsequent insertion of the substrate to the M-H bond.[62,63]

In principle, the general mechanistic steps involved for the inner-sphere mechanism all follow the same pathway i.e. coordination of the substrate to the metal followed by hydrogenation, however, the choice of ligand, metal, source of hydrogen and substrate all constitute to several different types of mechanisms observed.

1.3.2.1 Monohydride inner-sphere

Monohydride in this context refers to the hydride on the transition metal that is active in product formation, the second H atom is associated with the hydrogen source. The first step of this mechanism involves substrate coordination to the metal centre. Insertion of the substrate to the M-H bond, and dihydrogen is then split by the transition metal (oxidative addition) to yield

the metal dihydride.[33] Finally, the product is formed by reductive elimination – regenerating the metal hydride catalyst (**Scheme 1-6**).

The well-known $[Rh(H)(CO)(PPh_3)_3]$ catalyst used for the hydroformylation of alkenes, follows this mechanistic pathway.[64] The mechanism is proposed to occur *via* dissociation of one the PPh_3 which creates a vacant site for alkene coordination to the Rh centre.
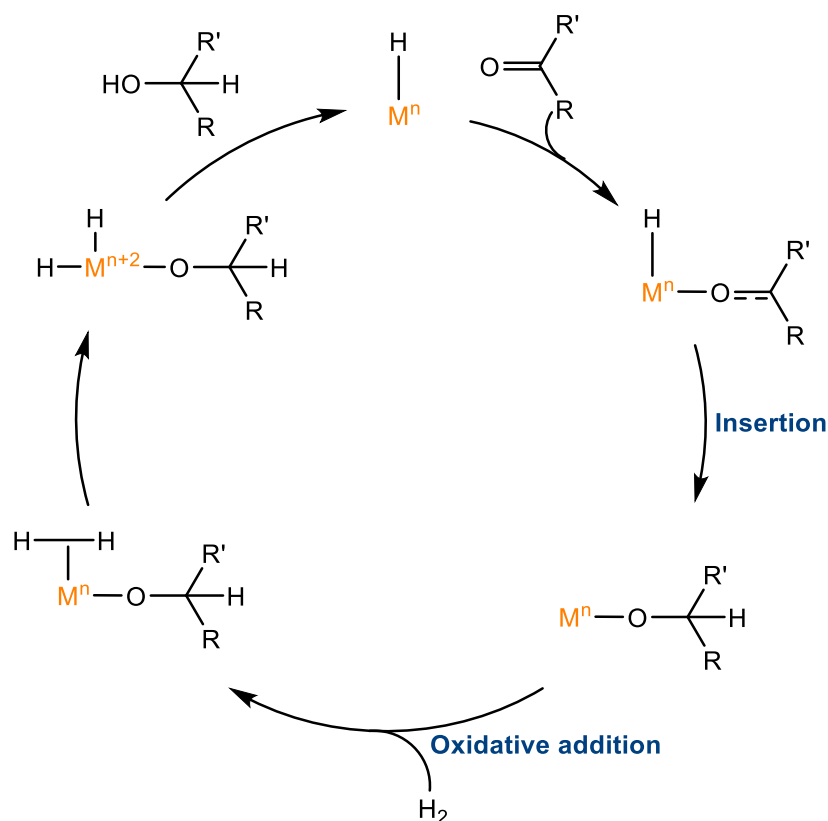
Scheme 1-6. Inner-sphere mechanism for hydrogenation – monohydride transition metal catalysts.

Transfer hydrogenation of functionalised ketones have been demonstrated with Ir^{III} catalysts acting *via* the monohydridic route, notably $[Ir(I)_2(bis\text{-}NHC)]^+$ (bis-NHC = methylenebis[(*N*-2-methoxyethyl)imidazole-2-ylidene]) (**1-7**) (**Scheme 1-7**).[65] The reaction mechanism proposed requires dissociation of the ether group and isopropoxide binds to the vacant site (**1-7a**). The second ether then dissociates allowing β-hydride elimination of the C-H group on the isopropoxide (**1-7b**). The directing effect of the NHC forces the complex to isomerize so that the hydride is now trans to the iodide (**1-7c**), in doing so the incoming ketone is coordinated to the iridium trans to the NHC group. Subsequent isomerization places the hydride cis to the ketone which is then reduced partially by the hydride (**1-7f**) and fully upon the addition of isopropanol.[66,67] The reaction shows high conversion approaching 99% in the presence of an external base which is presumably used to prompt the formation of isopropoxide and drive the

reaction forward.[68] Note how the first and second hydride used to initiate the reaction come from an external source, in this case the isopropanol.
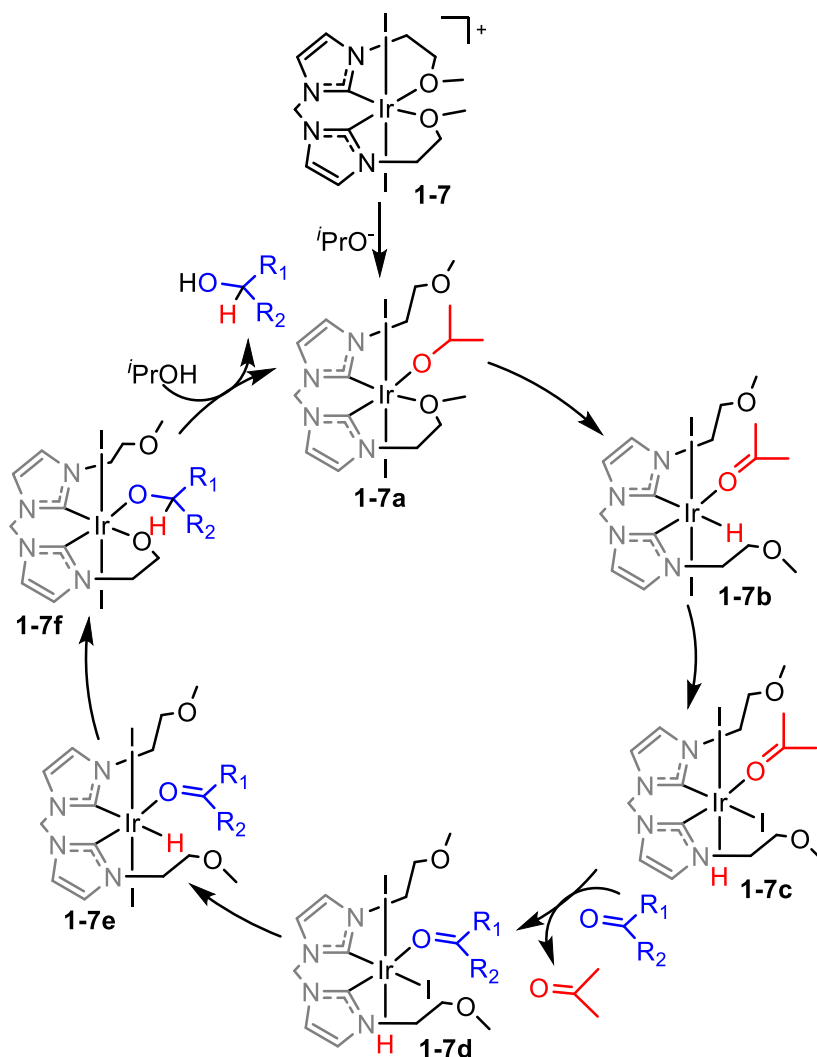
Scheme 1-7. Proposed catalytic cycle for the transfer hydrogenation of ketones through an inner-sphere mechanism – based on a DFT study.[66,67]

1.3.2.2 Dihydride inner-sphere

A variant of the inner-sphere mechanism, the dihydride inner-sphere mechanism proceeds through the application of a dihydride complex generated from a precatalytic species. The precatalyst typically contains weakly coordinating ligands that are readily removed upon H_2 activation. As such the oxidative addition of H_2 precedes substrate coordination, followed by H insertion and reductive elimination to generate the product. Loss of the product regenerates

the vacant coordination site on the metal, oxidative addition of dihydrogen then regenerates the dihydride species (**Scheme 1-8**).[69]
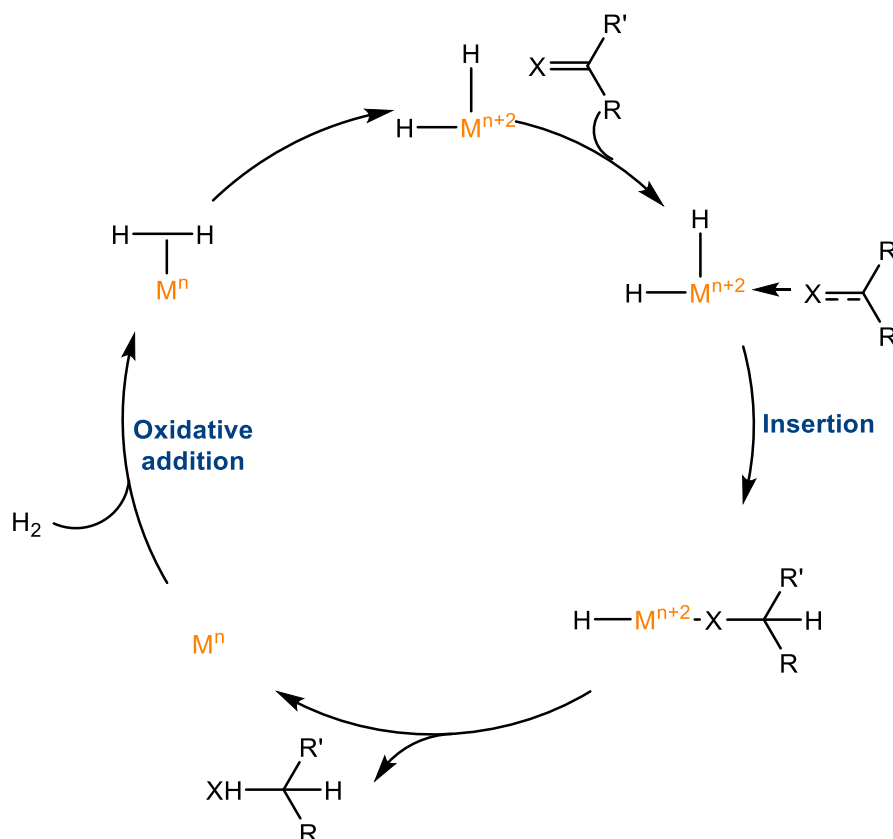
Scheme 1-8. Inner-sphere hydrogenation with a dihydride species. Note that after the reductive elimination of the product, a vacant coordination site is created along with a formal reduction of the transition metal.

The choice of ligand strongly influences the mechanism observed, i.e., either dihydride or monohydride inner sphere. To differentiate the mechanism, an experiment involving racemization of an optically active α-deuterated alcohol (*S*)-phenyl ethanol was set-up to distinguish the monohydride or dihydride route. The dihydride route results in deuterium scrambling between the carbon and oxygen atoms, whereas the monohydride route results in deuteration at the α-position only (**Scheme 1-9**).[70]

Notably Wilkinson's catalyst operates through the dihydride mechanism for the hydrogenation of alkenes. [39,40] Note how a vacant coordination site is first generated from the precatalyst to yield the active dihydride species involved in the catalytic cycle (**Scheme 1-10**).
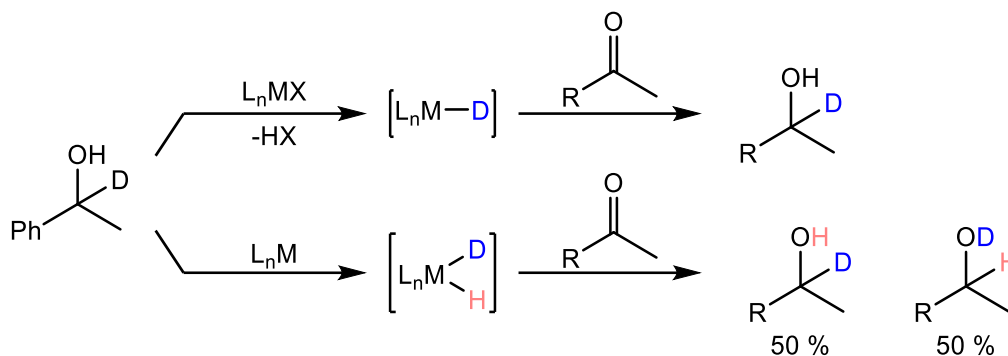
Scheme 1-9. Deuterium labelling experiment to determine the mechanism of hydrogenation. (Top) Monohydride, and (Bottom) dihydride routes of hydrogenation.[70]
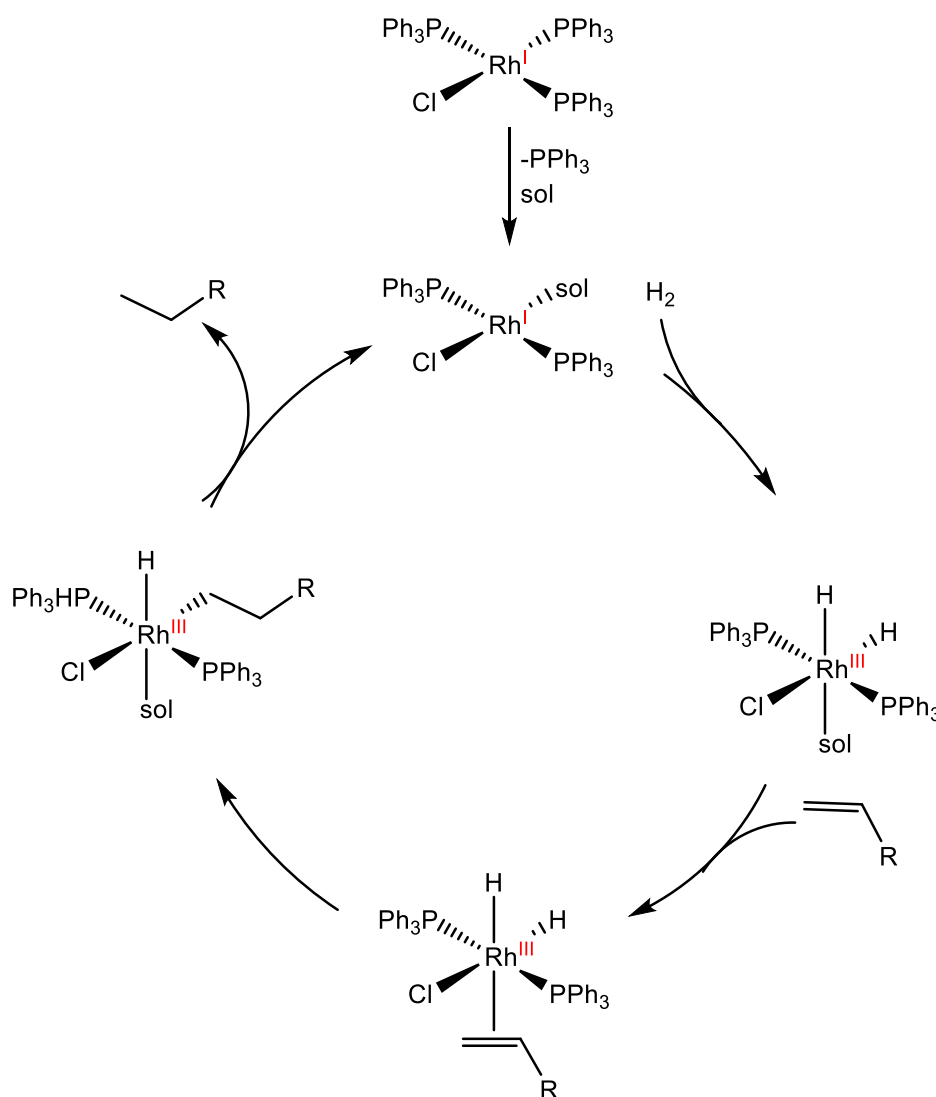
Scheme 1-10. Reduction of an alkene using Wilkinson's catalyst.

1.3.2.3 Metal-ligand cooperativity (MLC) Bifunctional catalysis

Bifunctional catalysis in this context refers to catalysts that operate *via* a mechanism of hydride and proton transfer. Hydrogen is delivered to the substrate in two components; a hydride is transferred from the first coordination sphere of the transition metal, and a proton from the ligand. To compensate for the loss of a proton, the ligand may temporarily change from a 2-electron donor to a 1-electron donor, however, upon the ionic activation of hydrogen, the ligand tautomerizes to its original form (**Scheme 1-11**). When an external proton source is used the catalyst is regenerated *via* splitting of H_2 within the coordination sphere of the metal and the external source.[46]
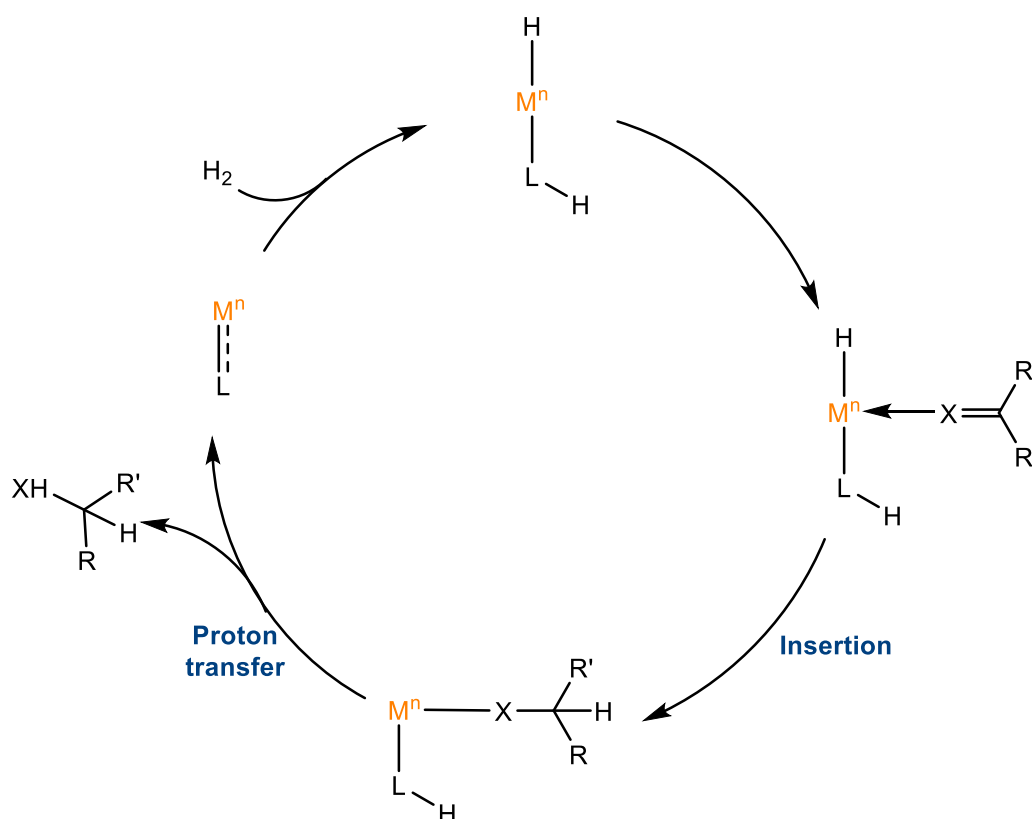
Scheme 1-11. Bifunctional mechanism of hydrogenation.

This mechanism was proposed for a Ru^{II} acetamido system that catalyses the hydrogenation of acetophenone. This process follows a stepwise H^-/H^+ transfer from ruthenium and ligand. In this example the ligand supplies the proton and stabilization of the catalyst is achieved through ligand tautomerization. A further DFT study on this mechanism, however, showed the preference for an inner-sphere mechanism rather than the outer-sphere alternative (**1.3.3.1**).[71,72]

1.3.2.4 Meerwein-Ponndorf-Verley (MPV)

The mechanism of the MPV reduction has been well-studied and follows direct coordination to the metal. This mechanism relies on hydrogen-transfer to facilitate the reduction and is typically observed for main group Lewis acid catalysts such as aluminium alkoxides,[73] used in the chemoselective reduction of ketones. Both the transfer reagent and substrate coordinate to the metal centre with the product being formed through a six-membered transition state (**Scheme 1-12**).[74]
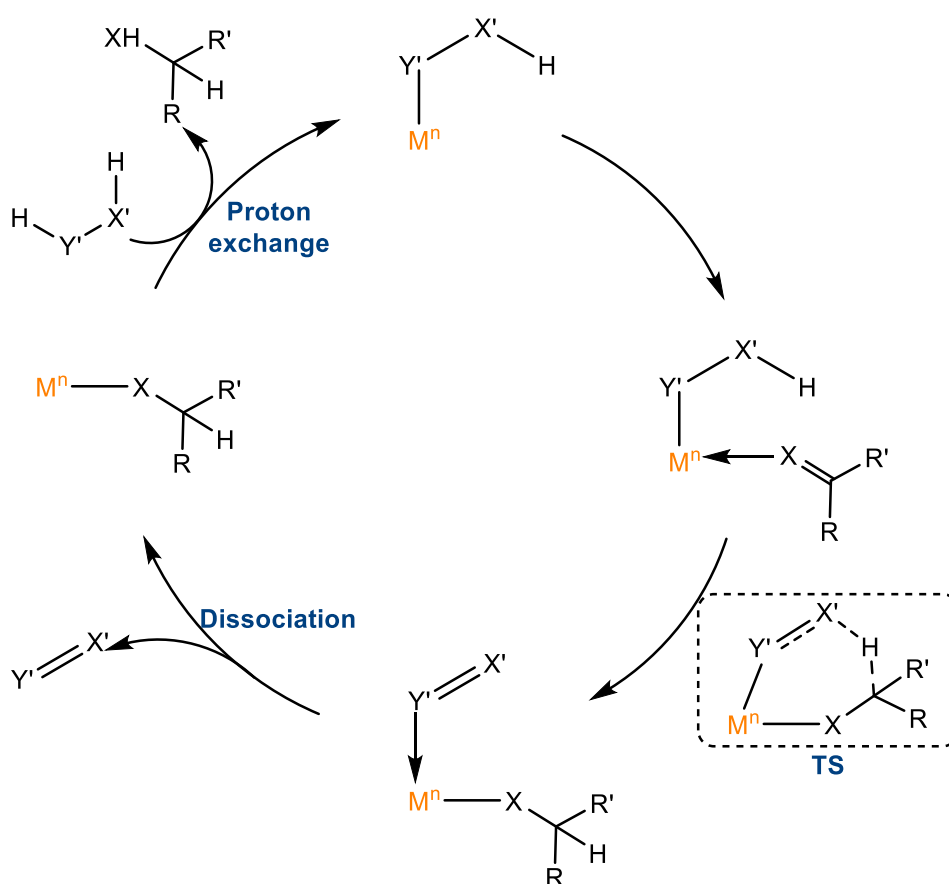
Scheme 1-12. MPV Mechanism of hydrogenation.

This mechanism has also been reported for some transition metal systems. Most notably a computational study on the 16 electron Ir-system, [Ir(MeS(CH$_2$)$_2$NH)(COD)], indicated the hydrogenation occurring through the MPV route. The COD ligand remains bound to Ir^{III} as the hydrogenation proceeds through direct hydrogen transfer between the ketone and alcohol (**Scheme 1-13**).[75] The significance of COD and ancillary ligands is discussed in later chapters (**1.4.1**) for its role in hydrogenation and stabilization of transition metal complexes.
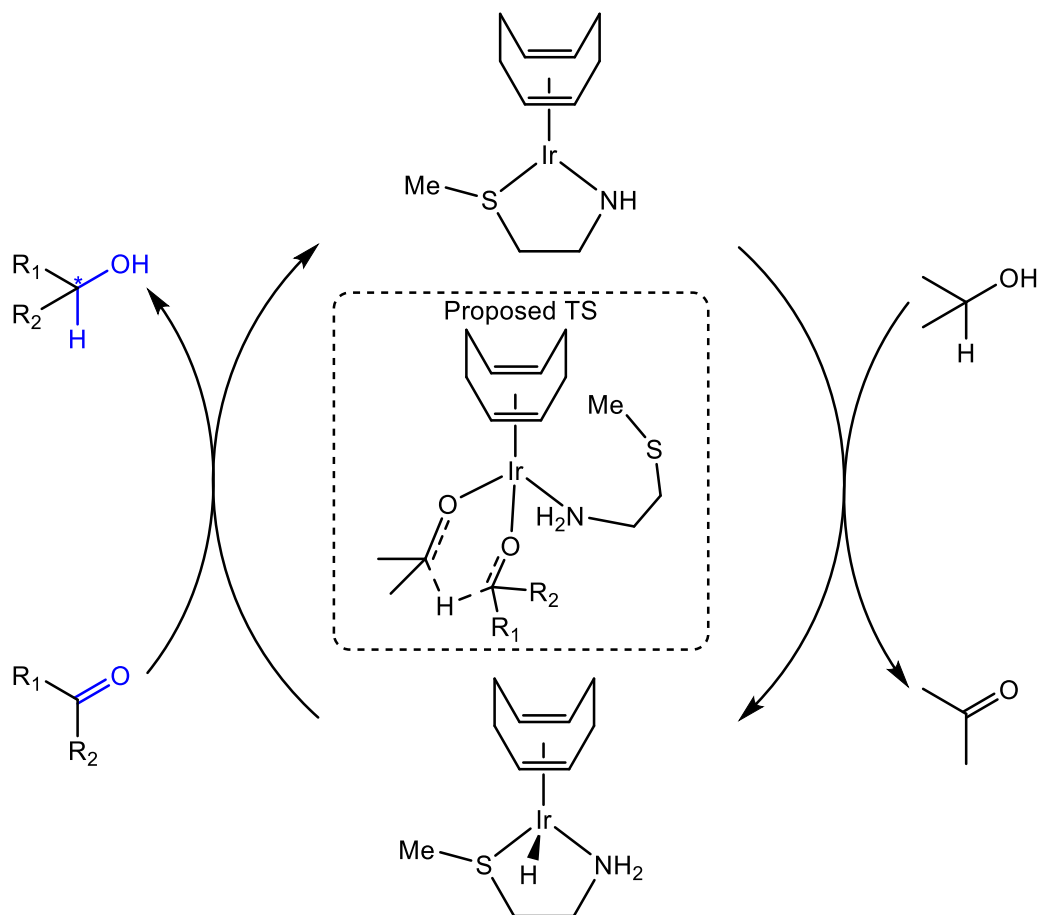
Scheme 1-13. Direct hydrogen transfer with an [Ir(COD)(aminosulfide)] complex.[75]

1.3.3 Outer-sphere mechanisms

The mechanisms discussed previously (**1.3.2**) all occur within the first coordination sphere of the metal. An alternative mechanism of hydrogenation that takes place outside of the coordination sphere of the metal, aptly named outer-sphere hydrogenation also exists. In these cases, there is no direct coordination of the substrate to metal or M-H insertion.

1.3.3.1 Bifunctional (MLC) outer-sphere

This mechanism follows the same basic principle of its inner-sphere counterpart, of H^+/H^- transfer to the substrate by the ligand and metal respectively. A preference for the outer-sphere was seen by Noyori and co-workers when computing the mechanism of hydrogenation for a Ru^{II} catalysed reduction of carbonyls. This work demonstrated that a more energetically favourable pathway (ca 10 kcal mol^{-1} lower in energy) is observed for the outer-sphere hydrogenation mechanism compared to the inner-sphere alternative.[62,76] The reaction is most

often established through hydrogen bonding between the proton on the ligand and the substrate (C=X⋯H-L).[52]

This mechanism was proposed by Zhang and co-workers for the asymmetric transfer hydrogenation of various alkyl aryl ketones, with an iridium f-Amphox complex. The computational study established a working mechanism *via* which the amino ligand and iridium donate H$^+$/H$^-$ to the substrate to yield chiral alcohols (**Scheme 1-14**).[77]
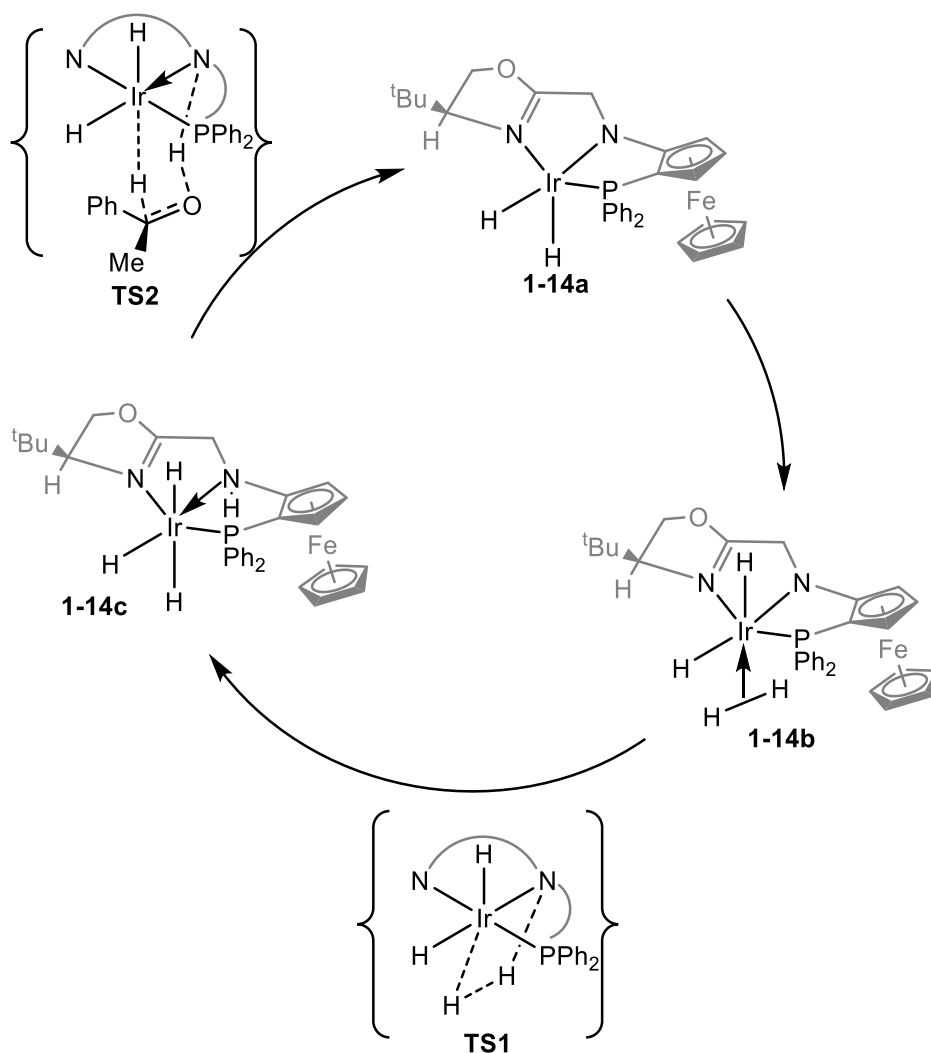
Scheme 1-14. Proposed mechanism for the transfer hydrogenation of a functionalized ketone using Ir^{III} f-Amphox.[77]

Special care must be taken when using computational methods to evaluate this reaction mechanism, however, as the solvation effects have been shown to influence the energy cycles of the proposed reaction. A result of this is the proposition of two different mechanisms that stem from the bifunctional outer-sphere mechanism. The proton and hydride transfer can occur synchronously or can occur in a stepwise fashion.[52]

This mechanism was proposed by Noyori and co-workers for their pioneering work on the asymmetric transfer hydrogenation of carbonyls by [RuH$_2$(diphosphine)(diamine)] complexes.[78] The reaction is accelerated in the presence of an excess of strong base such as KO^{t}Bu.[79] Bergens *et al.* investigated the effect of the base on the Noyori type catalyst and found that the formation of an alkoxide intermediate occurs in an irreversible manner. This alkoxy intermediate is the kinetic product and not the amido complex as originally proposed.[51,80]

Further work by Dub and co-workers showed that an alternative approach based on an excess of base deprotonating the proton on the N-H ligand serves to stabilise the transition state (N-K$^{..}$O-R) of the reaction intermediate (**Figure 1-9**).[81] The proposal is that the ligand acts as a spectator ligand in the proton transfer.[82] The subsequent H$_2$ activation step occurs through cation and hydrogen-bonding interactions.[83,84,79]
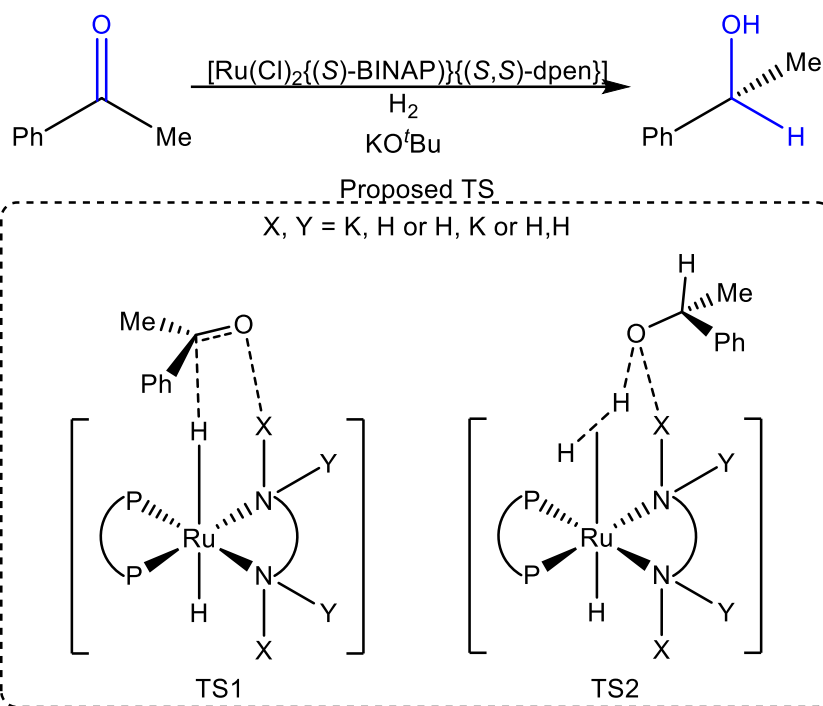
Figure 1-9. Key transition states in the asymmetric transfer hydrogenation of acetophenone with [Ru(H)$_2${(*S*)-BINAP)}{(*S*,*S*)-dpen)}] in the presence of excess KO^{t}Bu.[81]

However, this new mechanistic pathway cannot be universal, because when other catalysts with non-X-H ligands were employed for the asymmetric hydrogenation of prochiral ketones, it was found that the reaction still occurs.[84]

1.3.3.2 Dihydrogen outer-sphere

In this mechanism ionic dihydrogen activation takes place before the H^+/H^- transfer, a dihydrogen complex is formed *via* H_2 addition across the metal. Proton transfer then occurs resulting in an electrophilic carbocation which is presumably stabilized by solvent molecules in the reaction medium. Hydride transfer to the carbocation then occurs to yield the product and regenerate the metal complex. This mechanism is most common for cationic catalysts which increase the acidity of the (η^2)-H_2.[46,85] This mechanism was proposed for the hydrogenation of quinolines by a cationic $[Ir(H)_2(\eta^2\text{-}H_2)(NHC)(PPh_3)_2]^+$ (**1-15a**) system, importantly the mechanism proposed by DFT is consistent with the experimentally observed intermediates (**Scheme 1-15**).
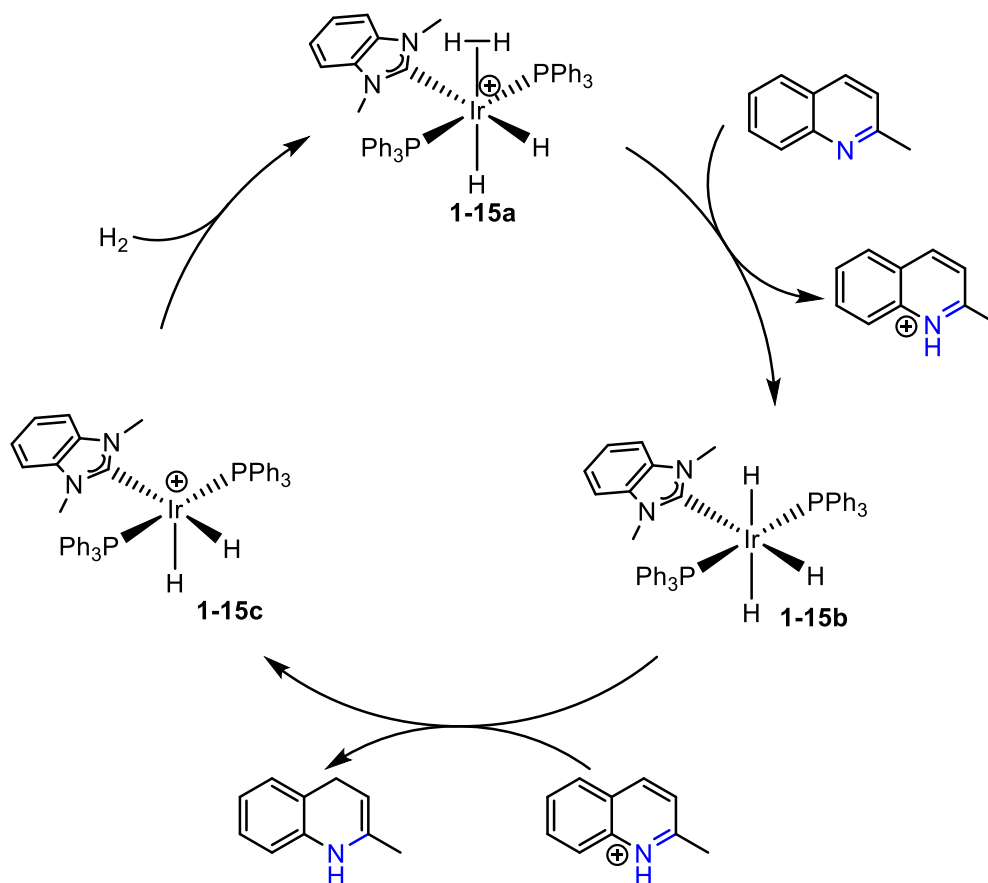
Scheme 1-15. Outer-sphere dihydrogen hydrogenation mechanism with cationic $[Ir(H)_2(\eta^2\text{-}H_2)(NHC)(PPh_3)_2]^+$.[85]

1.3.3.3 Cation-assisted hydrogenation

This is an ionic mechanism where a hydride is transferred to the prochiral substrate through an outer-sphere mechanism. The carbanion is stabilised by the coordinatively unsaturated metal, and the Lewis acid counterion. The catalyst then activates hydrogen through an ionic mechanism and a proton is abstracted by the carbanion to release the hydrogenated product. This mechanism is proposed for anionic catalysts that are stabilized through the presence of a suitable Lewis acid (Li^+, Na^+, and K^+).[82,86,87] The presence of a strong base had been proven to increase the activity of the catalytic system. Computational and experimental evaluations, support this notion and propose that an excess of base facilitates the hydrogenation mechanism through Lewis acid interactions with the substrate (**Scheme 1-16**).
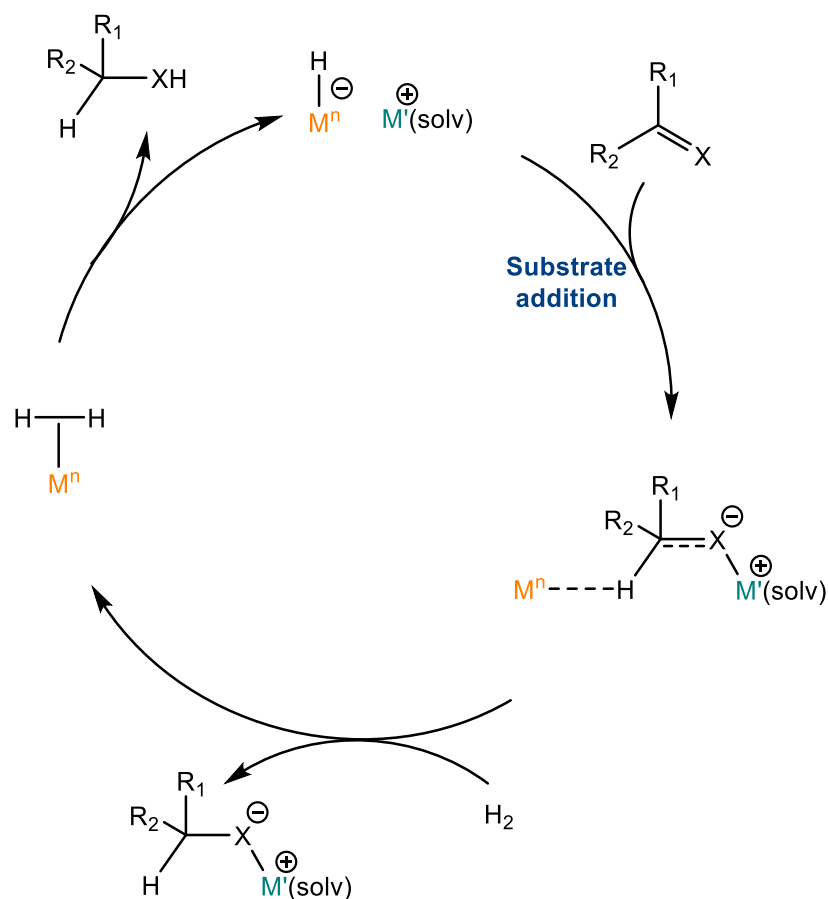
Scheme 1-16. Outer-sphere mechanism - cation-assisted hydrogenation.

Studies on an iridium phosphino thioether complex exemplified the necessity of a base to drive the transfer hydrogenation of acetophenone to completion. The $[Ir(COD)(P,S^{Ph})Cl]$ (P,S = {CpFe-[1,2-C_5H_3(PPh_2)(CH_2SR)]}) precatalyst in the presence of a strong base loses the chloride as a metal chloride salt. Computational investigations suggested that the active

catalyst is an anionic tetrahydrido iridium species, $[Ir(H)_4(PS)]^-$ generated after cyclooctadiene loss as cyclooctene or cyclooctane.[83,88]

In the absence of a base the reaction shows low conversion.[89] However, upon the addition of an excess of a strong base high turnover is restored.[90] The computational investigation suggests that the hydrogenation occurs through the outer-sphere with a cation (Na^+) assisting the reaction through non-covalent interactions with the substrate (**Scheme 1-17**). The study prompted questions about the existence of an anionic tetrahydrido iridium complex, and the effect the cation has on the asymmetric hydrogenation of prochiral ketones. This seminal work inspired the work presented in this thesis.
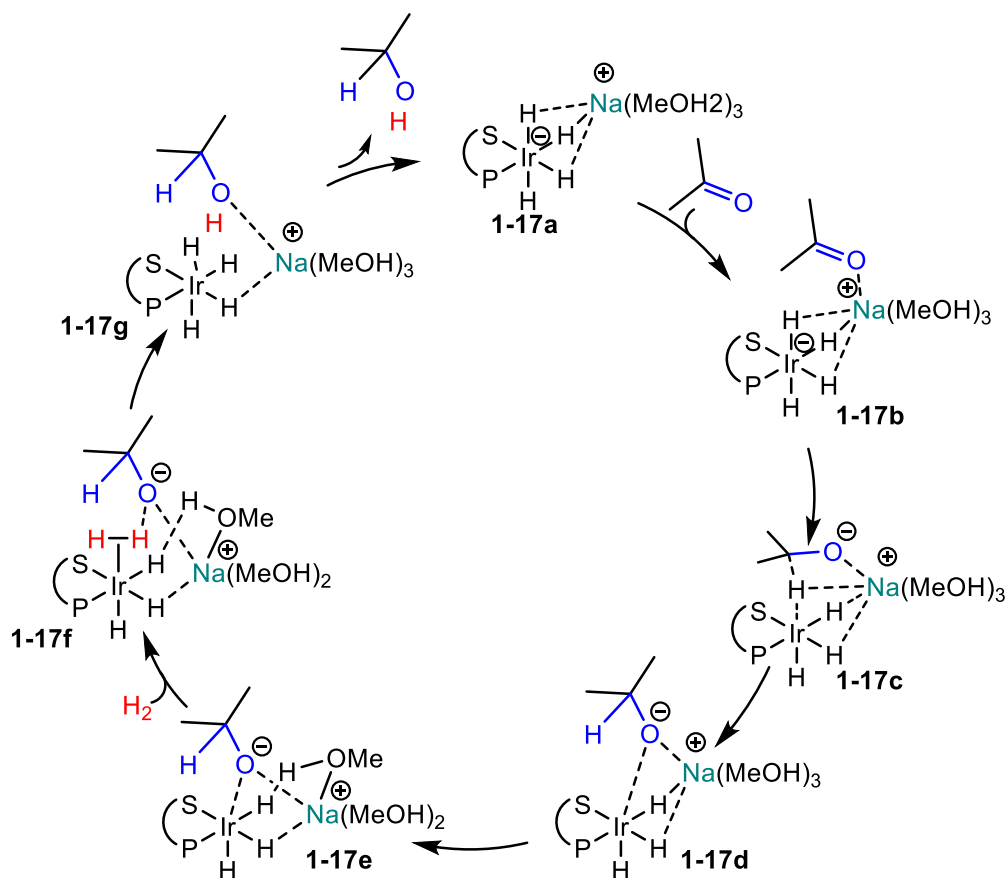
Scheme 1-17. The proposed cation assisted outer-sphere hydrogenation mechanism with a $Na^+[Ir(H)_4(P,S)]^-$ system based on DFT calculations.[87]

1.4 Ligand development

While metal ions readily activate H_2 (or hydrogen transfer reagents) for subsequent hydrogenation processes they rarely exist in solution as independent ions. Chemical selectivity is determined by the ligands within catalytic species.

One of the most well publicized examples of a neutral donor ligand was the introduction of BINAP with Ru to yield a Ru^{II}-BINAP complex. Ru^{II}-BINAP shows high selectivity for the hydrogenation of homoallylic alcohols and is used to generate enantiopure alcohols.[91] Substrate interactions with the active site of the catalyst are influenced by BINAP, and through molecular interactions stereospecific reactivity is promoted. This results in high enantiomeric excess (over 95%).

Iridium-phosphine complexes have also shown an application in the selective hydrogenation of carbonyl groups within α,β-unsaturated carbonyls. These complexes are generated in situ *via* the addition of a phosphine to a solution containing an iridium containing precursor, $[Ir(OMe)(COD)]_2$. The phosphine ligands readily displace the labile cyclooctadiene ligand to yield an active catalyst.[92]

Hydrogenation catalysts utilize varying types of ligands, some of these are aprotic neutral donor atoms, protic neutral ligands, and single electron donor ligands. Electron deficient Lewis acids (note BR_2) can also be used as ligands and/or to facilitate reactions (**Figure 1-10**).[93–95]
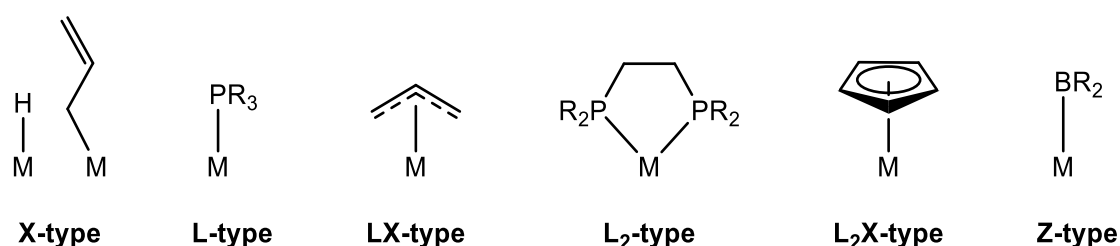
Figure 1-10. Different types of donor (X, L, LX, L_2, L_2X) and acceptor ligands (Z).

Whilst it may seem obvious, it is important that precatalytic systems are less reactive than the catalytically active species. This lack of reactivity allows the reagents, metal species and ligands to be manipulated under standard conditions. Hence, with the design of novel ligands, it is important to introduce systems that improve existing reactions (in terms of activity and selectivity) but are also robust to external conditions. Highly efficient ligands that can only be synthesised in low yields or are sensitive to external conditions will invariably be disfavoured for widespread applications.[96] A few different types of ligands relevant to the hydrogenation of

polar substrates are discussed below (**1.4.1**, **1.4.2**). The list is not exhaustive but aims to contextualize ligands involved in the scope of this thesis.

1.4.1 Ancillary ligands

Ancillary or spectator ligands provide stability to transition metal complexes through the occupation of otherwise vacant coordination sites. In a sense these ligands occupy vacant coordination sites that would otherwise render the complex too reactive.[97] In some cases, these ligands are involved in stabilization of species across the reaction coordinate, however, do not directly participate in the reaction.[98] In other cases, these ligands may dissociate upon the addition of different reagents.

Iridium precursors, $[IrCl(COD)]_2$ and $[Ir(OMe)(COD)]_2$, are frequently used in conjunction with phosphine or amine ligands to yield precatalytic systems.[22,58,85,99] One crucial question that remains is whether the COD ligands in precatalyst systems remain coordinated to the metal in the catalytically active species without being hydrogenated. Although it seems logical to presume that COD is removed under hydrogenation conditions (i.e., under H_2), whether this also occurs under transfer hydrogenation conditions (particularly in warm isopropanol) has been controversial. For instance, the $[IrCl(diene)]_2$/aminosulfide/HCOOH/NEt$_3$ system was reported to show diene-dependent activity in the order COD > 1,5-Me$_2$COD > (COE)$_2$ (COE = cyclooctene) at 60 °C.[100] These observations led the authors to propose that the diene or alkene remains metal bound in the active species, but the intimate nature of the active species remained obscure. In a combined experimental and computational investigation of the acetophenone transfer hydrogenation catalysed by $[Ir(OMe)(COD)]_2$/L at 60 °C in isopropanol, where L is a P- or N-donor ligand, the active species was also considered to have the diene in the metal coordination sphere.[98] On the other hand, several other studies on similar systems, conducted under similar conditions, have shown evidence for the release of COD (either in a hydrogenated form or not).[101–103]

Some precatalytic systems containing a bound COD ligand also exhibit interesting binding properties through isomerization of the ligand. It was shown that when a methanol solution of $[Ir(OMe)(COD)]_2$ is treated with a series L$_2$-type diphosphines (dppe or *o*-C$_6$H$_4$(PPh$_2$)$_2$) the regularly bound 1,5-cyclooctadiene complex $[Ir(H)(\eta^2,\eta^2\text{-}C_8H_{12})(L_2)]$ is observed in addition to an isomerized $[Ir(H)(\kappa^1,\eta^3\text{-}C_8H_{12})(L_2)]$ product.[104,105] The reactivity of COD was explored further *via* activation through the addition of acetonitrile to $[Ir(\eta^2,\eta^2\text{-}C_8H_{12})(NCCH_3)(PMe_3)]BF_4$ complexes, showing how the η^2,η^2 to κ^1,η^3 COD rearrangement is favoured.[106] Rearrangement of C$_8$H$_{12}$-COD ligands has also been demonstrated with electron deficient (cationic) iridium systems through acid catalysed mechanisms (**Figure 1-11**).[107]

Fabbian **Martin** **Raible**
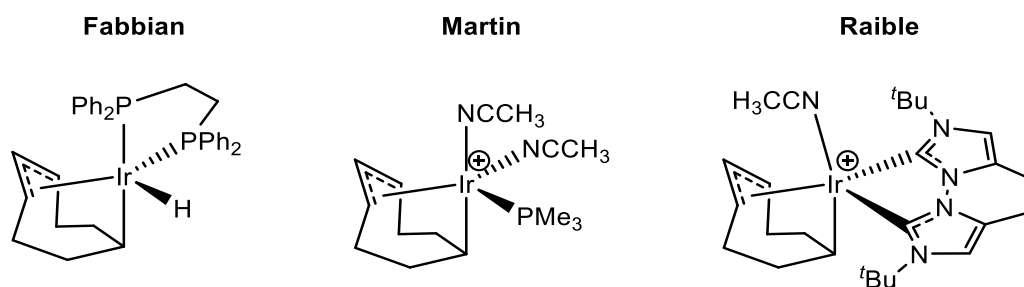
Figure 1-11. Reported complexes with κ^1,η^3-COD ligands.[105–107]

It is therefore important to evaluate precatalytic systems as their reactivity is not always straightforward, catalyst design relies on a thorough examination of the precatalyst so that reaction conditions can be optimized. The effect of the base on C_8H_{12}-ligands in iridium-phosphine complexes is explored in **Chapter 2:** and the fate of COD under transfer hydrogenation (and hydrogenation conditions) in **Chapter 3:**.

1.4.2 Phosphine containing ligands

Phosphines are also ancillary ligands; however, these do not dissociate upon addition of a substrate or during the course of a reaction (unlike COD). The successful implementation of hydrogenation catalysts is owed in large part to the wide array of different ligands available. Organophosphorus compounds are some of the most popular ligands used due to their electronic and steric tuneability and to the ability to form strong bonds with transition metals.[96,108] The P-M bond is formed through P to M σ-donation, and M to P π-back-bonding (**Figure 1-12**).[109]
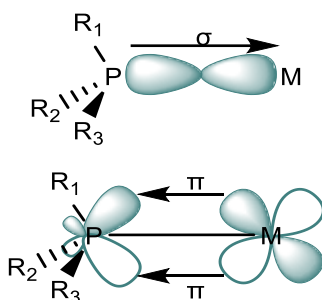
Figure 1-12. Classical σ and π interactions between M and P. The interactions are representative of M-P bonding interactions (a) σ donation; (b) π-back-bonding.

The interactions between M and P vary depending on the R groups on the phosphine, for example if a strongly electronegative R group is used, the PR_3 ligand shows weak σ-donation but is strongly π-accepting. Conversely, R groups that are weakly electronegative yield ligands

with stronger σ-donation properties. While these ligands are ancillary in nature too, they have a more significant effect on catalytic through structural modification (**1.4.2.1**).

1.4.2.1 Diphosphine ligands

This section discusses diphosphine ligands, as singly coordinating phosphines are less commonly employed for reaction processes requiring enantioselectivity. Multidentate phosphines also provide greater thermodynamic stability than monodentate ligands (chelate effect).[110,111] Multidentate ligands have the added advantage of supplying more conformational information to catalytic systems making these ligands desirable for asymmetric catalysis. Chiral diphosphine ligands, such as DIPAMP,[112] DIOP,[113] BINAP,[50,114] and Josiphos,[115] have all contributed greatly to the development of asymmetric hydrogenation catalysts (**Figure 1-13**).[108,116] The design of many 1,2-disubstituted diphosphine ferrocene ligands like Josiphos has been well documented, and importantly applied commercially for asymmetric catalysis.[58,115–119]

BINAP   **DIOP**   **DIPAMP**   **Josiphos**
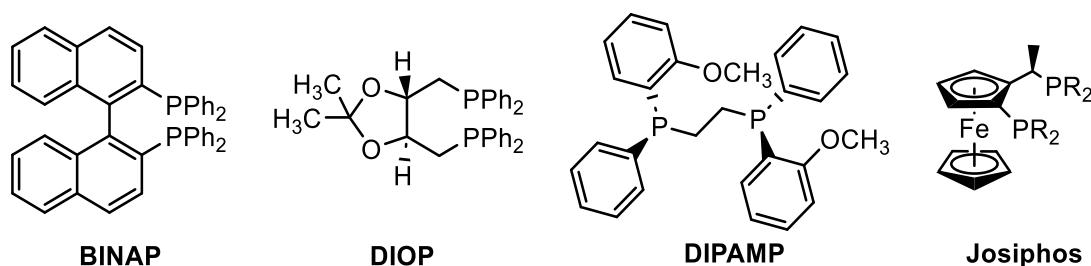
Figure 1-13. Historically relevant chiral diphosphine ligands used in asymmetric hydrogenation reactions.[112–115,120,121]

Modifications within the framework of these seminal ligands show wide-spread application in asymmetric catalysis, and have inspired numerous other P,P ligands in the past few decades. For example, BINAP was discovered in the 1980's[120] but, almost four decades later BINAP and its derivatives are still being explored for utilization in asymmetric reactions.[122–124] Some examples of hydrogenation of polar substrates utilizing structural variants of the diphosphines shown in **Figure 1-13** ligands are shown in **Scheme 1-18**.

It is important to recall that metal-phosphine complexes are also routinely studied using ^{31}P NMR spectroscopy. The in-situ analysis of key intermediates aids the proposal of catalytic mechanisms some of which are discussed in **1.3**.[69,125,126] Metal phosphines are also used to model isoelectronic complexes to explore the reactivity of more structurally complicated systems and are discussed in this thesis.
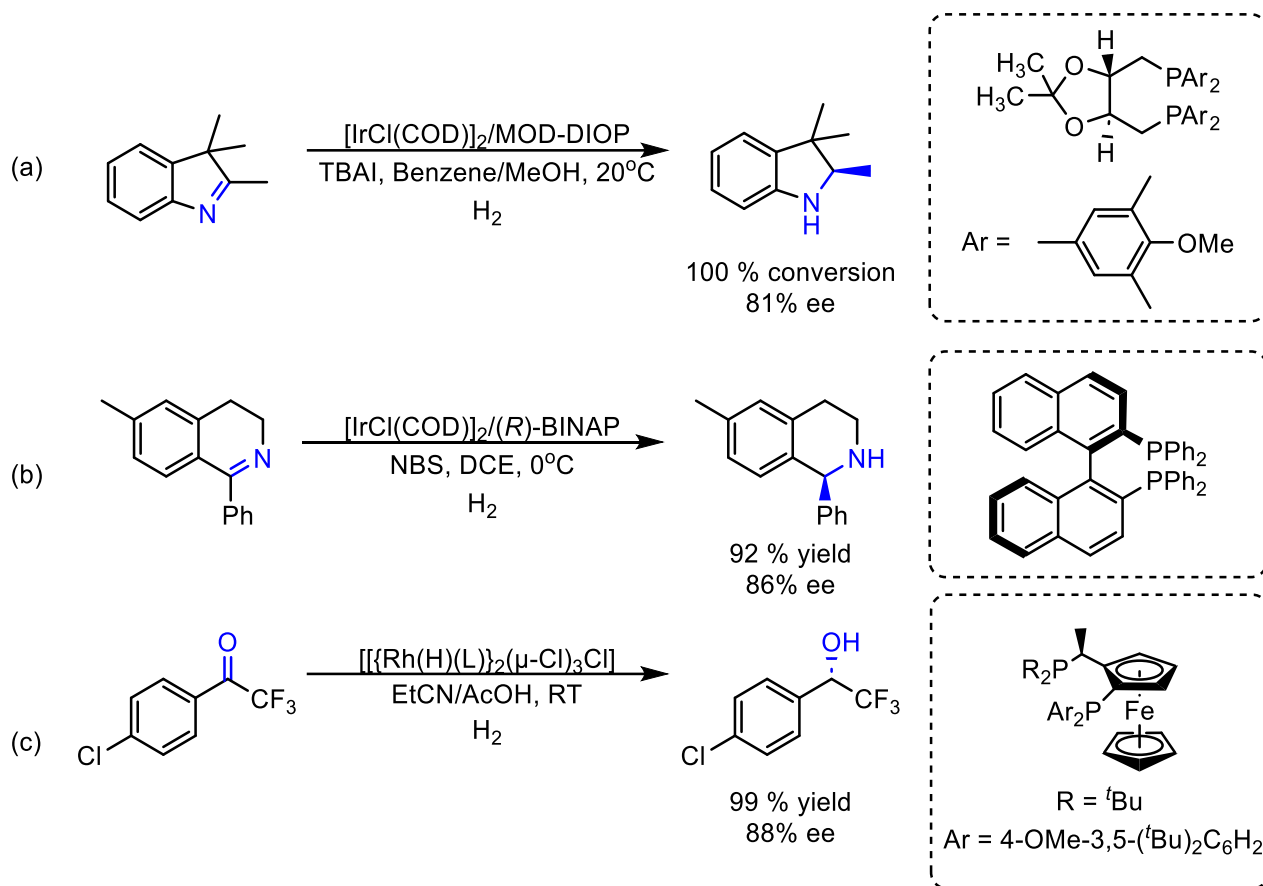
Scheme 1-18. Asymmetric hydrogenation reactions utilizing diphosphine ligands. (a) MOD-DIOP, Morimoto and co-workers, 1994; (b) (*R*)-BINAP, Ji and co-workers, 2018; (c) Josiphos derivative, Brüning and co-workers, 2019.[127–129]

1.4.2.2 Amino-phosphine ligands

The tunability of the phosphine group on the ligand has shown how ligand systems can be varied for specific catalysis. The introduction of a hard σ-donor N-group within a multidentate ligand allows for further structural variation of ligand systems. Even without considering the σ-donor properties by R group variation, the hybridization states of the N-donor can be manipulated to create amino, imino and cyclic imino N-donors to complement asymmetric catalytic processes (**Figure 1-14**).[130–135] Further, functionalization of the R groups on the N portion of the ligand influences the overall electronic and steric properties of the ligand, to aid enantioselectivity.[59,77,135–137]

47
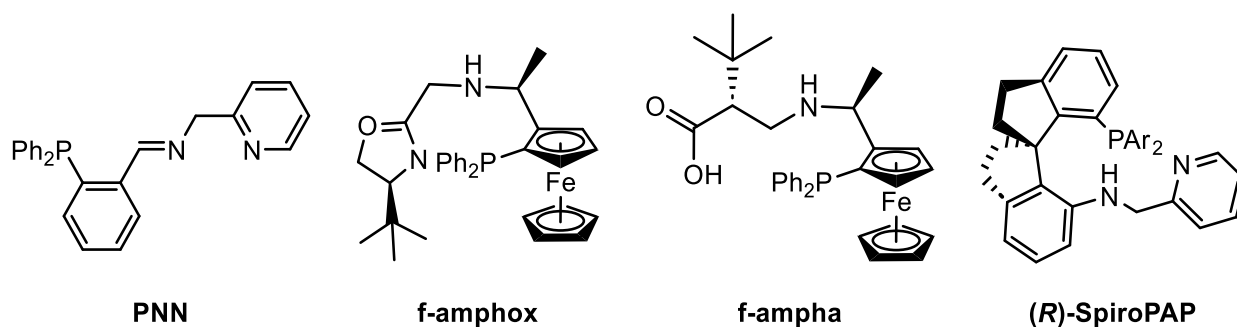
Figure 1-14. Mixed P,N ligand systems with amino, imino, and cyclic imino groups utlized in asymmetric catalysis. PNN = N-(2-(diphenylphosphino)benzylidene) (2-(2-pyridyl)ethyl)amine); Ar =3,5-^{t}Bu-Ph. Note all systems shown are tridentate ligands.[77,86,131,132]

Ligands f-amphox (**Scheme 1-14**) and f-ampha generate active catalysts by in situ mixing with [IrCl(COD)]$_2$ to yield active iridium complexes that are highly effective for the hydrogenation of prochiral ketones (reported > 95% ee). The planar chirality of these ligands induces enantioselectivity. (*R*)-SpiroPAP is also complexed with iridium to yield an active catalyst for asymmetric hydrogenation of simple ketones and β-ketoesters. The enantioselectivity in this case is induced by the chiral spiro centre and by the overall asymmetry of the ligand. These specific systems are highlighted as they are all involved in iridium catalysed hydrogenation, and the respective catalytic systems have been reported to be most active in the presence of a base (**Scheme 1-19**).
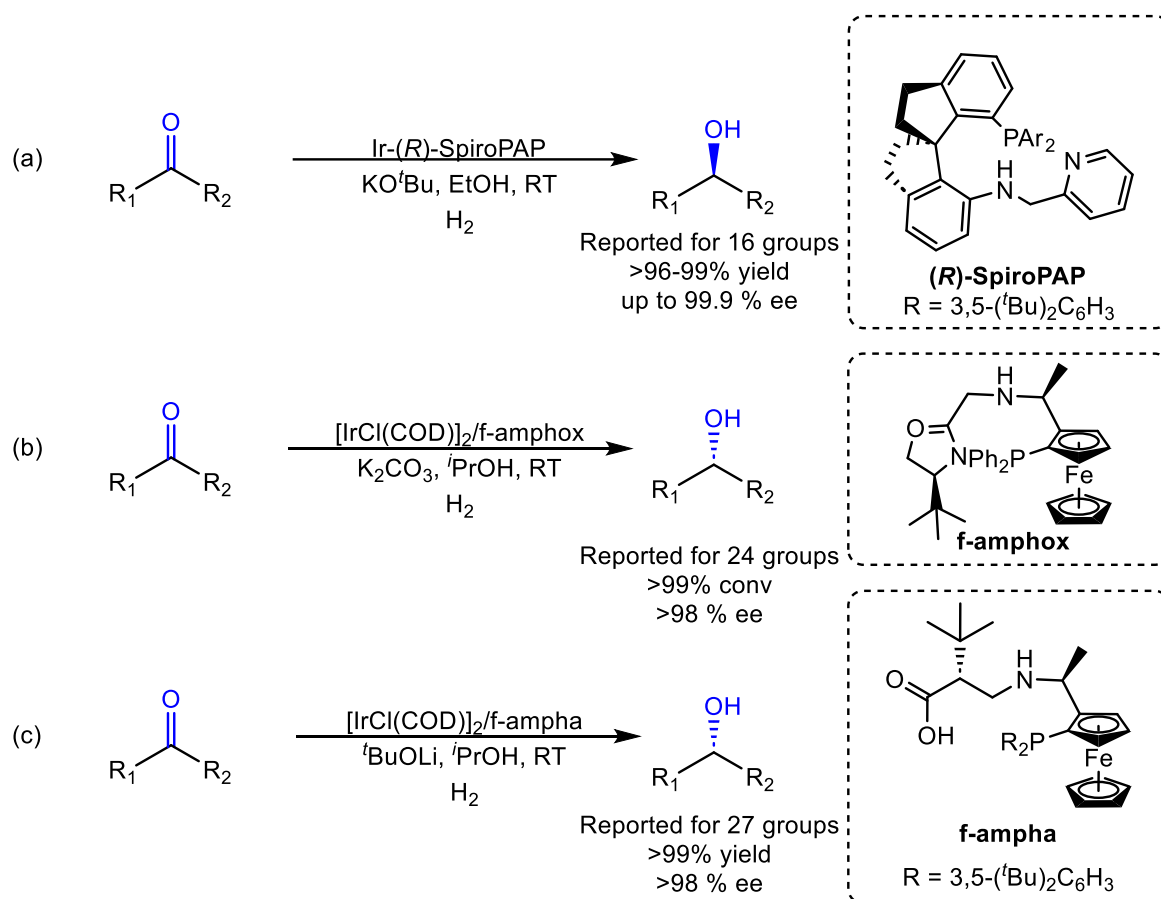
Scheme 1-19. Asymmetric hydrogenation of prochiral ketones with Ir-amino-phosphine based systems. (a)(*R*)-SpiroPAP, Yang and co-workers; (b) f-amphox, Wu and co-workers; (c) f-ampha, Yu and co-workers .[77,86,130–132]

The possibility of combining different donor atoms and R groups on ligands make the search for the perfect ligand seemingly endless. P,N, P,O and P,S type ligands have all been well documented.[138–140] Sulphur containing ligands, for example, while initially underrepresented in the realm of asymmetric hydrogenations have recently gained traction in asymmetric catalysis. Of these types, dithioether ligands have generally shown moderate to low activity and enantioselectivity for the hydrogenation of prochiral ketones.[141,142]

1.4.2.3 Phosphine-Thioether Ligands

More recently, mixed planar chiral thioether ligands have shown more promise than dithioether ligands and have been used successfully in asymmetric catalysis. These P,S-type ligands show excellent activity and enantioselectivity in the hydrogenation of minimally functionalized olefins with rhodium, or iridium.[143,144] The asymmetric hydrogenation of ketones, with iridium-P,S systems ([IrCl(COD)(P,S^R)]) (**Scheme 1-20**), obtained by addition of P,S^R to [IrCl(COD)]$_2$ has also been reported.[145,146] These systems are effective ketone hydrogenation catalysts in

isopropanol in the presence of a strong base, resulting in excellent activities and enantioselectivities; however, in the absence of a base prove to be rather inefficient.[87]

R = Ph, Et, ^{t}Bu, Bz
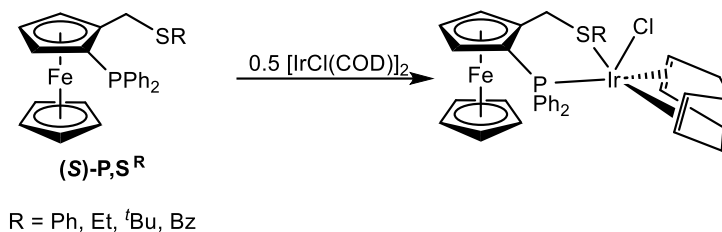
Scheme 1-20. Planar ferrocenyl phosphino thioether ligand (termed P,S^R) used in asymmetric hydrogenation catalysts, and its iridium precatalyst – prompted the study of this thesis.[87,140]

To decipher the role of the base and efficiency of the system, multiple examinations were conducted. One investigation revealed that the COD ligand is quantitatively removed from the catalytic system as a mixture of cyclooctene and cyclooctane, under hydrogenation conditions, and presumably forms [Ir(H)(P,S^R)(^{i}PrOH)] initially.

Using the alternative [Ir(OMe)(COD)]$_2$ precatalyst instead of [IrCl(COD)]$_2$ still requires the addition of a strong base to achieve the same high activities as the [IrCl(COD)]$_2$/(P,S^R)/NaOMe system. The role of the strong base, hence, could not be limited to the generation of an active neutral hydride complex. A parallel DFT study, carried out with inclusion of [MeO(MeOH)$_5$]$^-$ as a model of the strong base, revealed that the most stable species, i.e. likely to be the catalyst resting state, is not a neutral complex, but rather the [Ir(H)$_4$(P,S^R)]$^-$ ion.[87] This complex does not contain the mobile proton needed for a classical outer-sphere (bifunctional Noyori-type) mechanism, nor a vacant coordination site for ketone coordination/insertion. This implies that a cation containing strong base is necessary to stabilize the anionic [Ir(H)$_4$(P,S^R)]$^-$ species and presumably facilitate the reaction. The latter is supported by the DFT study that proposes the reaction takes place *via* an outer-sphere cation assisted mechanism (**Scheme 1-17**). Evidence of an anionic tetrahydride being formed under these conditions for this system has not yet been reported. Anionic iridium tetrahydrides formed with phosphine ligands have been reported elsewhere.[147,148]

1.5   Project outline

The research described in this thesis aims to enhance our understanding of the role the base plays in hydrogenation mechanisms in systems with non-deprotonable ligands.[87] It was inspired by the work described on iridium transfer hydrogenation in the introduction.

Firstly, the effect of a strong base on a model precatalytic system is tested. The model system is bis-phosphine based, using [IrCl(COD)(dppe)], which is isoelectronic with [IrCl(COD)(P,S^R)]. Under ambient conditions changes in the coordination of the cyclooctadiene are monitored by NMR to study the formation of new products and ultimately analyse the kinetics of their formation. The experimental analysis is supported by advanced DFT study, which rationalizes the formation of the four different products that are seen in the model system (**Chapter 2:**). This work demonstrates the chemical non-innocence of the COD ligand in the presence of the base, and how it is the alkoxide rather than the cation that influences these precatalytic transformations under mild conditions with no H_2.

Investigations of the formation of a proposed anionic iridium tetrahydrido species were then investigated under hydrogenation and transfer hydrogenation conditions. Once again, this process was examined in the presence of a base to determine its effect in stabilizing potential anionic species. The scope of model complexes was extended to ligands more typically involved in asymmetric hydrogenation such as BINAP, and with the inclusion of a ferrocene backbone (dppf). Different iridium-diphosphine systems were then tested for their application as hydrogenation catalysts. This was then followed by a thorough DFT investigation of the iridium-dppe tetrahydrido complex, to rationalize the activity of the catalytic species (**Chapter 3:**).

The overall aim is to clarify the operating cycle for [Ir(H)$_4$(P,S^R)] catalysts and identify the role of the base for these systems. Four different Ir-P,S^R catalytic systems were therefore screened, in the presence of three different bases (LiO^{i}Pr, NaO^{i}Pr, and KO^{i}Pr) for the hydrogenation of acetophenone. These results were complemented by an in-depth DFT study on the catalytic effect of the base on the Ir-P,S^{Ph} system with each different cation. Therefore, a detailed mechanistic study, based on the elucidation of new findings across the thesis is presented and combined to propose a mechanistic pathway for the action of [Ir(H)$_4$(P,S^R)] in transfer hydrogenation (**Chapter 4:**).

Chapter 2: Ir^I (η^4-diene) precatalyst activation by strong bases and formation of monohydrides

2.1 Introduction

An established method to generate an iridium-based hydrogenation precatalyst is ligand addition to metal-halide precursors. For example, [IrCl(COD)]$_2$ in the presence of a suitable chiral ligand can form pre-catalytic complexes,[37,77,149] used in the enantioselective hydrogenation of prochiral substrates. The active species is then obtained *in situ* in the presence of H$_2$ or hydrogen donors and, in addition, a base is usually required when the substrate is polar (e.g.*,* a ketone). These transformations are commonly conducted in isopropanol, either as a solvent in hydrogenation (increased H$_2$ solubility compared to non-polar solvents) or as a solvent and reagent in transfer hydrogenation. The role of the base in isopropanol is attributed to the generation of a metal hydride species, formed *via* chloride/isopropoxide exchange, followed by β-hydride elimination to expel acetone (***Scheme 2-1***). Chloride exchange is commonly observed with organolithium reagents, and used to produce Ir-alkyl species where the chloride is removed as a metal salt (MCl).[42,150] These findings highlight two key points concerning base addition. Firstly, the cationic component serves to remove the chloride through an exothermic reaction that drives the reaction forward by the formation of metal salt, and alkoxide coordination to the metal is possible and leads to a hydride species that may act in a catalytic manner.[87]
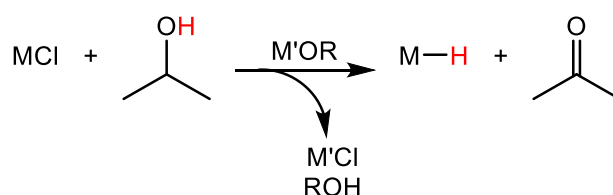
Scheme 2-1. Generation of a metal-hydride *via* chloride/isopropoxide exchange.

The effect of the alkoxide has been explored further. Catalyst precursors that contain an internal base, e.g. ([Ir(OMe)(COD)]$_2$) were shown to form monohydride iridium complexes in the presence of a ligand. These monohydride complexes are proposed to form *via* β-hydride elimination. This route was demonstrated by Oro *et al.*, when investigating [IrH(COD)L$_2$] (L$_2$ = dppe, dppp) complexes as hydrogen transfer catalysts. These complexes were reported as Ir^I complexes with η^2:η^2 cyclooctadiene ligands.[151] Work by Farnetti *et al.* later clarified that for [IrH(COD)(L$_2$)] (**2-1b**) (L$_2$ = dcpe, dppe) type complexes, the cyclooctadiene ligand can adopt

two binding geometries (η^2: η^2 or κ^1: η^3). This is based on the iridium bisphosphine chelate ring size affecting the coordination of COD (**Scheme 2-2**). For these systems cyclooctadiene rearrangement from a regular η^2: η^2 (**2-1b**) mode to a more thermodynamically favourable κ^1: η^3 (**2-1b'**) binding mode was observed.[105]
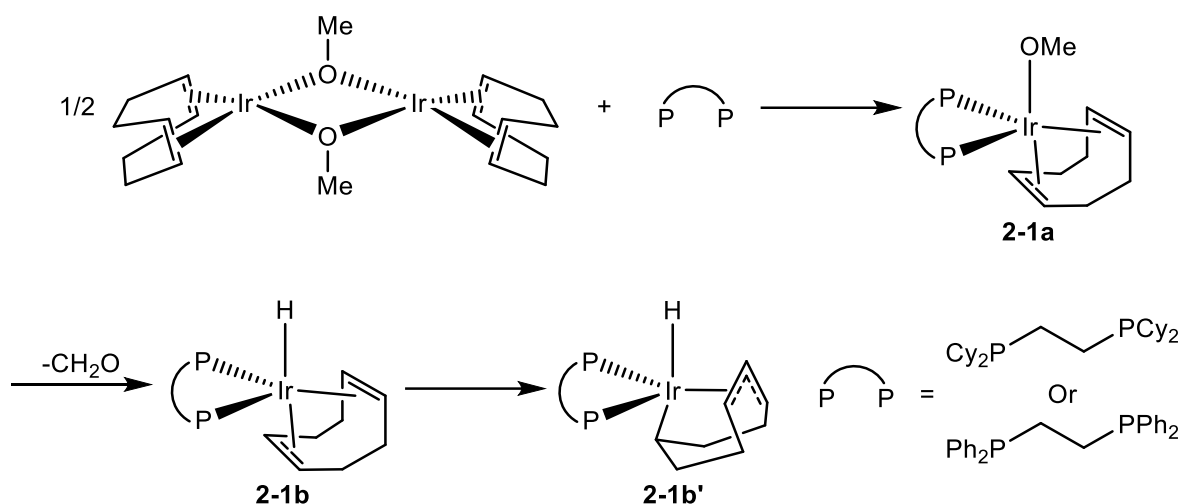
Scheme 2-2. Generation of [IrH(COD)(PP)] complexes from [Ir(OMe)(COD)].[105]

Later work investigated the possible coordination modes of the cyclooctadiene ligand by utilizing a cationic [Ir(PMe$_3$)(NCMe)(COD)]$^+$ complex, in the presence of acetonitrile, diphenylacetylene, and H$_2$. At room temperature in dichloromethane-d_2, the corresponding products were shown to contain cyclooctadiene and cyclooctadienyl ligands. To account for these products, it was proposed that [Ir(PMe$_3$)(NCMe)(COD)]$^+$ (**2-2a**) is in equilibrium with the corresponding hydride complex [Ir(H)(PMe$_3$)(NCMe)(1,2-η^2-4,5,6-η^3-C$_8$H$_{11}$)]$^+$ (**2-2b**) formed through β-hydride elimination (**Scheme 2-3**). When the hydride complex was treated with diphenylacetylene [Ir(1,2,3,5,6-η-C$_8$H$_{11}$)(*Z*-C(Ph)=CHPh)(NCMe)(PMe$_3$)]$^+$ (**2-2c**) was formed demonstrating the occurrence of H-migration from COD.[106]
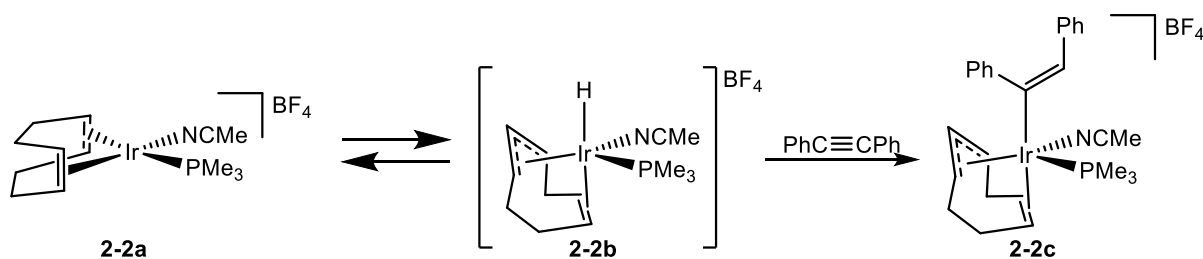
Scheme 2-3. Formation of [Ir(1,2,3,5,6-η-C$_8$H$_{11}$)(Z-C(Ph)=CHPh)(NCMe)(PMe$_3$)]BF$_4$ illustrating β-hydride elimination at the cyclooctadiene ligand leading to C$_8$H$_{11}$.[106]

The effect of the base on the diene ligand has not been extensively studied, and exploration of this, to fully understand precatalytic activation, is the focus of this chapter.

2.2 Aims and objectives

The aim of this chapter was to review the effect the base plays on the reactivity of the iridium complex [IrCl(COD)(dppe)], and thereby enhance the understanding of its role in subsequent transfer hydrogenation catalysis. This work has been published.[152] It highlights the contrasting reactivity that was seen with NaOMe and KO^{t}Bu, in deuterated and non-deuterated solvents, which led to different products.[5]

The reaction of [Ir(OMe)(COD)]$_2$ with dppe, has been explored in prior literature and showed that two monohydride isomers of [IrH(C$_8$H$_{12}$)(dppe)] were formed as a result.[104,105] The characterization and isomerization mechanism for the two isomers was not addressed in these publications. This chapter aimed to fully characterize each product for the reaction of [IrCl(COD)(dppe)] and NaOMe, which presumably lead to [IrH(C$_8$H$_{12}$)(dppe)] *via* β-hydride elimination of the methoxide. NMR techniques were used to characterize each product, and assess the kinetics involved in isomerization. DFT studies were used to propose a feasible mechanism, including transition states, and support kinetic studies. This was repeated with KO^{t}Bu to highlight the formation of new products. X-ray crystallography was planned to be used as a supporting tool to aid the computational analysis, where suitable crystals could be grown.

2.3   Model System Development – [IrCl(COD)(dppe)]

Previous attempts have been made to study precatalyst activation with catalytically relevant complexes, however, the inherent sensitivity of these complexes has made the detection of reaction intermediates difficult. The implementation of a model complex with a strongly chelating ligand proved necessary to facilitate the study of reaction intermediates. The synthesis and characterization of the model system precursor is discussed in the preliminary section of the chapter.

2.3.1   Iridium 1,2-diphenylphosphinoethane complexes

The starting point of this investigation was the synthesis of an iridium complex from [IrCl(COD)]$_2$. Treating this dimer with a stoichiometric amount of dppe proved to yield [IrCl(COD)(dppe)] (**1**$^{\textbf{dppe}}$) as a yellow powder (87%) as expected. **1**$^{\textbf{dppe}}$ is characterized by a single peak in the corresponding ^{31}P{^{1}H} NMR spectrum at δ 34.4, which is consistent with that reported for this known complex.[153] It is important to note that addition of dppe at level below or above the non-stoichiometric amount of dppe produces **1**$^{\textbf{dppe}}$ as well as several other dppe containing complexes. This inaccuracy meant the subsequent work-up to isolate **1**$^{\textbf{dppe}}$ as a pure compound was further complicated. In practice, by passing a dichloromethane solution of **1**$^{\textbf{dppe}}$ through an alumina column, and dissolving in toluene, pure **1**$^{\textbf{dppe}}$ can be isolated. **1**$^{\textbf{dppe}}$ is then crystallized from a dichloromethane/hexane solution to yield hexagonal yellow crystals. The resulting solid-state structure shows a square pyramidal Ir^{I} complex, confirming the literature proposition,[153] with the dppe and two COD CH=CH donating functions occupying equatorial positions and the chloride an axial position (**Figure 2-1**). The obtained structure rationalizes why a single peak is observed in the ^{31}P{^{1}H} NMR spectrum, as the plane across the vertical plane renders the two phosphorus atoms equivalent.
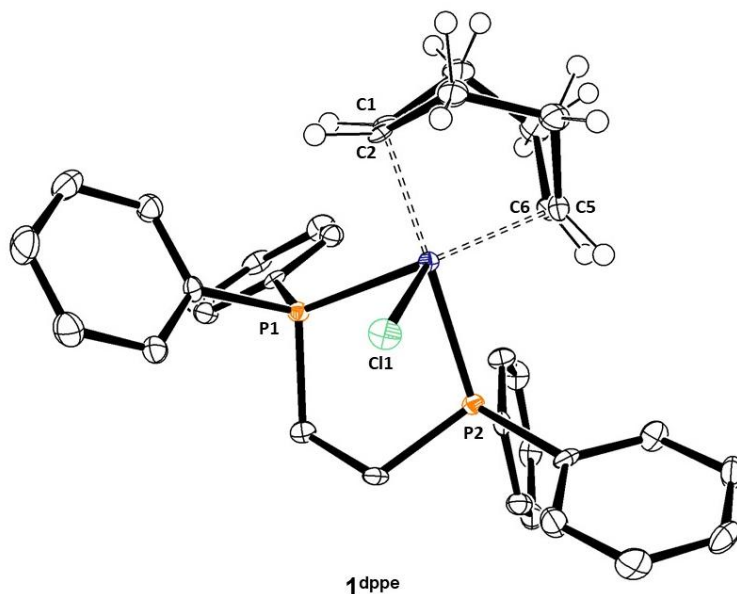
Figure 2-1. Solid-state structure of **1**^{dppe}. Anisotropic displacement ellipsoids are drawn at a probability level of 50 %. Hydrogen atoms on dppe are omitted for clarity. Selected bond lengths [Å] and angles [°]: **1**^{dppe} as shown, Ir1–Cl1 2.5317(8); Ir1–P1, 2.3117(9); Ir1–P2, 2.3072(9); Ir1–C1, 2.211(4); Ir1–C2, 2.177(3); Ir1–C5, 2.147(4); Ir1–C6, 2.142(4); Cl1–Ir1–P1, 90.64(3), Cl1–Ir2–P2, 83.93(3); P1–Ir1–P2, 81.84(3).

2.3.2 Interaction of [IrCl(COD)]₂ and dppe at variable ratios
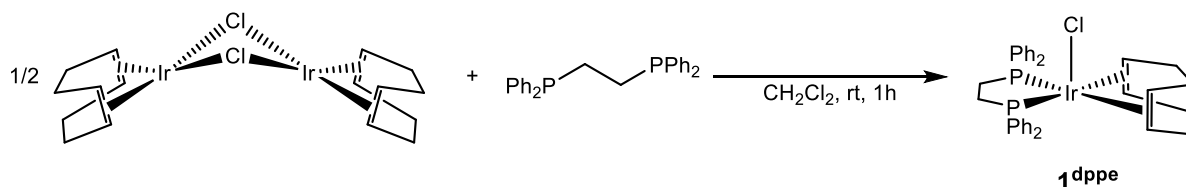
Scheme 2-4. Synthesis of **1**^{dppe}.[153]

The presence of more complex products when synthesising **1**^{dppe} using different dppe ratios necessitated a further study. ³¹P{¹H} NMR spectroscopy was used as a qualitative tool for *in situ* analysis. The addition of <1 equivalent of dppe per Ir atom yields, in addition to the expected **1**^{dppe} (³¹P{¹H} resonance at *δ* 33.4 in dichloromethane-*d₂*), a second product characterized by a resonance at *δ* 19.5 (**Figure 2-2**). This second resonance disappears upon addition of dppe to readjust the dppe/Ir stoichiometry to 1:1.

Based on the known behaviour for several other bidentate ligands, for instance α-diimines,[154] bis- and tris-pyrazoles,[155,156] phosphine-thioethers,[146] and for one diphosphine,[157] this is assigned to the salt [Ir(COD)(dppe)]⁺[IrCl₂(COD)]⁻. Addition of more dppe beyond the 1:1 ratio maintained the sharp ³¹P{¹H} resonance of **1**^{dppe}, but also generated an additional resonance at *δ* 50.0, which is assigned to [IrCl(dppe)₂], based on the follow-up reaction in the presence

of base, to yield [IrH(dppe)]$_2$ (*vide infra*). Compounds of analogous stoichiometry have been described for the reaction between [IrCl(COD)]$_2$ and excess of other bidentate ligands such as (C$_6$F$_5$)$_2$PCH$_2$CH$_2$P(C$_6$F$_5$)$_2$,[158] and a bis(phosphole).[159] The variable ratio experiment demonstrates the importance of using a stoichiometric amount of dppe (or to work-up) in the reaction mixture. The synthesis of pure **1^{dppe}** is essential to ensure experimental precision with respect to the qualitative and quantitative data discussed for the reaction products later (**2.4**, **2.5**).
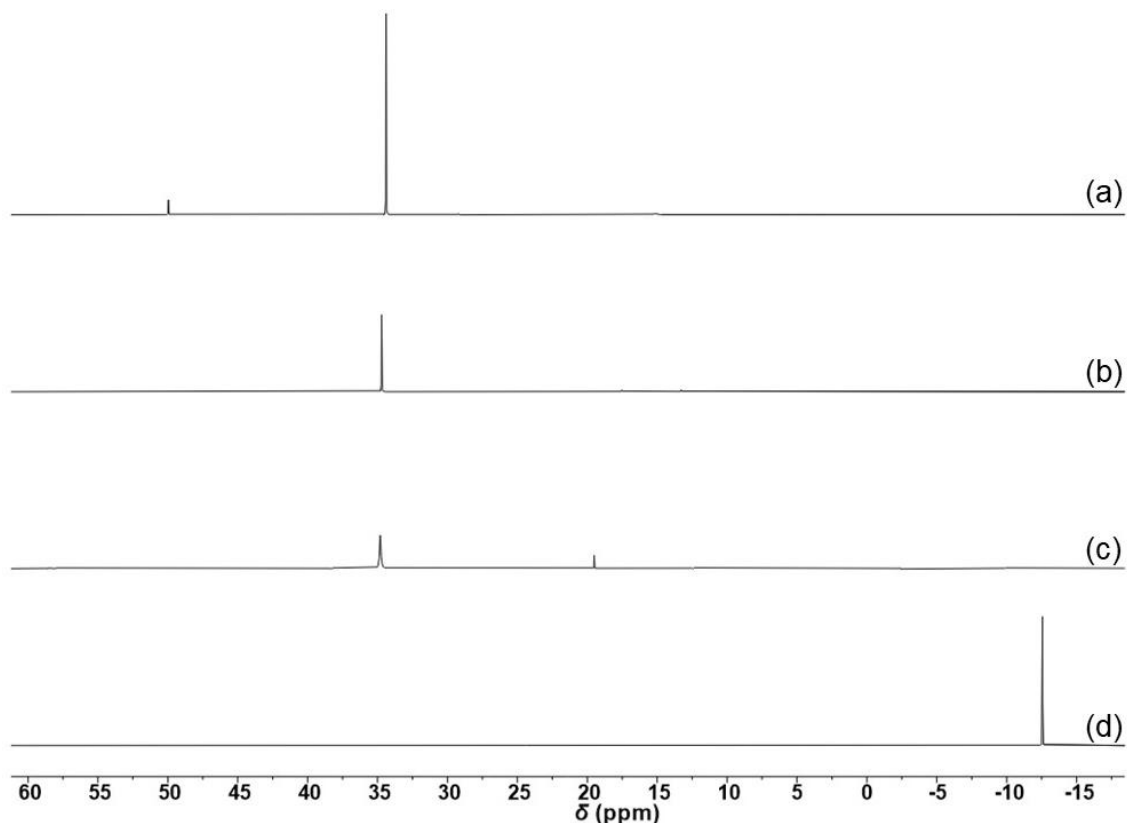
Figure 2-2. ^{31}P{^{1}H} NMR spectra of solutions obtained after the addition of dppe at different ratios to [IrCl(COD)]$_2$ in benzene-d_6 at 298 K. (a) dppe/Ir = 1.5; (b) dppe/Ir = 1; (c) dppe/Ir <1; (d) free dppe.

2.4 Activation with Methoxide and Isopropoxide Under Ambient Conditions

The addition of excess NaOMe or KOtBu (5 equiv) to a benzene-d_6 solution of **1^{dppe}** and spiked with isopropanol (1 equiv) produced two iridium hydride-dppe complexes. These complexes correspond to [IrH(COD)(dppe)]-type species, as already reported in the literature.[105,151] They are [IrH(η^2:η^2-1,5-C_8H_{12})(dppe)], **2^{dppe}**, which is formally Ir^I, and [IrH(1-κ-4,5,6-η^3-C_8H_{12})(dppe)], **3^{dppe}**, which is formally Ir^{III}.
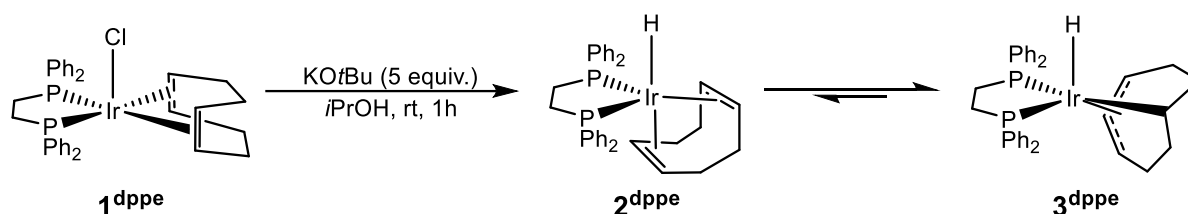
Scheme 2-5. Synthetic route towards [IrH(COD)(dppe)].

The formation of **2^{dppe}** is proposed to occur by alkoxide coordination to the iridium centre followed by β-hydride elimination. The transformation of and **2^{dppe}** to and **3^{dppe}** is addressed in **2.4.2**, and **2.4.3**. It is worth noting that a third hydride containing complex [IrH(dppe)$_2$] is formed if [IrCl(dppe)$_2$] is present in the reaction mixture.

[IrH(dppe)$_2$] has already been reported in the literature and is alternatively synthesised by treating [(C_6H_5)$_3$P]$_3$Ir-(CO)H.$C_6H_5CH_3$ with dppe in toluene. [IrH(dppe)$_2$] was reported as being unstable in dichloromethane-d_2 and exhibits a broad resonance in the ^{1}H NMR spectrum at δ -23.0.[160] These data are inconsistent with the observed hydride region for [IrH(dppe)$_2$] in benzene-d_6, when synthesised *via* the addition of excess NaO^{i}Pr to [IrCl(dppe)$_2$]. The ^{1}H NMR spectrum recorded in benzene-d_6 t shows a quintet at δ -12.64 ($^2J_{HP}$ = 8.7 Hz), and a single peak in the ^{31}P{^{1}H} NMR spectrum at δ 36.2. The quintet appearance arises from the hydride coupling to four chemically equivalent phosphorus atoms. However, the solid-state structure shows the molecule adopting a trigonal bipyramidal geometry (**Figure 2-3**). Based on the solid-state structure a doublet-of-doublets-of-triplets is expected to arise in the hydride region of the ^{1}H NMR spectrum and three distinct resonances in the ^{31}P{^{1}H} NMR spectrum. In the solid-state structure the hydride is in an axial plane *trans* to one of the phosphorus atoms, expected to show a large $^2J_{HP}$ coupling that is not observed. The lack of these coupling patterns implies that [IrH(dppe)$_2$] is fluxional on the NMR timescale (500 MHz) at 298 K and undergoes Berry pseudo rotation in solution (**Scheme 2-6**). A similar crystal structure has

been reported with dppf, [Ir(dppf)$_2$]$^+$.[161] When NaOMe was added to a solution containing **1$^{\text{dppe}}$** only [IrH(dppe)$_2$] was not observed.
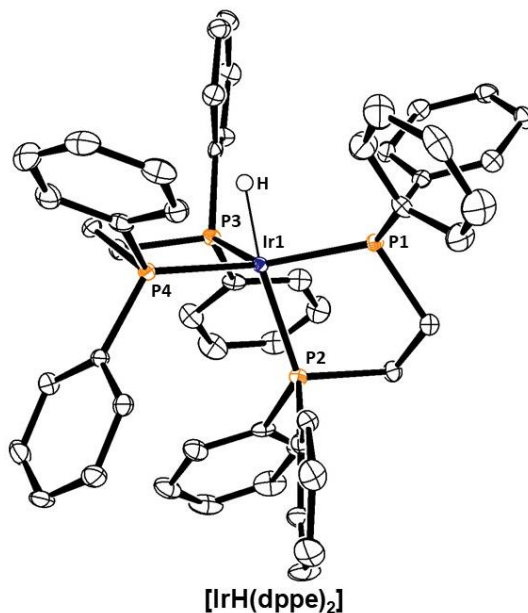
[IrH(dppe)$_2$]

Figure 2-3. Solid-state structure of [IrH(dppe)$_2$]. Anisotropic displacement ellipsoids are drawn at a probability level of 50 % The hydrogen atoms (except for the hydride) are omitted for clarity. Selected bond lengths [Å] and angles [°]: [IrH(dppe)$_2$] as shown, Ir1–H 1.62(4); Ir1-P1 2.2450(8); Ir1-P2 2.2791(9); Ir1-P3 2.2830(8); Ir1- P4 2.2701(9); P1-Ir1-P2 84.20(3); P1-Ir1-P3 124.45(3); P1-Ir1-P4 143.23(3); P2-Ir1-P3 104.21(3); P2-Ir1-P4 107.12(3); P3-Ir1-P4 87.41(3).

Solid-state **Solution-state**
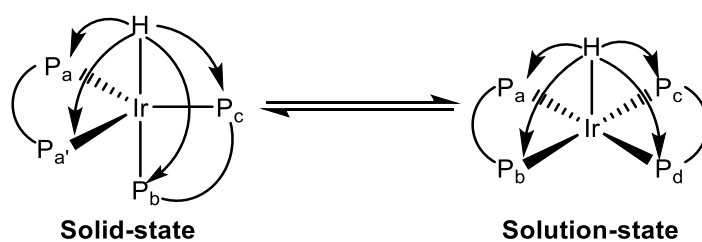
Scheme 2-6. Fluxionality of the solid- and solution-state isomers of [IrH(dppe)$_2$]. Note that in the solution state structure of [IrH(dppe)$_2$] all phosphorus atoms are chemically and magnetically equivalent ($^2J_{HPa} = {}^2J_{HPb} = {}^2J_{HPc} = {}^2J_{HPd}$).

2.4.1 Characterization

The formation of [IrH(COD)(dppe)] complexes under similar conditions as well as that of other related Ir complexes with *bis*-(diphenylphosphino)methane (dppm), *bis*-(diphenylphosphino)propane (dppp), *bis*-(diphenylphosphino)butane (dppb), *o*-$C_6H_4(PPh_2)_2$, and PPh_3 has previously been described.[105] Oro *et al.* obtained [IrH(COD)(dppe)] from the reaction of [Ir(OMe)(COD)]$_2$ with dppe in methanol. This was described as containing a regularly bound η^2: η^2-bound 1,5-COD ligand, **2^{dppe}**, based on the ^{1}H NMR properties in chloroform-*d*. This account did not contain any relevant ^{31}P{^{1}H} NMR data due to the apparent instability in chloroform-*d*. The mixture of monohydrides formed from **1^{dppe}** and NaOMe was found to be equally unstable in dichloromethane-d_2 and results in a mixture of mono, -di, and -tri substituted iridium chloride complexes in such solvents. These compounds were not fully characterized as they were deemed as irrelevant to this study, and the decomposition in chlorinated solvents prompted a switch to non-chlorinated solvents to maintain the hydride stability. Deuterated benzene, tetrahydrofuran, and toluene were used for subsequent characterization, where applicable.

The same group reported that the reaction of [Ir(OMe)(COD)]$_2$ with dppm, instead of dppe, yields a product with an isomerized COD ligand [IrH(1-κ-4,5,6-η^3-C_8H_{12})(dppm)], similar to **3^{dppe}**.[162] Farnetti *et al.* revisited the reaction with dppe, and found that two isomeric monohydrides are formed, **3^{dppe}** with the same geometry as Oro's dppm complex, and the other with the η^2: η^2-bound 1,5-COD ligand (**2^{dppe}**). Furthermore, studies using diphosphine ligands with longer backbones (Ph$_2$P(CH$_2$)$_n$PPh$_2$) revealed that the dppp ligand (*n* = 3) gave both η^2: η^2 and isomerized κ^1: η^3 products (**2^{dppp}** and **3^{dppp}**), and the dppb (*n* = 4) ligand gave only the η^2: η^2 product (**2^{dppb}**).[105] In our work the addition of excess KO^{t}Bu (5 equiv.) to **1^{dppe}** with isopropanol produced both **2^{dppe}** and **3^{dppe}** in a ratio of 5:95 at equilibrium at 298 K.

Although the two compounds **2^{dppe}** and **3^{dppe}** correspond to those previously described by Oro *et al.* and by Farnetti *et al.*, a few spectral assignments required some clarification. The C_8H_{12} allyl region establishes the peak positions for each of the κ^3 CH resonances seen in **3^{dppe}**, and a minor COD-CH peak at *δ* 3.81 for **2^{dppe}**. The previous work by Oro *et al.*, did not mention the observation of an allylic peak due to the decomposition. However, in benzene-d_6 this compound appeared to be stable (no decomposition after one week in solution). The structural unambiguity of **2^{dppe}** was clarified by the application of DFT calculated chemical shifts, using tetramethylsilane (proton chemical shift taken as *δ* = 0) as a reference standard. The computed chemical shift is the difference in isotropic shielding calculated for the proton in TMS
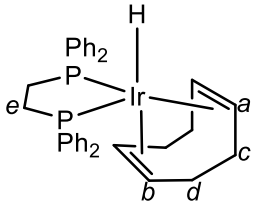
(σ_H^{TMS}, in ppm), and that of the isotropic shielding calculated for the proton in **2^{dppe}** or **3^{dppe}** ($\sigma_H^{molecule}$, **Equation 2-1**).

$$\delta\,(H_i) = \sigma_H^{TMS} - \sigma_H^{molecule}$$

Equation 2-1. DFT-calculated chemical shifts for the ^{1}H proton resonances.

The DFT-calculated resonances give two separate chemical shift values for the alkene groups on **2^{dppe}**, with one of the signals arising from an alkene in the equatorial plane (*δ* 3.6) and the other from the alkene in the axial plane (*δ* 2.7) *trans* to the hydride. Two ^{1}H signals are observed for the ethylene backbone of the dppe and are assigned based on the ^{31}P-^{1}H HMQC NMR experiment. The major difference between the experimental and calculated chemical shifts arise from the COD CH$_2$ groups. Two signals are observed experimentally, each corresponding to the distinct CH$_2$ groups (*c* and *d*), whereas there are four calculated chemical shifts for the *exo* and *endo* hydrogens on each carbon 2*c*, and 2*d* (**Table 2-1**).

Table 2-1. Observed and calculated ^{1}H NMR properties of the C$_8$H$_{12}$ ligand and Ir-H of **2^{dppe}** in benzene-d_6 at 298 K.

Group	^{1}H chemical shift (*δ*)	DFT calculated chemical shift
COD CH	3.81 (bs) (*a,b*)	3.62 (*b*) 2.78 (*a*)
COD CH$_2$	2.45 (*c*), 2.36 (*d*)	2.52 (*exo*), 2.50 (*endo*) 1.78 (*exo*), 1.91 (*endo*)
dppe CH$_2$	2.21, 1.81 (*e*)	2.22, 2.73
Ir-H	-14.0 (t, $^{2}J_{HP}$ = 21.6)	N/A

Two closely placed multiplets are observed for **3^{dppe}** around *δ* 5 and do not change in shape upon ^{31}P decoupling, whereas the doublet-of-triplets signal at *δ* 3.91 collapses to a triplet (**Figure 2-4**). These three signals are assigned to the allyl protons on the C$_8$H$_{12}$ ligand *trans* to the two phosphorus atoms. The difference in shape upon ^{31}P decoupling aids the distinction of each individual resonance for the η-bound portion of the ligand, specifically 3H$_a$. The chemical shifts for each of the CH$_2$ protons are not significantly different from those previously

reported. In this case, the calculated DFT results show similarly observed values to the experimentally determined chemical shifts (**Table 2-2**).

The phenyl region of the ^{1}H (and ^{1}H{^{31}P}) NMR spectra show several multiplets arising from HP and HH coupling of the protons on the phenyl rings. When the HP coupling is removed, the aromatic region is easier to interpret and allows the chemical assignment of protons at each corresponding position on the phenyl ring.
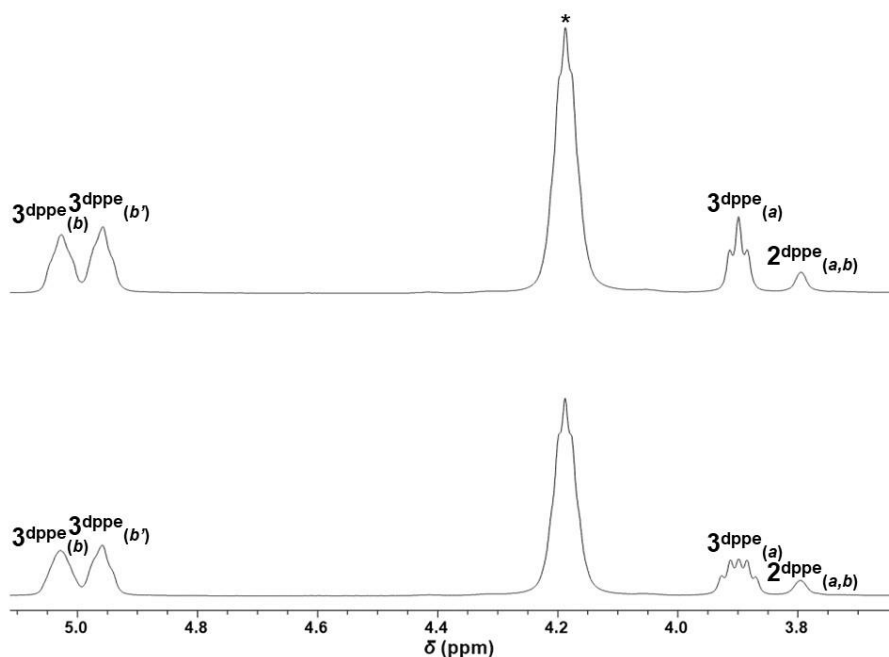
Figure 2-4. ^{1}H (below) and ^{1}H{^{31}P} (above) NMR spectra of the COD CH proton resonances for the mixture of **2^{dppe}** and **3^{dppe}** in benzene-d_6 at 298 K. The large-starred resonance at δ 4.2 belongs to CH protons of residual isopropanol.

Given the minor amount of **2^{dppe}** (~5% as synthesised), ^{31}P-^{1}H HMQC NMR methods were used to resolve minor peak positions. More importantly through the application of heteronuclear 2D experiments the specific phenyl and CH$_2$ groups both on the C$_8$H$_{12}$ ligand and on the ethylene bridge of the dppe ligand could be assigned for each isomer. The sp^3 CH region of the ^{1}H spectrum shows a complex region of multiplets, even when decoupled from ^{31}P, as protons for both COD CH$_2$ groups on **2^{dppe}** and **3^{dppe}** are observed (16H in total). This is further complicated by the CH$_2$ resonances on the C$_2$H$_4$ fragment on the dppe ligand; however, the specific resonance signals (without coupling constants) could be fully resolved.

Notably, no H-P couplings could be clearly discerned. These experiments allow the CH$_2$ peaks to be assigned based on the coupling to known proton resonances in the other regions of the spectrum.

Table 2-2. ^{1}H NMR properties of **3^{dppe}** in benzene-d_6 at 298 K.

Group	^{1}H chemical shift (δ)	DFT calculated chemical shift
COD allyl	5.06 (bm) (*b*)	4.5
	4.97 (bm) (*b'*)	2.7
	3.91 (dt, $^2J_{HP}$ = 14.3; $^2J_{HH}$ = 7.5) (*a*)	3.2
COD CH$_2$	2.47, 2.17 (*d'*)	1.3, 2.1
	2.50, 2.26 (*d*)	1.4, 1.8
	2.23, 1.88 (*e'*)	1.9, 2.0
	2.10, 1.78 (*e*)	1.8, 1.9
dppe CH$_2$	2.07 (up), 1.47(down) (*f*)	Peaks could be assigned
	2.46 (down), 1.94(up) (*g*)	based on NMR data

The ^{13}C-^{1}H HMQC spectrum highlights the correlation between the proton and carbon resonances of the allyl protons (**Figure 2-5**), adding further credence to the assignment of each proton. With the chemical shift peak positions of the ^{13}C resonances corresponding to allyl-type bonding for **3^{dppe}**. The identity of each isomer could thus be fully resolved using the NMR data.
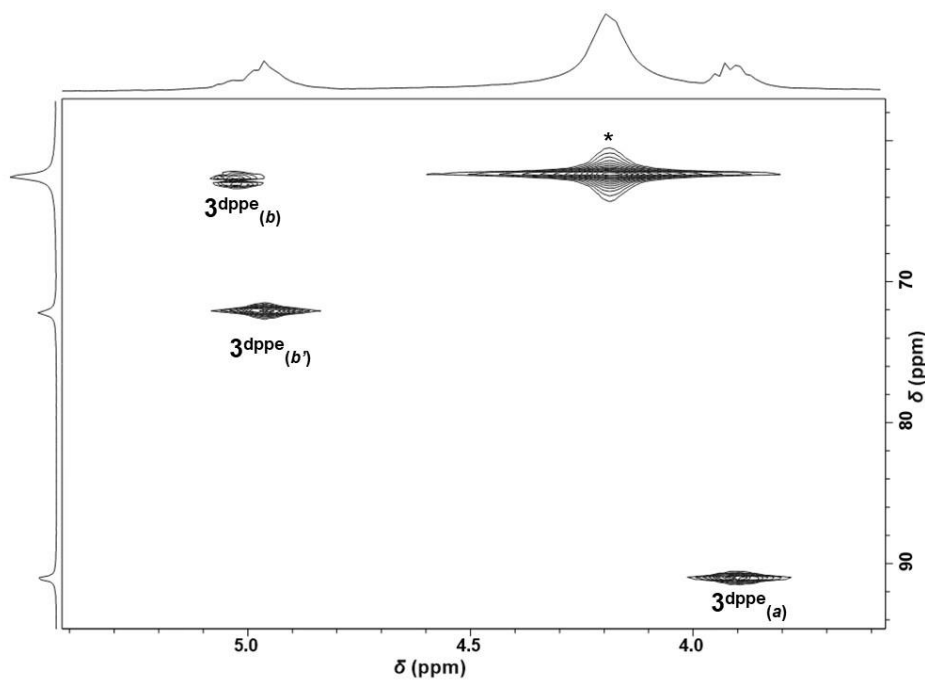
Figure 2-5. ^{13}C-^{1}H HMQC experiment highlighting the correlation between the allyl protons and carbon in benzene-d_6 at 298 K. The large-starred resonance at δ 4.2 belongs to CH protons of residual isopropanol.

2.4.2 Kinetic analysis of the isomerization

Following the successful synthesis of [IrH(C$_8$H$_{12}$)(dppe)], an alternative approach was taken to study the isomerization mechanism of **2$^{\text{dppe}}$** to **3$^{\text{dppe}}$**. This involved the addition of L-selectride to **1$^{\text{dppe}}$** in THF-d_8. By using a hydride source, direct access to both hydride products were accessible without the formation of a proposed akoxide intermediate. When the reaction was monitored at 263 K, the ^{1}H NMR spectrum collected directly after mixing showed a single hydride resonance at δ -14.20 (t, $^{2}J_{HP}$ = 21.6 Hz) indicating that **2$^{\text{dppe}}$** is formed first, with no other hydride resonances observed. After 10 minutes, a second hydride resonance at δ -11.55 (dd, $^{2}J_{HP}$ = 20.6, 14.7 Hz) for **3$^{\text{dppe}}$** was observed. When the reaction mixture was brought to 298 K further isomerization of **2$^{\text{dppe}}$** to **3$^{\text{dppe}}$** occurred, and a stable equilibrium was reached where the ratio of the two isomers was 5:95. The same ratio was observed when [IrH(C$_8$H$_{12}$)(dppe)] was synthesised at scale with NaOMe in isopropanol, implying that a stable equilibrium between the two isomers is achieved at 298 K irrespective of the reagent used to form the hydride. This finding led to an examination of the isomerization process by the addition of NaOMe to **1$^{\text{dppe}}$** in THF-d_8 at constant temperature (298 K) with integration of the ^{1}H NMR resonances (**Figure 2-6**), and ^{31}P{^{1}H} spectra recorded at 45-minute intervals. The

reaction was complete in 10 hours. At the end of the reaction there was no evidence of residual **1^{dppe}** and the **2^{dppe}**/ **3^{dppe}** ratio was 5:95.
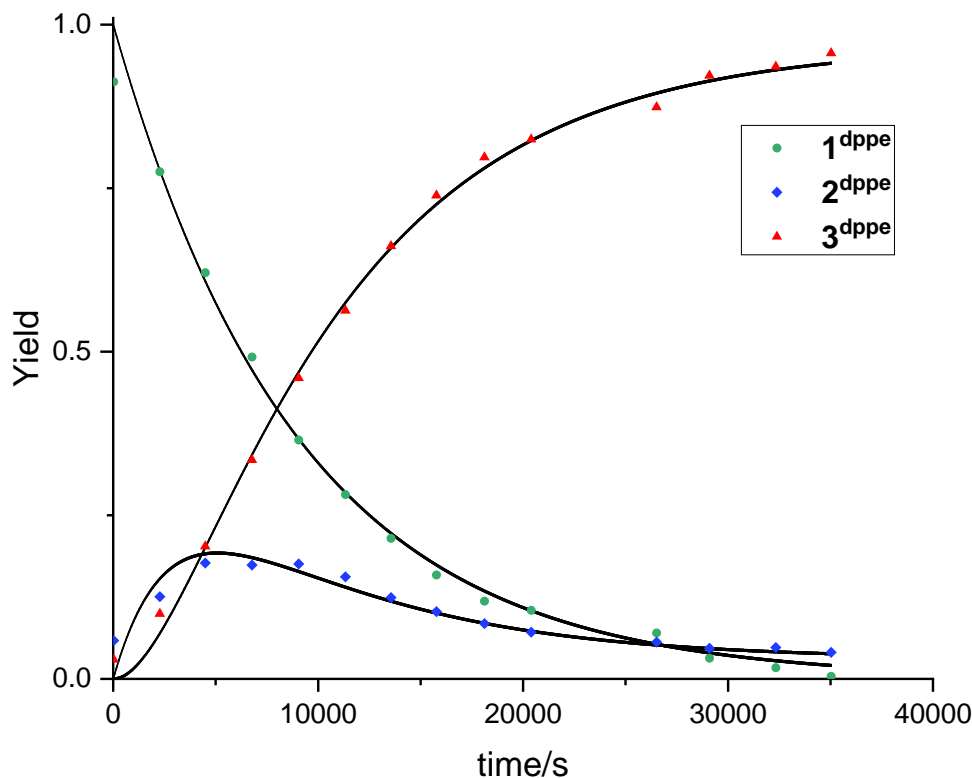
Figure 2-6. Time evolution of the ^{31}P{^{1}H} data for the **1^{dppe}** decay and **2^{dppe}-3^{dppe}** isomerization. The continuous lines are the result of the non-linear least-squares fit.

The kinetic analysis by a global fit yields $k_{(1\text{-}2)}{}^{dppe}$ = (1.11 ± 0.02) x 10^{-4} s^{-1}; $k_{(2\text{-}3)}{}^{dppe}$ = (3.4 ± 0.2) x 10^{-4} s^{-1} and $k_{(3\text{-}2)}{}^{dppe}$ = (1.1 ± 0.3) x 10^{-5} s^{-1} ($K_{(2\text{-}3)}{}^{dppe}$ = $k_{(2\text{-}3)}{}^{dppe}$/$k_{(3\text{-}2)}{}^{dppe}$ = 32 ± 10). The decay of **1^{dppe}** could also be treated independently as a clean first order process, to yield $k_{(1\text{-}2)}{}^{dppe}$ = (1.13 ± 0.03) x 10^{-4} s^{-1}, in agreement with the value obtained from the global fit. Importantly, the kinetic plot verifies that **1^{dppe}** is first converted to **2^{dppe}**, which subsequently isomerizes to **3^{dppe}**. A separate DFT investigation was undertaken to propose a feasible mechanism for the rearrangement of the cyclooctadiene ligand.

2.4.3 DFT investigation of the isomerization mechanism

The investigation began with the optimization of the **2^{dppe}** and **3^{dppe}** geometries. The greater stability for **3^{dppe}** by 3.5 kcal mol^{-1} relative to **2^{dppe}** agrees fairly well with the experimental equilibrium, which returned a Gibbs energy difference of 2.06 ± 0.16 kcal mol^{-1} in favour of **3^{dppe}**. The optimized structure of **2^{dppe}** is trigonal bipyramidal with the hydride and one of the COD double bonds occupying axial positions. **3^{dppe}**, on the other hand, is best described by a

pseudo-octahedral geometry. The hydride occupies a position *cis* to the two P atoms and *cis* to the 1-κ-C donor atom of the ligand. The two phosphorus atoms are one *cis* and one *trans* to the 1-κ-C donor atom, this renders them chemically inequivalent, justifying the observation of two distinct resonances in the $^{31}P\{^1H\}$ NMR spectrum.

An alternative isomer of **3$^{\text{dppe}}$** (**3'$^{\text{dppe}}$**) with the 1-κ-C donor *trans* to the hydride was computed and is located 6.8 kcal mol^{-1} higher in Gibbs energy than **3$^{\text{dppe}}$** (**Figure 2-7**). The large increase in relative energy is due to two strong σ-donors located *trans* to each other. **3'$^{\text{dppe}}$** has a higher level of symmetry across the horizontal plane (σ_v) with two chemically equivalent phosphorus atoms. This symmetry would inevitably lead to a single resonance in the $^{31}P\{^1H\}$ NMR spectrum, which is not observed. The higher relative energy and lack of supporting evidence in the experimental data meant that **3'$^{\text{dppe}}$** could be deemed as irrelevant to the isomerization process of **2$^{\text{dppe}}$** to **3$^{\text{dppe}}$**.
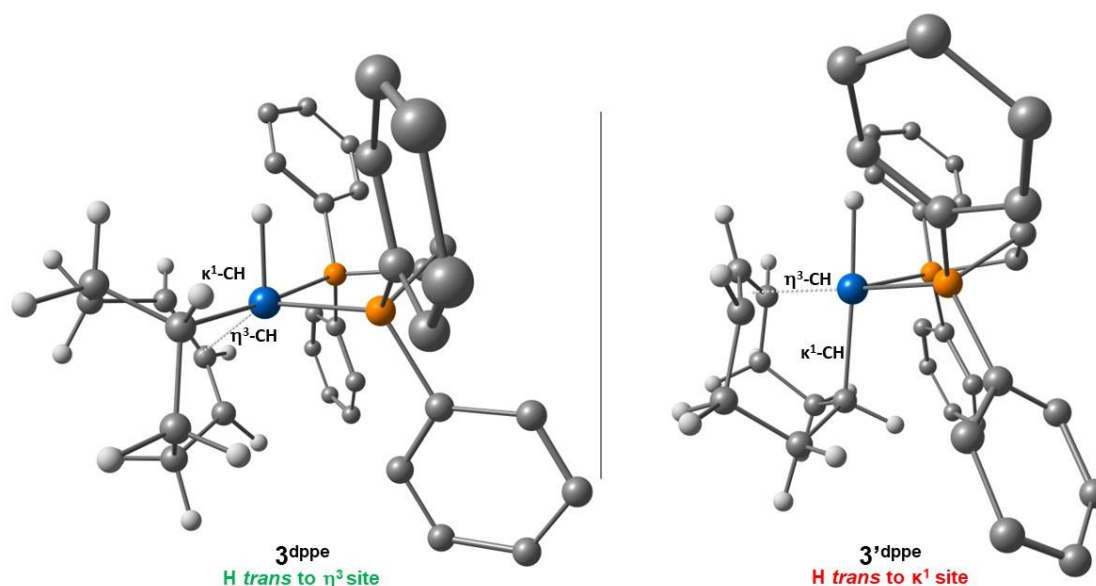
Figure 2-7. Comparison of the optimized geometries for two possible isomers of [IrH(1-κ-4,5,6-η^3-C$_8$H$_{12}$)(dppe)], **3$^{\text{dppe}}$** (lower energy isomer), and **3'$^{\text{dppe}}$** (higher energy isomer). Hydrogen atoms on dppe omitted for clarity.

A working hypothesis for this isomerization consists of a two-step process, involving a neutral 16-electron Ir^I intermediate, [Ir(1-κ-4,5-η^2-C$_8$H$_{13}$)(dppe)] (**I$^{\text{dppe}}$**). DFT calculations could optimize the geometry of **I$^{\text{dppe}}$**, located 1.3 kcal mol^{-1} higher than **2$^{\text{dppe}}$** (4.8 kcal mol^{-1} than **3$^{\text{dppe}}$**). Two transition states relating **I$^{\text{dppe}}$** to **2$^{\text{dppe}}$** (**TS$_{(2\text{-}I)}$$^{\text{dppe}}$**) and to **3$^{\text{dppe}}$** (**TS$_{(I\text{-}3)}$$^{\text{dppe}}$**) were determined. The highest free energy transition state is **TS$_{(I\text{-}3)}$$^{\text{dppe}}$**, located at 19.8 kcal mol^{-1} from **2$^{\text{dppe}}$** (23.3 kcal mol^{-1} from **3$^{\text{dppe}}$**). This value is consistent with the experimentally derived barrier of 22.19 ± 0.04 kcal mol^{-1}; hence, the observable barrier is the transition from **I$^{\text{dppe}}$** to **3$^{\text{dppe}}$**. The **2$^{\text{dppe}}$**/**I$^{\text{dppe}}$** step is pre-equilibrium, and therefore precedes the rate-determining

conversion of **I**^{dppe} to **3**^{dppe}. The Gibbs energy of **I**^{dppe} is computed as 1.3 kcal mol^{-1} higher than that of **2**^{dppe} (**Figure 2-8**), which is consistent with its non-observation during the reaction monitoring.

The mechanism proceeds via an increase in the Ir-H bond length (of **2**^{dppe}) from 1.61 Å to 1.70 Å (**TS_(I-3)**^{dppe}) with the C-H distance to the appropriate C atom shortening (2.63 Å to 1.56 Å) and subsequent hydride migration to the C atom. The C_8H_{13} ligand on **I**^{dppe} then partially rotates across the κ^1-CH axis placing a CH_2 group adjacent to iridium. The bond length of the *endo* H bond increases (**TS_(I-3)**^{dppe}) until it is near the iridium. The H atom is then transferred to the Ir atom, resulting in a hydride-containing complex **3**^{dppe}.
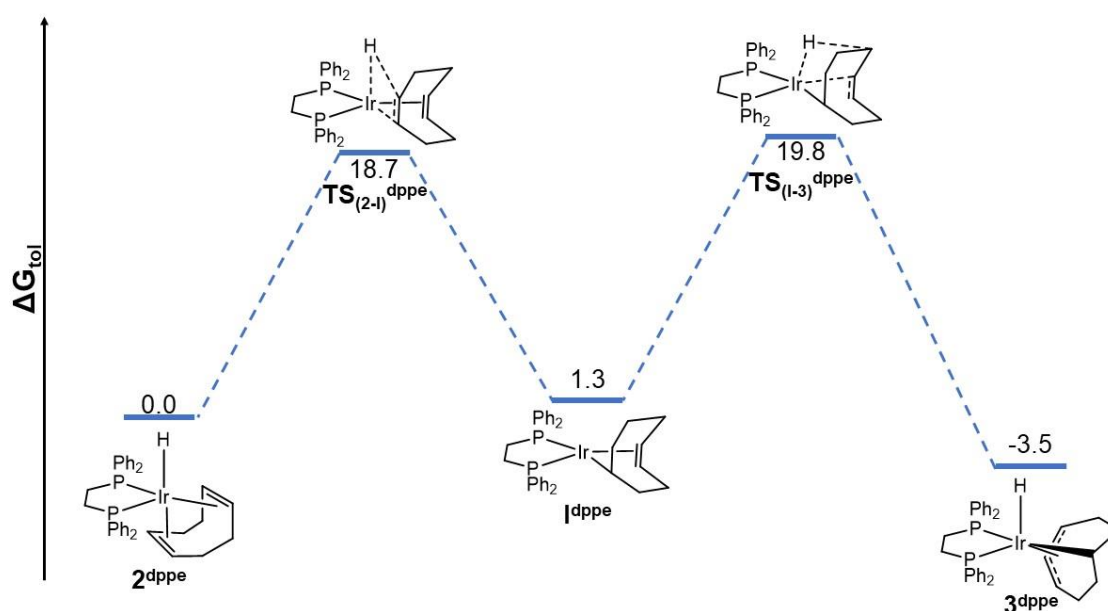
Figure 2-8. Gibbs energy profile (in kcal mol^{-1}) for the isomerization of **2**^{dppe} to **3**^{dppe}. Relative energies shown with **2**^{dppe} as the reference point.

2.5 Activation with *tert*-Butoxide Under Ambient Conditions

To evaluate the effect of different bases, NaOMe was replaced by KO^{t}Bu. Consequently, KO^{t}Bu was added to **1^{dppe}** in THF-d_8 and the NMR tube shaken for 1 minute at room temperature. A ^{1}H NMR spectrum was then recorded at this stage of reaction, at 263 K, which revealed the presence of two iridium hydride complexes. Surprisingly, these appeared at different chemical shifts to those of **2^{dppe}** and **3^{dppe}**. Subsequent analysis revealed that these complexes are isomeric (**2.5.1**). The first of them, **4^{dppe}**, is characterized by a resonance at δ -11.43 (dd, $^2J_{HP}$ = 21.8, 14.1 Hz) and the second one, **5^{dppe}**, by a resonance at δ -11.57 (t, $^2J_{HP}$ = 19.5 Hz). They appeared in an 86:14 ratio in this first measurement. When the solution was brought to 298 K an equilibrium position was reached where **5^{dppe}** predominates, and the ratio of these species became 32:68. The ^{1}H NMR properties of these two compounds are summarized in **Table 2-3**. When the reaction was repeated in benzene-d_6 (**Figure 2-9**) the same products were formed, and the same evolution of the relative concentration occurred.
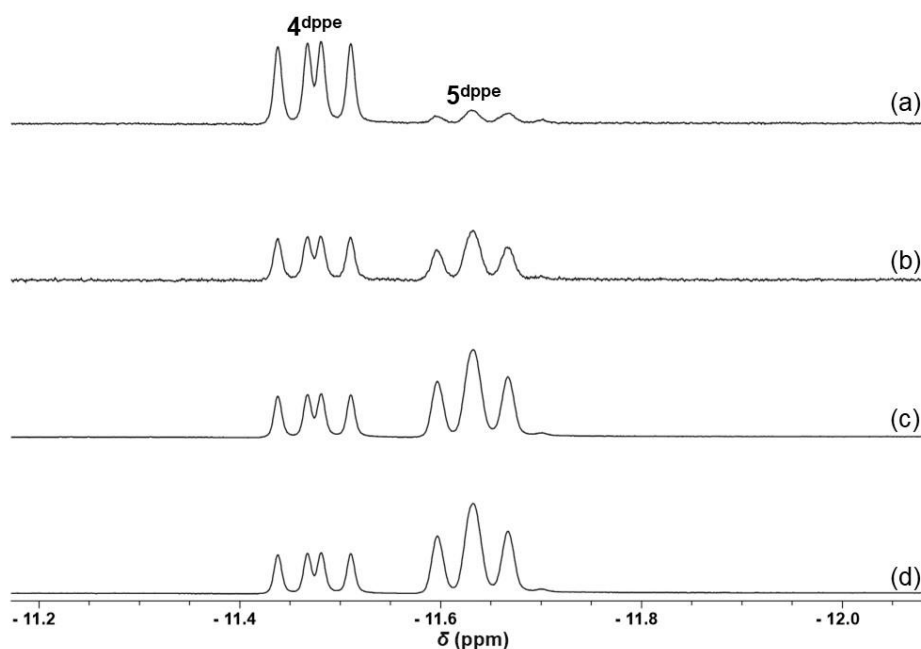
Figure 2-9. A series of ^{1}H NMR spectra monitoring the change in appearance of signals observed in the hydride region during the reaction of **1^{dppe}** with KO^{t}Bu in benzene-d_6 at 263 K. The isomerization of **4^{dppe}** to **5^{dppe}** is indicated at different times; (a) 300 s; (b) 3000 s; (c) 3900 s; (d) 4800 s.

The addition of a base not possessing a β-hydrogen had a significant effect on the products formed. The two new products, **4^{dppe}** and **5^{dppe}** were therefore thoroughly examined to determine their respective structures and isomerization process.

2.5.1 Characterization

The NMR spectra for these samples proved to be highly complex, and multiple measurements on different samples when **4^{dppe}** and **5^{dppe}** were present in different amounts were required. This approach enabled the resonances for **4^{dppe}** and **5^{dppe}** to be distinguished from one another. Consequently, the hydride resonance of **4^{dppe}** proved to correlate with two resonances in the ^{31}P{^{1}H} NMR spectrum at δ 30.6 (d, $^{2}J_{PP}$ = 2.4 Hz), and δ 46.7 (d, $^{2}J_{PP}$ = 2.4 Hz). An NOE measurement connected the hydride ligand to the *ortho* phenyl resonances and to a resonance at δ 2.59 corresponding to the Ir-CH proton on the 1-κ-4,5,6-η^{3}-C$_8$H$_{10}$ ligand. Subsequent COSY, HSQC and HMQC data yielded the closed group of 10 protons resonances detailed in **Table 2-3**.

It is noteworthy that this group of 10 resonances contains two broad peaks at δ 5.94 and δ 5.47 in the ^{1}H NMR spectrum due to the unbound olefin moiety. This deduction was confirmed by their connections to ^{13}C resonances at δ 146.4 and δ 129.9, respectively. Three additional resonances were observed in the bound alkene region of the ^{1}H NMR spectrum in accordance with the allylic-η^{3} interaction.

Two pairs of inequivalent CH$_2$ proton signals, and a CH signal, were located. Collectively, this information therefore confirms that [IrH(1-κ-4,5,6-η^{3}-C$_8$H$_{10}$)(dppe)] (**4^{dppe}**) has been characterized.

Consequently, discrete ^{31}P couplings to ^{13}C carbon signals can be seen for the σ bound Ir-CH located *trans* to one of the P donor atoms with strong P-C coupling ($^{2}J_{CP}$ = 70 Hz), and for one of the η^{3} carbons ($^{2}J_{CP}$ = 50 Hz). The uncoordinated double bond lies in the equatorial plane, as confirmed by the lack of NOE interactions between the hydride and the unbound alkene. A 1-κ-4,5,6-η^{3} binding mode for a C$_8$H$_{10}$ ligand was previously demonstrated in the related complex [IrH(1-κ-4,5,6-η^{3}-C$_8$H$_{10}$)(dppb)], which is homologous with **4^{dppe}**.[163]

The hydride resonance of **5^{dppe}** proved to also couple to two ^{31}P resonances, which appear at δ 32.4 (d, $^{2}J_{PP}$ = 2.7 Hz), and δ 39.4 (d, $^{2}J_{PP}$ = 2.7 Hz). **5^{dppe}** is a structural isomer of **4^{dppe}** with a similar C$_8$H$_{10}$ ligand but a different binding mode; the saturated ethylene bridge and uncoordinated alkene have exchanged position (as suggested by the NOESY). This isomer exhibits ^{1}H resonances for an unbound alkene at δ 5.61 and δ 5.52, with connections to ^{13}C signals at δ 127.5 and δ 148.1.

The *ortho*- phenyl protons on **4^{dppe}** and **5^{dppe}** are readily identified by their downfield signals because they show a large difference in appearance when decoupled from ^{31}P, resulting in perceived doublet signals. The phenyl region of the spectrum shows significant overlap of the

resonances for each isomer, possessing in total 20 H (and 24 C) signals for each isomer. Hence, it is much more difficult to assign individual proton resonances based solely on the ^{1}H NMR spectrum. To fully characterize each complex, COSY (**Figure 2-10**) and ^{31}P-^{1}H HMQC (**Figure 2-11**) NMR spectra were used.

Table 2-3. Comparison of the ^{1}H NMR data for **4^{dppe}** and **5^{dppe}** in benzene-d_6 at 298 K.

Complex	4^{dppe}	5^{dppe}
Structure		
Group	^{1}H chemical shift (δ)	^{1}H chemical shift (δ)
C_8H_{10} C-H (olefin)	5.47 (dd, $^3J_{HH}$ = 4.0, 6.4 Hz) (*a*) 5.94 (ddd, $^3J_{HH}$ = 4.0, 6.4; J_{HP} = 4.0 Hz) (*b*)	5.61 (dd, $^3J_{HH}$ = 4.2, 7.0 Hz) (*a*) 5.52 (dd, $^3J_{HH}$ = 4.2, 8.3 Hz) (*b*)
COD C-H (allyl)	4.98 (dd, $^3J_{HH}$ = 4.0, 7.1; J_{HP} = 4 Hz) (*c*) 3.79 (t, $^3J_{HH}$ = 7.1 with J_{PH} = 7.3 Hz) (*d*) 5.02 (m) (*e*)	4.31 (dd, $^3J_{HH}$ = 4.2, 8.3 Hz) (*c*) 3.83 (t, $^3J_{HH}$ = 8; $^3J_{HP}$ = 8 Hz) (*d*) 5.11 (dd, $^3J_{HH}$ = 8, 4 Hz) (*e*)
C_8H_{10} CH_2	2.14 (up), 1.98 (down) (*f*) 1.96 (up), 2.41 (down) (*g*)	2.43, 2.12 (*f*) 2.82, 2.12 (*g*)
C_8H_{10} Ir-C-H	2.59 (br)	2.78 (br)
Ir-H	-11.43 (dd, $^2J_{HP}$ = 14.1, 21.8)	-11.57 (t, $^2J_{HP}$ = 19.5)
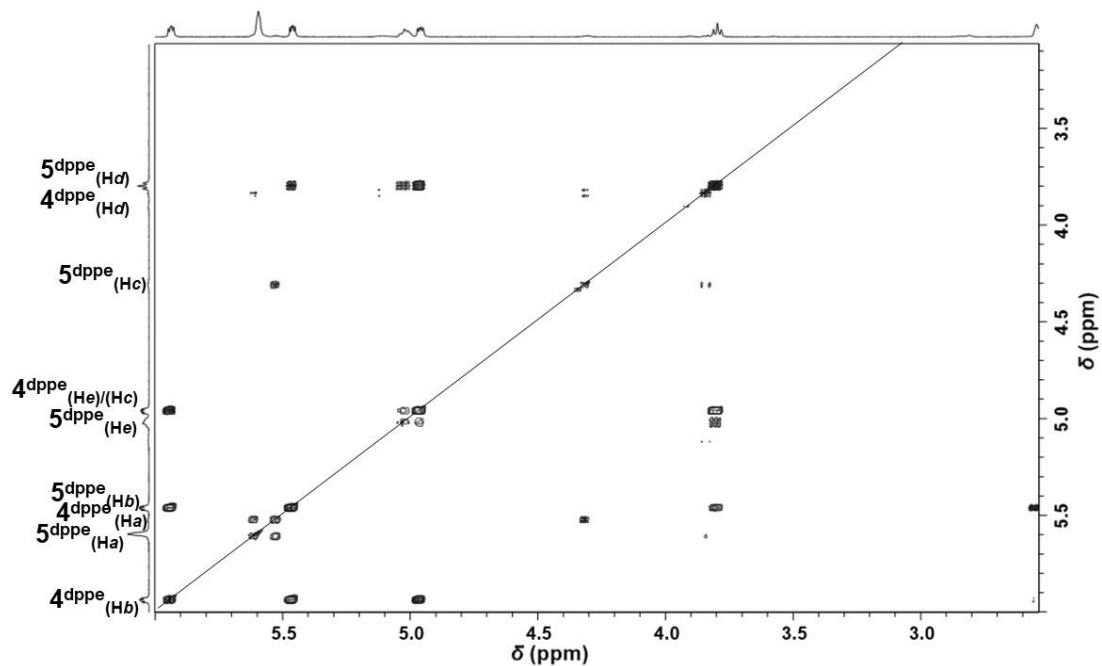
Figure 2-10. ^{31}P-decoupled H-H COSY spectrum of the mixture of **4^{dppe}** and **5^{dppe}** in the sp^2-CH region. In benzene-d_6 at 298 K.
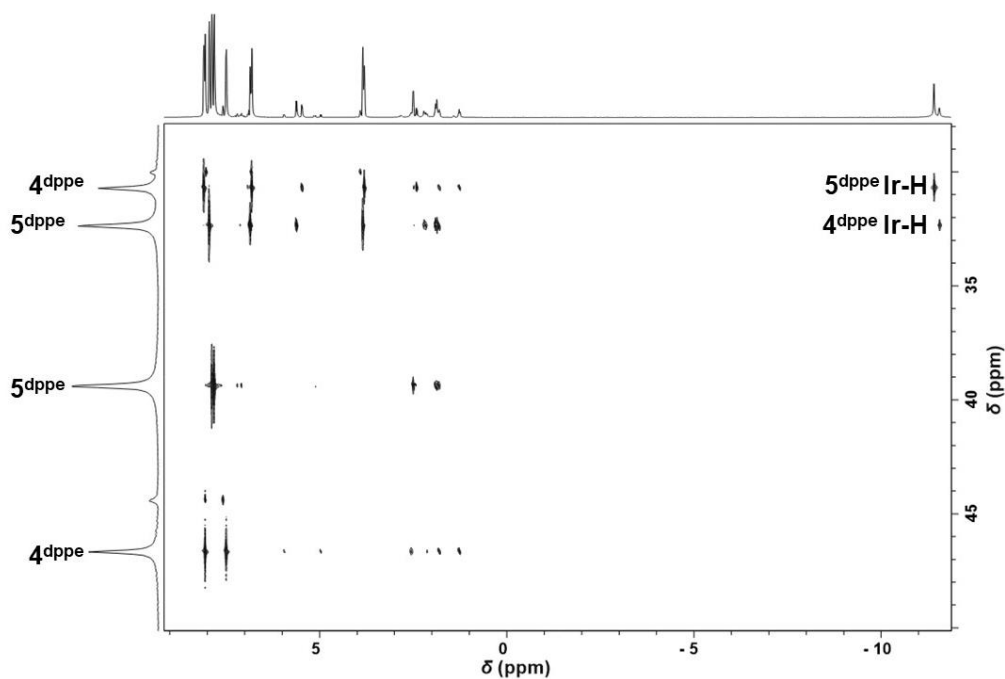
Figure 2-11. [31]P-^{1}H HMQC spectrum of **4^{dppe}** and **5^{dppe}** in benzene-d_6 at 298 K. The Ir-H resonances are highlighted to distinguish the two isomers.

2.5.2 Kinetic analysis of the isomerization
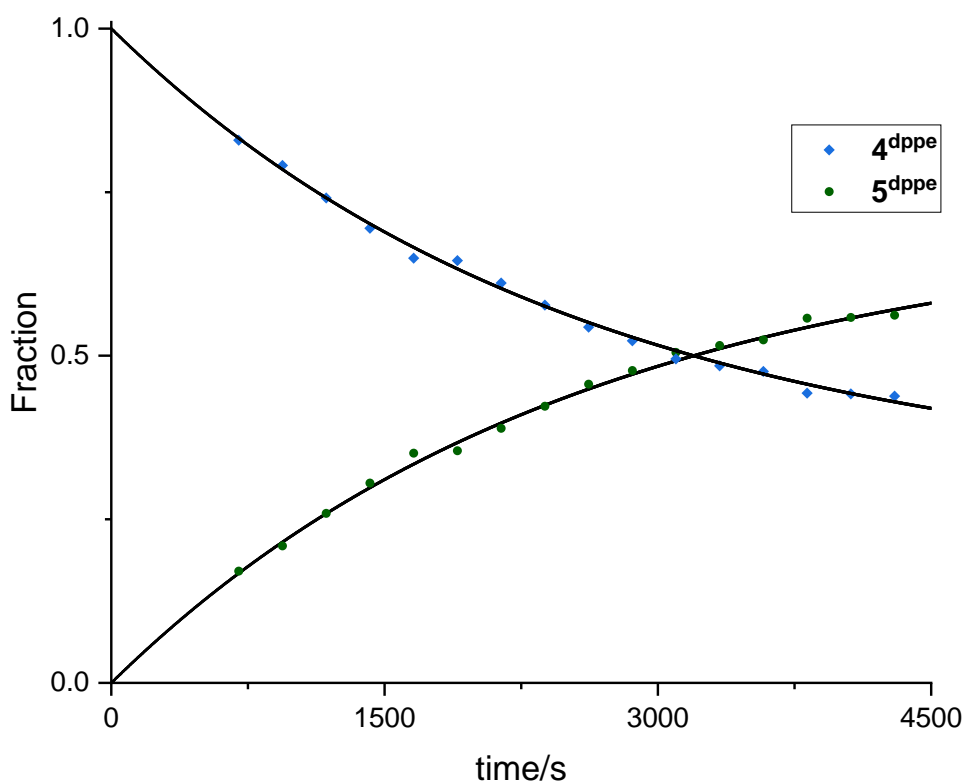
Figure 2-12. Time evolution of the $^{31}P\{^{1}H\}$ NMR data for the first order kinetics of the **4$^{\text{dppe}}$** to **5$^{\text{dppe}}$** isomerization in benzene-d_6 at 298 K.

The isomerization of **4$^{\text{dppe}}$** and **5$^{\text{dppe}}$** was analysed kinetically in benzene-d_6 at 298 K. The immediate disappearance of **1$^{\text{dppe}}$** (within the time needed to record the first $^{31}P\{^{1}H\}$ NMR spectrum after the addition of KO^{t}Bu to **1$^{\text{dppe}}$**) reflects a rapid first step, allowing clean timescale separation from the second step, such that analysis of the latter by standard reversible first-order reaction kinetics was possible, yielding $k_{(4\text{-}5)}^{\text{dppe}} = (2.75 \pm 0.06) \times 10^{-4}$ s^{-1} and $k_{(5\text{-}4)}^{\text{dppe}} = (1.16 \pm 0.08) \times 10^{-4}$ s^{-1}; $K_{(4\text{-}5)}^{\text{dppe}} = k_{(4\text{-}5)}^{\text{dppe}}/k_{(5\text{-}4)}^{\text{dppe}} = 2.83 \pm 0.26$ (**Figure 2-12**). The spectrum recorded 10 minutes after the addition KO^{t}Bu showed a **4$^{\text{dppe}}$**:**5$^{\text{dppe}}$** ratio of 4:1. After 50 minutes, there was a 1:1 mixture of both isomers, until **5$^{\text{dppe}}$** predominated at around the 1-hour mark. After 75 minutes the conversion of **4$^{\text{dppe}}$** to **5$^{\text{dppe}}$** stopped, and after 12 hours the ratio remained unchanged (32:68). Heating the reaction mixture to 323 K did not alter the ratio of each isomer.

2.5.3 DFT investigation of the deprotonation of [IrCl(COD)(dppe)]

The identity and relative energy of the two [IrH(1-κ-4,5,6-η^3-C$_8$H$_{10}$)(dppe)] isomers **4^{dppe}** and **5^{dppe}** were supported by DFT calculations, which could also rationalize the selective formation of **4^{dppe}** by deprotonation, and the mechanism of its conversion to **5^{dppe}**. The detection of *^{t}*BuOH in the reaction mixture implies deprotonation of **1^{dppe}** by *^{t}*BuO$^-$. Deprotonation of **1^{dppe}** is expected to produce, after chloride elimination, a neutral 16-electron [Ir(C$_8$H$_{11}$)(dppe)] intermediate, which was not observed. The *^{t}*BuO$^-$ anion can abstract a proton from the cyclooctadiene fragment in one of four possible positions (**Scheme 2-7**) in solution. This leads in each case to two possible structural isomers of [Ir(C$_8$H$_{11}$)(dppe)]: [Ir(1-κ-5,6-η^2-C$_8$H$_{11}$)(dppe)] (**II^{dppe}**, **II'^{dppe}**) and [Ir(1,2,3-κ^3-C$_8$H$_{11}$)(dppe)] (**II''^{dppe}**, **II'''^{dppe}**) (**Figure 2-13**), each one adopting two possible conformations depending on the orientation of the Ir(dppe) chelate ring (flip-flop). **II'''^{dppe}** was not explored due to the higher relative energy of **II''^{dppe}** compared to **II^{dppe}** and **II'^{dppe}**.
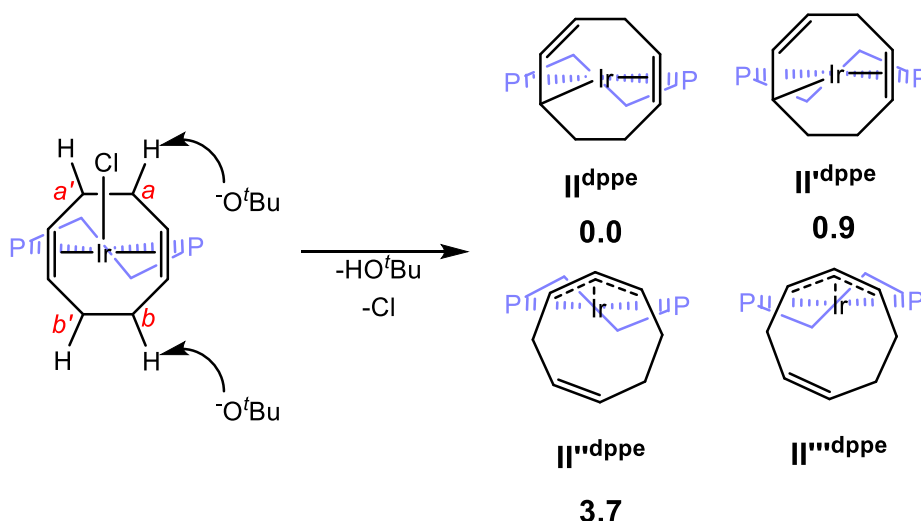
Scheme 2-7. Deprotonation of the COD ligand leading to two different [Ir(C$_8$H$_{11}$)(dppe)] (**II^{dppe}** and **II''^{dppe}**) isomers and their respective conformers with a flipped Ir(dppe) moiety (**II'^{dppe}** and **II'''^{dppe}**) (phenyl rings removed for clarity).
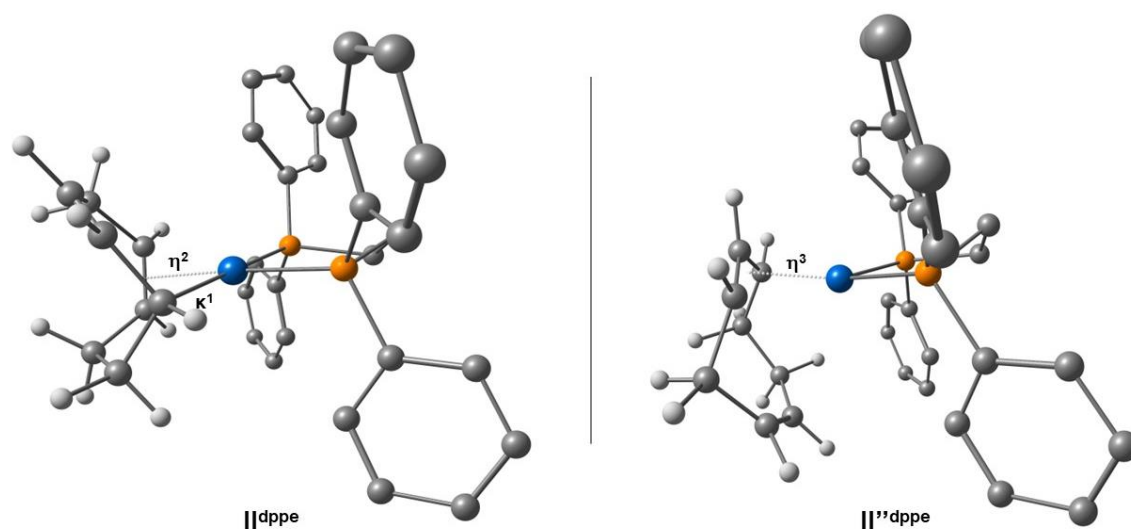
II$^{\text{dppe}}$ II''$^{\text{dppe}}$

Figure 2-13. Computed structures for the two low energy isomers resulting from the deprotonation of **1**$^{\text{dppe}}$ – at position (a) **II**$^{\text{dppe}}$ and at position (b) **II''**$^{\text{dppe}}$ (only one of the two possible conformations are shown). Hydrogen atoms on the dppe ligand removed for clarity.

2.5.3.1 Evolution of [Ir(1-κ-5,6-η^2-C$_8$H$_{11}$)(dppe)]
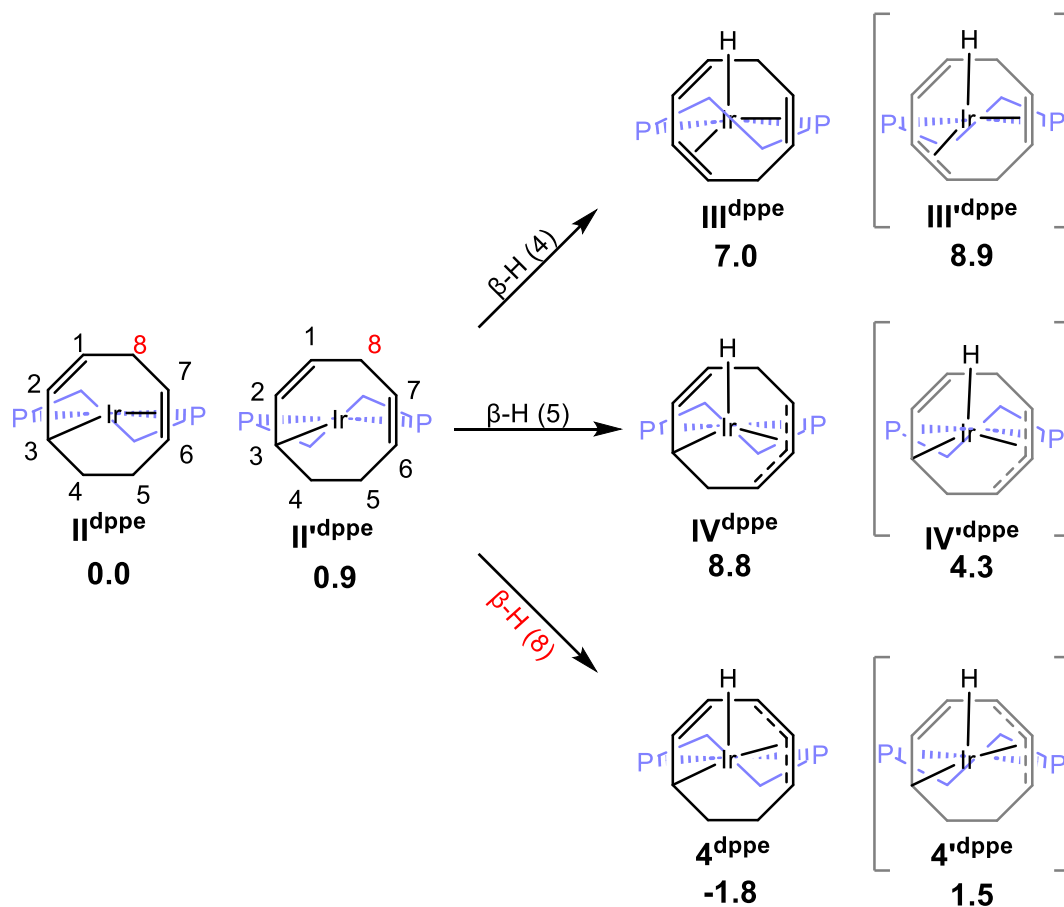
Scheme 2-8. Reaction scheme for the generation of **4^{dppe}**. The phenyl groups on the dppe are omitted for clarity. The complexes in square brackets indicate complexes with dppe in the opposite orientation (Relative energy profiles in kcal mol^{-1}).

As shown in **Scheme 2-8**, the β-hydride elimination from the [Ir(1-κ-5,6-η^2-C$_8$H$_{11}$)(dppe)] isomer (conformers **II^{dppe}** and **II'^{dppe}**) may occur at either C4, C5 or C8. The β-H (4) yields the corresponding monohydride diastereomers **III^{dppe}** and **III'^{dppe}**. These have a 1,3,6-COT ligand coordinated *via* the 3,4 and 6,7 unsaturations and two separate methylene groups at positions C5 and C8. The high relative energy is a consequence of the two methylene groups breaking the delocalization across the cyclooctatriene ligand. If the hydride elimination occurs at C5 two unsaturated moieties (1-κ-5,6,7-η^3-C$_8$H$_{10}$; **IV^{dppe}** and **IV'^{dppe}**) are obtained.

A methylene bridge is placed on each side of the allyl system, separating it from the localized 1,2-alkene-3-κ fragment, yielding again a relatively high energy. The most feasible pathway is when β-hydride elimination occurs at the C8 position. This leads to the lowest energy product, with a largely delocalized system with the η^3 donor situated next to the uncoordinated double

bond, **4^{dppe}**. Most importantly, the structure of **4^{dppe}** matches the experimentally predicted structure (based on the NMR data). The resonance structures for each system are shown in **Scheme 2-9**.
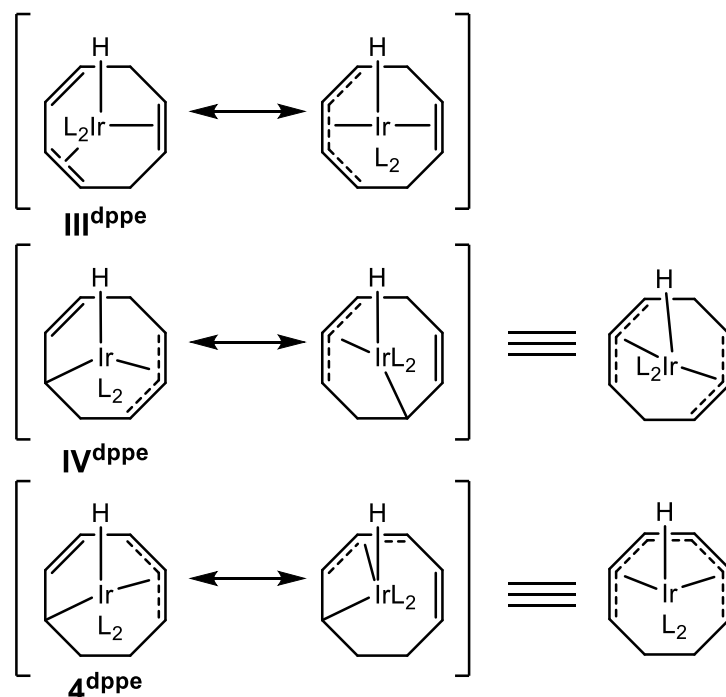
Scheme 2-9. Delocalization across the C_8H_{10} ligand on Ir. Note the delocalization of the ligand on **4^{dppe}** provides the most delocalized electron distribution across the six C atoms. L$_2$ = dppe.

The transition state for β-H elimination at C8 (**TS$_{(II-4)}$^{dppe}**) is the lowest energy transition state leading to the generation of **4^{dppe}**. The transition states for **III^{dppe}** (**TS$_{(II-III)}$^{dppe}**) and **IV^{dppe}** (**TS$_{(II-IV)}$^{dppe}**) are higher energy than **TS$_{(II-4)}$^{dppe}**, and the higher energy of the corresponding products rationalise their non-observation (**Figure 2-14**).

The view of each transition state highlights the observed reactivity and formation of each monohydride product (**Figure 2-15**). Given the orientation of the C_8H_{11} ligand, the hydrogen at the C8 position is best placed for hydride transfer to form **4^{dppe}**. The transition states show that the Ir-H bond length is consistent at 1.7 Å for all isomers of [IrH(C_8H_{10})(dppe)].

The difference in relative energies is best demonstrated by the corresponding C-H distance. For **TS$_{(II-4)}$^{dppe}** the proton is close to the iridium facilitating β-hydride elimination (C-H distance = 1.47 Å), decreasing the energy associated with ligand rearrangement. **TS$_{(II-III)}$^{dppe}** and **TS$_{(II-IV)}$^{dppe}** have longer C-H distances (1.57 Å), making the process of forming a hydride more energetically demanding.
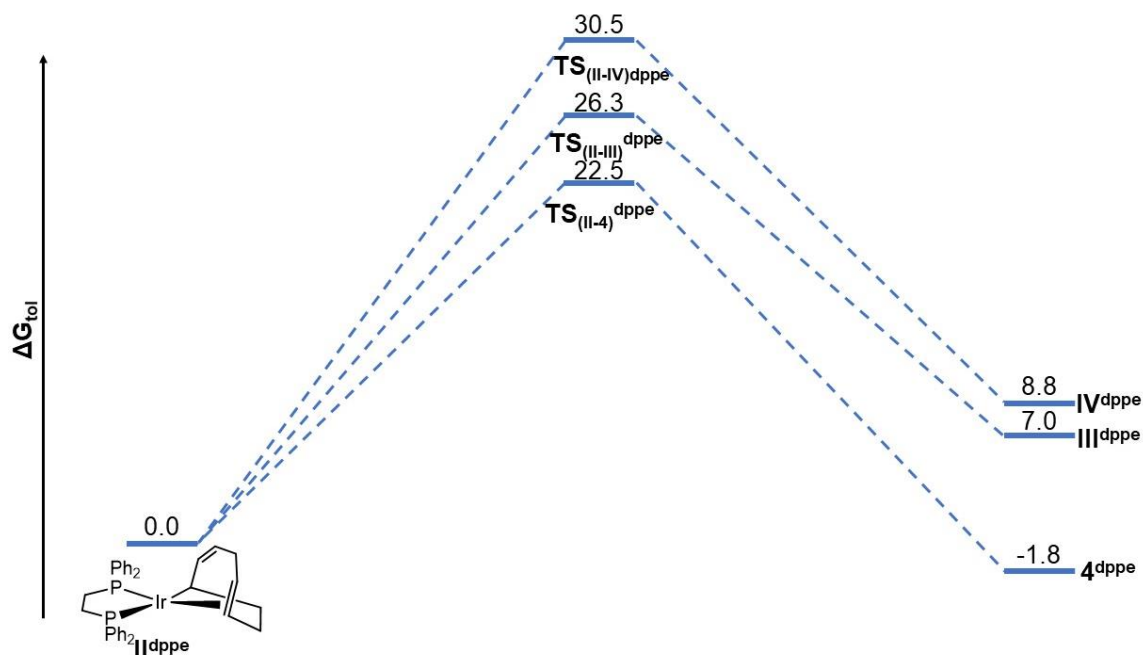
Figure 2-14. Gibbs-energy profile (in kcal mol^{-1}) for all possible β-H elimination reactions from intermediate **II^{dppe}**.
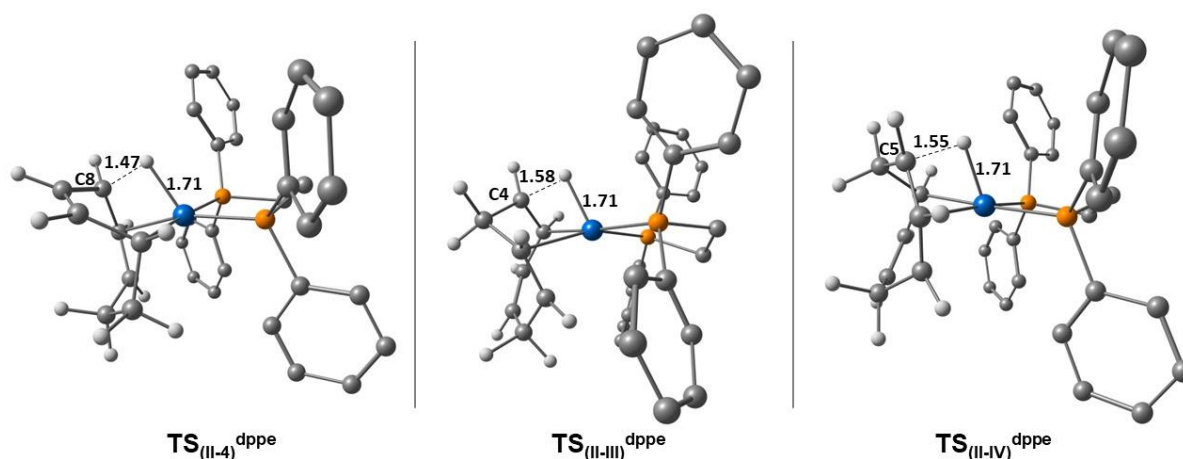
Figure 2-15. Transition states for β-hydride elimination at C8, C4, and C5. Dashed bonds illustrate calculated distances between H and C. Hydrogen atoms on the dppe ligand have been removed for clarity.

It is worth noting that the lowest energy transition state is that leading from **II'^{dppe}** to **4'^{dppe}** (**TS$_{(II'\text{-}4')}$^{dppe}**), which is 1.5 kcal mol^{-1} lower in energy than **TS$_{(II\text{-}4)}$^{dppe}** (**Figure 2-16**). The barrier for the flip-flop conformational change should be even lower, however, a reliable energy for this transition could not be located. Thus, it is suggested that these two conformers are at rapid equilibrium on the NMR timescale and only one set of signals is observed.
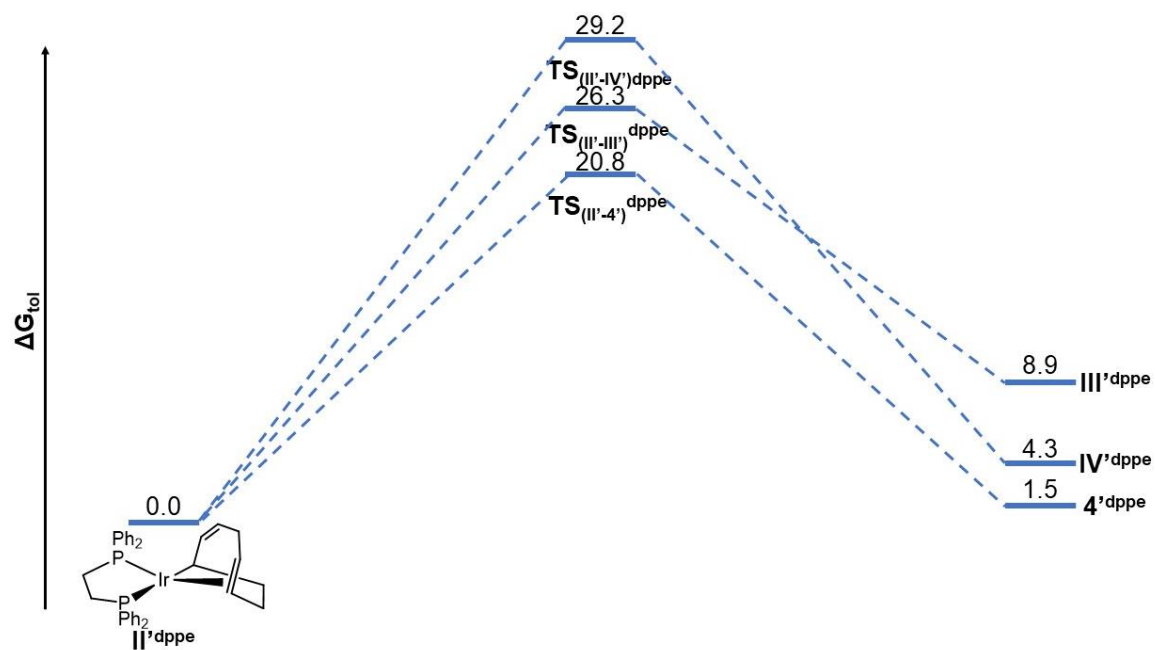
Figure 2-16. Gibbs-energy profile (in kcal mol^{-1}) for all possible β-H elimination reactions from intermediate **II'$^{\text{dppe}}$**. Note the inversion of the conformation of the dppe ligand.

2.5.3.2 Evolution of [Ir(1,2,3-κ³-C₈H₁₁)(dppe)]
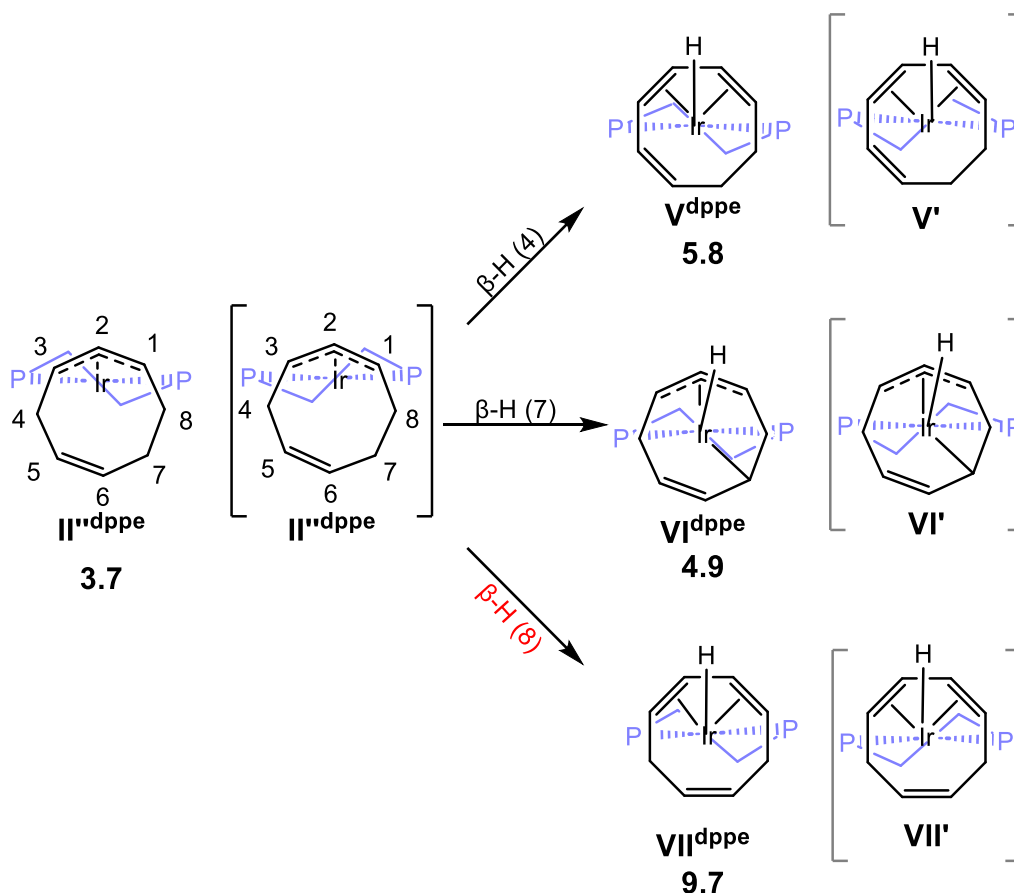
Scheme 2-10. Reaction scheme for β-hydride elimination at C4, C7, and C8 for **II''ᵈᵖᵖᵉ** (and **II'''ᵈᵖᵖᵉ**). The phenyl groups are omitted for clarity.

The η^3 isomer **II''ᵈᵖᵖᵉ** is located 3.7 kcal mol⁻¹ higher than **IIᵈᵖᵖᵉ** and the corresponding diastereomer **II'''ᵈᵖᵖᵉ** was not explored. The β-H elimination process from **II''ᵈᵖᵖᵉ** (and **II'''ᵈᵖᵖᵉ**) may in principle occur from carbon atoms 4, 7 and 8 (**Scheme 2-10**). The β-elimination at C4 may lead, upon rearrangement of the C4-C5-C6 electron density, to the new isomer **Vᵈᵖᵖᵉ** (and **V'ᵈᵖᵖᵉ**), in which the COT ligand binds as a conjugated η^4 diene. The elimination from C7 leads to **VIᵈᵖᵖᵉ** (and **VI'ᵈᵖᵖᵉ**), in which the ligand is bonded to the Ir atom as in **IVᵈᵖᵖᵉ** (and **IV'ᵈᵖᵖᵉ**) but is oriented differently with respect to the H and dppe ligands. Finally, elimination at C8 leads to another two configurations **VIIᵈᵖᵖᵉ** (and **VII'ᵈᵖᵖᵉ**) with a 1,3,6-COT ligand bonded as a conjugated η^4 diene, like **IIIᵈᵖᵖᵉ** (and **III'ᵈᵖᵖᵉ**), but in a different orientation. The geometries of **Vᵈᵖᵖᵉ**, **VIᵈᵖᵖᵉ** and **VIIᵈᵖᵖᵉ** were optimized and found to have significantly higher relative energies than **4ᵈᵖᵖᵉ** (5.8, 4.9, and 9.7 kcal mol⁻¹, respectively). The higher energy of each hydride product, coupled with the higher energy of the [Ir(C₈H₁₁)(dppe)] intermediate, indicated that the corresponding transition-state calculations were not worth exploring.

Of particular interest is the fact that the ligand prefers to adopt a 1-κ-4,5,6-η^3-C_8H_{10} geometry with an uncoordinated C2-C3 double bond in both **4^{dppe}** and **5^{dppe}**, hence yielding two formally Ir^{III} isomers, rather than an 18-electron 1,3,5-COT structure with a formally Ir^I complex (*e.g.,* the optimized higher energy **V^{dppe}**). There are literature precedents for the 1,2,5,6-η^2, η^2 binding mode of COT in iridium chemistry, for instance [IrCl(COT)]$_2$ and CpIr(COT), although none has been structurally characterized. Structures featuring this type of COT coordination are however available for Co^I,[164] Mo^0, and Ru^0.[165]

2.5.3.3 Transformation of 4^{dppe} to 5^{dppe}

It is notable that the lowest-energy product obtained from **II^{dppe}** (**4^{dppe}**) features the uncoordinated alkene moiety *syn* relative to the hydride ligand. No direct pathway is available to transform intermediate **II^{dppe}** to isomer **5^{dppe}**, for which, on the other hand, the uncoordinated alkene moiety is located *anti* relative to the hydride ligand. Hence, the isomerization must occur through a different pathway. Exploration of the various possibilities to rotate the C_8H_{10} around the metal coordination sphere revealed a low-energy pathway linking **4^{dppe}** to a different structural isomer of **5^{dppe}**, **5'^{dppe}**. **5'^{dppe}** has an ethylene bridge in the equatorial plane, essentially a diastereomer of **5^{dppe}**, 0.7 kcal mol^{-1} higher than **5^{dppe}** and 0.2 kcal mol^{-1} higher than **4^{dppe}**. The isomerization of **4^{dppe}** to **5^{dppe}** proceeds *via* the rearrangement schematically illustrated in **Figure 2-17**. This entails a rotation of the C_8H_{10} ligand relative to the Ir-H axis *via* **TS$_{(4-5')}$^{dppe}** with simultaneous displacement toward the Ir atom of the two CH groups of the uncoordinated alkene, which becomes part of coordinated η^3 moiety, and the inverse displacement of the two CH groups of the coordinated η^3 moiety that end up forming the uncoordinated alkene moiety. This process, which is rate-determining, has a calculated barrier of 24.0 kcal mol^{-1} from **4^{dppe}**, quite close to that obtained from the measured rate constant $k_{(4-5)\text{-dppe}}$ by application of the Eyring relationship (22.3 ± 0.1 kcal mol^{-1}). The product of this rearrangement, however, is the higher-energy conformer (**5'^{dppe}**) of the most stable geometry for **5^{dppe}**. The electronic rearrangement of the C_8H_{10} ligand occurs through a small energy barrier located at a relatively low G (10.4 kcal mol^{-1}). Therefore, **5'^{dppe}** converts to the more stable structure **5^{dppe}** very rapidly on the NMR timescale at room temperature. The calculated energy difference between **4^{dppe}** and **5^{dppe}** (-0.5 kcal mol^{-1}) agrees extremely well with the experimental value of -0.51 ± 0.04 kcal mol^{-1} in benzene-d_6.
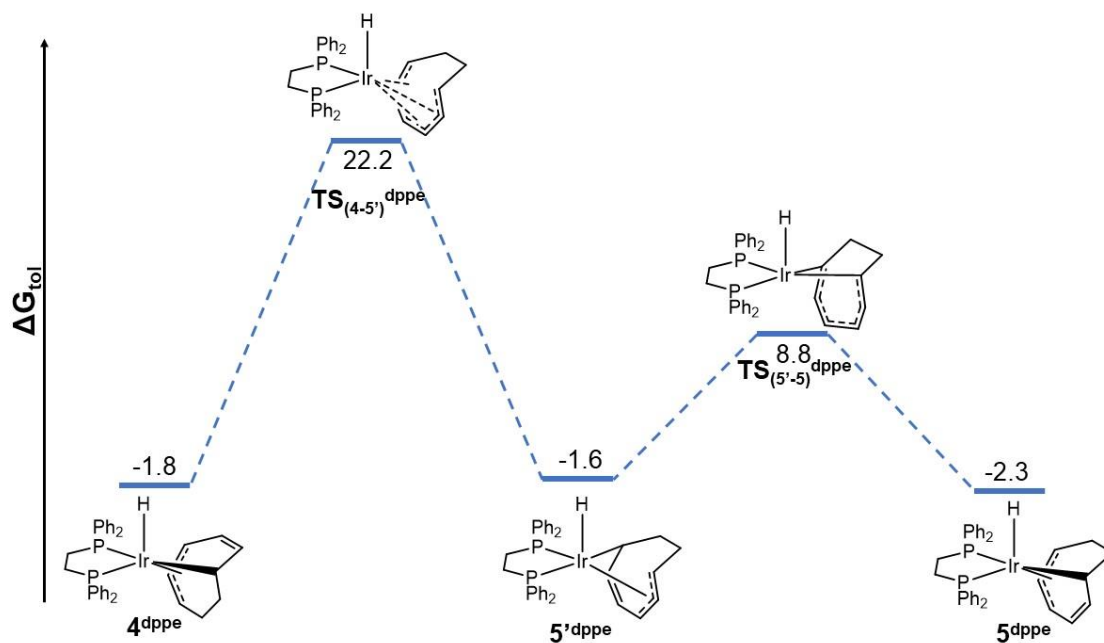
Figure 2-17. Gibbs energy profile (in kcal mol^{-1}) for the isomerization of **4^{dppe}** to **5^{dppe}**.

2.6 Solid-state characterization of 4^{dppe} and 5^{dppe}

The 1-κ-4,5,6-η^3 binding mode is documented for the homologous complex [IrH(1-κ-4,5,6-η-C$_8$H$_{10}$)(dppb)], obtained by the addition of dppb to [Ir(NH$_2$)(COD)]$_2$.[163] However, the presence of more than one isomer was not mentioned in that contribution (**Scheme 2-11**). That reaction is closely related because a bridging amido ligand serves as an internal base to deprotonate the COD ligand with elimination of ammonia. Thus, the action of a strong base on the COD ligand in compound **1^{dppe}**, in the absence of more acidic reagents such as isopropanol that can themselves be deprotonated, coordinate to the metal and then deliver a hydride ligand by β-H elimination, induces a COD deprotonation. In this respect, it is also relevant to note the work of Kubiak *et al.*,[166] where the treatment of [Ir(COD)(triphos)]$^+$Cl$^-$ (triphos = bis(diphenylphosphinoethyl)phenylphosphine) with a variety of bases gave the [Ir(1-κ-5,6-η-C$_8$H$_{11}$)(triphos)] product. Here, the triphos hinders the β-H elimination process after deprotonation through tridentate bonding.
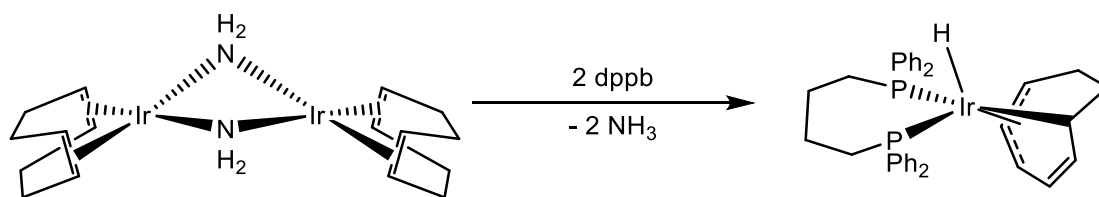
Scheme 2-11. Formation of a homologous [IrH(1-κ-4,5,6-η-C$_8$H$_{10}$)(dppb)] complex by the addition of dppb to [Ir(NH$_2$)(COD)]$_2$.[28]

Attempts to crystallize **4^{dppe}/5^{dppe}** were unsuccessful at first. When a benzene-d_6 solution of the two isomers formed *in situ* was layered with hexane, the complexes did not crystallize. An alternative approach was thus taken. **4^{dppe}/5^{dppe}** can be synthesised at scale (45 %), and when dissolved in dry toluene and layered with hexane, crystals were obtained upon slow evaporation of the solvent.

The solid-state structure indicates that the cyclooctadienyl ligand is disordered with respect to C2 and C8. The atomic displacement parameters of the disordered pairs of carbons were constrained to be equal (C2 & C2A, C8 & C8A). This disorder is due to the two possible positions of the uncoordinated double bond (C2=C3 or C7=C8A) (**Figure 2-18**). Separation of the two superimposed structures, leads to two different structural isomers, that represent **4^{dppe}** and **5^{dppe}**.

In both the solid-state structures and those predicated by DFT calculations, the allylic carbons are *trans* to P2, and the κ^1 C-H is *trans* to P1. The measured distance for the allylic η^3 (C4,

C5, and C6) are the same regardless of the unbound alkene. The difference between the two isomers is due to the C_8H_{10} alone, hence, the only observable metrics that change are those associated with the bond distances (and angles) associated with C1 through to C8. This gives credence to the proposed isomerization mechanism depicted in **2.5.3.3**, in which the ligand is rearranged rather than a complete change in the backbone. The computed bond distances and structural outputs are consistent with those obtained experimentally (**Figure 2-19**, **Table 2-4**, **Figure 2-20**, **Table 2-5**).

[IrH(1-κ-4,5,6-η³-C₈H₁₀)(dppe)]
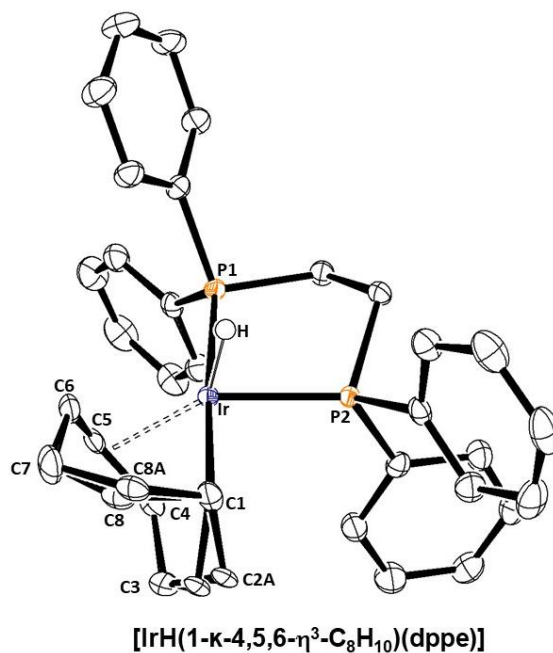
Figure 2-18. Solid-state structure for [IrH(1-κ-4,5,6-η³-C_8H_{10})(dppe)]. Anisotropic displacement ellipsoids are shown at 50% probability level. The hydrogen atoms on dppe are omitted for clarity. Unconstrained bond lengths [Å] and angles [°]: Ir–P1 2.3124(6); Ir–P2, 2.2559(5); Ir-H, 1.55(2); Ir–C1, 2.145(3); Ir–C4, 2.293(2); Ir–C5, 2.170(2); Ir1–C6, 2.217(2); P1–Ir–P2, 84.74(2), C1–Ir–C5, 93.71(9); P1–Ir1–P2, 81.84(3); C1-Ir-P1 174.51(6); C6-Ir-P2 174.77(6).

DFT 4^{dppe}   **Solid-state 4^{dppe}**
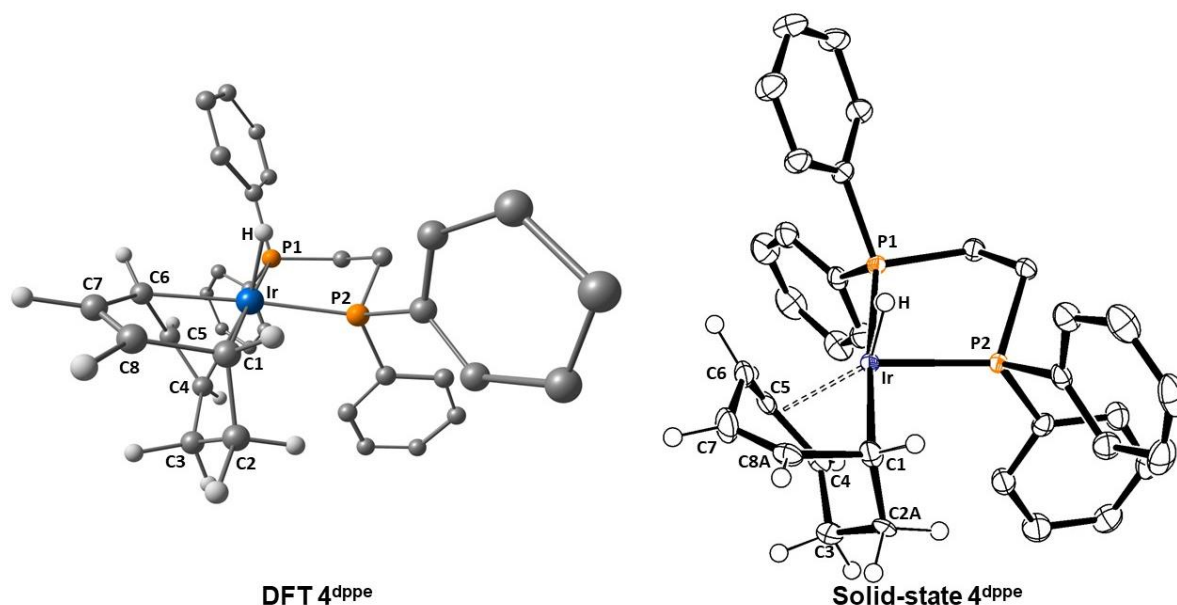
Figure 2-19. DFT and solid-state structure of **4^{dppe}**. Anisotropic displacement ellipsoids are shown at 50% probability level. The hydrogen atoms on dppe are omitted for clarity.

Table 2-4. Comparison of experimental (X-ray) and calculated (DFT) selected bond lengths (Å) for **4^{dppe}**.

Atom1	Atom2	X-ray	DFT
Ir	P1	2.3124 (6)	2.3591
Ir	P2	2.2559(5)	2.3006
Ir	H	1.55 (2)	1.6115
Ir	C1	2.145 (3)	2.1586
Ir	C4	2.293(2)	2.3658
Ir	C5	2.170(2)	2.2094
Ir	C6	2.217(2)	2.2213
C1	C2A	1.41(1)	1.5440
C2A	C3	1.59(1)	1.5404
C3	C4	1.506(4)	1.5314
C4	C5	1.419(3)	1.4155
C5	C6	1.436(3)	1.4438
C6	C7	1.506(4)	1.4942
C7	C8A	1.29(2)	1.3351

DFT 5$^{\text{dppe}}$ **Solid-state 5$^{\text{dppe}}$**
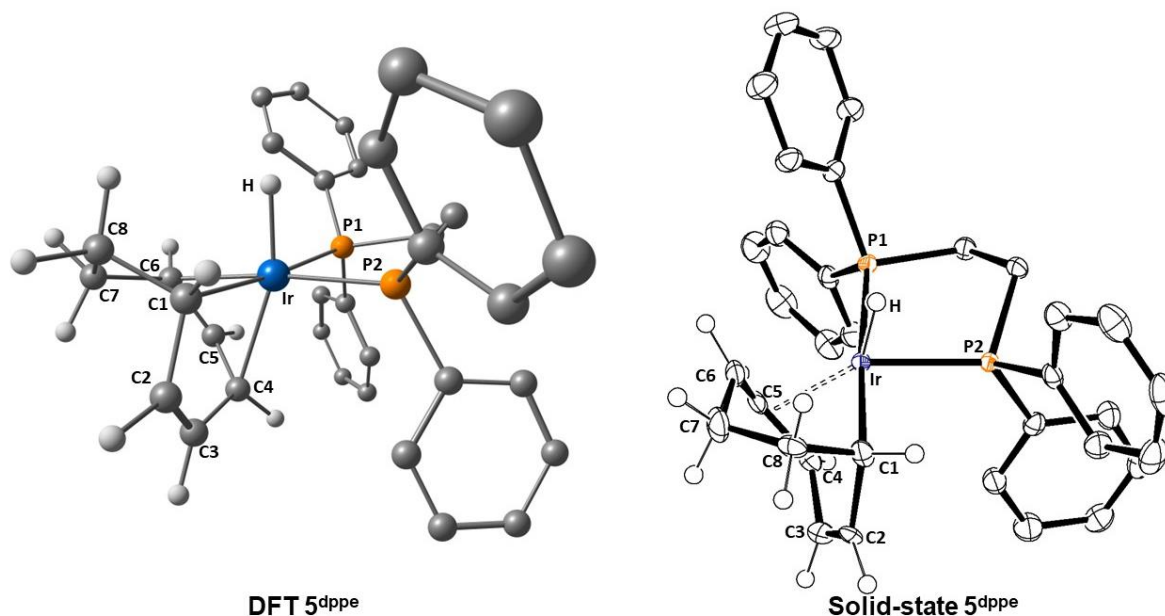
Figure 2-20. DFT and solid-state structure of **5$^{\text{dppe}}$**. Anisotropic displacement ellipsoids are shown at 50% probability level. The hydrogen atoms on dppe are omitted for clarity.

Table 2-5. Comparison of experimental (X-ray) and calculated (DFT) selected bond lengths (Å) for **5$^{\text{dppe}}$**.

Atom1	Atom2	X-ray	DFT
Ir	P1	2.3124 (6)	2.3611
Ir	P2	2.2559(5)	2.3009
Ir	H	1.55 (2)	1.6169
Ir	C1	2.145 (3)	2.1600
Ir	C4	2.293(2)	2.3311
Ir	C5	2.170(2)	2.2051
Ir	C6	2.217(2)	2.2376
C1	C2	1.6123	1.5073
C2	C3	1.2327	1.3375
C3	C4	1.5062	1.4907
C4	C5	1.4189	1.4202
C5	C6	1.4357	1.4398
C6	C7	1.5055	1.5352
C7	C8	1.5380	1.5363

2.7   Summary

Under ambient conditions in the absence of an alcohol in the solvent, the type of alkoxide used as a base has a marked effect on **1**$^{\textbf{dppe}}$. When a β-hydrogen is present on the base, the COD ligand maintains its chemical composition and two isomers of [IrH(C$_8$H$_{12}$)(dppe)], **2**$^{\textbf{dppe}}$ and **3**$^{\textbf{dppe}}$, are produced. **2**$^{\textbf{dppe}}$ isomerizes to **3**$^{\textbf{dppe}}$ through H-migration from the hydride to the cyclooctadiene through a C$_8$H$_{13}$-containing intermediate. The relative energy of this intermediate is located slightly above **2**$^{\textbf{dppe}}$ explaining its non-observation on the NMR timescale.

When a base with no β-hydrogen is used, on the other hand, deprotonation of the COD fragment occurs with subsequent β-H elimination from a C$_8$H$_{11}$ ligand to yield two isomers of [IrH(C$_8$H$_{10}$)(dppe)], **4**$^{\textbf{dppe}}$ and **5**$^{\textbf{dppe}}$. The isomerization mechanism proceeds through rotation of the C$_8$H$_{10}$ ligand. The structures predicted by DFT match with the solid-state structures obtained through X-ray crystallography. Importantly the DFT study provided consistent thermodynamic and kinetic parameters to those obtained experimentally.

The results of this section provide an insight into the activation of [IrCl(COD)(LL)] complexes in the presence of difference bases by demonstrating that the formations of certain products are heavily alkoxide dependent.

Chapter 3: Characterization of Anionic Ir[III] Tetrahydride Complexes and their role in Transfer Hydrogenation

3.1 Introduction

Previous work by Poli and co-workers showed how a base was necessary if iridium systems like [IrCl(P,S^R)(COD)] were to achieve high turnover for the hydrogenation of acetophenone and its derivatives.[145] In fact, catalytic activity in the absence of an external base, even in the presence of an internal base (*i.e.* methoxide for the system generated *in* situ from [Ir(μ-OMe)(COD)]$_2$ and the (P,S^R) ligands), is significantly lower. However, upon addition of a strong external base to this system high catalytic activity can be achieved. One of the proposed mechanisms of operation for this reaction is cation-assisted where an anionic tetrahydrido species features as the active catalyst. The cation (provided by the base) facilitates H-transfer through non-covalent interactions, which provide stability to an otherwise highly reactive anionic Ir[III] complex. This proposal was supported by complementary experimental work that demonstrated a match between the experimentally determined turnover frequency and the calculated energy span of the catalytic cycle.[87] Attempts to isolate intermediate species involved in the catalytic cycle proved difficult due to the extreme sensitivity of the complexes. Dihydride species for the corresponding rhodium P,S complexes have though been characterized under catalytically relevant conditions,[36] however, a specific tetrahydrido species for iridium and a P,S ligand is yet to be reported.

Tetrahydrides and their derivatives have been reported to be involved in alkene dehydrogenation catalysts, and feature with iridium pincer complexes.[167–169] Anionic tetrahydride Ir[III] derivatives have also been obtained from the reaction of KH with [IrH$_5$L$_2$] (L = PPh$_3$,P^{i}Pr$_3$) in THF (**Figure 3-1**).[147,148] However, the DFT study proposed for hydrogenation with [Ir(H)$_4$(P,S^R)]$^-$ implied that such complexes are quantitatively generated by H$_2$ addition to [IrHL$_2$(^{i}PrOH)] through a sequence of deprotonation, H$_2$ oxidative addition and ^{i}PrOH reductive elimination steps.
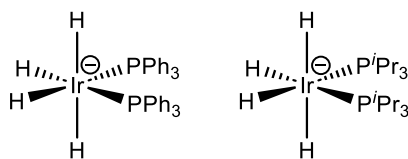
Figure 3-1. Structurally relevant reported anionic [Ir(H)$_4$(L)$_2$]$^-$ complexes, the counter ion is omitted for clarity.[147,148]

Less intuitively, the same complexes were suggested by the DFT to form favourably in the absence of free H_2, with the H equivalents needed being provided by isopropanol under transfer hydrogenation conditions. In fact though, under catalytically relevant conditions neutral trihydride complexes, $[Ir(H)_3(PPh_3)_3]$ (-*fac*, and -*mer*) (**Scheme 3-1**) have been reported to form in the absence of hydrogen, under transfer hydrogenation conditions in the presence of a base.[99] In this study the cyclooctadiene was lost as both cyclooctene and cyclooctane. The preferential formation of $[Ir(H)_3(PPh_2)_3]$, rather than anionic $[Ir(H)_4(PPh_3)_2]^-$ may relate to the monodentate nature of PPh_3, allowing the coordination of three neutral ligands.
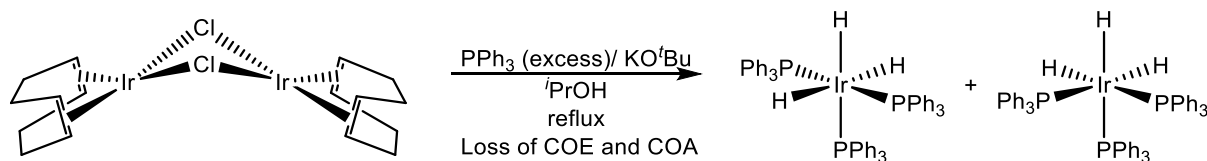
Scheme 3-1. Formation of $[Ir(H)_3(PPh_3)_3]$ under transfer hydrogenation conditions.[99]

The detection of anionic tetrahydrido iridium complexes under catalytically relevant conditions has rarely been explored, hence, the focus of this chapter is the formation of such complexes in the presence of a base.

3.2 Aims and Objectives

The aim of this chapter was to demonstrate how anionic tetrahydride complexes could form under catalytically relevant conditions, whilst illustrating the influence of a base on the hydrogenation reaction. Three iridium precatalysts [IrCl(COD)(L$_2$)] (L$_2$ = dppe, dppf and (*S*)-BINAP) were selected as model complexes to evaluate the potential formation of tetrahydrides. The dppe,[152,153] and dppf[149] containing precatalysts have been previously reported, with the reactivity of the former, with a base examined extensively in **Chapter 2:**.

The hydrogenation activity of some of these systems has been demonstrated in the literature,[98,105] but do not explicitly examine the potential formation of an anionic species as the active catalyst nor, study this phenomenon. The previous work does however show that a base was required for high turnover, which was also explored.

This chapter aims to examine why a base is required for higher turnover, as well as propose a feasible mechanism for hydrogenation under such conditions. DFT calculations utilizing an explicit solvent model were conducted to map the proposed operating cycle for K[Ir(H)$_4$(dppe)], and the conversion of acetone to isopropanol.

3.3   Characterization of M[Ir(H)$_4$L$_2$] complexes

3.3.1   Activation of [IrCl(COD)(dppe)] in the presence of KO^{t}Bu

3.3.1.1 Transfer hydrogenation of COD

Chapter 2: covered the reaction of **1^{dppe}** with methoxide and *tert*-butoxide under ambient conditions. In isopropanol these bases led to **2^{dppe}** and **3^{dppe}** exclusively.
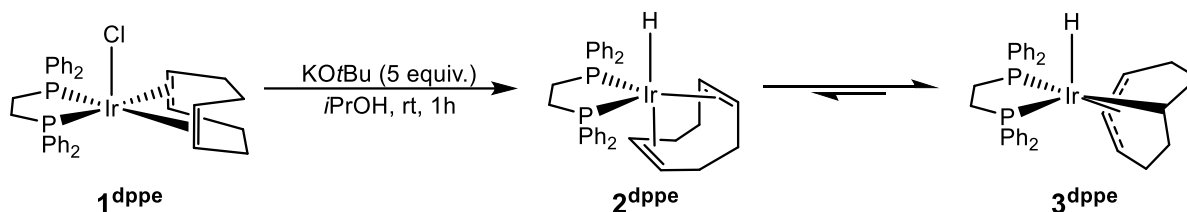
Scheme 3-2 Synthesis of **2^{dppe}** and **3^{dppe}**.

However, when an equilibrium mixture of **2^{dppe}** and **3^{dppe}** with isopropanol (2 equiv.), in toluene-d_8, was warmed to 353 K and a ^{31}P{^{1}H} NMR spectrum recorded, a new peak was observed to appear at *δ* 44.2. After 30 minutes, this peak reflected the sole phosphorus-containing reaction product as no starting material (**Figure 3-2**) signals remained. This phosphorus resonance proved to couple to two hydride resonances, at *δ* -12.20 and *δ* -13.62 in the ^{1}H NMR that appear in a 1:1 ratio (**Figure 3-3**). The complex giving rise to these signals is **6^{dppe}** based on further NMR spectroscopic assignments (**Table 3-1**). The corresponding ^{13}C NMR spectrum showed resonances that could readily be attributed to bound dppe, acetone, isopropanol, and cyclooctene.
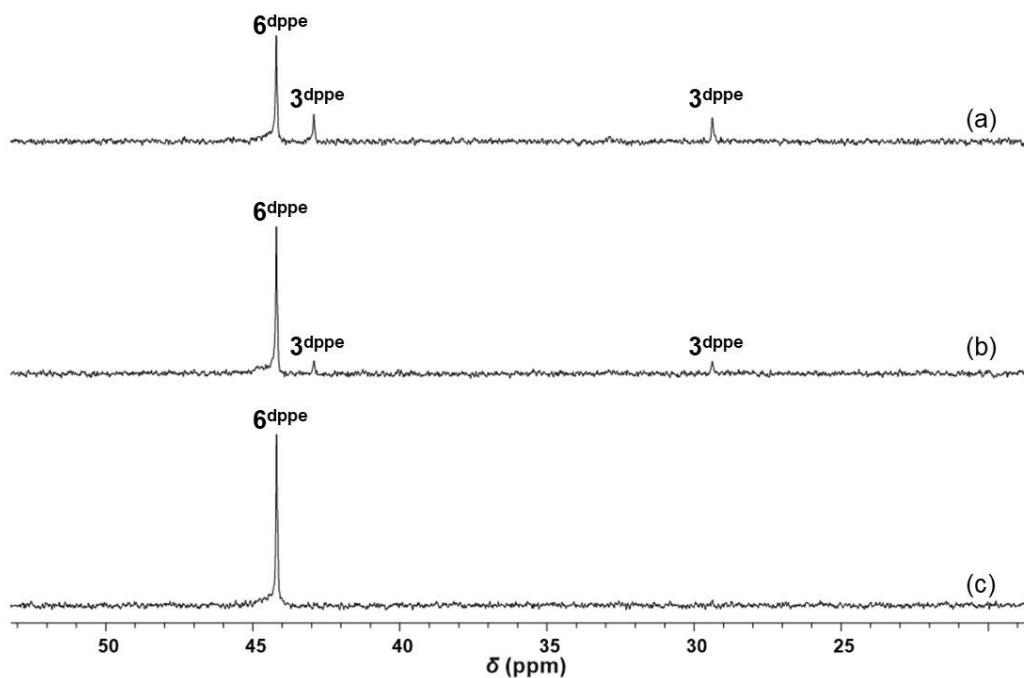
Figure 3-2. Series of four $^{31}P\{^1H\}$ NMR spectra showing the conversion of 2^{dppe} and 3^{dppe} in toluene-d_8 upon reaction with isopropanol and KO^{t}Bu at 353 K. (a) 3 minutes; (b) 5 minutes; (c) 10 minutes.
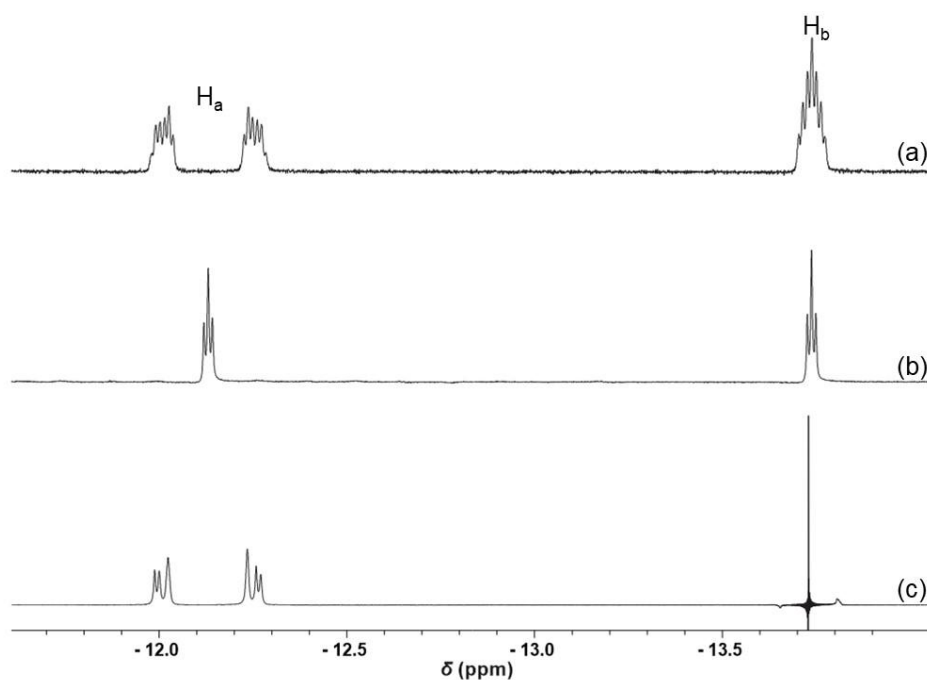
Figure 3-3. Hydride region of the ^1H NMR spectra for 6^{dppe} in toluene-d_8 at 353 K. (a) ^1H spectrum; (b) $^1H\{^{31}P\}$ spectrum; and (c) $^1H\{H_b\}$ spectrum

The presence of cyclooctene and acetone in the reaction mixture alludes to the successful transfer hydrogenation of the initial cyclooctadiene ligand (in either the η^2:η^2 or κ^1:η^3 form).

91

This would leave a highly electron poor iridium centre which must gain electron density through ligand binding. Consequently, the anionic tetrahydride complex $[Ir(H)_4(dppe)]^-$ (**6^{dppe}**) forms. The appearance of the hydride ligands NMR signals is fully diagnostic of this structure. Two lie *trans* to one phosphorus donor and *cis* to the other one (H_a and H_a'), while the remaining two are *cis* to both phosphorus donors (H_b), and couple equally to the two other hydride ligands. Thus, the full spin system is $AA'B_2XX'$ (A, A' = *trans*-H, B = *cis*-H and X, X' = P). Further proof for this comes from selective decoupling experiments and simulation using gNMR v5.0, which lead to the data in **Table 3-1**. Consequently, for H_a, four distinct couplings are observed ($^2J_{HaHa'}$, $^2J_{HaHb}$, $^2J_{HPcis}$ and $^2J_{HPtrans}$) while for H_b, symmetry restricts this to $^2J_{HaHb}$ and $^2J_{HbPcis}$. This is illustrated in **Figure 3-3**.

The diagnostic signal for H_a contains a large splitting which is reflective of the modulus of the two coupling constants ($|J_{HPcis} \pm J_{HPtrans}|$). In the fully coupled ^1H NMR spectrum, the chemical and magnetic equivalence of the two H_b atoms result in a single signal, a septet, where decoupling from ^{31}P yields a triplet due to the $^2J_{HaHb}$ coupling.

Table 3-1. NMR properties for **6^{dppe}** in toluene-d_8 at 353 K.

Group	Chemical Shift (δ)
^{1}H, Ph (*ortho*)	7.98 (dd, $^3J_{HH}$ = 7.6)
(*meta*)	7.26 (t, $^3J_{HH}$ = 7.4)
(*para*)	7.17 (dd, $^3J_{HH}$ = 7.6)
dppe CH$_2$	2.20 ($^2J_{HH}$ = 5.5)
Ir-H$_a$	-12.12 ($^2J_{HaHa'}$ = 6.0, $^2J_{HHb}$ = 5.7, $^2J_{HPcis}$ = -15.2, $^2J_{HPtrans}$ = 121.6)
Ir-H$_b$	-13.80 ($^2J_{HHa}$ = 5.7, $^2J_{HPcis}$ = 17.8)
^{13}C, Ph (*ortho*)	133.1
(*meta*)	126.8
(*para*)	127.8
dppe CH$_2$	32.9
^{31}P, dppe	44.4 (s)

The structure shown in the table header depicts an Ir complex with a chelating dppe ligand (P atoms bearing Ph$_2$ groups), a negative charge ($\ominus$), and hydride ligands labeled H$_b$ (axial top and bottom), H$_a$ and H$_{a'}$.

K[**6^{dppe}**] was also generated when H$_2$ was added to an equilibrated solution of **4^{dppe}** and **5^{dppe}** in the presence of KO^{t}Bu, as detailed in **Figure 3-4**. Free cyclooctene was again released *via* the partial hydrogenation of the C$_8$H$_{10}$ ligand as revealed by ^{1}H NMR spectroscopy.
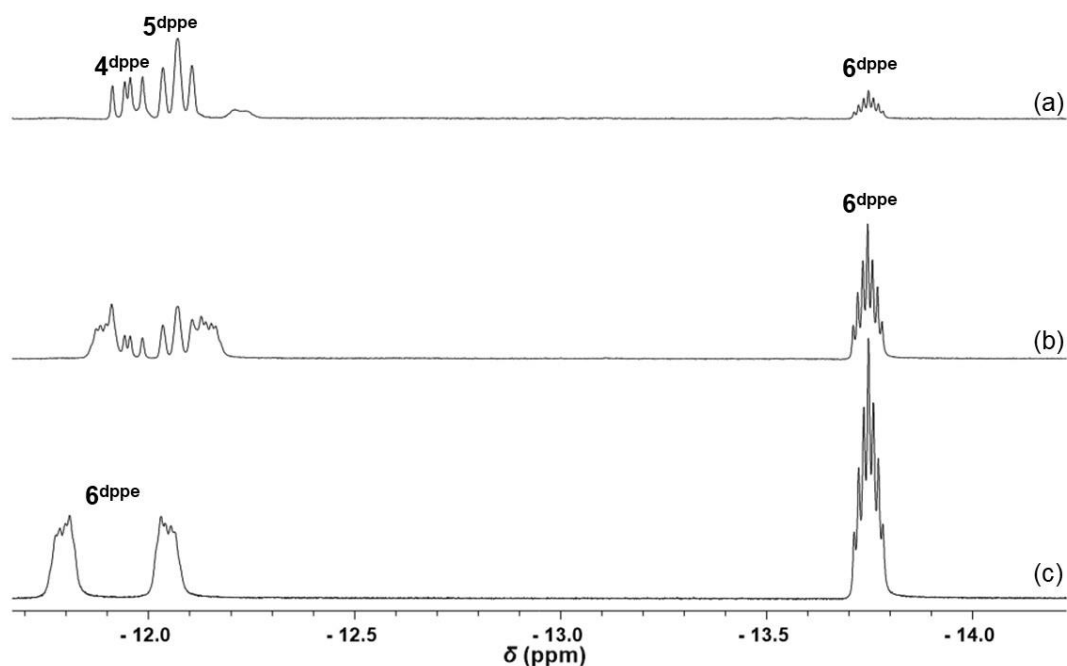
Figure 3-4. ^{1}H NMR for the reaction of 4^{dppe}/5^{dppe} + KO^{t}Bu (5 equiv.) and H$_2$ in THF-d_8 at 298 K. Recorded at (a) 5 minutes; (b) 2 hours; (c) 20 hours.

To further investigate this reaction, H$_2$ (3 bar) was added to a solution of 4^{dppe}/5^{dppe} in THF-d_8 without base. In this case, both the ^{1}H (hydride region) and ^{31}P{^{1}H} NMR spectra proved to be very complex, indicating the formation of several products, including 2^{dppe} and 3^{dppe} as very minor resonances but not 6^{dppe} (**Figure 3-5**). When 5 equivalents of KO^{t}Bu was added to this solution, K[6^{dppe}] proved to form selectively.
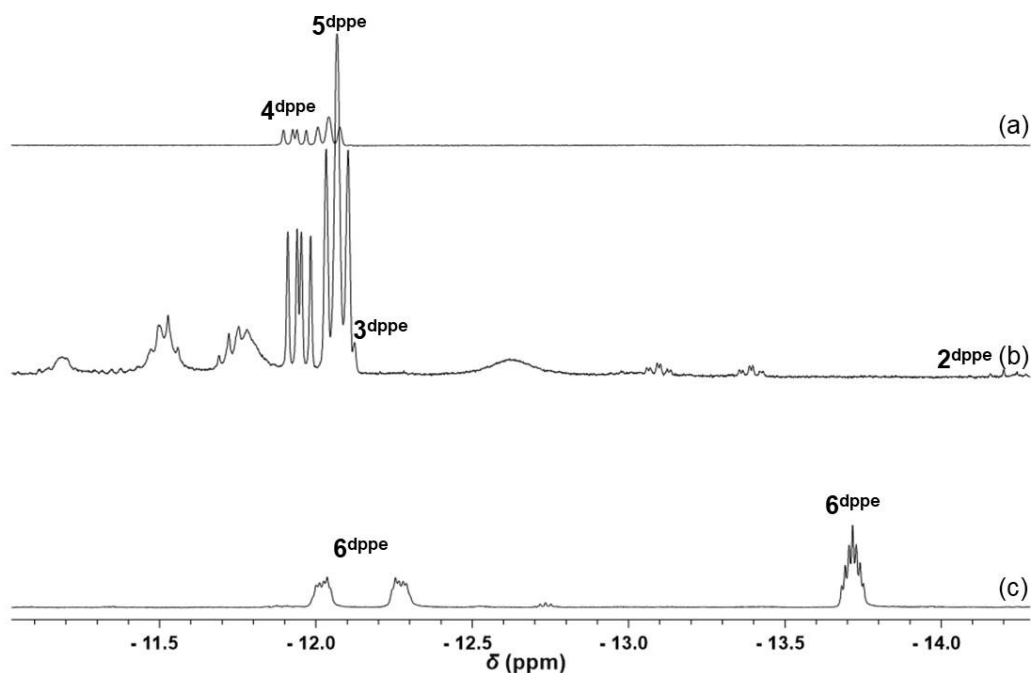
Figure 3-5. ^{1}H NMR spectra of the hydride region for the reaction of **4^{dppe}**/**5^{dppe}** (a) recorded after the addition of H$_2$; (b) 10 min after H$_2$ addition; (c) 12 hours after the addition of KO^{t}Bu.

It should be noted that the addition of H$_2$ to solutions of **2^{dppe}**/**3^{dppe}** or **4^{dppe}**/**5^{dppe}** in benzene-d_6 also produced **6^{dppe}**, over 18 hours at room temperature, but only in the presence of a suitable base. The base leads to *tert*-butanol, and the potassium counter ion needed to form **6^{dppe}**.

Equally complex situations resulted from the treatment of THF-d_8 solutions of pre-formed **2^{dppe}**/**3^{dppe}** or **4^{dppe}**/**5^{dppe}** with H$_2$ (3 bar) in the absence of base. Subsequent addition of KO^{t}Bu to these complex mixtures once again led to the selective production of K[**6^{dppe}**]. However, when 5 equivalents of KO^{t}Bu were first added to **2^{dppe}**/**3^{dppe}** or **4^{dppe}**/**5^{dppe}** mixtures, then exposed to H$_2$, they were selectively transformed into K[**6^{dppe}**].

These results establish the feasibility of forming the anionic tetrahydride complex K[**6^{dppe}**] from **1^{dppe}** under both hydrogenation and transfer hydrogenation conditions in the presence of a suitable base, according to **Scheme 3-3**.
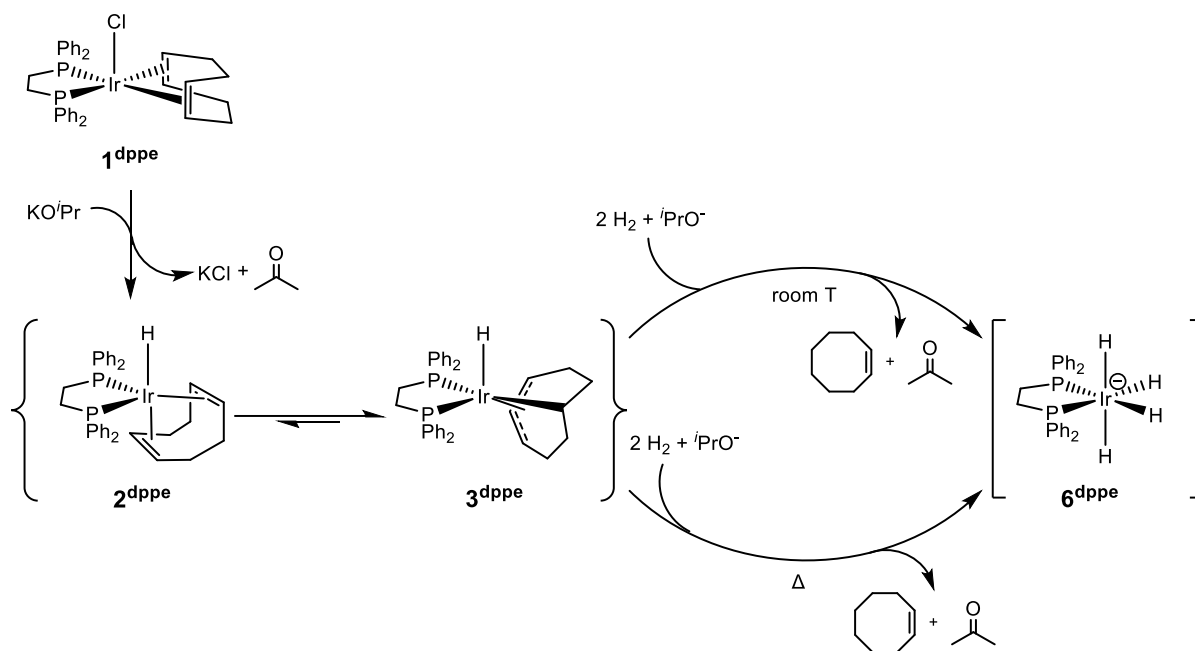
Scheme 3-3. Idealized stoichiometry for the **6^{dppe}** – generation from **1^{dppe}** under both hydrogenation and transfer hydrogenation conditions in isopropanol.

3.3.1.2 Crystallization of a neutral trihydride dimer

Several attempts were made to crystallize K[**6^{dppe}**], where its solutions were layered with hexane, and the solvent left to slowly evaporate under an inert atmosphere. While K[**6^{dppe}**] was not obtained, the related neutral trihydride dimer [Ir(H)$_3$(dppe)]$_2$ did crystalize. **Figure 3-6** shows the solid-state structure for this compound, with relevant bond distances, angles and dihedrals shown. While the exact positions of the hydride ligands could not be located accurately in the difference map. The neutral trihydride dimer is presumably formed by loss of 2 molecules of KH. However, synthesising the neutral trihydride dimer in a controlled way and bulk quantities proved difficult, as studies involving adjusting the ratio of the base only led to M[**6^{dppe}**] (M = Na$^+$, K$^+$).
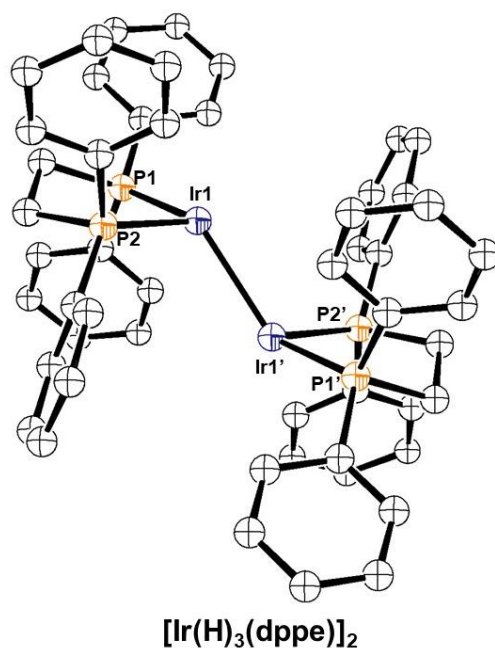
[Ir(H)$_3$(dppe)]$_2$

Figure 3-6. X-Ray structure of [Ir(H)$_3$(dppe)]$_2$. Anisotropic displacement ellipsoids are drawn at the 50% probability level. Hydrogen atoms on dppe are omitted for clarity. Selected bond lengths [Å], angles, and dihedrals [°]: [Ir(H)$_3$(dppe)]$_2$ as shown, Ir1-Ir1', 2.723(1); Ir1–P1, 2.218(6); Ir1–P2, 2.326(6); P1-Ir1-P2, 86.1(2); P1-Ir1-Ir1', 140.1(2); P2-Ir1-Ir1', 101.1(1); P1-Ir1-Ir1'-P2, 82.2(3); P1-Ir1-Ir1'-P1', -180.0(3).

The crystal structure obtained is sufficient to support the dimerization process, however, this structure does not pinpoint the exact positions of the hydride ligands. Based on other dimeric iridium hydride complexes with diphosphine ligands reported in the literature such as [Ir(H)$_2$(dtbpe)]$_2^+$ (dtbpe = 1,2-bis(di-*tert*-butylphosphino)ethane)[170] and [Ir(H)$_3$(dfepe)]$_2$[171] (dfepe = (C$_2$F$_5$)$_2$-PCH2CH2P-(C$_2$F$_5$)$_2$)[172], a DFT investigation was conducted. Using the asymmetric unit cell structure of [Ir(dppe)]$_2$, six hydride ligands were added to create three isomers, with bridging hydride ligands as shown in **Scheme 3-4**. Each of these systems were then computed to find a local minimum. The isomer with two bridging hydride ligands was found to be the most stable of the three computed, and the only structure that reached a local minimum (**Figure 3-7**).
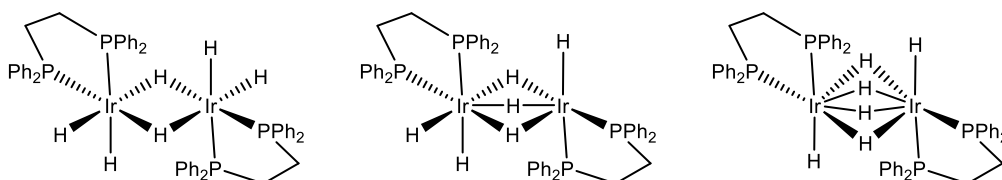
Scheme 3-4. Geometries of the different isomers computed. The isomer on the left was found to be the lowest energy system.

The structural data obtained *via* DFT methods showed bond distances (Ir-P$_{axial}$ (2.26 Å), Ir-P$_{equatorial}$ (2.39 Å), and Ir-Ir (2.80 Å)) that were close to those obtained experimentally for the iridium dimer in **Figure 3-6**.
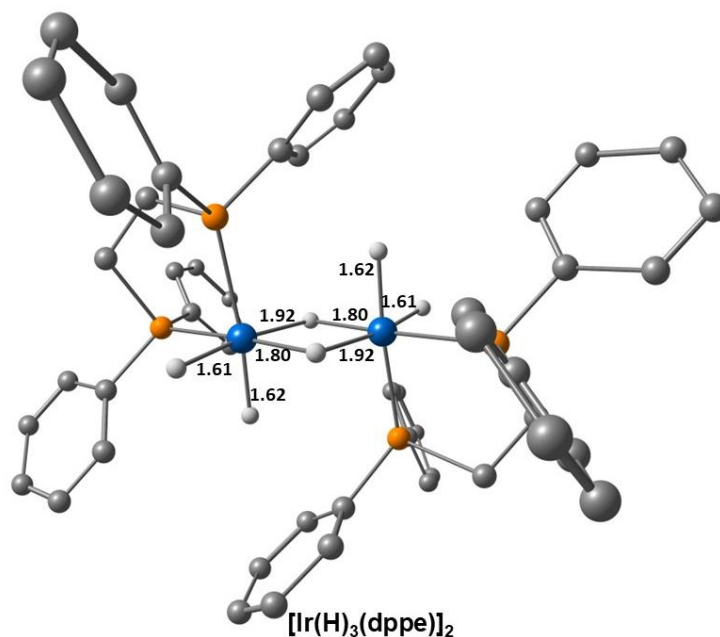
Figure 3-7. Optimized structure for [Ir(H)$_3$(dppe)]$_2$. All Ir-H Distances shown are in Å. C-H bonds are omitted for clarity.

To demonstrate the reactivity of K[**6^{dppe}**] and to an extent [Ir(H)$_3$(dppe)]$_2$, a controlled experiment using DMSO was conducted to trap the proposed mononuclear [Ir(H)$_3$(dppe)]$^+$ intermediate.

3.3.1.3 Reaction with DMSO – 1^{dppe}

DMSO was added to a solution of **1^{dppe}** in toluene-d_8 with KO^{t}Bu (and 0.5 equivalents of isopropanol to aid H$_2$ solubility). A ^{1}H NMR spectrum recorded at this point showed peaks for **2^{dppe}**/**3^{dppe}** (as minor products) and **4^{dppe}**/**5^{dppe}** (as major products), with the different ratios of each hydride containing species arising from the non-stoichiometric addition of isopropanol. The reaction products obtained *via* β-hydride elimination and COD deprotonation occur faster than DMSO binding once the chloride is lost, however, the spectrum showed no evidence for [Ir(DMSO)(COD)(dppe)].

When H$_2$ was then added, the ^{1}H NMR spectrum recorded after mixing showed two distinct hydride peaks at *δ* -9.20 and *δ* -15.41 in a 2:1 ratio (**Figure 3-8**). Neither of these peaks correspond to those observed for **2^{dppe}**/**3^{dppe}**/**4^{dppe}**/**5^{dppe}**/**6^{dppe}**. Instead, these peaks are a result of [Ir(H)$_3$(DMSO)(dppe)]. A single peak at *δ* 36.8 in the ^{31}P{^{1}H} spectrum couples with both

peaks in the hydride region of the ^1H NMR spectrum. Based on the NMR properties, [Ir(H)$_3$(DMSO)(dppe)] is predicted to have an octahedral geometry and the full characterization is shown in **Table 3-2**.
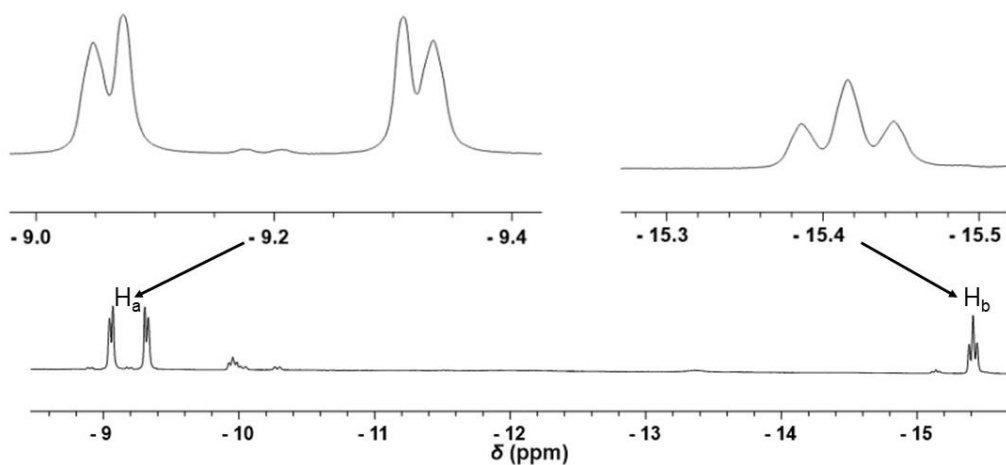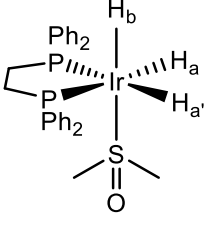
Figure 3-8. Hydride region for the ^1H NMR spectrum of [Ir(H)$_3$(DMSO)(dppe)] in toluene-d$_8$ at 298K.

The structure features a *fac* arrangement of the three hydride ligands, two are *trans* to the dppe P donor atoms, and one *trans* to the DMSO ligand. The two mutually *cis* hydride ligands located trans to the P donors are characterized by a resonance at δ -9.20 as a complex feature because of the complex AA'BXX' spin system with a stronger *trans* $^2J_{HP}$ (114.6 Hz) and weaker *cis* $^2J_{HP}$ (-14.3 Hz) and $^2J_{HH}$ (2.9 Hz) couplings. The strong *trans* HP coupling is reflected in the ^{31}P NMR spectrum, when the phosphorus signal is decoupled from H a singlet is observed, whereas without decoupling a doublet with a large coupling constant is seen ($^2J_{PH}$ = 126.2 Hz). The *cis* HH coupling constant is derived from the axial hydride resonance. The axial hydride signal is a simple triplet-of-triplets at δ -15.42 with $^2J_{HH}$ = 4.7 Hz and $^2J_{HP}$ = 15.9 Hz. No peaks are detected in either the $^{31}P\{^1H\}$ or ^1H NMR that correspond to **6^{dppe}**. This indicates that the presence of a coordinating ligand prevents the formation of a tetrahydrido complex.

Table 3-2. NMR data for $[Ir(H)_3(DMSO)(dppe)]$ in toluene-d_8 at 298 K.

Group	Chemical Shift (δ)
^{1}**H**, Ph (*ortho*)	7.98 (dd, $^2J_{HH}$ = 8.0)
(*meta*)	7.67 (dd, $^2J_{HH}$ = 7.6)
(*para*)	7.07 (m)
dppe CH_2	2.78 ($^2J_{HH}$ = 5.5), 1.97 ($^2J_{HH}$ = 5.5)
DMSO CH_3	2.47 (s)
Ir-H$_a$	-9.20 ($^2J_{HaHa'}$ = 6.0, $^2J_{HHb}$ = 3.4, $^2J_{HPcis}$ = -14.3, $^2J_{HPtrans}$ = 114.6)
Ir-H$_b$	-15.42 ($^2J_{HHa}$ = 3.4, $^2J_{HPcis}$ = 15.0)
^{13}**C**, Ph (*ipso*)	139.3 ($^1J_{CP}$ = 42.3)
(*ortho*)	134.8 (d, $^3J_{CP}$ = 12.8)
(*meta*)	131.6 (d, $^4J_{CP}$ = 10.9)
(*para*)	125.2*
dppe CH_2	31.3
DMSO	42.8
^{31}**P**, dppe	36.8 (s)

*Peak overlaps with solvent

Unlike the solution of K[6^{dppe}], a solution containing $[Ir(H)_3(DMSO)(dppe)]$ does not form $[Ir(H)_3(dppe)]_2$ upon release of H$_2$ pressure from the NMR tube. Any vacant sites generated upon the hydrogenation of COD are immediately trapped by the DMSO ligand, thus preventing the release of H$_2$ to form the trihydride dimer.

3.3.2 Activation of [IrCl(COD)(dppf)]

Ruthenium-dpen based dppf complexes have been reported to show higher activity for the hydrogenation of prochiral ketones, than their corresponding dppe analogues. The increased efficiency including higher *ee*'s is attributed to the bite angle of the dppf ligand .[173,174] Based on these findings, an iridium-based dppf complex ([IrCl(COD)(dppf)] (**1**^{dppf}) was synthesised to evaluate the potential to form an anionic tetrahydride like **6**^{dppe}. The synthesis of **1**^{dppf} has been described in the literature.[149]

Switching the solvent from in the reported method (THF) to dichloromethane significantly decreases the reaction time to obtain **1^{dppf}** (ca. 30 minutes) and it was obtained here in high yield (96 %). The NMR analysis of **1^{dppf}**, synthesized *via* the adapted procedure, led to the expected single ^{31}P{^{1}H} NMR peak at δ 0.83 in toluene-d_8. Further structural elucidation by NMR was performed in dichloromethane-d_2, where it was more soluble. The X-ray analysis of **1^{dppf}** reported by Grela and co-workers reveals that is adopts a five-coordinate trigonal bipyramidal structure that is comparable to that of **1^{dppe}**.[152]

3.3.2.1 Formation of [IrH(COD)(dppf)]

As expected, the reaction of **1^{dppf}** under ambient conditions with isopropoxide led to the formation of a new hydride-containing product (**Scheme 3-5**). This species is defined by a single peak in the hydride region of the ^{1}H NMR spectrum at δ -13.08 (t, $^2J_{HP}$ = 24.0 Hz). The hydride ligand giving rise to this signal couples to a peak in the ^{31}P{^{1}H} spectrum at δ 4.9, and when this is decoupled the hydride resonance changes to a singlet. Hence the splitting is a result of a *cis* coupling to two equivalent phosphorus atoms. Furthermore, the remaining resonances are indicative of a bound η^2:η^2 COD ligand.

The reaction product is proposed therefore to correspond to [IrH(COD)(dppf)] (**2^{dppf}**), with an η^2:η^2-1,5-cyclooctadiene ligand. One of the alkene moieties lies *trans* to the hydride ligand, and the other one *cis*. ^{1}H NMR characterization data for **2^{dppf}** are listed in **Table 3-3**.
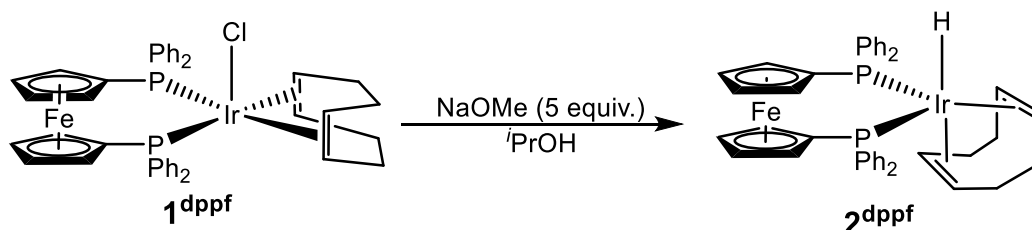
Scheme 3-5. Synthesis of **2^{dppf}** in the presence of NaO^{i}Pr at room temperature.

The selective formation of **2^{dppf}**, without a putative κ:η^3-C$_8$H$_{12}$ isomer such as that seen for **3^{dppe}**, agrees with previous studies that suggest that an increase in the iridium phosphine chelate ring size disfavours the COD rearrangement due to restricted hydride migration.[105,152] Furthermore, the rigidity of the ferrocene backbone makes any isomerization energetically demanding.

Table 3-3. ^{1}H NMR properties of 2^{dppf} in toluene-d_8 at 298K.

Group	Chemical Shift (δ)
^{1}**H**, Ph (*ortho*)	7.97
(*meta*)	7.66
(*para*)	7.16
COD CH	4.31 (*a*)
	3.91 (*b*)
COD CH$_2$	2.23 (*c*)
	1.76 (*d*)
Cp (*ortho*)	4.31
(*meta*)	3.84
Ir-H	-13.08 (t, $^2J_{HP}$ = 24.0 Hz)

3.3.2.2 Transfer hydrogenation of COD

When a solution containing 1^{dppf} in the presence of a base and isopropanol was heated to 353 K, and a ^{31}P NMR spectrum recorded, a new peak was observed in the ^{31}P{^{1}H} spectrum at δ 13.8. This peak correlates to two hydride resonances that appear at δ -13.37 and δ -12.71 in the corresponding ^{1}H-^{31}P HMQC NMR spectrum. The two hydride ligand signals are observed in a 1:1 ratio and suggest that K[Ir(H)$_4$(dppf)] (6^{dppf}) has formed. Signals for bound dppf, isopropanol, acetone, and cyclooctene were observed in the corresponding ^{13}C NMR spectrum.

The hydride region of the ^{1}H NMR spectrum of 6^{dppf} is directly comparable to that of 6^{dppe}, although the order of the chemical shifts is inverted. The equatorial hydride ligands (H$_a$ and H$_a$') are again equivalent but differ in the magnitude of their couplings to ^{31}P. The axial hydride ligands produce a triplet-of-triplets in the ^{1}H NMR spectrum and as such the $^2J_{HP}$ coupling can be directly observed. The H$_a$H$_b$ coupling constant can be determined from the ^{1}H{^{31}P} NMR spectrum (**Figure 3-9**), and an AA'MM'X$_2$ spin system is observed.
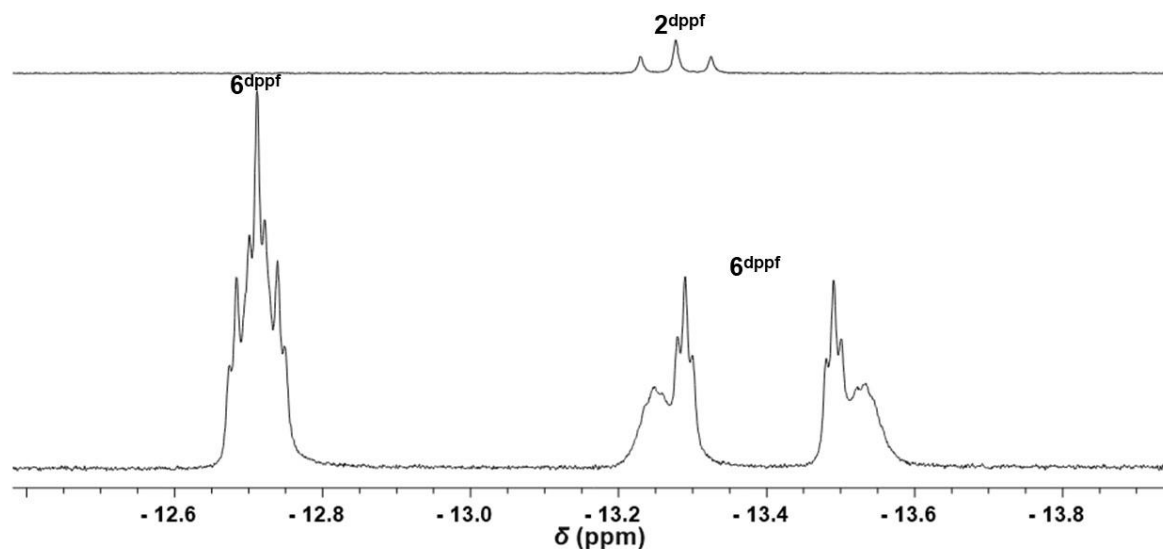
Figure 3-9. Hydride region ^{1}H NMR spectra of **2$^{\text{dppf}}$** (above); and **6$^{\text{dppf}}$** (below) in toluene-d_8 at 298 K.

The base again proved to be essential for the formation of **6$^{\text{dppf}}$**, with the corresponding reactions with H_2 alone again leading to a complex range of hydride-containing products. A change of cation, from K$^+$ to Na$^+$ under hydrogenation conditions does not change the appearance of the NMR signals, and in fact K[**6$^{\text{dppf}}$**] and Na[**6$^{\text{dppf}}$**] are equally stable. It is worth noting that out of three bases tested (LiO^{i}Pr, NaO^{i}Pr, KO^{i}Pr), a lithium-containing base is the only one that seemingly provides no suitable stabilization to **6$^{\text{dppf}}$** i.e., the non-observation of Li[**6$^{\text{dppf}}$**]. The effect of the cation is extensively discussed in **Chapter 4:**.
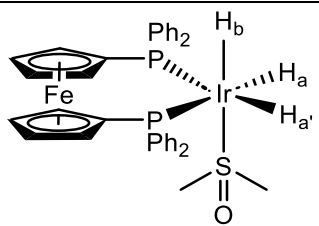
Table 3-4. NMR properties of 6^{dppf} in toluene-d_8 at 298 K.

Group	Chemical Shift (δ)
^1H, Ph (*ortho*)	8.16 (td, $^3J_{PH} = 14.3$, $^3J_{HH} = 7.2$)
(*meta*)	7.18 (t, $^3J_{HH} = 7.7$)
(*para*)	7.08 (t, $^3J_{HH} = 7.6$)
dppf Cp	4.40 (s)
	3.99 (s)
Ir-H_b	-12.71 (tt, $^2J_{HPcis} = 14.5$, $^2J_{HHcis} = 5.2$)
Ir-H_a	-13.37 (dddt, $^2J_{HPtrans} = 106.2$, $^2J_{HPcis} = -17.2$, $^2J_{HHcis} = 5.2$, $^2J_{HHcis} = 4.7$)
^{13}C, Ph (*ipso*)	129.1
Ph (*ortho*)	134.4 (d, $^2J_{CP} = 11.9$)
Ph (*meta*)	126.8 (d, $^3J_{CP} = 9.3$)
Ph (*para*)	124.8 (s)
dppf Cp (*ortho*)	75.1 (d, $^2J_{CP} = 8.9$)
(*meta*)	70.8 (d, $^3J_{CP} = 4.2$)
^{31}P, dppf	13.8

*Peak overlapped due to isopropanol.

It is also worth noting that a neutral trihydride DMSO adduct ([Ir(H)$_3$(DMSO)(dppf)]) was formed when 1^{dppf} is subjected to pressurised H$_2$ (3 bar) in the presence of KO^{t}Bu (5 equiv.) and DMSO (1 equiv.). The NMR data for this product are presented in **Table 3-5**, and closely resemble the data obtained for the isoelectronic [Ir(H)$_3$(DMSO)(dppe)] (**Table 3-2**).

Table 3-5. NMR properties of [Ir(H)$_3$(DMSO)(dppf)] in tetrahydrofuran-d_8 at 298 K.

Group	Chemical Shift (δ)
^{1}**H**, Ph (*ortho*)	7.99 (td, $^3J_{HP} = 7.3$, $^3J_{HH} = 4.4$)
(*meta*)	7.63 (m, $^3J_{HP} = 6.2$, $^3J_{HH} = 4.4$)
(*para*)	7.32 (m)
dppf CH, (*ortho*)	5.16
(*meta*)	4.01
DMSO CH$_3$	2.41 (s)
Ir-H$_a$	-11.36 (dddd, $J_{HaHa'} = 1.8$, $J_{HHb} = 3.4$, $J_{HPcis} = $ -15.6, $J_{HPtrans}$
Ir-H$_b$	$= 94.5$)
	-15.72 (tt, $J_{HHa} = 3.4$, $J_{HPcis} = 18.3$)
^{13}**C**, Ph (*ortho*)	136.4
(*meta*)	132.5
(*para*)	127.4
dppf Cp, (*ortho*)	75.1
(*meta*)	70.6
DMSO	55.6
^{31}**P**, dppf	5.7 (s)

3.3.3 Activation of [IrCl(COD)((*S*)-BINAP)]

The use of BINAP as a ligand is well-established for the enantioselective hydrogenation of polar substrates.[45,114] As a consequence, the complexation of (*S*)-BINAP to [IrCl(COD)]$_2$ was undertaken and this yielded [IrCl(COD)(*S*-BINAP)] (**1$^{S\text{-BINAP}}$**) in dry dichloromethane at 298 K. A single peak was observed for this product in the corresponding ^{31}P{^{1}H} NMR spectrum at *δ* -2.7 in chloroform-*d*. Dichloromethane-*d*$_2$ proved to be the preferred solvent for characterization purposes due to the need to identify naphthyl and phenyl groups, which would be obscured in toluene-d$_8$, thereby hindering integration and characterization. Diagnostic ^{1}H NMR peaks due to coordinated COD appeared in the chemical shift region of *δ* 3.5 – 1.4 ppm (**Figure 3-10**).
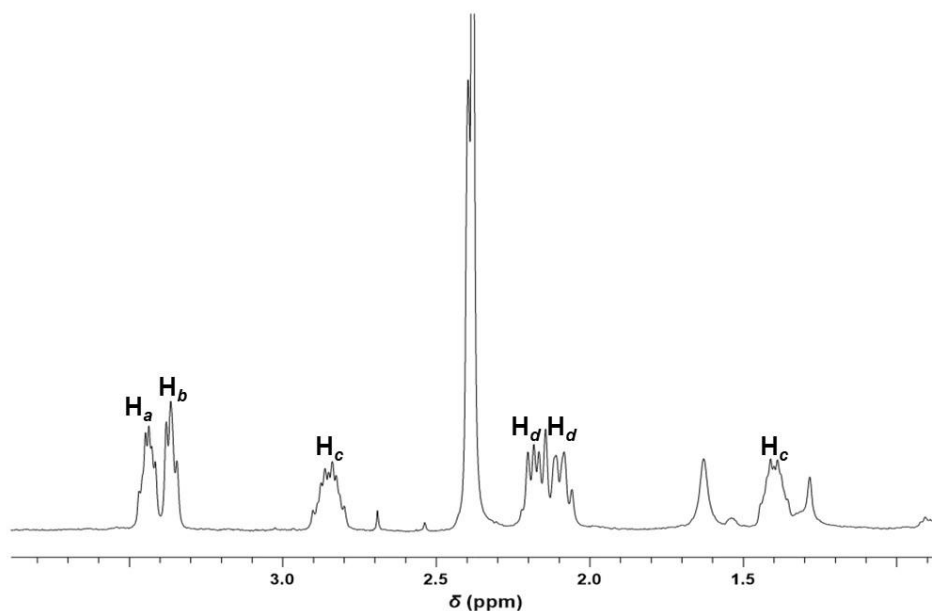
Figure 3-10. ^{1}H NMR spectrum highlighting the diagnostic signals for bound 1,5-cyclooctadiene on **1$^{S\text{-BINAP}}$** in toluene-*d*$_8$.

The characterization data for **1$^{S\text{-BINAP}}$** are presented in **Table 3-6**, and based on this the complex is predicted again to have a trigonal bipyramidal geometry. Two phosphorus atoms and one alkene (of COD) occupy the equatorial plane, this results in a loss of symmetry of the COD. The loss of symmetry is induced by the presence of *S*-BINAP

Table 3-6. NMR characterization of **1**[S-BINAP] in toluene-d_8.

Group	Chemical Shift (δ)
^{1}H, Ph	8.02 – 6. 48*
COD CH	3.44 (*a*)
	3.36 (*b*)
COD CH$_2$	2.84, 1.38 (*c*)
	2.18, 2.09 (*d*)
^{13}C, Ph	134.3 – 124.7
COD CH	73.9 (*a*)
	72.4 (*b*)
COD CH$_2$	27.8 (*c*)
	34.1 (*d*)
^{31}P, (*S*)-BINAP	-2.7

*Spectral assignment of each individual proton could not be deciphered

While iridium complexes with BINAP and COD have been previously reported, these are usually cationic and often used to induce chirality,[17,175] and hence chemoselectivity during hydrogenation.[176] When **1**[S-BINAP] was treated with KO^{t}Bu (5 equiv.) and an excess of isopropanol in toluene-d_8, two hydride peaks result at δ -12.47 (dd, $^2J_{HP}$ = 19.2, 23.1) and δ -10.02 (t, $^2J_{HP}$ = 17.0) in the ^{1}H NMR spectrum. The complex leading to the former signals also produces two peaks at δ 7.9 (d, $^2J_{PP}$ = 18.6) and δ 3.2 (d, $^2J_{PP}$ = 18.6) in the ^{31}P{^{1}H} spectrum, with the latter linking to a single peak at δ 14.3 (s). Upon ^{31}P decoupling both these hydride peaks appear as singlets (**Figure 3-11**). Based on the similar complexes described earlier, these peaks are attributed to [Ir(H)(COD)(S-BINAP)] (**2**[S-BINAP]) and [Ir(H)(1-κ-4,5,6-η^3-C$_8$H$_{12}$)(S-BINAP)] (**3**[S-BINAP]). **3**[S-BINAP] proves to be the major isomer in solution (ca 95 % based on the quantitative ^{1}H{^{31}P} NMR experiment) and its formation is expected to occur in a similar manner to **3**[dppe]. While this pathway was not explicitly explored by NMR spectroscopy, **Table 3-7** contains the appropriate characterization data.[104,105,152]
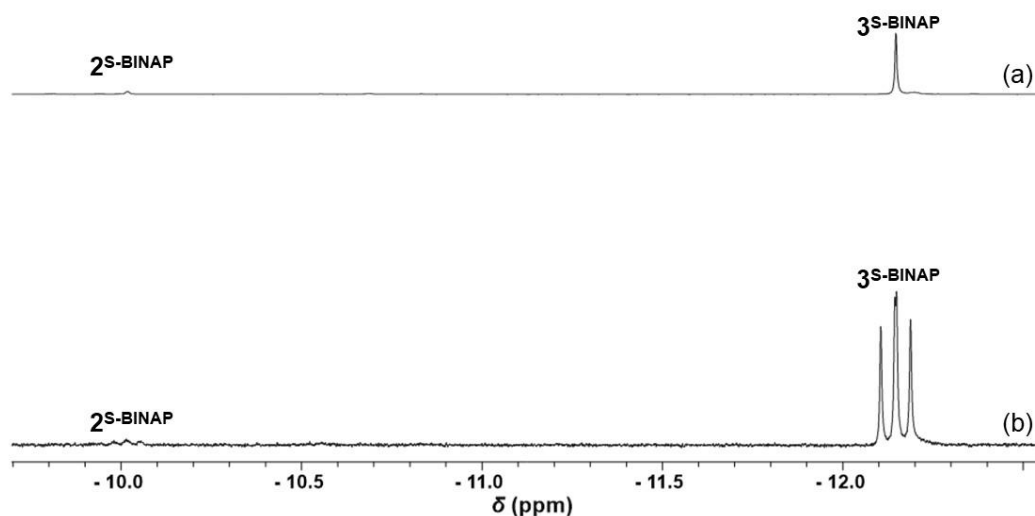
Figure 3-11. ^{1}H NMR spectra for the hydride region of **2**[S-BINAP] and **3**[S-BINAP] in toluene-d_8 at 298 K. (a) ^{31}P decoupled; (b) ^{31}P coupled.

Table 3-7. Characteristic NMR data for [IrH(COD)(L$_2$)] complexes.
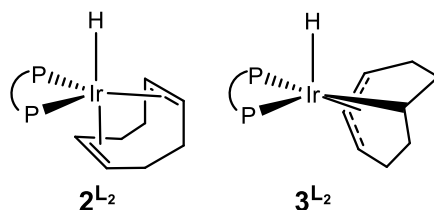
Complex	^{31}P{^{1}H}	^{1}H (Ir-H)
[IrH(COD)(dppp)][a]	-13.1 (s)	-13.35 (t, $^2J_{HP}$ = 21.5)
[IrH(COD)(dppb)][a]	+0.8 (s)	-13.51 (t, $^2J_{HP}$ = 21.6)
[IrH(COD)(dppe)] (**2**[dppe])[a]	+33.2 (s)	-14.00 (t, $^2J_{HP}$ = 21.6)
[IrH(1-κ-4,5,6-η^3-C$_8$H$_{12}$)(dppe)] (**3**[dppe])[a]	+43.9 (d, $^2J_{PP}$ = 2.8); +29.1 (d, $^2J_{PP}$ = 2.8)	-11.66 (dd, $^2J_{HP}$ = 22.2, 14.9)
[IrH(COD)(dppf)] (**2**[dppf])[b]	+4.9 (s)	-13.08 (t, $^2J_{HP}$ = 24.0)
[IrH(COD)(S-BINAP)] (**2**[S-BINAP])[b]	+14.3 (s)	-10.02 (t, $^2J_{HP}$ = 17.0)
[IrH(1-κ-4,5,6-η^3-C$_8$H$_{12}$)(S-BINAP)] (**3**[S-BINAP])[b]	+7.9 (d, $^2J_{PP}$ = 18.6); +3.2 (d, $^2J_{PP}$ = 18.6)	-12.47 (dd, $^2J_{HP}$ = 23.1, 19.2)

Experimental conditions: [a] benzene-d_6, 298 K;[105,152] [b] toluene-d_8, 298 K. Chemical shifts in ppm; coupling constants expressed in Hz.

Adding H_2 to a solution containing a mixture of **2$^{S\text{-BINAP}}$** and **3$^{S\text{-BINAP}}$** that is produced in this way resulted in the formation of a single product that exhibits at ^{31}P signal at δ 24.6. Two peaks in the hydride region of the ^{1}H NMR spectrum result, at δ -12.20 and δ -13.19 (**Figure 3-12**).

The appearance of the hydride resonances is indicative of an iridium tetrahydrido complex, K[Ir(H)$_4$(S-BINAP)] (**6$^{S\text{-BINAP}}$**). An HMQC (^{31}P-^{1}H) NMR experiment was used to link the aromatic and hydride ^{1}H NMR signals (**Figure 3-13**) in this complex to yield the NMR data of **Table 3-8**.
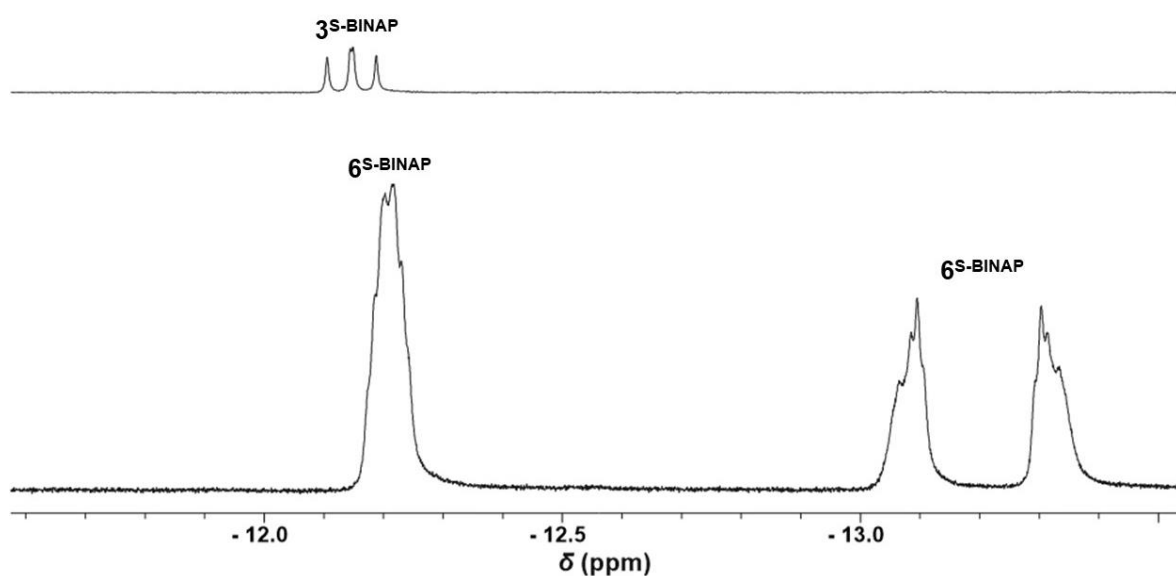
Figure 3-12. Hydride region ^{1}H NMR spectra of **3$^{S\text{-BINAP}}$** (above); and **6$^{S\text{-BINAP}}$** (below) in toluene-d_8 at 298 K.
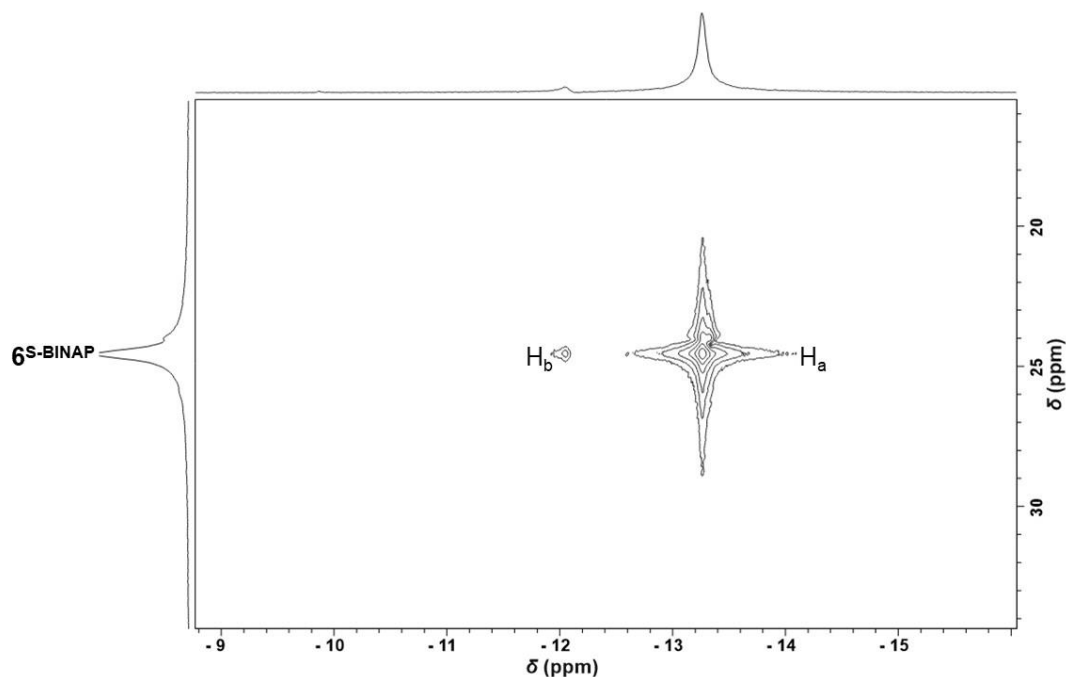
Figure 3-13. Excerpt of the [31]P-^{1}H HMQC spectrum of K[$6^{S-BINAP}$] in the hydride resonance region, in toluene-d_8. $^1J_{HX}$ = 15 Hz.

As expected, when decoupled from ^{31}P, the two hydride signals appear as triplets due to the mutual *cis* $^2J_{HH}$ coupling of 5.9 Hz. The ^{1}H NMR signal for the axial hydrides (H$_b$) appears at δ -12.20 and a broad triplet is seen upon [1]H{H$_a$} decoupling, with a $^2J_{HP cis}$ coupling of 12.1 Hz. H$_b$ and is again at lower field than the equatorial ligand signal which shows a complex splitting pattern, the coupling constants are listed in **Table 3-8**.

The aromatic region of the ^{1}H NMR showed many peaks due to the four phenyl rings and naphthyl groups having characteristic peaks in this region. Some of the peaks could be assigned using a ^{1}H-^{1}H COSY experiment (**Figure 3-14**). The specific phenyl resonance frequencies were deemed as less important for the application of **$6^{S-BINAP}$** as a catalyst. Detection of the anionic tetrahydrido complex was able to be observed with a single resonance frequency in the ^{31}P{^{1}H} NMR spectrum.
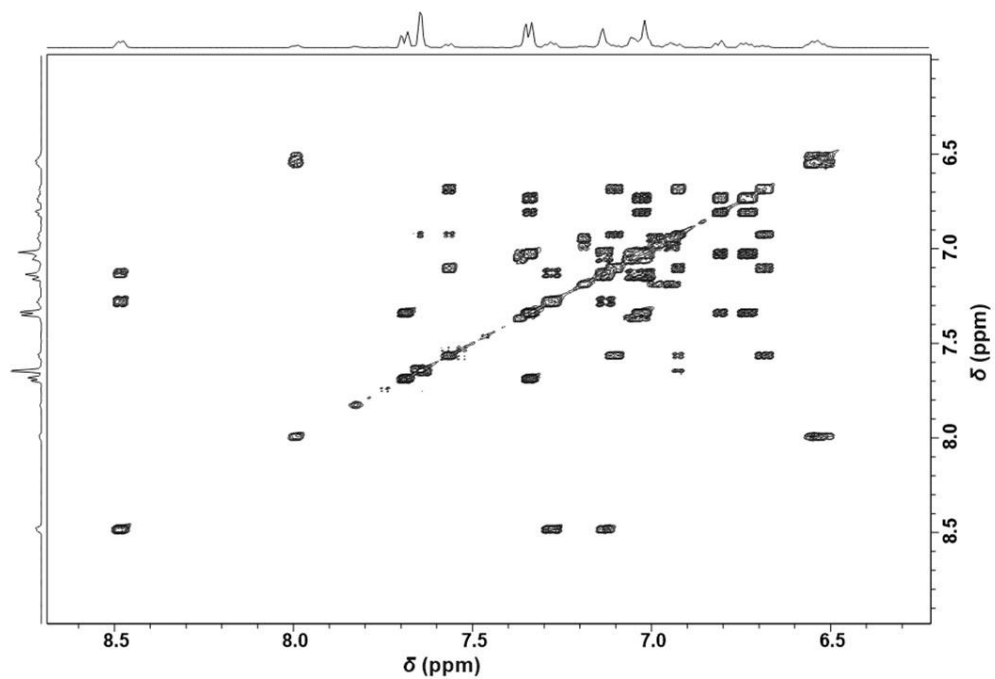
Figure 3-14. Aromatic region of the ^{1}H-^{1}H COSY spectrum for **6$^{S-BINAP}$** in toluene-d_8 at 298 K

Table 3-8. NMR properties of **6^{S-BINAP}** in toluene-d_8 at 298 K.

Group	Chemical shift (δ)
¹H, Ph	8.50 – 6.53
Ir-H$_a$	-13.19 (tddd, $^2J_{HPtrans}$ = 92.0, $^2J_{HPcis}$ = -12.7, $^2J_{HHcis}$ = 6.4, $^2J_{HHcis}$ = 5.9)
Ir-H$_b$	-12.20 (tt, $^2J_{HPcis}$ = 12.1, $^2J_{HHcis}$ = 5.9)
¹³C, Ph	136.5 – 127.2
³¹P, (*S*)-BINAP	24.6
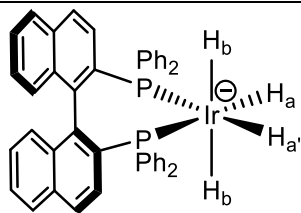
3.4 Hydrogenation of acetophenone

The three [IrCl(COD)(L$_2$)] (L$_2$ = dppe, dppf, *S*-BINAP) precursors have all been shown to form M[Ir(H)$_4$(L$_2$)] (M = Na, K) under hydrogenation (or transfer hydrogenation) conditions when a base is present (**3.3**). The reaction time needed to form each species from the chloride precursor varies. However, when solutions were spiked with isopropanol and H$_2$ the process takes just a few minutes at 298 K. Hence, the hydrogenation reactions containing an excess of isopropanol would result in faster reaction times owing to precatalytic activation occurring rapidly. A series of hydrogenation experiments was conducted under 20 bar of H$_2$ at 298 K. Acetophenone was used as a model substrate to determine catalyst efficiency and selectivity (enantioselectivity). The results from these studies are shown in **Table 3-9**.
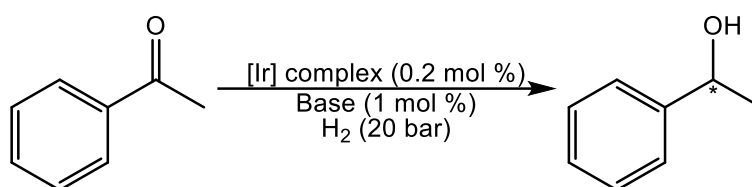
Table 3-9. Asymmetric hydrogenation of acetophenone.

Entry	Catalyst	Additive	Time	Conversion (%) (e.e %)
1	**1**^{dppe}	/	2	6 (*rac*)
2	**1**^{dppe}	KO^{t}Bu	2	35 (*rac*)
3	**1**^{dppe}	KO^{t}Bu + 18-crown-6	2	16 (*rac*)
4	**1**^{dppf}	/	2	0 (*rac*)
5	**1**^{dppf}	KO^{t}Bu	2	34 (*rac*)
6	**1**^{dppf}	KO^{t}Bu + 18-crown-6	2	15 (*rac*)
7	**1**$^{S\text{-}BINAP}$	/	2	2 (13)[c]
8	**1**$^{S\text{-}BINAP}$	KO^{t}Bu	2	8 (6)[d]
9	**1**$^{S\text{-}BINAP}$	KO^{t}Bu + 18-crown-6	2	3 (3)[d]

[a] Conditions: p(H$_2$) = 20 bar; t = 2 h; T = 25°C; [PhCOMe] = 3.2 mmol in isopropanol (1.7 mL); [Ir] = 6.4 x10^{-3} mmol; [KO^{t}Bu] = 3.2 x 10^{-2} mmol. [b] 18-crown-6/K = 1.5.; [c] *R* enantiomer; [d] *S* enantiomer

Entry 1 shows very low catalytic activity under H$_2$ and isopropanol alone. This is expected based on previous studies on similar systems.[145,177] However, once KO^{t}Bu was added more effective hydrogenation resulted, as expected, based on the notion that a tetrahydrido species (**6**^{dppe}) is the active catalyst for this process. Interestingly, these results are comparable to previous work reported using [Ir(OMe)(COD)]$_2$/dppe/KOH systems (TOF = 12.2).[98]

The hydrogenation procedure as opposed to the transfer hydrogenation procedure produces a higher TOF even in the presence of a coordinating ether.

However, when compared to entry 1, entry 3 shows that sequestration of the potassium ion by 18-crown-6 hinders the catalytic activity. The same trend was observed in both **1^{dppf}** (entries 4 and 5), and **1$^{S-BINAP}$** (entries 7 and 8); in all cases the addition of a base vastly increased the activity. This effect is most pronounced for **1^{dppf}** wherein the addition of a base increased the reactivity by a factor of 100. As expected, **1^{dppe}** and **1^{dppf}** do not induce enantioselectivity – the symmetry of the corresponding tetrahydrido complexes suggest there is no chiral factor. This means that there is an equal probability of hydrogenation occurring from the *re* or *si* face. Surprisingly, **1$^{S-BINAP}$** shows low reactivity and very low enantioselectivity. The addition of the base in this case whilst increasing the activity also inverted the observed enantioselectivity. This is attributed to the effect of the cation, which selectively facilitates the reaction on one face of the tetrahydrido complex, this phenomenon is discussed in later chapters (**Chapter 4:**). The substrate preferentially interacts with one face of the catalyst and induces a level of enantioselectivity. The reactivity of each system was reduced drastically when the cation was sequestered from the anionic iridium complex. This clearly reduces the efficiency of the conversion, and it can be deduced that the cation is necessary to facilitate the reaction.

The most effective catalyst amongst the complexes with chelating diphosphine ligands is **1^{dppe}** for the hydrogenation of acetophenone. Under these conditions experimental evidence dictates the formation of **6^{dppe}**. However, even this system has a relatively low activity compared to the previously published catalytic systems with (P,S^{R}) ligands.[87,145]

3.5 DFT Investigation of the Catalytic Cycle for 6^{dppe}

3.5.1 Importance of a solvent model

A series of DFT calculations was performed to assist in the assessment of the reaction of **6^{dppe}** for the hydrogenation of acetophenone. These investigations involved modelling the catalytic behaviour of **6^{dppe}** for the hydrogenation of acetone to isopropanol. The calculations were based on Entry 2 in **Table 3-9**, that showed the highest activity, however, to accurately compute the catalytic cycle, a suitable model for the cation-anion pair must be selected.

Potassium *tert*-butoxide is best visualized as a contact ion pair due to the ionic nature of the K$^+$ cation and $^-$O^{t}Bu anion in solution. Computational studies on similar systems demonstrate how tetrameric cubane-type clusters are often the reactive species in catalytic transformations and thermodynamically accessible. These structures are accessible in aprotic and protic solvents (**Scheme 3-6**).[57,178]
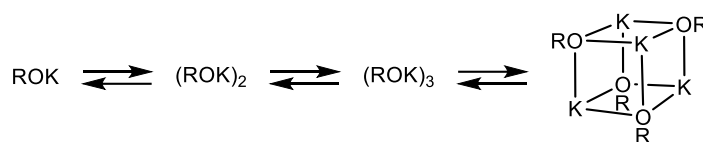
Scheme 3-6. Different contact ion-pairs of K$^+$ in alcoholic solvents (R = ^{t}Bu).[57]

The reactions of a cation in solution go along with the reorganization of the cation solvation sphere, invariably in isopropanol the *tert*-butoxide anion deprotonates isopropanol to yield isopropoxide. A more realistic system for this reaction thus does not contain KO^{t}Bu aggregates but rather K(O^{i}Pr)$_n$ solvation shells. Hence, it is expected that an appropriate description of the first solvation shell of the cation is a requirement for a reliable description of the catalytic cycle process. The solvent model in the work by Lledós and co-workers only included three methanol molecules, in the previous study of a similar reaction mechanism with [M(MeOH)$_3$][Ir(H)$_4$(P,S^R)].[87]

Figure 3-15 shows the optimized structures of the [Na(MeOH)$_3$(Me$_2$CO)][Ir(H)$_4$(P,S^R)] intermediate and the transition state. With this model, the carbonyl substrate is already in contact with the cation before hydride transfer, hence there is no need to displace a solvent molecule from the cation along the hydride transfer. Moreover, the Na$^+$ cation cannot reach the optimal octahedral-like solvation shell.

$[Na(MeOH)_3(Me_2CO)][Ir(H)_4(P,S^R)]$ $[Na(MeOH)_3(Me_2O)CHIr(H)_3(P,S^R)]$
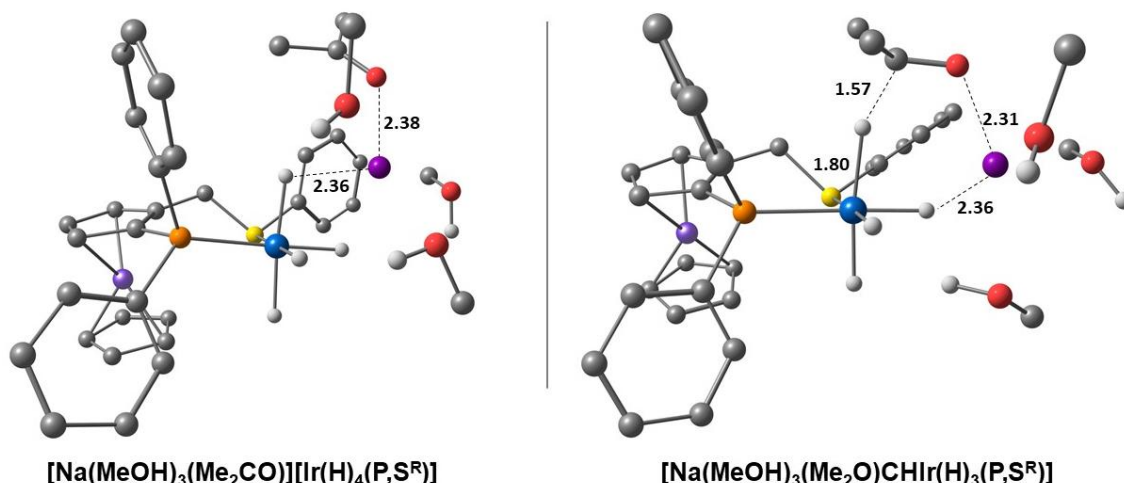
Figure 3-15. Optimized structures along the hydride transfer step with the $[Na(MeOH)_3]^+$ solvent model. All distances are in Å. C-H hydrogen atoms have been omitted for clarity.[87]

Thus, a model, that more accurately depicts the behaviour of a cation in solution was chosen to understand the catalytic action of **6^{dppe}**. A simpler model for the catalytic cycle is the inclusion of methanol rather than isopropanol for the clusters, as such a $[K(MeOH)_5]^+$ model was employed.

3.5.2 Catalytic cycle

The cycle starts with **7^{dppe}** (**Scheme 3-7**, **Figure 3-16**), which is a representation of **6^{dppe}** in contact with $[K(MeOH)_5]^+$. The inclusion of acetone (**8^{dppe}**) makes the corresponding complex slightly more unstable (3.9 kcal mol^{-1}) and does not feature a cation ketone adduct. Rather, the ketone prefers to hydrogen-bond to two metal molecules. Hydride transfer to the carbonyl (**TS$_{(8-9)}$^{dppe}**) then occurs to yield an alkoxide (**9^{dppe}**), which is only marginally more stable than the pre-formed species **8^{dppe}** by around 0.1 kcal mol^{-1}. Rearrangement of the alkoxide then occurs to yield a more stable speciation with an Ir-O bond (**10^{dppe}**) further complemented by H-bonding interactions observed with H atoms on MeOH. The additional stability is reflected in the relative energy with **10^{dppe}** having a lower energy than the starting complex (-1.4 kcal mol^{-1}). At this point H$_2$ was introduced into the model to displace the $^-$O^{i}Pr to form an η^2-dihydrogen complex (**12^{dppe}**), however, the transition state for the alkoxide displacement (**TS$_{(11-12)}$^{dppe}**) and proton transfer step (**TS$_{(12-13)}$^{dppe}**) could not be found. As such the energetic span for the cycle could not be determined for this system.
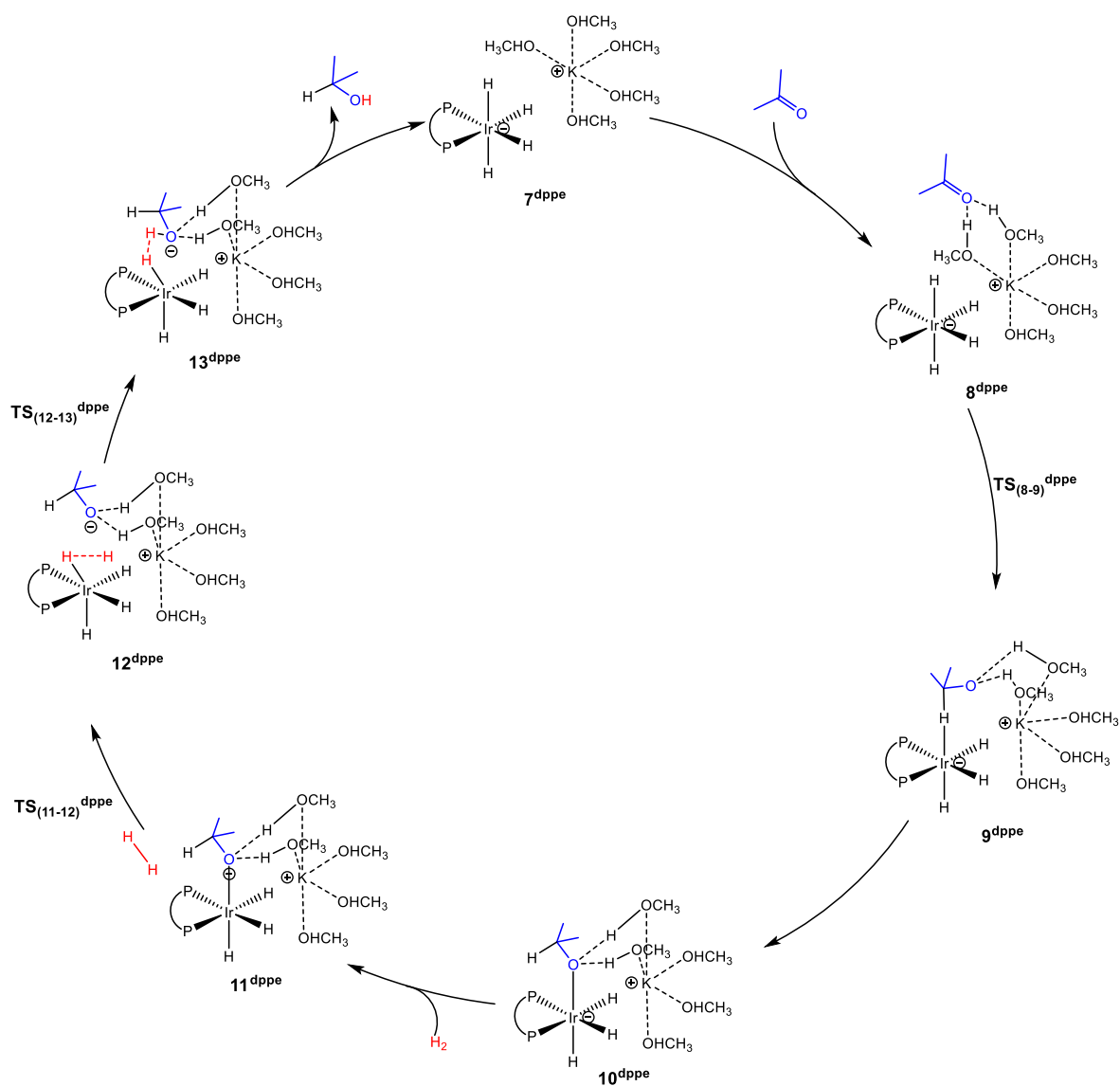
Scheme 3-7. Proposed cycle for acetone hydrogenation catalysed by **7^{dppe}**.
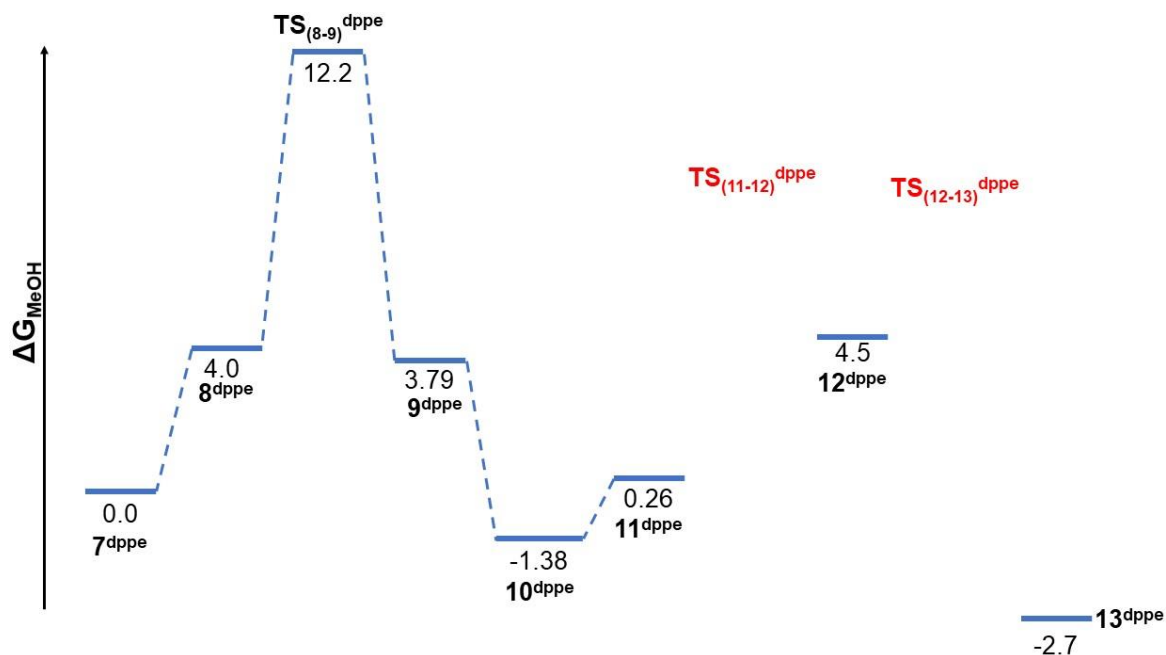
Figure 3-16. Computed Gibbs energy profiles for the hydrogenation of acetone with **7^{dppe}**. Energy profiles is in kcal mol^{-1}. The labels shown reference the cycle in **Scheme 3-7**, **TS$_{(11-12)}^{dppe}$** and **TS$_{(12-13)}^{dppe}$** could not be located (shown in red).

The investigation, did however, demonstrate the importance of the solvation around the cation, and how the MeOH molecules are reorganized upon substrate inclusion into the model.

3.5.2.1 Hydride transfer step

The input of the correct starting geometry for the model is of the utmost importance. The lowest energy structure for **7^{dppe}**, is obtained when the cation is placed near the hydride side of the Ir anion rather than the ligand side, plus an acetone molecule infinitely far apart. When the acetone is closer to the catalyst, it can be observed that stabilization of the cation is provided by the MeOH molecules, and one of the hydrides (**Figure 3-17**). After the hydride transfer to the substrate, the K-H distance increases by 0.14 Å. At this point stabilization of the cation is provided by the substrate and is reflected in the close energy difference between **8^{dppe}** and **9^{dppe}**.
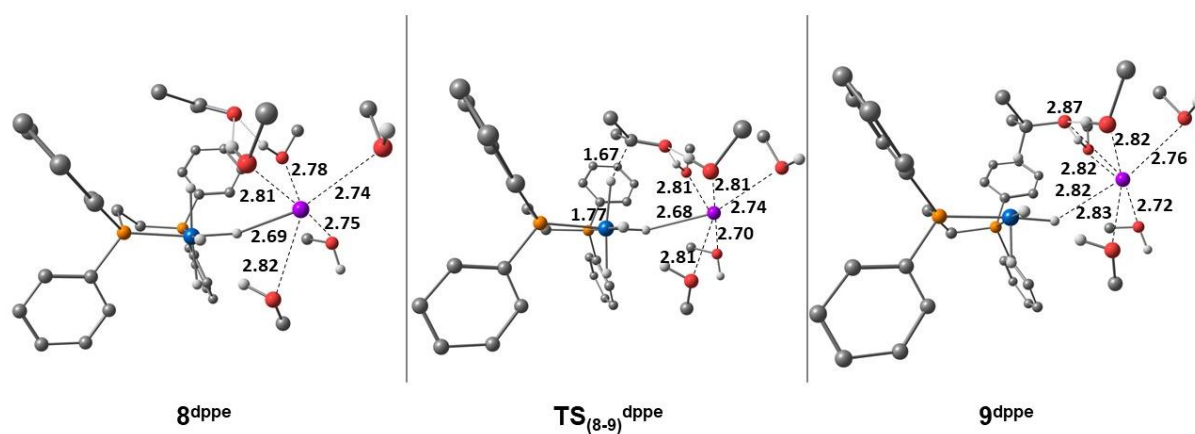
Figure 3-17. Optimized structures for the hydride transfer step with **6^{dppe}**. Distances shown are in Å. C-H hydrogen (except on the alkoxide) atoms have been omitted for clarity.

3.6 Summary

This chapter outlined a reproducible route to form three different anionic Ir^{III} tetrahydride complexes from the chloride containing precursors ([IrCl(COD)(L$_2$)] (L$_2$ = dppe, dppf, *S*-BINAP) under hydrogenation and transfer hydrogenation conditions. In all cases the cyclooctadiene ligand was selectively removed as cyclooctene. The tetrahydrido complexes were only formed in the presence of a strong base (NaOMe, NaO^{i}Pr, NaO^{t}Bu, KO^{i}Pr, and KO^{t}Bu). In contrast, in the absence of a base, under hydrogenation conditions, a complicated mixture of iridium hydride derived products was observed, however, the subsequent addition of base to these mixtures results in a single tetrahydride product.

In the absence of a substrate, and when H$_2$ pressure was released, the tetrahydride complex dimerized to form a neutral trihydride dimer. However, in the case of dppe, the presence of coordinating DMSO suppressed the formation of the tetrahydrido species and a neutral trihydride resulted from the reaction. Upon removal of DMSO the isolation of an analogous iridium-hydride dimer was possible.

The three different [IrCl(COD)(L$_2$)] complexes were then evaluated for the hydrogenation of acetophenone, which all showed negligible *ee*. The activity for each system increased drastically in the presence of KO^{t}Bu. This was accredited to the formation of the anionic tetrahydrido complexes which are formed in higher concentration when a base is present. A DFT study was conducted to provide a plausible hydrogenation mechanism, two key transition states were not found which meant that the energy span could not be calculated. The study did however, give an insight into the implication on how the solvent shell around the cation is important in stabilisation of intermediate species.

Chapter 4:   Ketone Hydrogenation Catalysed by Anionic Tetrahydrido Ir^{III} Complexes and the Cation Effect

4.1 Introduction

The asymmetric hydrogenation of polar prochiral substrates, particularly aryl ketones, has been the topic of intensive investigation.[177,179,180] For the pre-catalysts listed thus far, the presence of a strong base is required to form the tetrahydrido Ir^{III} complex needed for high activity (see **Chapter 3:**). The role of the base is usually attributed to stabilization of a more active neutral hydride species, relative to a cationic complex that may not otherwise form in protic reaction solvents (typically an alcohol).[45] When a chloride containing complex is used as a pre-catalyst, as is often the case, the base is also invoked for the activation step where substitution of the chloride by alkoxide is followed by β-H elimination. This leads to the formation of neutral monohydride complexes as discussed in (**Chapter 2:Chapter 2:**). But these are insufficient for ketone hydrogenations involving [IrCl(COD)]$_2$/LL', where LL' is a planar chiral 1,2-disubstituted ferrocene ligand containing diphenylphosphino and thioether groups (P,S^R; R = Et, ^{i}Pr, ^{t}Bu, Bz, Ph).[87,140]

The stoichiometric reaction between the Ir complex and P,S^R was shown to yield well-defined [IrCl(COD)(P,S^R)] complexes with either a 5-coordinate square pyramidal or a 4-coordinate square planar (for R = ^{t}Bu) geometry (**Scheme 4-1**).[146]
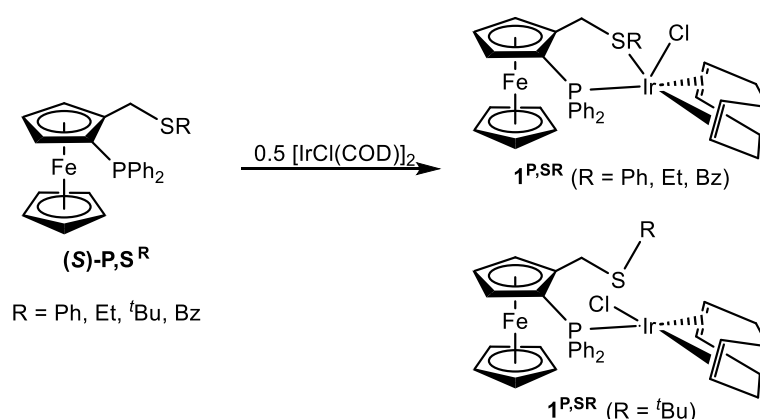
Scheme 4-1. [IrCl(COD)(P,S^R)] precatalysts formed with different R groups.[146,177]

These complexes (either isolated or made in situ) proved very active and enantioselective for aromatic ketone hydrogenation, though only in the presence of an excess of a strong base (e.g. 5 equiv of NaOMe per Ir).[145] However, the alternative use of [Ir(OMe)(COD)]$_2$, which

contains an internal methoxide base, still required the presence of additional strong base to yield an active catalyst, suggesting the implication of an anionic active catalyst. A parallel DFT investigation revealed that, using $[MeO(MeOH)_3]^-$ as a model of the methoxide ion in isopropanol and $(MeOH)_5$ as its conjugate acid, the most stable species generated by a sequence of COD hydrogenation and H_2 oxidative addition steps is the anionic tetrahydrido complex $[Ir(H)_4(P,S^R)]^-$.[87] While the latter was not fully NMR characterised, isoelectronic $[Ir(H)_4(L_2)]^-$ (L = dppe, dppf, (*S*)-BINAP) complexes were detected as potential catalyst resting states **Chapter 3:Chapter 3:**.[152] However, $[Ir(H)_4(P,S^R)]^-$ does not contain mobile protons for a classical outer-sphere bifunctional (Noyori-type)[45] mechanism, nor a vacant coordination site for an inner sphere mechanism.

DFT calculations could rationalize this reaction though through a mechanistic variant of the outer-sphere bifunctional mechanism (**Scheme 4-2**). It involves the cooperative action of an alkali cation for ketone activation, and the iridium centre for hydride transfer to the carbonyl C atom, generating an alkoxide intermediate. This is followed by transfer of a proton originating from the ionic activation of H_2. The calculated free energy span of the catalytic cycle, 18.2 kcal mol^{-1}, is consistent with the experimental activity (TOF = 500 h^{-1}). However, this model neither accounts for proper solvation around the cation nor different cation effects.
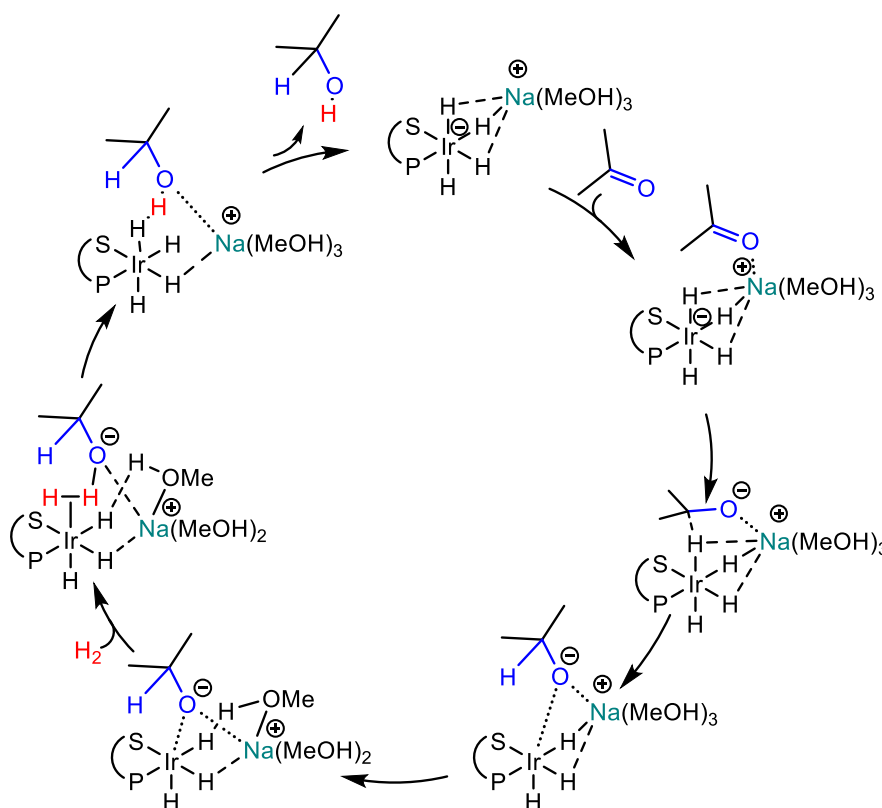
Scheme 4-2. Proposed catalytic cycle for the hydrogenation of acetophenone with $[Na(MeOH)_3][Ir(H)_4(P,S^{Ph})]$. The mechanism is reproduced for clarity.[87]

The action of anionic hydride complexes as (transfer) hydrogenation catalysts and their generation by strong bases is not a widespread concept. Pez *et al.* suggested the involvement of anionic Ru hydride complexes, e.g.$[K(L_n)][RuH_2(\kappa^2:C,P\text{-}o\text{-}C_6H_4PPh_2)(PPh_3)_2]$ and $[K(L_n)][(PPh_3)_3(PPh_2)RuH_2]$($L_n$ = solvent or crown ether), as active species for the catalysed reduction of aromatic compounds as well as aldehydes, ketones, esters and nitriles.[181–184] Of special note is the fact that the addition of crown ether or cryptands was shown to dramatically reduce the catalytic activity through sequestration of the cation. However, subsequent work demonstrated that the anionic $[RuH_3(PPh_3)_3]^-$ complex, which is generated from the Pez systems under H_2,[185,186] is reversibly protonated in alcohol solvents to $[RuH_2(H_2)(PPh_3)_3]$ and that the latter "tetrahydride" complex is the real catalytically active species.[187] Prior to the above-mentioned contribution on $[Ir(H)_4(P,S^R)]^-$, Dub *et al.* suggested that the active species of Noyori's $[RuH_2(diphosphine)(NH_2CHPhCHPhNH_2)]$ catalyst is, in fact, the deprotonated amine-amido complex $[RuH_2(diphosphine)(NH(K)CHPhCHPhNH_2)]$.[51]

For an anionic active catalyst, the activity may somewhat be affected by the nature of the counter-cation. In addition to the above-mentioned investigation by Pez *et al.* the effect of an alkali metal counterion on the activity (and/or selectivity) of a (transfer) hydrogenation catalyst has been pointed out in a few cases but has generally been attributed to cooperation with a neutral hydride system.

4.2   Aims and objectives

[IrCl(COD)(P,S^R)] precatalysts were shown to be highly effective asymmetric hydrogenation catalysts, but only in the presence of a base (particularly NaOMe).[145] This was attributed to the active catalyst being an anionic iridium complex, based on a mechanism proposed by Lledós and co-workers. If this mechanism is indeed accurate, the conversion should be dependent on the cation. The aim of this chapter is to gain an appreciation of the effect a cation has on the hydrogenation of acetophenone with these systems. A combination of DFT and catalyst screening were used to identify if the cation has an effect on the activity.

The sensitive nature of these systems has meant that so far, no NMR characterization exists for the proposed [Ir(H)$_4$(P,S^R)]$^-$ anion. Nevertheless, previous studies have demonstrated the formation of dihydride iridium and rhodium complexes with the P,S^R ligand.[36,37] A new iridium preacatalytic system ([IrCl(COD)(P,S^{Cy})]) was thus synthesised to demonstrate if an anionic species could be detected.

DFT calculations were conducted to find the role of the alkali metal cation in ketone activation and its importance in the rate-determining hydride transfer step. Based on the previous chapter, a proper solvent model was important for the accurate prediction and modelling of the catalytic cycle.

4.3   Synthesis of phosphino ferrocenyl thioether ligands

This investigation began with the synthesis of ferrocenyl thioether ligands through a previously established method.[140,188] Starting from the amino functionalized ferrocene, the target molecules can be synthesised *via* a 7-step process (**Scheme 4-3**). It is important to highlight two steps: (iii) and (v). Step (iii) forms two diastereomeric products (**(*S*)-4^{Fe}** and **(*R*)-4^{Fe}**) from a racemic mixture of **3^{Fe}** (note in **Scheme 4-3**, no absolute configuration is shown for (**1-3**)^{Fe}. This step forms two diastereomers as opposed to enantiomers allowing them to be separated and the desired optically pure ligand to be isolated, in the current example the S-enantiomer. Synthesis of **(*S*)-6^{Fe}** in step (v), makes the eventual synthesis of **(*S*)-P,S^R** easily accessible *via* substitution of -OH and subsequent deprotection of the phosphine. Hence, for this study the isolation of **(*S*)-6^{Fe}** provides accessibility to the range of R group functionalised **(*S*)-P,S^R** ligands.
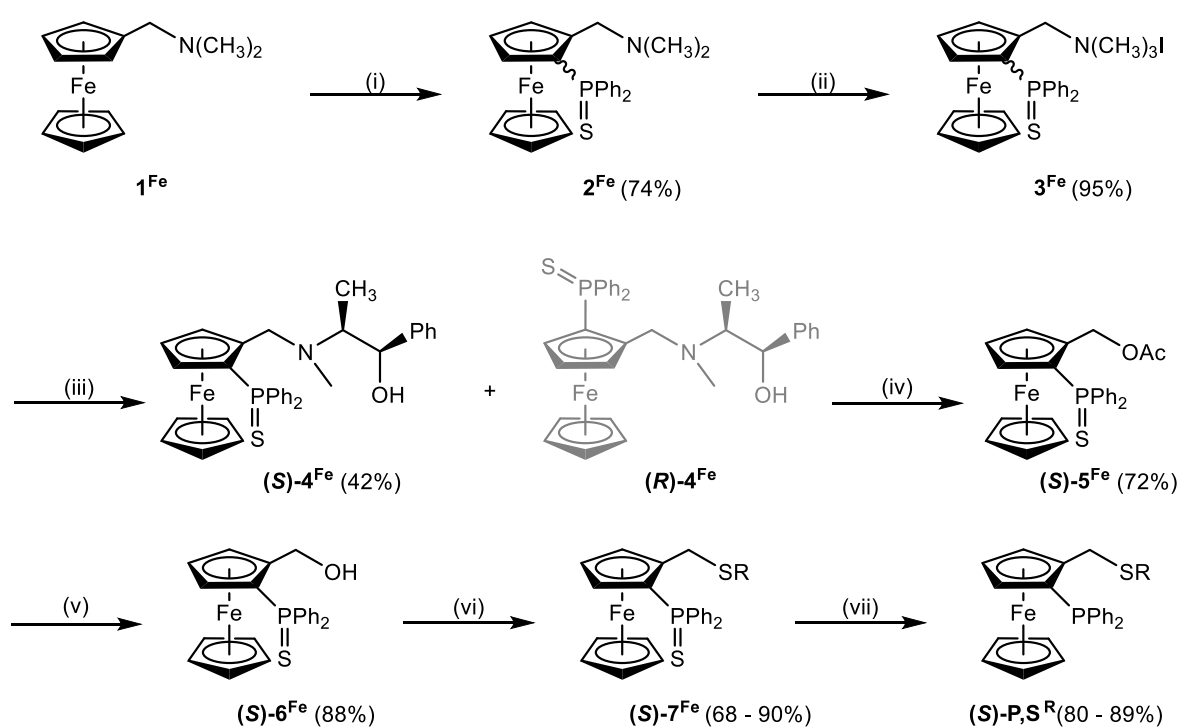
Scheme 4-3. 7-step synthesis ferrocenyl phosphino thioether ligands **(*S*)-P,S^R**. (i)(a)^{*n*}BuLi, PPh₂Cl, Et₂O, (b)S₈, CH₂Cl₂; (ii) CH₃I, Et₂O; (iii) (1*R*,2*S*)-(-)-Ephedrine, toluene; (iv) Ac₂O; (v) NaOH/MeOH; (vi)HBF₄, RSH; (vii) P(NMe₂)₃. R = ^{*i*}Pr, Ph, Bz, Cy.

4.4 (*S*)-P,S^R complexation and characterization of [IrCl(P,S^R)(COD)] complexes

Once the ligands were synthesised the catalytic activity of each iridium-**P,S^R** system was tested. Iridium precatalysts generated in situ *via* the addition of **P,S^R** to [IrCl(COD)]$_2$ have shown similar catalytic activity to their respective isolated complexes i.e. ([IrCl(COD)(P,S^R)] (**1^{P,SR}**).[145] Two of these complexes **1^{P,SPh}** and **1^{P,SCy}** were isolated for characterization purposes.

4.4.1 Synthesis of of [IrCl(COD)(P,S^{Ph})] (1^{P,SPh})
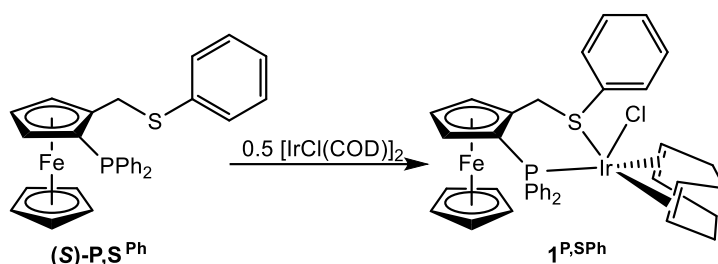
Scheme 4-4. Synthesis of **1^{P,SPh}**.

1^{P,SPh} is formed *via* the addition of 2 equivalents of (*S*)-P,S^{Ph} to a dichloromethane solution of [IrCl(COD)]$_2$ to generate a solid product, upon precipitation in high yield (94%) (**Scheme 4-4**). The ^{31}P{^{1}H} NMR spectra show distinct differences in the chemical shift for the free ligand ($δ$ -24.4) and the Ir-complex ($δ$ 5.4). The change in chemical shift is indicative of the complexation of (*S*)-P,S^{Ph} to iridium. This ligand is reported to show a high affinity for Ir bonding; hence, it is important to maintain the correct stoichiometry as [Ir]>1, leads to bimetallic iridium systems due to the lability of the sulphur on the ligand.[146] Unlike the diphosphine ligands that seemingly prefer biscoordination (see [IrCl(dppe)$_2$], **2.3.2**)

4.4.2 Synthesis of [IrCl(COD)(P,S^{Cy})] (1^{P,SCy})

Iridium-**P,S^{Cy}** type complexes have been reported by Biosca and co-workers. In this work a cationic iridium-**P,S^{Cy}** complex ([Ir(COD)(**P,S^{Cy}**)]$^+$), with a [BAr$^F_4$]$^-$ (tetrakis[3,5-bis(trifluoromethyl)phenyl]borate) counterion was reported and shows low %*ee* but high conversion for the asymmetric hydrogenation of functionalized olefins (**Scheme 4-5**).[144] Note that in this work the ligand is the configurational enantiomer (i.e. (*R*)-P,S^{Cy}) of the P,S^{Cy} ligand. However, these iridium complexes are more commonly applied in alkene hydrogenation due to the electrophilicity of the cationic iridium complex, generally favouring an inner-sphere mechanism *via* direct complexation of the substrate to iridium.[141,142,189–192]
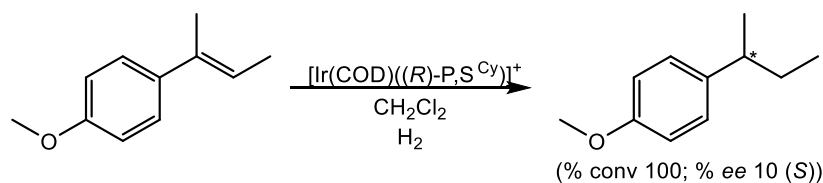
Scheme 4-5. Asymmetric hydrogenation with [Ir(COD)(P,S^{Cy})]$^+$.[144]

The ^{31}P{^{1}H} NMR spectra for **(S)-P,S^{Cy}** and **1^{P,SCy}** show distinct differences in their chemical shift window. The ^{31}P{^{1}H} NMR signals for **P,S^{Cy}** (δ -24.1) and **1^{P,SCy}** (δ 2.2) in chloroform-*d* appear in the upfield and downfield region respectively. The ^{1}H NMR data for the complex are less clear for the assignment of each proton, this is due to the crowded saturated CH region of the spectrum resulting in overlapping peaks (**Figure 4-1**). Nevertheless, the peaks could be assigned based on the known chemical shifts using a combination of ^{1}H-^{1}H COSY (**Figure 4-2**) and ^{13}C-135 DEPT (**Figure 4-3**) experiments for the CH$_2$ groups on the cyclohexyl and COD groups. The full characterization of **1^{P,SCy}** is presented in **Table 4-1**.
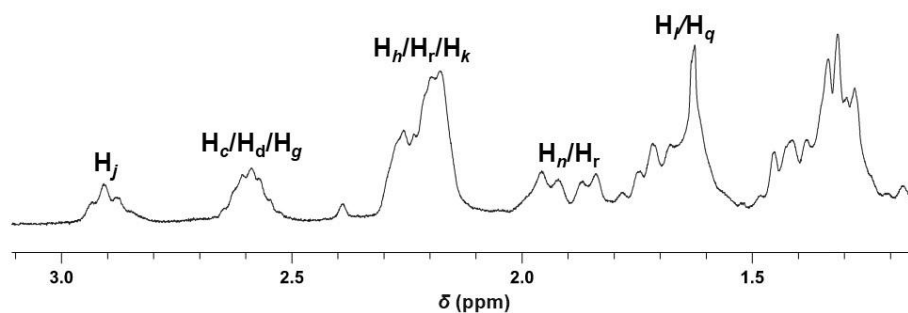
Figure 4-1. ^{1}H NMR spectrum for the sp^3 hybridized region for **1^{P,SCy}** in chloroform-*d* at 298 K.
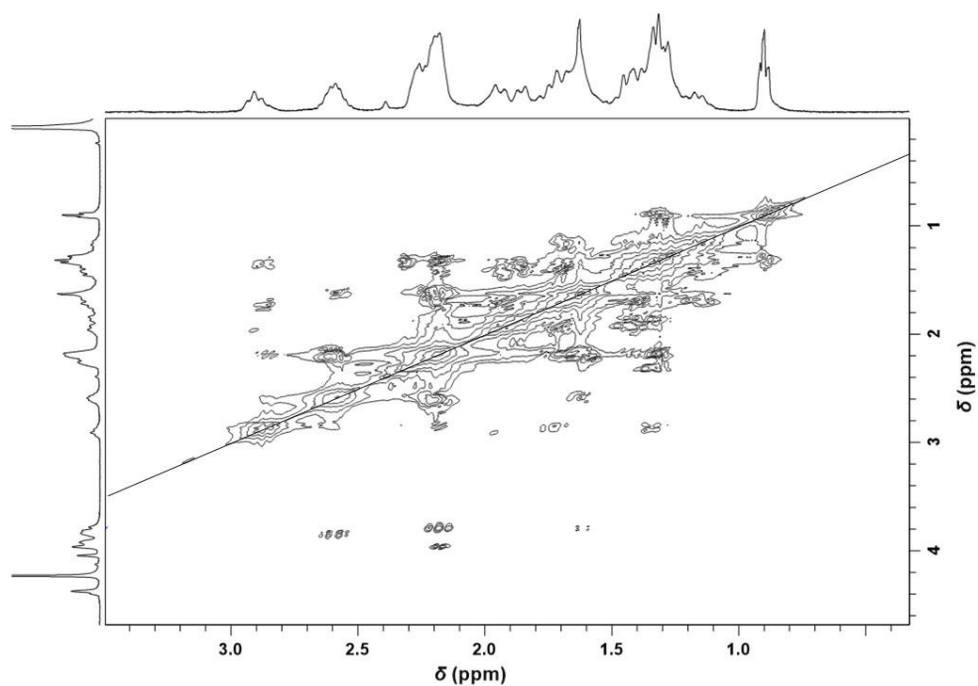
Figure 4-2. ^{1}H-^{1}H COSY NMR spectrum of **1^{P,SCy}** in chloroform-*d* at 298K.
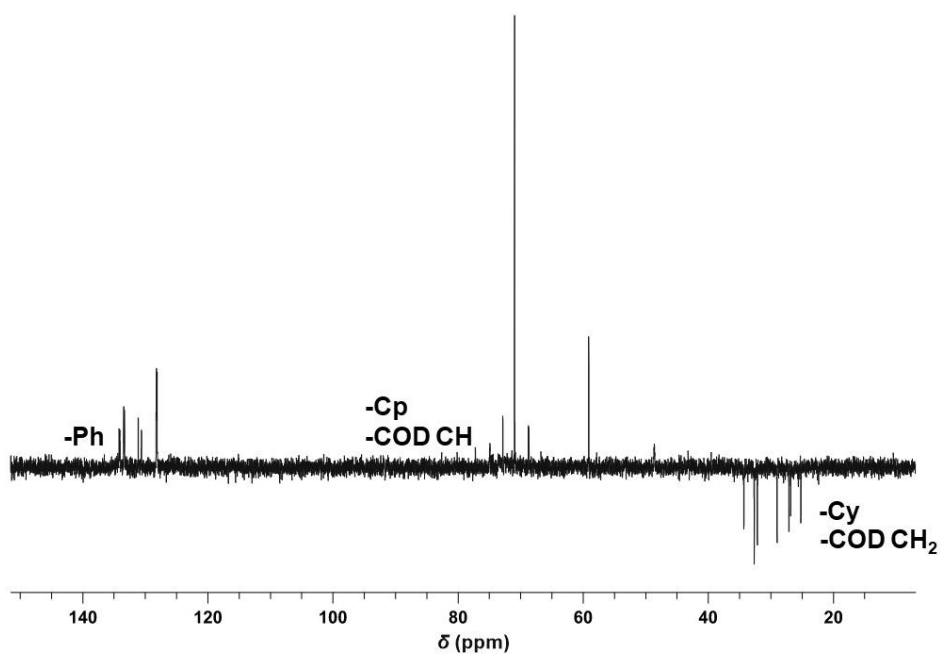
Figure 4-3. ^{13}C 135-DEPT NMR spectrum highlighting the different CH regions on **1^{P,SCy}**.

128

Table 4-1. NMR data for **1^{P,SCy}** in chloroform-*d* at 298 K.

Group	Chemical Shift (δ)
1H, Ph (*ortho*)	7.91 (*o*); 7.32 (*o'*)
Ph (*meta*)	7.56 (*m*); 7.36 (*m'*)
Ph (*para*)	7.55 (*p*); 7.39 (*p'*)
C$_8$H$_{12}$ CH	3.80 (*a*); 3.86 (*b*); 3.82 (e); 3.98 (*f*)
C$_8$H$_{12}$ CH$_2$	2.61, 2.23 (*c*); 2.58, 1.65 (*d*); 2.65, 2.25 (*g*); 2.19, 1.63 (*h*)
C$_6$H$_{11}$ CH	2.84 (*j*)
C$_6$H$_{11}$ CH$_2$	2.35, 1.34 (*k*); 1.64, 1.31 (*l*); 1.95, 1.47 (*n*); 1.43, 1.18 (*q*); 2.33, 1.76 (*r*)
S – CH$_2$	4.30, 3.90 (*s*)
Cp	4.04 (*t*); 4.34 (*u*); 4.78 (*v*); 4.20 (*w*)
13C, Ph (*ortho*)	134.0 ($^3J_{CP}$ = 10.8, *o*); 133.2 (d, $^3J_{CP}$ = 11, *o'*)
Ph (*meta*)	128.2 ($^3J_{CP}$ = 7.0, *m*); 128.3 (d, $^3J_{CP}$ = 7.3, *m'*)
Ph (*para*)	131.1 ($^4J_{CP}$ = 2.5, *p*); 133.2 (s, *p'*)
C$_8$H$_{12}$ CH	71.8 (*a*); 60.1 (*b*); 71.4 (e); 71.3 (*f*)
C$_8$H$_{12}$ CH$_2$	34.8 (*c*); 32.1 (d, J_{CP} = 1.9, *d*); 27.1 (d, J_{CP} = 1.9, *g*); 31.9 (*h*)
C$_6$H$_{11}$ CH	48.6 (*j*)
C$_6$H$_{11}$ CH$_2$	34.3 (*k*); 31.8 (*l*); 24.7 (*n*); 26.8 (*q*); 31.7 (*r*)
S – CH$_2$	27.1 (*s*)
Cp	72.8 (d, $^3J_{CP}$ = 2.2, *t*); 68.7 (d, $^3J_{CP}$ = 6.1, *u*); 75.0 (d, $^2J_{PC}$ = 6.6, *v*); 70.9 (*w*)
31P, P,S^{Cy}	2.24
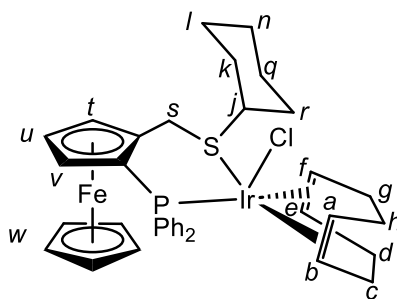
Attempts were made to form the anionic tetrahydride complexes **6^{P,SR}** under transfer hydrogenation and hydrogenation conditions (identical protocols to those used for the diphosphine ligand derivatives see – **3.3.1.1**). However, these experiments showed no evidence of tetrahydrido species.

4.5 Asymmetric transfer hydrogenation of Acetophenone – Cation effect

The effect of the alkali cation on the catalytic activity of the systems generated from $[IrCl(COD)(P,S^R)]/MO^iPr/H_2$ (M = Li, Na, K) was probed for the four different (**(S)-P,S^R**) ligands, under similar conditions to those mentioned in **Chapter 3:**. The reaction was run at 276 K in an attempt to increase the enantioselectivity (*ee*) based on **Equation 1-10**. The hydrogenation was carried out under 30 bars of H_2 with 0.1 % catalyst loading, and 0.5 % of a strong base (5 equivalents relative to [Ir]) in isopropanol. The Ir complexes with **1^{P,SiPr}**, **1^{P,SPh}** and **1^{P,SBz}** were previously reported for this reaction, whereas the **1^{P,SCy}** has not yet been described. The operating base (**Table 4-2**) is isopropoxide in each case, because the employed KO^{t}Bu in the experiments of entries 3 and 4 is a stronger base and thus immediately captures a solvent proton to generate isopropoxide.
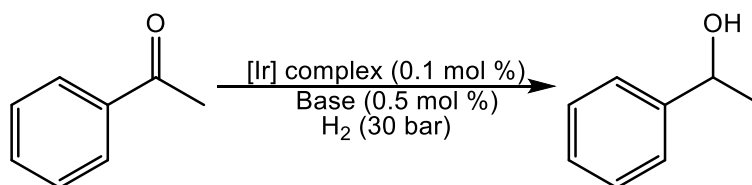
Table 4-2. Results of the acetophenone hydrogenation using different Ir-**P,S^R** complexes and bases (the major enantiomer is shown).[a]

Entry	Base (+ additive)	Conversion/% (e.e./%)			
		R = ^{i}Pr[b]	R = Ph[c]	R = Bz[b]	R = Cy[c]
1	LiO^{i}Pr	19.9 (34.2)	12.4 (64.5)	7.7 (77.5)	1.9 (69.3)
2	NaO^{i}Pr	60.9 (50.8)	25.7 (60.4)	19.3 (80.3)	59.8 (74.4)
3	KO^{t}Bu	90.3 (58.4)	34.3 (65.7)	20.9 (78.2)	70.3 (68.6)
4	KO^{t}Bu + 18-crown-6[d]	13.5 (59.7)	11.5 (59.6)	3.7 (80.5)	14.2 (67.1)
5	KO^{t}Bu + H$_2$O[e]	92.8 (28.9)	29.6 (67.4)	22.5 (49.8)	83.5 (74.5)

[a] Conditions: $p(H_2)$ = 30 bar; t = 4 h; T = 3°C; [PhCOMe] = 3.2 mmol in isopropanol; [Ir] = 3.2 x 10^{-3} M; [Base] = $1.6·10^{-2}$ M. [b] Pre-catalyst prepared *in situ* from [IrCl(COD)]$_2$ and (**(S)-P,S^R**);[c] With isolated **1^{P,SR}**. [d] 18-crown-6/K = 1.5. [e] H$_2$O/K = 1.5. Major enantiomer is shown.

The results of entries 1-3 indicate a significant effect of the base cation on the activity, confirming the proposition that the alkali metal is implicated in the catalytic cycle. Notably, all four **P,S^R** systems show the same trend of activity (Li < Na < K). When using the same base, the R = isopropyl system consistently gives the highest catalytic activity. The addition of 18-crown-6 to the potassium system (entry 4) results in a dramatic quench of the catalytic activity. Once again, a comparable effect is shown by all four **P,S^R** systems. This result is also in agreement with the proposed cycle because of the high affinity of 18-crown-6 for K$^+$.[193,194] It is

interesting to note that previously reported $[IrH_4L_2]^-$ (L = PiPr$_3$, PPh$_3$) complexes were crystallized and structurally investigated as crown ether adducts of the K$^+$ salts, and all structures that feature *cis* L ligands also reveal K···H interactions with three *mer* hydride ligands, as found by the DFT calculations for the $[Na(MeOH)_3][IrH_4(P,S^{Ph})]$ model (**1** in 3MeOH). Finally, the deliberate addition of degassed[147,148] water to the reaction mixtures has little or no effect on the catalytic activities (*cf.* entries 3 and 5).

The observed enantioselectivity trends are also interesting. The highest ee values were obtained for the R = Bz system, in agreement with the previous report.[145] For this system, as well as for the R = Ph and Cy systems, all three alkali cations yield essentially the same ee. For the R = *i*Pr system, however, the nature of the cation significantly affects the ee, which decreases in the order K > Na > Li. It is particularly interesting to note that, for all **P,S^R** systems, the presence of the crown ether, although strongly quenching the activity, does not significantly affect the ee. Conversely, the presence of water, although not significantly changing the activity, results in a %ee decrease approximately by a factor of 2 for the *i*Pr and Bz systems, both of which are formed in situ. The decrease in enantioselectivity is presumably caused by the disruption of hydrogen bonding within the catalytic framework, as the presence of water does not affect the activity.[195] The precomplexed Ph and Cy systems, on the other hand, yield ee's similar to those of entries 1-3. The general trend for each of the four catalytic systems shows that the order of activity decreases with decreasing cation size K > Na > Li. If an anionic tetrahydride complex ($[Ir(H)_4(\mathbf{P,S^R})]^-$ (**6^{P,SR}**) is the active species, the comparatively low activity of **1^{P,SR}** with lithium can be partially rationalized by comparing the reactivity of the model complex **6^{dppe}** in **Chapter 3:**.This is most evident for the cyclohexyl system which shows very low activity in the presence of a Li containing base compared to the Na, and K cations.

4.6 DFT study on the proposed catalytic cycle

4.6.1 Cation effect on $6^{P,SPh}$

Even though the presence of a tetrahydrido iridium-**P,S**^{R} species could not be detected through spectroscopic methods. The evidence of complexes 6^{dppe}, 6^{dppf}, and $6^{S\text{-}BINAP}$, combined with previous DFT studies supports the potential presence of $6^{P,SR}$ as a catalytically active species. Hence, this was used as the starting point for the DFT investigation on the cation effect.[87,152]

DFT calculations were performed on $7^{P,SPh}$ ([$6^{P,SPh}$][M(MeOH)$_5$] (M = Li, Na, K)) as this system is deemed the most chemically comparable to 6^{dppe}. This was done to better understand the influence of the cation on catalyst activity. These calculations used a hybrid implicit-explicit solvent model, in which 5 explicit MeOH molecules were introduced (along the solvent continuum) to depict cation solvation more accurately.[57] The previously reported model by Hayes and co-workers utilized 3 explicit methanol molecules, that while good for predicting the overall reaction mechanism, failed to reproduce the experimental trend observed with each cation. With an [M(MeOH)$_3$]$^+$ model, the predicted activity follows the reverse of what is observed experimentally i.e., Li > Na > K. The catalytic cycle utilizing the [M(MeOH)$_5$]$^+$ model is shown in **Scheme 4-6** and the corresponding Gibbs free energy plot in **Figure 4-4**.
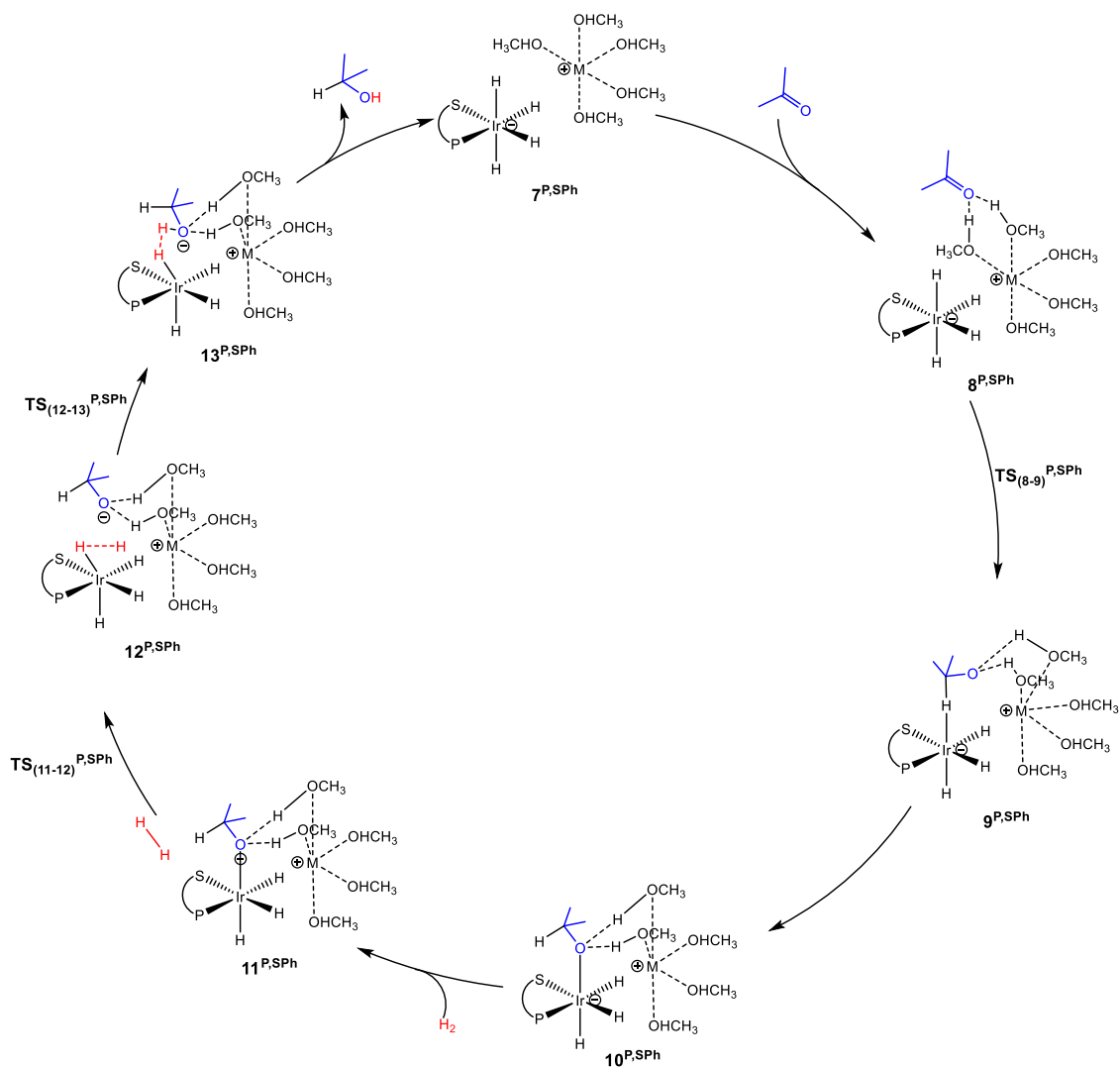
Scheme 4-6. Catalytic cycle of ketone hydrogenation catalysed by $7^{S,Ph}$ proposed by DFT calculations (M = Li$^+$, Na$^+$, K$^+$).

As seen in **Figure 4-4**, the cation influences the energy span of the catalytic cycle. This energy span corresponds to the difference between the transition state of the outer-sphere hydride transfer (**TS$_{(8-9)}^{P,SPh}$**) and the initial state **$7^{P,SPh}$**, which is the [$6^{P,SPh}$][M(MeOH)$_5$] ion pair plus an acetone molecule infinitely far apart. The barrier of the hydride transfer step changes appreciably with each cation, following the expected trend (based on experimental evidence): K (9.8 kcal mol^{-1}) < Na (14.1 kcal mol^{-1}) < Li (16.6 kcal mol^{-1}). After this step, which generates an O-coordinated alkoxide **$10^{P,SPh}$** *via* a less stable isomeric σ-complex **$9^{P,SPh}$**, the cation influence is much smaller. From **$10^{P,SPh}$**, H$_2$ is then introduced into the model, first displacing the alkoxide (**TS$_{(11-12)}^{P,SPh}$**) to form an η^2-H$_2$ complex (**$12^{P,SPh}$**). The latter is able to protonate the displaced alkoxide *via* **TS$_{(12-13)}^{P,SPh}$**, yielding the alcohol and regenerating the catalytic system **$7^{P,SPh}$**.
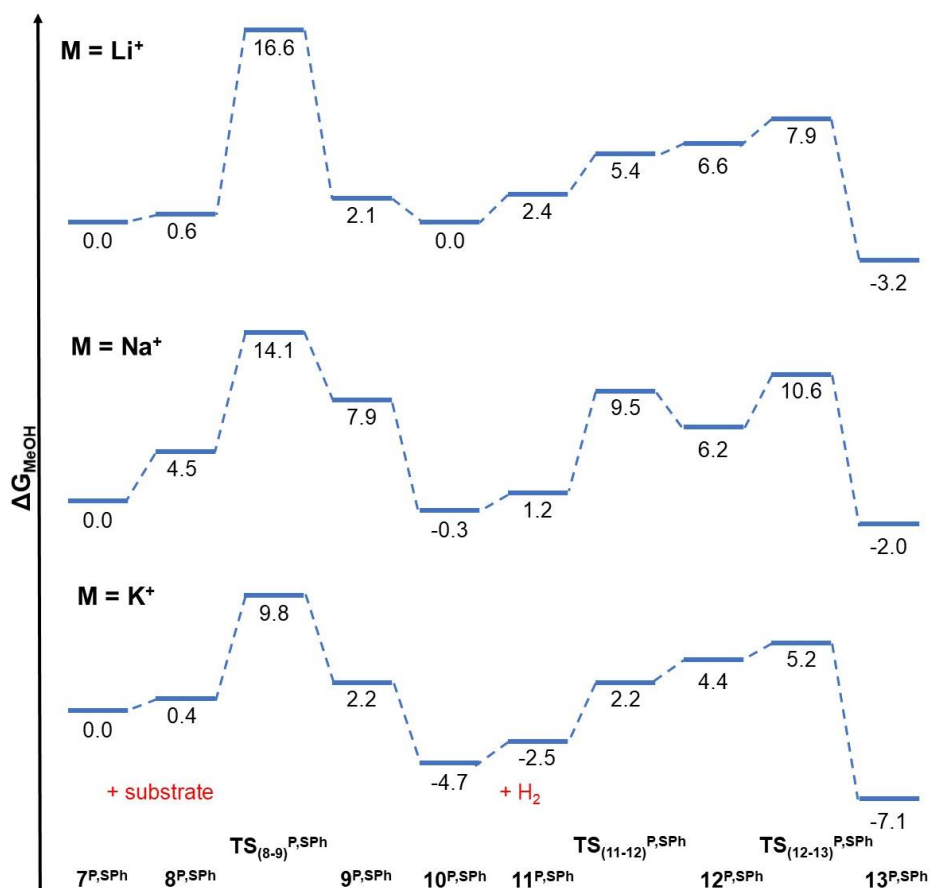
Figure 4-4. Computed Gibbs energy profiles for the hydrogenation of acetone with **7^{P,SPh}**. All energy profiles in kcal mol^{-1}. The labels shown reference the cycle in **Scheme 4-6.**

Overall, the calculations using the [M(MeOH)$_5$]$^+$ solvent model correctly reproduces the cation effect on the hydrogenation rate. This model stresses the importance of the changes in the solvation sphere of the cation along the reaction. The effect of the solvation sphere is discussed below (**4.6.1.1**, **4.6.1.2**, **4.6.1.3**).

4.6.1.1 Hydride transfer step – TS$_{(7-8)}$^{S,Ph}

The implementation of this model relies on each cation being placed in the hydride cavity opposite to **P,S^{Ph}**, and thus not directly interacting with the ligand. The cation in this position stabilizes the hydridic component (active site) of the catalyst. The methanol molecules in **7^{P,SPh}** form a well-defined solvation sphere around each cation (**Figure 4-5**).
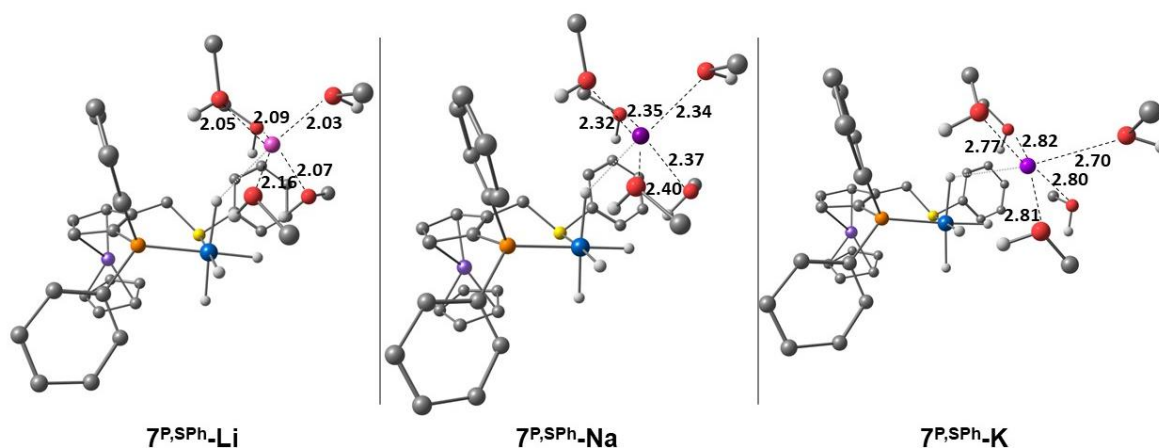
Figure 4-5. Computed structures for **7^{P,SPh}-M**. C-H hydrogen atoms have been omitted for clarity. All distances are in Å.

In each structure of **7^{P,SPh}-M** the methanol molecules around the cation show consistent distances for the M-O bonding (Li-O between 2.03 and 2.16 Å; Na-O 2.32 and 2.40 Å; K-O 2.70 and 2.82 Å). These values are indicative of covalent type interactions between the cation and methanol, with similar values reported for the covalent radii of M-O (Li-O 1.94; Na-O 2.32: K-O 2.69 Å).[196] Introduction of the substrate to **7^{P,SPh}** (**8^{P,SPh}**) shows that the coordination sphere around the cation remains intact and the average of the M-O bond lengths remains within the same range (**Figure 4-6**).
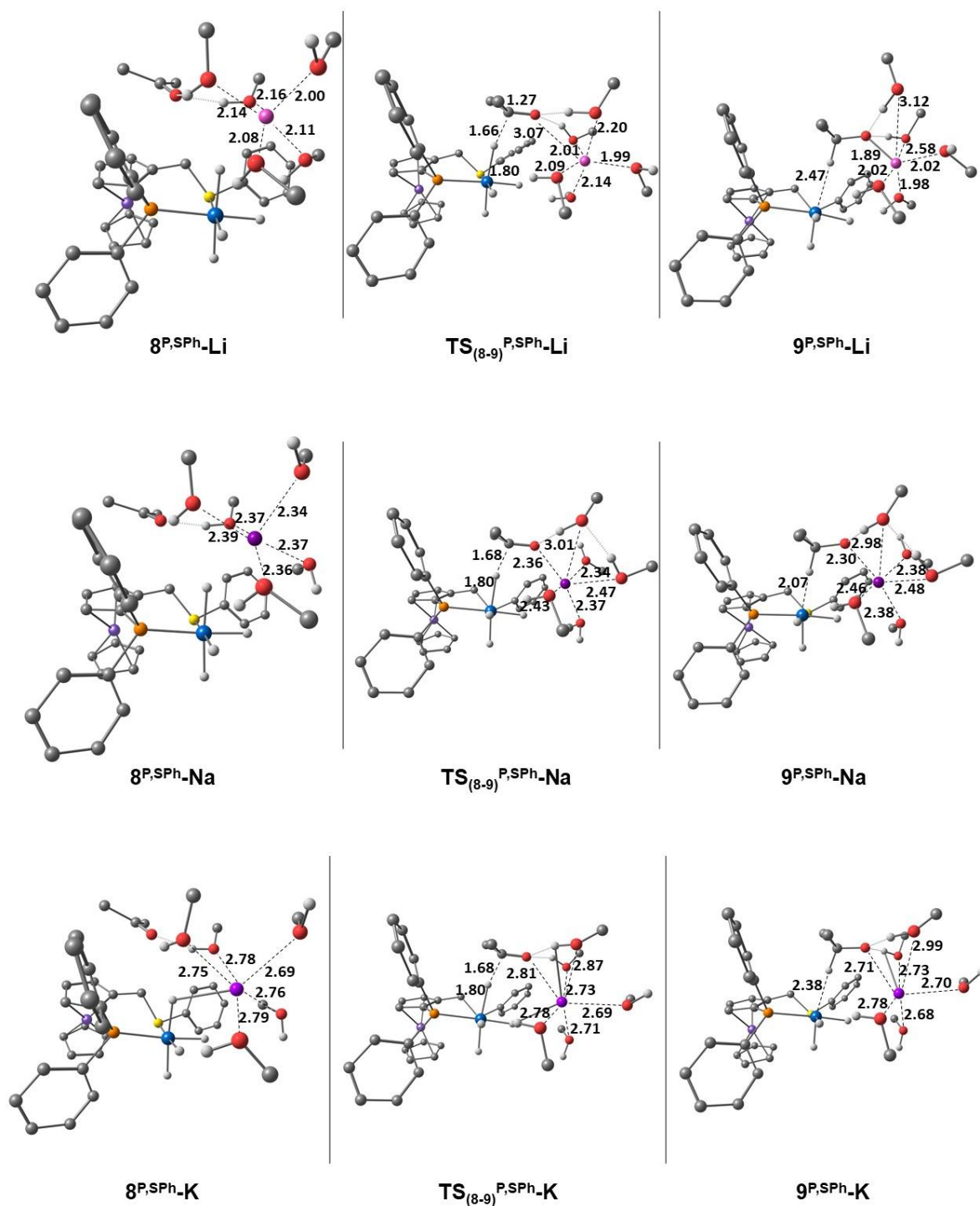
Figure 4-6. Optimized structures for the hydride transfer step for each of the three cations. Li⁺ (top), Na⁺ (middle), K⁺ (bottom). Distances shown are in Å. C-H hydrogen atoms have been omitted for clarity.

For the reaction to take place the substrate must approach one of the axial Ir-H bonds, this occurs *via* the partial displacement of one of the methanol molecules. Once the substrate is sufficiently close to the Ir-H bond (~1.67 Å) the hydride transfer can occur (**TS$_{(8-9)}$^{P,SPh}**).

After hydride transfer ($9^{P,SPh}$) the solvent shell around the cation is depicted as including the alkoxide with mutual stabilization of the alkoxide by the cation and vice-versa. It is worth noting that the increase in radii of each cation means that the solvation shell around each cation is different. This is most evident when comparing $9^{P,SPh}$-**Li** and $9^{P,SPh}$-**K**, the solvent shell around the potassium ion is less effected by the presence of the alkoxide and the K-O bond distances show less variation. The change of the solvation shell around the cation is reflected in the energy differences between $8^{P,SPh}$ and $9^{P,SPh}$ where the greatest difference is seen for the Na$^+$ system. Previously published work related to carbonyl cationic interactions mention direct activation by the cation without the inclusion of explicit solvent effects and hence, do not include substrate displacement.[86,197,198]

4.6.1.2 Change in the coordination mode of the alkoxide - $9^{P,SPh}$ to $10^{P,SPh}$

While the alkoxide is sufficiently stabilized by the MeOH molecules within the solvation shell of the cation, a more stable form of the overall system $9^{P,SPh}$ exists. In this form there is direct coordination between the iridium atom and the alkoxide oxygen atom to form an Ir-O bond ($10^{P,SPh}$) (**Figure 4-7**).
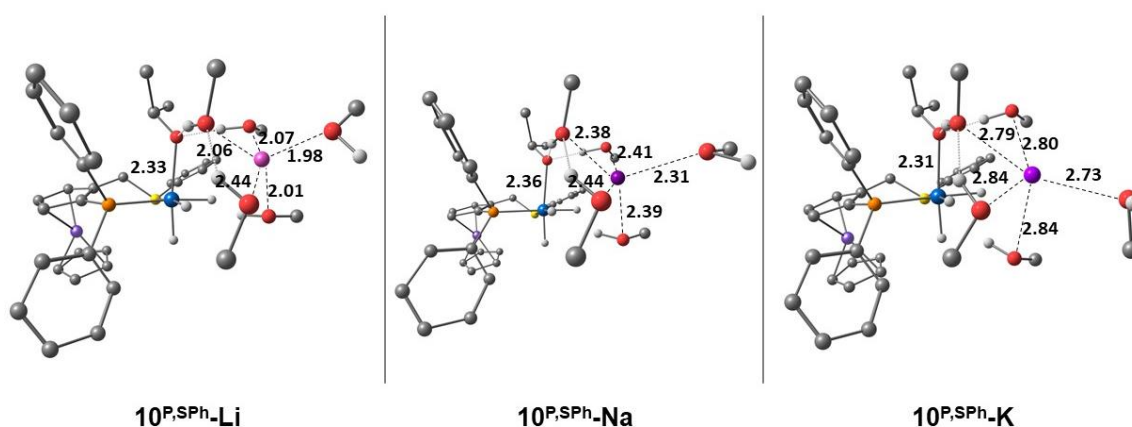
Figure 4-7. Optimized structures for $10^{P,SPh}$-**M** for each of the three cations. Distances shown are in Å. C-H hydrogen atoms have been omitted for clarity.

The isomerization of $9^{P,SPh}$ to $10^{P,SPh}$ results in a lower relative energy speciation. In all cases the change in coordination results in an Ir-O bond that is around 2.3 Å, regardless of the cation, and the iridium is stabilized through the O bond, that results in a negative charge distribution to the O. Upon the change in coordination of the alkoxide the MeOH molecules are rearranged to resemble the solvation shell in $7^{P,SPh}$ (**Figure 4-6**). This rearrangement around the cation, combined with the apparent stability of the Ir-O complex results in a more energetically stable cluster evidenced by the decrease in relative energy (**Table 4-3**). The direct coordination of

the alkoxide to iridium is comparable to the trihydride adduct obtained with the Ir-dppe system ([Ir(H)$_3$(DMSO)(dppe)]) (**3.3.1.3**). While in the case of DMSO coordination there is no net negative charge distribution within the system, with preference for sulphur binding.

Table 4-3. Computed energy differences for the alkoxide isomerization. All values in kcal mol^{-1}.

	9^{P,SPh}	**10**^{P,SPh}	$\triangle G_{MeOH}$ **(9-10)**^{P,SPh}
Li$^+$	2.1	0.0	2.1
Na$^+$	7.9	-0.3	8.2
K$^+$	2.2	-4.7	6.9

4.6.1.3 Alkoxide H$_2$ exchange (TS$_{(11\text{-}12)}$^{P,SPh})

Along the energy profile of the hydrogenation reaction, the introduction of H$_2$ into the catalytic model regenerates the catalyst. The step preceding proton transfer is the displacement of the alkoxide by H$_2$ within the coordination sphere of iridium to form an η^2-H$_2$ complex (**12**^{P,SPh}). This displacement of the alkoxide results in a higher energy transition state(**TS$_{(11\text{-}12)}$^{P,SPh}**), as the alkoxide is no longer stabilized by Ir but through H-bonding interactions with OH groups on the methanol molecules, and M-O interactions with the cation in the case of Li$^+$ (**Figure 4-8**). In these two steps the solvation shell of the methanol molecules around the cation remains consistent and the increase in relative energy is a result of the movement of the alkoxide. Upon formation of **12**^{P,SPh} the H$_2$ bond is partially elongated (**Table 4-4**). At this point one of the protons is transferred to the alkoxide to yield the product (isopropanol) regenerating the iridium tetrahydrido species.

Table 4-4. H-H bond distances at each step of the reaction coordinate to form **12**^{P,SPh}. All distances in Å.

	TS$_{(11\text{-}12)P,SPh}$	**12**^{P,SPh}
Li$^+$	0.75	0.84
Na$^+$	0.75	0.84
K$^+$	0.75	0.84
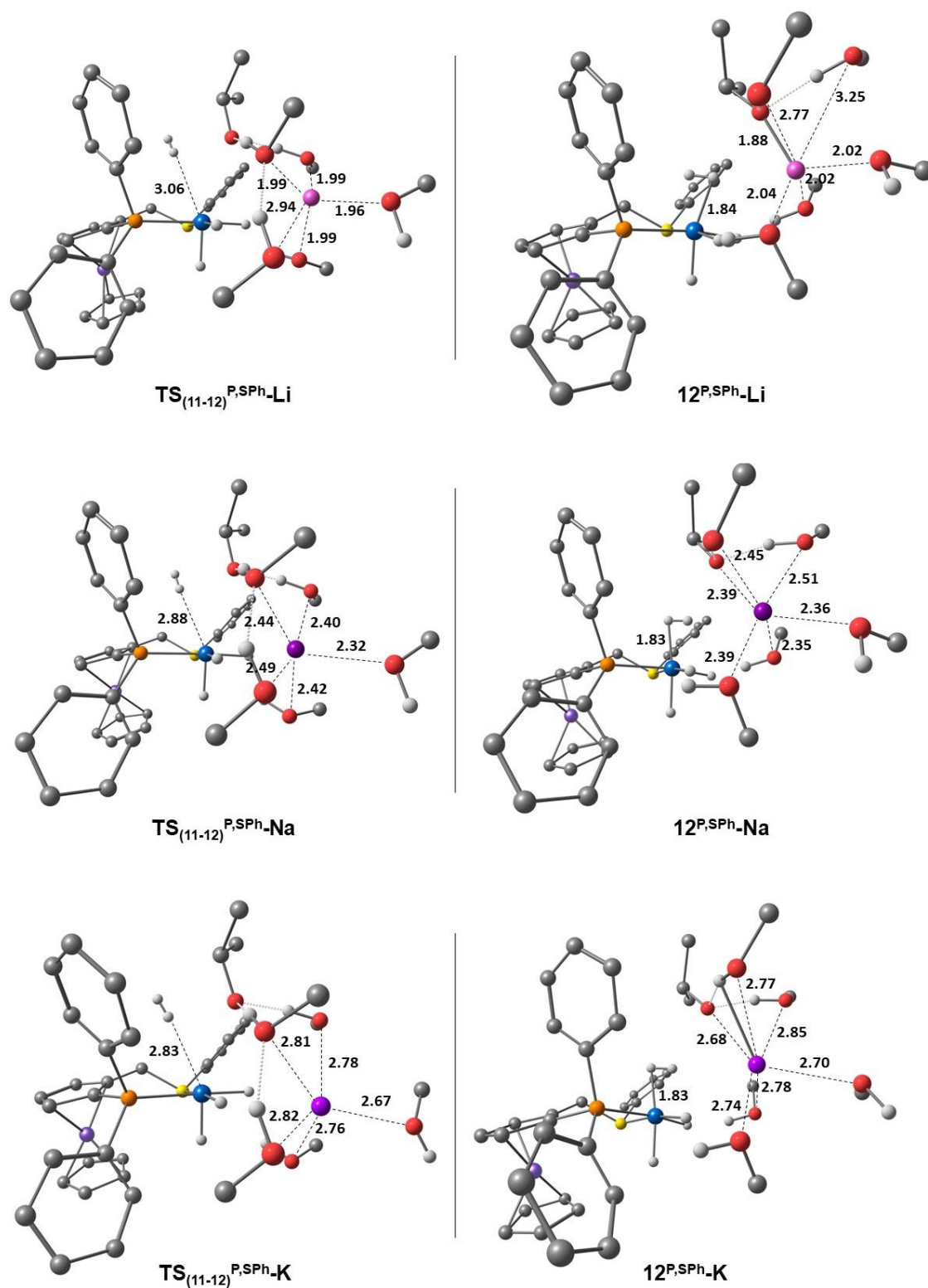
Figure 4-8. Optimized structures for the introduction of H_2 into the coordination sphere of Ir in the presence of Li^+ (top), Na^+ (middle) and K^+ (bottom). All distances are in Å. C-H hydrogen atoms have been omitted for clarity.

4.6.2 DFT investigations of the cation effect in the enantioselectivity

Contrarily to the strong alkali cation effect on the catalytic activity, its influence on enantioselectivity is small (**Table 4-2**). To understand the origin of this behaviour, DFT calculations have been performed on the enantio-determining hydride transfer step using the real prochiral acetophenone substrate while employing the (P,S^{Ph}) ligand.

For this system, the *S* enantiomer of the ligand leads to a formation preference for the *S* enantiomer of the 1-phenylethanol product consistent with the experimental data, with all three alkali metal cations yielding essentially the same *ee*. The *pro-R* and *pro-S* transition states **TS$_{(7-8)}$**$^{\text{dppe}}$ were computed for the three [M(MeOH)$_5$]$^+$ cations, **Figure 4-9**, shows the resulting transition state geometries, and important distances for each cation. The main interaction that discriminates between the two diastereomeric transition states involves a phenyl group of the phosphine ligand. This group interacts with the acetophenone methyl group (C-H-π) in the *pro-S* TS and with the acetophenone phenyl group (π-π) is the *pro-R* TS. The cation is in the less crowded space opposite to this key P-phenyl group. Consequently, the cation nature does not significantly alter the main interactions that govern the *ee*. The calculated $X_{Ph}\cdots HC_{Me}$ and $X_{Ph}\cdots X_{Ph}$ distances for all computed systems, together with the Gibbs energy difference between both transition states ($\Delta\Delta G_{R-S}$) is given in **Table 4-5**. The geometrical parameters describing the substrate-ligand interaction are very similar in all cases, in agreement with the limited influence of the cation on enantioselectivity.
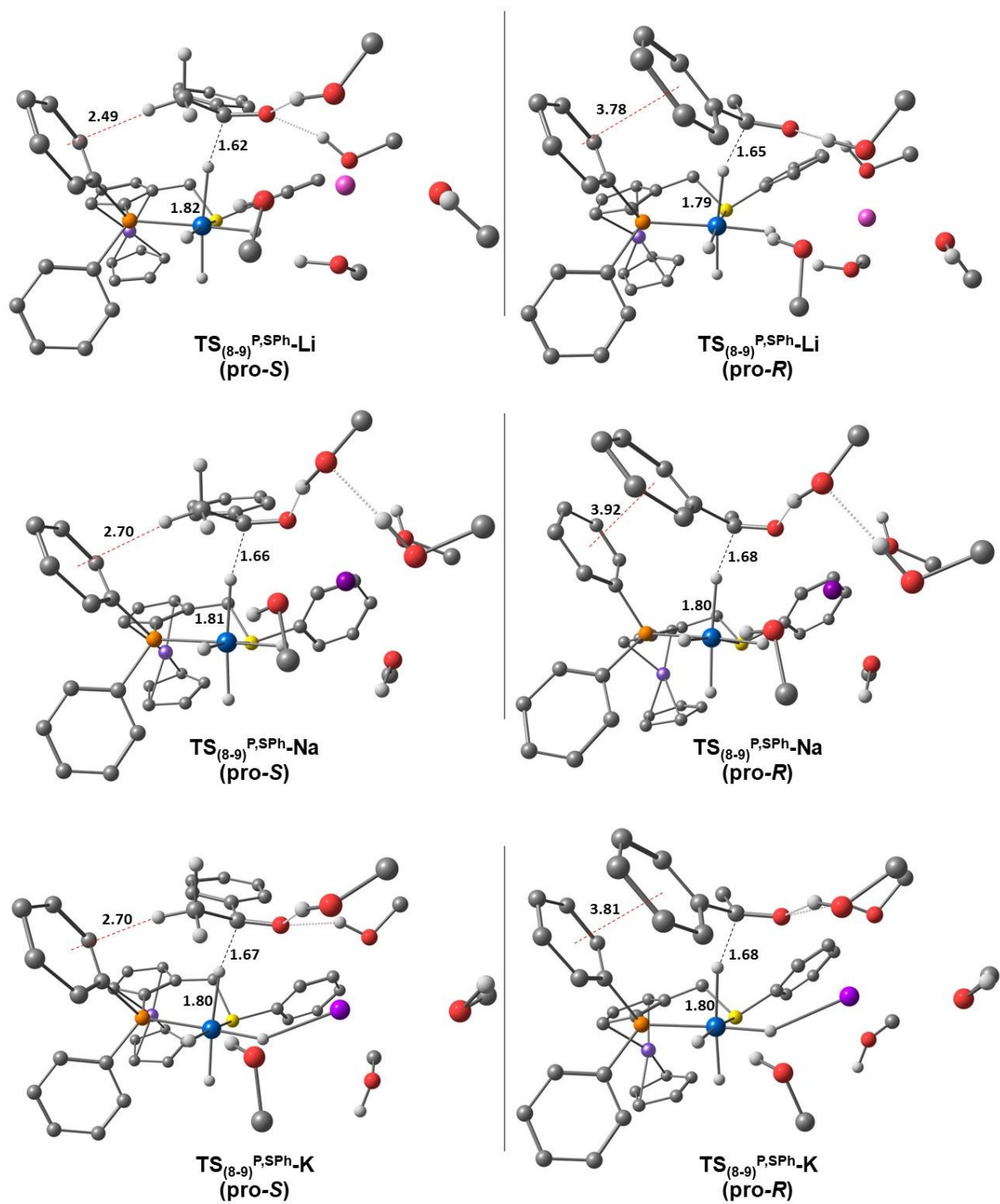
Figure 4-9. pro-*S* and pro-*R* transition states for hydride transfer to acetophenone, in presence of each cation. Distances in Å.

Table 4-5. Main distances (Å) and Gibbs energy differences (kcal mol^{-1}) between the pro-*S* and pro-*R* transition states for hydride transfer to acetophenone with the $[M(MeOH)_5]^+$ model.

	$X_{Ph}\cdots HC_{Me}$	$X_{Ph}\cdots X_{Ph}$	$\Delta\Delta G_{R\text{-}S}$
Li$^+$	2.486	3.777	2.6
Na$^+$	2.695	3.917	7.4
K$^+$	2.612	3.809	3.7

In each case, the *pro-S* transition state is lower than that of *pro-R*, in qualitative agreement with the experimental results. However, the computed $\Delta\Delta G_{R\text{-}S}$ are too high to account for the experimental *ee's* of about 65%. Several factors can be invoked to justify this discrepancy. On one hand, the calculations were performed with methanol as a model of the experimental solvent (isopropanol). On the other hand, the balance between the relative strength of the C-H-π and π-π interactions may be functional-dependent. Finally, the energies are very sensitive to the methanol molecule positions. Slightly different arrangements of the five solvent molecules appreciably modifies the value of $\Delta\Delta G_{R\text{-}S}$. However, the calculations correctly predict that the *S* isomer is preferred and rationalizes the little influence of the cation nature on the *ee's*.

4.6.3 Hydride transfer with 6^{P,SiPr}

The previous study (**4.6.1**) highlights the effect of the cation on the hydrogenation of ketones and shows how the cation influences reactivity. This combined with the experimental data shows that the most favourable conditions for hydrogenation with Ir-P,S^R is in the presence of K$^+$. These calculations helped locate the rate determining step, which is the hydride transfer step. With this knowledge, a set of calculations were performed on Ir-P,S^{iPr} using the $[K(MeOH)_5)]$ model for the hydride transfer (**TS$_{(8-9)}$^{P,SiPr}**) and for the preceding step (formation of **8^{P,SiPr}** from **7^{P,SiPr}**) (**Scheme 4-7**).
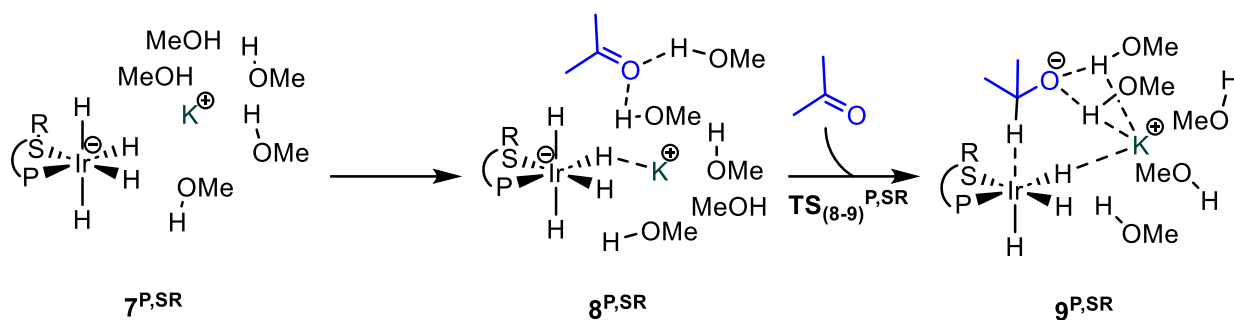
Scheme 4-7. Hydride transfer step to the ketone. R = Ph, ^{i}Pr.

Comparing the relative energy of each step across the reaction coordinate (**Table 4-6**) it is seen that relative energy difference for **TS$_{(8-9)}$$^{P,S{i}Pr}$** is in fact lower than that observed for **TS$_{(8-9)}$^{P,SPh}** by 2.8 kcal mol^{-1}. **TS$_{(8-9)}$$^{P,S{i}Pr}$** has a lower energy barrier for the hydride transfer and hence, a higher activity system is observed.

Table 4-6. Comparison of the relative energies for the hydride transfer steps. Energies listed in kcal mol^{-1}.

	R = Ph	R = ^{i}Pr
7^{P,SR}-K	0	0
8^{P,SR}-K	0.3	1.0
TS$_{(8-9)}$^{P,SR}-K	9.8	7.0
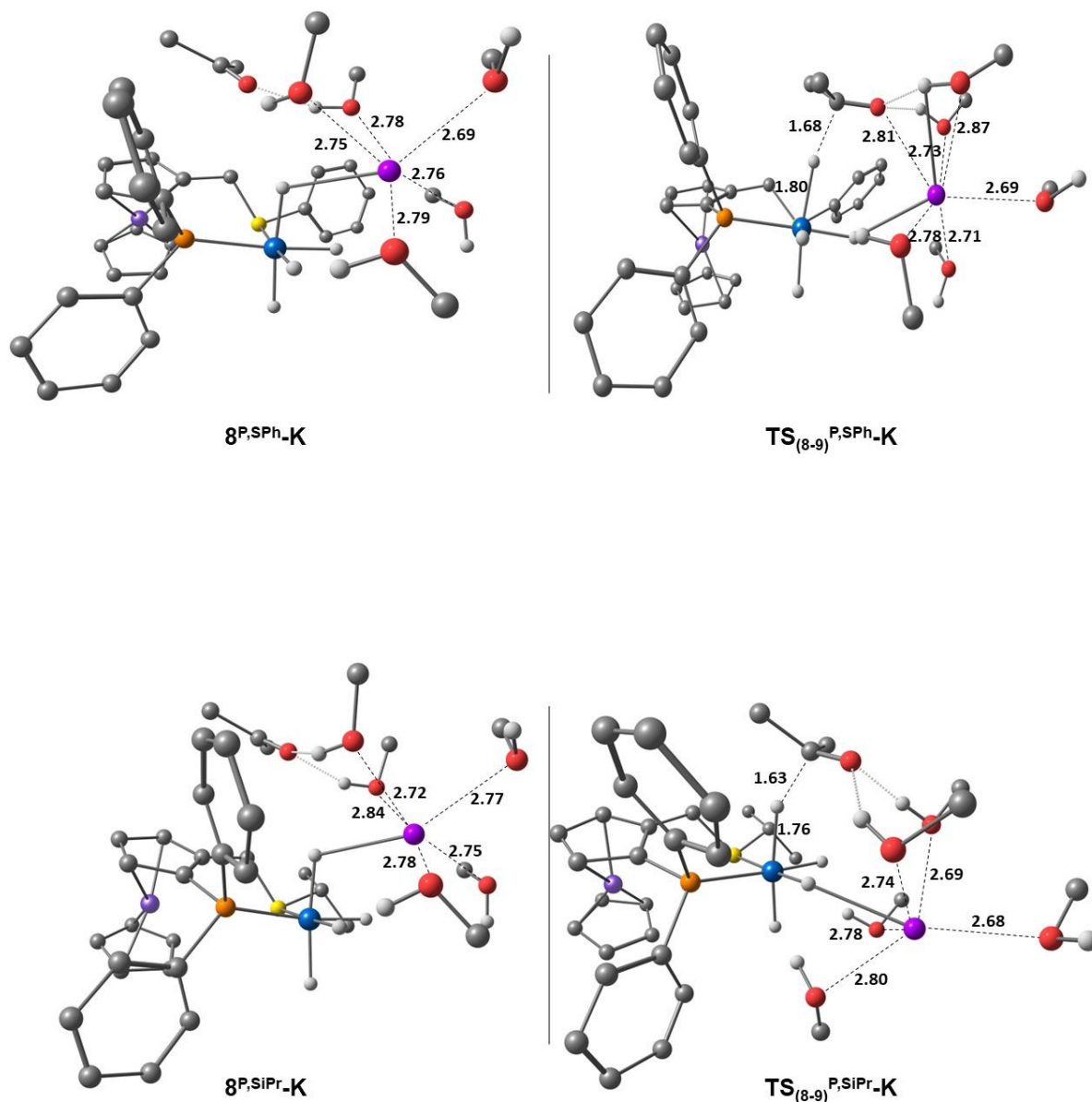
Figure 4-10. Optimized structures for $8^{P,SPh}$-**K** and $TS_{(8-9)}^{P,SPh}$-**K** (above), and $8^{P,SiPr}$-**K** and $TS_{(8-9)}^{P,SiPr}$-**K** (below). All distances are in Å. C-H hydrogen atoms have been omitted for clarity.

A structural comparison of $8^{P,SR}$ and $TS_{(8-9)}^{P,SR}$, based on the R group illustrates a major factor in the transition state. In each case, the solvation sphere around the cation changes upon entry of the ketone, but in a comparatively similar fashion (**Figure 4-10**). The energy difference is attributed to conformation changes for the respective R group, for the Ir-P,S^{Ph} system, the approach of the substrate relies on a change in the geometry of the phenyl. This phenomenon of rotation is much less prominent for the isopropyl group on Ir-P,S^{iPr}. The conformational changes of the R group on the ligand are the most likely cause for the increased transition state energy.

Table 4-7. Comparison of the Ir-S-C bond angle for the different ligands. Angles are in $^{\circ}$.

	R = Ph	R = ^{i}Pr
8^{P,SR}-K	107.9	107.6
TS$_{(8-9)}^{P,SR}$-K	115.7	108.5

4.7 Conclusions

The role of anionic hydride complexes as active catalysts in hydrogenation and hydrogen transfer reactions has now become well-established. The present chapter has illustrated one such case for the active catalyst produced *in situ* by activation of [IrCl(COD)(P,S^R)] under H$_2$ in the presence of a strong base. The stark dependence of the catalytic activity on the nature of the base alkali cation (K$^+$ > Na$^+$ > Li$^+$) and the severe activity dampening observed when 18-crown-6 is added to the K$^+$ system confirm previous suggestions of an anionic active complex.[87] The proposition, made solely on the basis of DFT calculations in the same contribution,[87] that such a species is the Ir^{III} tetrahydrido complex M$^+$[IrH$_4$(P,S^R)], has found strong support by the observed formation of the related (and more stable) K$^+$[IrH$_4$(dppe)]$^-$ from [IrCl(COD)(dppe)] in isopropanol and KO^{t}Bu under hydrogenation conditions (H$_2$ gas at 298 K) and even under transfer hydrogenation conditions (without H$_2$ at 353 K).[152] This hypothesis is further supported by the DFT calculations carried out in this chapter, where the experimental trend of alkali metal cation-dependent activity has not only been reproduced but also rationalized, at the condition of using a fully explicit cation coordination sphere, M(MeOH)$_5$$^+$. Most intriguingly, the activity does not appear to depend on any activating effect by the cation on either the ketone substrate or the iridium hydride species, but rather on the coordination sphere rearrangement at the alkali metal cation when, in the turnover-determining transition state, the incipient alkoxide binds and establishes a bond with the alkali metal cation, replacing one or more alcohol molecules. These results indicate that the inclusion of explicit solvent molecules (and enough of them) is of paramount importance for the DFT calculations. So that the appropriate interpretation of certain effects that may be observed in catalytic cycles that involve anionic active species.

Chapter 5:   Experimental

5.1 General methods

All non-aqueous reactions were carried out under argon using high-vacuum or Schlenk line techniques using flame dried glassware. NMR analysis and manipulation were carried out using NMR tubes fitted with J. Young's valves. All deuterated solvents were dried using sodium metal and degassed *via* freeze-pump-thaw methods. Chemical shifts are quoted as parts per million. Coupling constants (*J*) are quoted in Hertz. All NMR data was manipulated using TopSpin 3.2 and spectra presented using CorelDraw. All DFT images were produced using ChemCraft. Kinetic data was processed using Microsoft Excel. The chromatographic analyses were obtained on an HP 5890 instrument equipped with a chiral Supelco BETA DEX 225 column. The **P,S^R** ligands were synthesised according to the published procedures.[140,145] [IrCl(COD)]$_2$.[199] was synthesised according to the previously published procedures, along with **1^{dppe}**.[152,153] **1^{dppf}** was synthesized using an adapted method to that reported.[149] The NMR spectroscopic characterization of each iridium complex is tabulated. Key NMR characterization data of previously unreported complexes is included in the main text, with only the synthetic method included in this section – to avoid redundancy.

5.2   Experimental for Chapter Two

All reactions and purifications were carried out under nitrogen using high-vacuum or Schlenk-line techniques unless specified otherwise.

5.2.1   Synthesis of [IrCl(COD)]$_2$

Iridium trichloride hydrate (9 g, 30 mmol) was dissolved in 135 mL of distilled water, to which a mixture of 270 mL of isopropanol and 27 mL of 1,5-COD was added portion wise and stirred at reflux for about 18 hours under argon atmosphere. This resulted in a colour change from brown toward intense red. The resulting solution was left to cool to room temperature and then concentrated to about 50% of its original volume *in vacuo*. Shiny red crystals of [IrCl(COD)]$_2$ precipitated, which were filtered, and washed with cold methanol (60 mL) and dried under vacuum resulting in bright red crystals (7.4 g, 10 mmol). Yield = 30 %.

5.2.2   Synthesis of [IrCl(COD)(dppe)] (1^{dppe})

A solution of [IrCl(COD)]$_2$ (240 mg, 0.36 mmol) and dppe (286 mg, 0.72 mmol), was made in dichloromethane (15 mL) and stirred for 1 hr. The solvent was then removed *in vacuo* resulting in an orange solid. The solid was then dissolved in toluene (20 mL), and the solution filtered through a pipette lined with cotton wool, and a third of the depth of Al$_2$O$_3$. The resultant pale-yellow solution was then concentrated *in vacuo*, resulting in a fine yellow powder (480 mg, 0.65 mmol). Yield = 90 %. Yellow crystals were grown by layering a concentrated solution of **1^{dppe}** in toluene with hexane, after 48 hrs yellow crystals were collected. The NMR data are presented in **Table 5-1**.[153]

Table 5-1. NMR data for **1**^{dppe} in benzene-d_6 at 298 K.

1H (500 MHz)	
Ph (*ortho*)	7.69 (t, $^3J_{HP}$ = 8.9, $^3J_{HH}$ = 7.6)
Ph (*meta*)	7.58 (m)
Ph (*para*)	7.12 (t, $^3J_{HH}$ = 7.6)
COD C-H (olefin)	3.83 (s)
COD CH$_2$	2.51 (bd, $^2J_{HH}$ = 9.2); 1.99 (q, $^2J_{HH}$ = 8.1)
dppe CH$_2$	2.89 (m, $^2J_{HH}$ = 6.5); 1.78 (m, $^2J_{HP}$ = 9.8, $^2J_{HH}$ = 6.5)
13C (125 MHz)	
Ph (*ortho*)	133.1
Ph (*meta*)	134.3
Ph (*para*)	127.4
Ph (*ipso*)	129.2
COD C-H (olefin)	67.7
COD CH$_2$	33.2
dppe CH$_2$	29.6
31P (202 MHz)	
dppe P	34.4

5.2.3 Synthesis of [Ir(H)(C$_8$H$_{12}$)(dppe)] (2^{dppe} & 3^{dppe})

KO^{t}Bu (77 mg, 0.69 mmol) was added to an isopropanol (10 mL) solution of **1**^{dppe} (100 mg, 0.14 mmol) and stirred at room temperature for 1 h, generating a cream-coloured solution. The solution was concentrated to dryness, the solid residue was dissolved in toluene (8 mL), and the resulting mixture was passed through an alumina lined pipette. The solution was then concentrated *in vacuo*, to yield a cream powder (98 mg, 0.14 mmol) .Yield 99 %. This reaction can also be performed using an equivalent amount of NaOMe. ESI-HRMS (*m/z* relative intensity %): [M−H]$^+$calculated: 699.1930; found: 699.1933. The NMR analysis of the product reveals that it contains a mixture of isomers **2**^{dppe} and **3**^{dppe}.[152] NMR data for **2**^{dppe} and **3**^{dppe} are presented in **Table 5-2** and

Table 5-3 respectively.

<p align="center">**Table 5-2.** NMR data for **2^{dppe}** in benzene-d_6 at 298 K.</p>

^{1}**H** (500 MHz)	
Ph	8.01 – 7.0 (m)
COD CH	3.81 (bs)
COD CH$_2$	2.45 (m), 2.36 (m)
dppe CH$_2$	2.21 (m), 1.81 (m)
Ir-H	-14.00 (t, $^2J_{HP}$ = 21.6)
^{13}**C** (125 MHz)	
Ph	134.5 (*o*), 128.9 (*p*), 127.9 (*m*)
COD CH	63.2
COD CH$_2$	35.5
dppe CH$_2$	29.3
^{31}**P** (202 MHz)	
dppe P	33.2 (s)

Table 5-3. NMR data for **3^dppe** in benzene-d_6 at 298 K.

3^dppe

^{1}H (500 MHz)	
Ph (*ortho*)	8.05 (m, $o_{B,down}$), 8.00 (m, $o_{A,up}$), 7.60 (m, $o_{B,up}$), 6.83 (m, $o_{A,down}$)
Ph (*meta*)	7.23 (m, $m_{B,down}$), 7.15 (m, $m_{A,up}$), 7.05 (m, $m_{B,up}$), 6.92 (m, $m_{A,down}$)
Ph (*para*)	7.18 (m, $p_{B,down}$), 7.10 (m, $p_{A,up}$), 6.99 (m, $p_{B,up}$), 6.85 (m, $p_{A,down}$)
C_8H_{12} allyl	5.06 (bm, H*b*), 4.97 (bm, H*b'*), 3.91 (dt, $^3J_{HP}$ = 14.3, $^3J_{HH}$ = 7.5, H*a*)
C_8H_{12} Ir-CH	2.34 (bm)
C_8H_{12} CH$_2$	2.47, 2.17 (*d'*), 2.50, 2.26 (*d*), 2.23, 1.88 (*e'*), 2.10, 1.78 (*e*)
dppe CH$_2$	2.46, 1.94 (*f*), 2.07, 1.47 (*g*)
Ir-H	-11.66 (dd, $^2J_{HP}$ = 22.2, $^2J_{HP}$ = 14.9)
^{13}C (125 MHz)	
Ph (*ipso*)	137.1 (d, $^1J_{CP}$ = 30, $i_{A,down}$), 136.9 (d, $^1J_{CP}$ = 53, $i_{B,up}$), 135.4 (d, $^1J_{CP}$ = 38, $i_{A,up}$), 134.3 (d, $^1J_{CP}$ = 34, $i_{A,up}$)
Ph (*ortho*)	135.5 ($o_{A,up}$), 134.8 ($o_{B,down}$), 132.0 ($o_{B,up}$), 130.8 ($o_{A,down}$)
Ph (*meta*)	127.9 ($m_{B,up}$), 127.8 ($m_{A,down}$), 127.7 ($m_{A,up}$), 127.6 ($m_{B,down}$)
Ph (*para*)	129.9 ($p_{B,down}$), 129.8 ($p_{A,up}$), 128.9 ($p_{B,up}$), 128.2 ($p_{A,down}$)
C_8H_{12} allyl	91.0 (s) (*a*), 72.0 (s) (*b'*), 62.8 (s) (*b*)
C_8H_{12} CH$_2$	56.2 (*d'*), 54.9 (*d*), 29.1 (*e'*), 26.7 (*e*)
C_8H_{12} Ir-CH	32.7 (d, $^2J_{CP}$ = 30)
dppe CH$_2$	35.1 (*g*), 29.4 (*f*)
^{31}P (202 MHz)	
dppe P$_A$	29.1 (d, $^2J_{PP}$ = 2.8)
dppe P$_B$	43.9 (d, $^2J_{PP}$ = 2.8)

5.2.4 Synthesis of [Ir(H)(1-κ-4,5,6-η³-C$_8$H$_{10}$)(dppe)] (4$^{\text{dppe}}$ & 5$^{\text{dppe}}$)

1$^{\text{dppe}}$ (102 mg, 0.14 mmol) and KO*t*Bu (71 mg, 0.63mmol) were added to toluene (15mL) and the solution stirred at room temperature for 1 h, yielding a deep-orange solution. The solvent was then removed *in vacuo*. The orange solid was dissolved in toluene (5 mL) and the resulting mixture was passed through an alumina-lined pipette. The resulting solution was concentrated to dryness yielding an orange powder. Yield = 40 mg (0.06 mmol, 43%). ^{1}H NMR analysis of the product reveals that it contains a mixture of the isomers **4$^{\text{dppe}}$** and **5$^{\text{dppe}}$**. NMR data for **4$^{\text{dppe}}$** and **5$^{\text{dppe}}$** are presented in **Table 5-4** and

Table *5-5* respectively. Suitable crystals for x-ray diffraction were grown by dissolving the orange powder in toluene and layering with hexane.[152]

Table 5-4. NMR data for **4**^{dppe} in toluene-d_8 at 298 K.

¹H (500 MHz)	
Ph (*ortho*)	8.11 ($o_{\text{B,up}}$), 8.09 ($o_{\text{A,down}}$), 7.55 ($o_{\text{A,up}}$), 6.85 ($o_{\text{B,down}}$)
Ph (*meta*)	7.25 ($m_{\text{A,down}}$), 7.15 ($m_{\text{B,up}}$), 7.05 ($m_{\text{A,up}}$), 6.92 ($m_{\text{B,down}}$)
Ph (*para*)	7.21 ($p_{\text{A,down}}$), 7.12 ($p_{\text{B,up}}$), 7.02 ($p_{\text{A,up}}$), 6.85 ($p_{\text{B,down}}$)
C_8H_{10} C-H (olefin)	5.47 (dd, $^3J_{\text{HH}} = 6.4, 4.0$, H$a$), 5.94 (dd, $^3J_{\text{HH}} = 6.4, 4.0$; $J_{\text{HP}} = 4.0$, Hb)
C_8H_{10} C-H (allyl)	4.98 (dd, $^3J_{\text{HH}} = 7.0, 4.0$; $^4J_{\text{HP}} = 4.0$, Hc),
	3.79 (t, $^3J_{\text{HH}} = 7.1$; $^3J_{\text{HP}} = 7.0$, Hd), 5.02 (m, He)
C_8H_{10} CH$_2$	2.14 (up), 1.98 (down) (f), 2.41 (down), 1.96 (up) (g)
C_8H_{10} Ir-CH	2.59 (br)
dppe CH$_2$	2.48, 1.80 (j), 2.15, 1.26 (k)
Ir-H	-11.43 (dd, $^2J_{\text{HP}} = 21.8, 14.1$)
¹³C (125 MHz)	
Ph (*ortho*)	136.1 ($o_{\text{B,up}}$), 135.4 ($o_{\text{A,down}}$), 132.0 ($o_{\text{A,up}}$), 130.8 ($o_{\text{B,down}}$),
Ph (*meta*)	128.1 ($m_{\text{B,up}}$), 128.0 ($m_{\text{A,down}}$), 127.7 ($m_{\text{B,down}}$), 127.6 ($m_{\text{A,up}}$)
Ph (*para*)	130.3 ($p_{\text{A,down}}$), 130.0 ($p_{\text{B,up}}$), 128.9 ($p_{\text{A,up}}$), 128.3 ($p_{\text{A,down}}$)
C_8H_{10} C-H (olefin)	146.4 (a), 129.9 (b)
C_8H_{10} C-H (allyl)	93.1 (d), 72.4 (e), 62.5 (d, $^3J_{\text{CP}} = 50.2$) (c)
C_8H_{10} CH$_2$	54.3 (g), 22.9 (f)
C_8H_{10} Ir-C-H	35.5 (d, $^2J_{\text{CP}} = 70.1$)
dppe CH$_2$	35.1 (j), 28.9 (k)
³¹P (202 MHz)	
dppe P$_A$	30.6 (d, $^2J_{\text{PP}} = 2.4$)
dppe P$_B$	46.7 (d, $^2J_{\text{PP}} = 2.4$)

Table 5-5. NMR data for **5^{dppe}** in toluene-d_8 at 298 K.

^{1}**H** (500 MHz)	
Ph (*ortho*)	7.96 ($o_{A,up}$), 7.91 ($o_{B,up}$), 7.84 ($o_{B,down}$), 6.88 ($o_{A,down}$)
Ph (*meta*)	7.19 (m_B, down), 7.11 ($m_{A,up}$), 7.08 ($m_{B,up}$), 6.90 ($m_{A,down}$)
Ph (*para*)	7.12 ($p_{B,down}$), 7.07 ($p_{A,up}$), 7.01 ($p_{B,up}$), 6.86 ($p_{A,down}$)
C_8H_{10} C-H (olefin)	5.61 (dd, $^3J_{HH}$ = 7.1, 4.0, H*a*), 5.52 (dd, $^3J_{HH}$ = 8.2, 4.0, H*b*)
C_8H_{10} C-H (allyl)	4.31 (dd, $^3J_{HH}$ = 8.2, 4.0, H*c*), 3.83 (t, $^3J_{HH}$ = 8.2; $^3J_{HP}$ = 8.0, H*d*),
	5.11 (dd, $^3J_{HH}$ = 8.2, 4.0, H*e*)
C_8H_{10} CH$_2$	2.82, 2.12 (*f*); 2.43, 2.12 (*g*)
C_8H_{10} Ir-C-H	2.78 (br)
dppe CH$_2$	2.51, 1.89 (*j*); 1.89, 1.85 (*k*)
Ir-H	-11.57 (t, $^2J_{HP}$ = 19.5)
^{13}**C** (125 MHz)	
Ph (*ipso*)	135.1 ($i_{B,down}$), 135.0 ($i_{A,down}$), 133.0 ($i_{A,up}$), 130.9 ($i_{B,up}$)
Ph (*ortho*)	134.9 ($o_{A,up}$), 133.3 ($o_{B,up}$), 132.7($o_{B,down}$), 130.8 ($o_{A,down}$)
Ph (*meta*)	128.0 ($m_{B,up}$), 127.9 ($m_{A,up}$), 127.8 ($m_{A,down}$), 126.7 ($m_{B,down}$)
Ph (*para*)	129.8 ($p_{A,up}$), 129.4 ($p_{B,up}$), 129.3 ($p_{B,down}$), 128.4 ($p_{A,down}$)
C_8H_{10} C-H (olefin)	127.5 (*a*), 148.1 (*b*)
C_8H_{10} C-H (allyl)	94.1 (*d*), 73.3 (*c*), 62.9 (d, $^2J_{CP}$ = 50) (*e*)
C_8H_{10} CH$_2$	52.1 (*g*), 25.4 (*f*)
C_8H_{10} Ir-CH	34.5 (d, $^2J_{CP}$ = 70) (*h*)
dppe CH$_2$	33.8 (*k*), 30.6 (*j*)
^{31}**P** (202 MHz)	
dppe P$_A$	32.4 (d, $^2J_{PP}$ = 2.7)
dppe P$_B$	39.4 (d, $^2J_{PP}$ = 2.7)

5.2.5 Kinetic plots

Quantitative data to produce the necessary kinetic plots were obtained by integration of appropriate NMR spectra recorded using inverse gated decoupling methods. The kinetic analysis mapped the generation of 2^{dppe} from 1^{dppe}, followed by its equilibrated transformation into 3^{dppe} according to the general scheme below.

$$1^{dppe} \xrightarrow{\;k_1\;} 2^{dppe} \underset{k_{-2}}{\overset{k_2}{\rightleftharpoons}} 3^{dppe}$$

The boundary conditions:

Time zero: $[1^{dppe}] = [1^{dppe}]_0$; $[2^{dppe}]_0 = [3^{dppe}]_0 = 0$

Time infinity (equilibrium): $[1^{dppe}] = 0$; $[2^{dppe}] = [2^{dppe}]_{eq}$; $[3^{dppe}] = [3^{dppe}]_{eq}$; $[3^{dppe}]_{eq}/[3^{dppe}]_{eq} = k_2/k_{-2}$

Mass conversion: $[1^{dppe}] + [2^{dppe}] = [3^{dppe}] = [1^{dppe}]_0$

were used in fitting.

1. Time course data (integral):

Time/s	1^{dppe}	2^{dppe}	3^{dppe}
30	0.9124	0.0584	0.0292
2280	0.7752	0.1256	0.0992
4500	0.6207	0.1769	0.2024
6780	0.4919	0.1736	0.3345
9060	0.3648	0.1755	0.4597
11340	0.2814	0.1559	0.5627
13560	0.2147	0.1239	0.6614
15780	0.1586	0.1026	0.7389
18120	0.1186	0.0842	0.7972
20400	0.1045	0.0711	0.8245
26500	0.0701	0.0561	0.8738
29100	0.0313	0.0466	0.9221
32340	0.0168	0.0476	0.9356
35040	0.0036	0.0402	0.9562

2. Modelling decay of **1^{dppe}**:

The first-order decay $(-\frac{d[\mathbf{1}^{dppe}]}{dt} = k_1[\mathbf{1}^{dppe}])$ yields the well-known solution

1^{dppe} = **[1^{dppe}]**$_0$e^{-k1t} or $\ln\frac{[1^{dppe}]_0}{[1]} = k_1 t$

Analysis of the first-order decay of **1^{dppe}** yields k_1 = (6.09 ± 0.16) x 10^{-3} min^{-1} = (1.13 ± 0.03) x 10^{-4} s^{-1}.

3. Global fit:

The three rate constants k_1, k_2 and k_{-2} were obtained by numerical integration of the differential equations;

$$-\frac{d[1^{dppe}]}{dt} = k_1[1^{dppe}];$$

$$-d[1^{dppe}] = k_1[1^{dppe}]dt$$

$$\frac{d[2^{dppe}]}{dt} = k_1[1^{dppe}] - k_2[2^{dppe}] + k_{-2}[3^{dppe}];$$

$$d[2^{dppe}] = \left(k_1[1^{dppe}] - k_2[2^{dppe}] + k_{-2}[3^{dppe}]\right)dt$$

$$\frac{d[3^{dppe}]}{dt} = k_2[2^{dppe}] - k_{-2}[3^{dppe}];$$

$$d[3^{dppe}] = \left(k_2[2^{dppe}] - k_{-2}[3^{dppe}]\right)dt$$

To yield the concentration variations during each short time interval Δt, which was set to 1 s for the analysis, as follows:

$$[1^{dppe}]_{t+\Delta t} = [1^{dppe}]_t - k_1[1^{dppe}]_t \Delta t$$

$$[2^{dppe}]_{t+\Delta t} = [2^{dppe}]_t - (k_1[1^{dppe}]_t - k_2[2^{dppe}]_t + k_{-2}[3^{dppe}]_t)\Delta t$$

$$[3^{dppe}]_{t+\Delta t} = [3^{dppe}]_t - (k_2[2^{dppe}]_t - k_{-2}[3^{dppe}]_t)\Delta t$$

Since all elementary steps are first order processes, the analysis was more conveniently carried out on the molar fractions:

$$x_1 = \frac{[1^{dppe}]}{([1^{dppe}] + [2^{dppe}] + [3^{dppe}])};$$

$$x_2 = \frac{[2^{dppe}]}{([1^{dppe}] + [2^{dppe}] + [3^{dppe}])};$$

$$x_3 = \frac{[3^{dppe}]}{([1^{dppe}] + [2^{dppe}] + [3^{dppe}])}$$

$$x_{1,t + \Delta t} = x_{1,t} - k_1 x_{1,t} \Delta t$$

$$x_{2,t + \Delta t} = x_{2,t} + (k_1 x_{1,t} - k_2 x_{2,t} + k_{-2} x_{3,t}) \Delta t$$

$$x_{3,t + \Delta t} = x_{3,t} + (k_2 x_{2,t} - k_{-2} x_{3,t}) \Delta t$$

By imposing the initial condition at time zero ($x_{1,0} = 1$; $x_{2,0} = 0$; $x_{3,0} = 0$), the calculated **1^{dppe}**, **2^{dppe}**, and **3^{dppe}** fractions at the times t_i of the experimental observations ($x_{1,i,calc}, x_{2,i,calc}, x_{3,i,calc}$) were derived by numerical integration on the basis of initial guess values of the rate constants k_1, k_2 and k_{-2}, which were treated as adjustable parameters during the fit. A non-linear least-squares fit was then performed to minimize the function.

$$SUM = \sum \left[(x_{1,i} - x_{1,i})^2 + (x_{2,i} - x_{2,i})^2 + (x_{3,i} - x_{3,i})^2 \right]$$

By using the Solver tool of Excel. The resulting fits of the time evolutions could be plotted. The standard deviations on the optimized parameters were obtained with the Excel Macro Solver Aid.

5.2.6 Computational results

The computational work undertaken for this study was carried out using the Gaussian09 suite of programs.[200] Geometry optimizations were carried out without any symmetry constraints using the B3LYP functional [201–203] combined with Grimme's D3 correction to account for dispersion effects.[204] Optimizations were performed in toluene (ε = 2.3741) using the SMD continuum model[205] with basis set 1 (BS1). BS1 includes the 6-31G(d,p) basis set for the main-group atoms,[206,207] and the scalar relativistic Stuttgart-Dresden SDD effective core potential (ECP) and its associated double-ζ basis set,[208] complemented with a set of f polarization functions,[209] for Ir. Frequency calculations were performed for all the optimized geometries to characterise the stationary points as either minima or transition states. Connections between the transition states and the corresponding minima were checked by displacing in both directions, following the transition vector, the geometry of the transition states, and subsequent geometry optimization until a minimum was reached. Energies in toluene were refined by means of single-point calculations at the optimised BS1 geometries using an extended basis set (BS2). BS2 consists of the def2-TZVP basis set for the main-group atoms, and the quadruple-ζ def2-QZVP basis set for Ir, together with the def2 ECP (60 core electrons: [Kr] + 4d + 4f).[210] Gibbs energies in toluene were calculated by adding to the BS2 energies in toluene

the thermal and entropic corrections obtained with BS1. An additional correction of 1.9 kcal mol^{-1} was applied to all Gibbs energies to change the standard state from the gas phase (1 atm) to the condensed phase (1 M) at 298.15K ($\Delta G^{1atm \rightarrow 1\ M}$).[211] In this way, all the energy values given in the article are Gibbs energies in toluene solution calculated using the formula:

G = E(BS2) + G(BS1) − E(BS1) + $\Delta G^{1\ atm \rightarrow 1\ M}$

5.3 Experimental for Chapter Three

5.3.1 Synthesis of [IrCl(COD)(dppf)] (1^{dppf})

A solution of [IrCl(COD)]$_2$ (240 mg, 0.36 mmol) and dppf (400 mg, 0.72 mmol), was made with dichloromethane (15 mL) and stirred for 1 hr. The solvent was then removed *in vacuo* resulting in a yellow solid. The solid was subsequently dissolved in toluene (20 mL), and the solution filtered through a pipette lined with cotton wool, and a third of the depth of Al$_2$O$_3$. The resultant pale-yellow solution was concentrated *in vacuo*, resulting in a fine yellow powder (500 mg, 0.56 mmol). Yield = 78 %. Yellow crystals were grown by layering a concentrated solution of **1^{dppf}** in toluene with hexane, after 48 hrs yellow crystals were collected.[149] CHN analysis of **1^{dppf}**. Calcd for C$_{42}$H$_{40}$P$_2$FeIr: C, 58.38; H, 4.63. Found: C, 59.21; H, 4.62. NMR data for **1^{dppf}** are presented in **Table 5-6**.

Table 5-6. NMR data for **1^{dppf}** in toluene-d_8 at 253 K.

^{1}H (500 MHz)	
Ph	8.18 – 8.06 (m), 7.15 – 7.07
COD CH	3.53 (s), 3.31 (s)
COD CH$_2$	2.56 (dd, $^2J_{HH}$ = 7.8 $^3J_{HH}$ = 6.6), 1.75 ($^2J_{HH}$ = 7.8, $^3J_{HH}$ = 6.2)
dppf Cp	4.03 (s, *o'*), 3.61 (s, *m'*)
^{13}C (125 MHz)	
Ph	137.3 (*o*), 133.32 (*m*), 127.3 (*p*)
COD CH	69.9 (t, $^3J_{CP}$ = 8.5), 69.2 (s)
COD CH$_2$	32.8 (s)
dppf Cp	74.6 (s, *meta*), 71.9 (d, $^3J_{CP}$ = 5.0, *ortho*), 76.3 (d, $^2J_{CP}$ = 6.3 Hz)
^{31}P (202 MHz)	
dppf	0.83 (s)

5.3.2 Synthesis of [IrCl(COD)((S)-BINAP)] (1$^{S\text{-BINAP}}$)

A solution of [IrCl(COD)]$_2$ (240 mg, 0.36 mmol) and (*S*)-BINAP (286 mg, 0.72 mmol), was made with dichloromethane (15 mL) and stirred for 1 hr. The solvent was then removed *in vacuo* resulting in an orange solid. The solid was washed twice with pentane (10 mL) the solid was recovered by the removal of pentane by concentration *in vacuo*. (480 mg, 0.50 mmol). Yield = 67 %. The NMR characterization of **1$^{S\text{-BINAP}}$** is presented in **Table 3-6** in **Chapter 3:**.

5.3.3 General NMR-scale synthesis of anionic tetrahydrides

6^{L_2} (L$_2$ = dppf, (*S*)-BINAP) (0.01 mmol), and KO^{t}Bu (7 mg, 0.06 mmol), were added to a solution of isopropanol (0.01 mL) and toluene-d_8 (0.6 mL). The solution was heated to 353 K and NMR spectra were recorded. The formation of K[Ir(H)$_4$(L$_2$)] is complete within 30 minutes of heating the mixture. Since this was done at an NMR scale level all data presented in **Chapter 3**:.

5.3.4 General procedure for Asymmetric Hydrogenation

Solutions of [IrCl(COD)(L$_2$)] (6.4 x 10^{-3} mmol) (L$_2$ = dppe, dppf, (*S*)-BINAP), KO^{t}Bu (3.2 x 10^{-2} mmol; 5 equiv), acetophenone (381 mg, 3.2 mmol) and 18-crown-6 (15 mg, 5.68 x 10^{-2} mmol) (where appropriate), in 2 mL of ^{i}PrOH were transferred to a glass vial with a stirrer bar. The glass vials were then placed into a stainless-steel autoclave.

The reaction vessel was pressurized to the required H$_2$ (20 bar) pressure and stirred for 2 hrs at 298 K. After 2 hrs the reaction was stopped by release of the H$_2$ pressure. The resultant solution was filtered on silica with dichloromethane into a vial with an external standard of *n*-decane (150 mg, 1.05 mmol). This solution was analysed by chiral GC.

5.3.5 Computational results

The solvent was described by means of a cluster-continuum approach, also referred as hybrid implicit-explicit solvation scheme. In addition to the SMD polarizable continuum model for methanol (ε = 35.688),[212] n explicit methanol molecules (n = 5) were introduced to describe the solvation sphere of the cation. The effect of the solvent was included both during geometry optimizations and single point calculations. Optimizations were performed using basis set BS1, which includes the 6-31G(d,p) basis set for the main-group atoms, [206,207] and the scalar relativistic Stuttgard-Dresden (SDD) effective core potential (ECP) and its associated double-ξ basis set,[208] complemented with a set of f polarization functions[209] for the Fe and Ir atoms.

Frequency calculations were carried out for all the optimized geometries to characterize the stationary points as either minima or transition states. Connections between the transition states and the corresponding minima were checked by displacing in both directions, following the transition vector, the geometry of the transition states, and subsequent geometry optimization until a minimum was reached.

Energies in methanol were refined by means of single-point calculations at the optimized BS1 geometries using the same functional (M06), adding Grimme's D3 correction to account for long-range dispersion effects,[204] and an extended basis set (BS2). BS2 consists in the def2-TZVP basis set for the main group atoms, and the quadruple-ζ def2-QZVP basis set for transition metals, together with the Def2 ECP for Ir.[210,213] Gibbs energies in methanol were calculated adding to the BS2 energies in methanol the thermal and entropic corrections obtained with BS1. An additional correction of 1.9 Kcal mol^{-1} was applied to all Gibbs energies to change the standard state from the gas phase (1 atm) to the condensed phase (1 M) at 298.15K ($\Delta G^{1atm \rightarrow 1M}$).[211] In this way, all the energy values given in the article are Gibbs energies in methanol calculated using the formula:
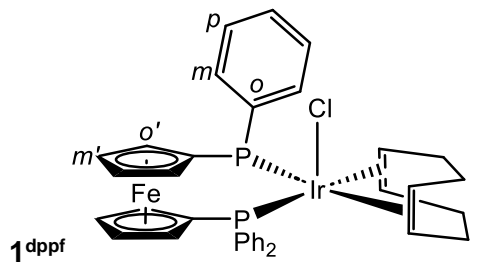
$$G = E(BS2) + G(BS1) - E(BS1) + \Delta G^{1atm \rightarrow 1M}$$

5.4   Experimental for Chapter Four

5.4.1   Synthesis of 2-(diphenylthiophosphino)-dimethylaminomethylferrocene (*R/S*) - 2^{Fe}

(Dimethylaminomethyl)ferrocene (7 g, 28.8 mmol) was dissolved, and stirred in a solution of diethyl ether (120 mL) resulting in a dark brown solution. The solution was then cooled to -78 ^{o}C, and ^{n}BuLi (2 equiv.) in hexanes (2.5 M) added dropwise whilst the solution was stirring. The solution was then warmed to room temperature and stirred for 3 hours. PPh$_2$Cl (5 equiv., 30 mL, 160 mmol) (isolated by prior condensation) was then added dropwise to the cooled, -78 °C solution. Once the addition was complete, the solution was stirred for 15 minutes before warming to room temperature and stirring for a further 12 hours. A dichloromethane (60 mL) solution of S$_8$ (5g, 0.16 mol), was added, and the resulting mixture stirred for a further 12 hrs. At this point the dichloromethane was partially removed *in vacuo*, and the remaining solution washed with 2M NaOH (100 mL). The organic layer was isolated and passed through a through a silica column using a 1:1 mixture of diethyl ether: dichloromethane. To yield 9.78 g (21.3 mmol) of 2^{Fe} as an orange solid. Yield 74 %.

^{1}H NMR (400 MHz, CDCl$_3$) *δ* (ppm) 7.86 (ddd, $^3J_{HP}$ = 14.7, $^3J_{HH}$ = 5.7, $^4J_{HH}$ = 2.4, 2H, *ortho*-PPh$_2$); 7.72 (ddd, $^3J_{HP}$ = 14.7, $^3J_{HH}$ = 5.7, $^4J_{HH}$ = 2.4, 2H, *ortho*-PPh$_2$); 7.54 – 7.43 (m, 4H, *meta*-PPh$_2$); 7.40 – 7.36 (m, 2H, *para*-PPh$_2$); 4.64 (bm, 1H, subst.-Cp); 4.32 (s, 5H, Cp); 4.31 (m, 1H, subst.-Cp); 3.88 (dd, $^3J_{HP}$ = 6.1, $^3J_{HH}$ = 2.1, 1H, subst.-Cp); 3.84 (d, $^2J_{HH}$ = 11.5, 1H, CH$_2$); 3.26 (d, $^2J_{HH}$ = 11.5, 1H, CH$_2$); 1.97 (s, 6H, N(CH$_3$)$_2$). **^{31}P{^{1}H} NMR** (162 Hz, CDCl$_3$) *δ* (ppm) 41.93.[139]

5.4.2   Synthesis of (2-diphenylthiophsphinoferrocenyl)-trimethylammonium iodide – 3^{Fe}

2^{Fe} (5 g, 10.8 mmol) was stirred in 100 mL of diethyl ether at room temperature and 10 mL of CH$_3$I (161 mmol) added dropwise to the solution. The solution was stirred overnight and the next morning the solvent was removed *via* rotary evaporation to yield 6.19 g (10.3 mmol) of 3^{Fe} as bright yellow crystals. Yield 95%.

¹H NMR (400 MHz, CDCl$_3$) δ (ppm) 7.89 (ddd, $^3J_{HP}$ = 13.7, $^3J_{HH}$ = 7.0, 1.7, 2H, *ortho*-PPh$_2$); 7.77 (ddd, $^3J_{HP}$ = 13.7, $^3J_{HH}$ = 7.0, 1.7, 2H, *ortho*-PPh$_2$); 7.56 (m, 2H, *meta*-PPh$_2$); 7.52 (m, 2H, *meta*-PPh$_2$); 7.47 (m, 1H, *para*-PPh$_2$); 7.42 (m, 1H, *para*-PPh$_2$); 5.95 (d, $^2J_{HH}$ = 13.2, Cp-CH$_2$); 5.53 (d, $^2J_{HH}$ = 13.2, Cp-CH$_2$); 5.39 (m, 1H, subst-Cp); 4.69 (m, 1H, subst-Cp); 4.39 (s, 5H, Cp); 4.20 (s, 1H, subst.-Cp); 3.07 (s, 9H, N-(CH$_3$)$_3$). **¹³C NMR** (101 Hz, CDI$_3$) δ (ppm) 134.2 (s, *para*); 132.0 (d, $^3J_{CP}$ = 11.0, *meta*); 131.9 (d, $^1J_{CP}$ = 30.9, *ipso*); 131.6 (d, $^3J_{CP}$ = 10.9, *meta*); 131.2 (d, $^1J_{CP}$ = 30.9, *ipso*); 130.2 (s, *para*) 128.9 (d, $^2J_{CP}$ = 12.3, *ortho*); 128.3 (d, $^2J_{CP}$ = 12.3, *ortho*); 79.0 (d, $^3J_{CP}$ = 8.1, subst.-Cp); 76.5 (d, $^2J_{CP}$ = 11.4, subst.-Cp); 72.8 (d, $^2J_{CP}$ = 10.2, subst.-Cp); 64.0 (s, Cp); 52.7 (s, N-(CH$_3$)$_3$). **³¹P{¹H} NMR** (162 Hz, CDCl$_3$) δ (ppm) 40.18.[139]

5.4.3 Synthesis of *N*-(2-diphenylthiophosphinoferrocenylmethyl) ephedrine – (*S*)-4^{Fe} and (*R*)-4^{Fe}

(1*R*,2*S*)-(−)-Ephedrine (5 g, 30 mmol) was dried in a round bottom flask, 75 mL of dry toluene was subsequently added, the solution was stirred for 5 minutes before the 5 g (8.3 mmol) of 3^{Fe} was added. The solution was then set to reflux for 12 hrs. At this point the solution was concentrated *in vacuo* and the resultant solid was dissolved in dichloromethane. Products were isolated by flash chromatography on silica gel using a 1:1 mixture of pentane/diethyl ether. Each fraction of (*S*)-4^{Fe} and (*R*)-4^{Fe} yielded an orange solid (~2 g; 3.45 mmol). The presence of each diastereomer was confirmed by NMR spectroscopy. Yield 41.6 %.

¹H NMR (400 MHz, CDCl$_3$) δ (ppm) 7.84 (m, 2H, *ortho*-PPh$_2$); 7.73 (m, 2H, *ortho*-PPh$_2$); 7.54 – 7.46 (m, 5H, Ar); 7.45 – 7.40 (m, 2H, Ar); 7.21 – 7.17 (bm, 4H, Ar); 4.57 (bm, 1H, CH$_2$); 4.52 (m, 1H, subst.-Cp); 4.33 (s, 5H, Cp); 4.31 (m, 1H, subst.-Cp); 4.29 (m, 1H, CH$_2$); 3.73 (m, 1H, subst.-Cp); 3.31 (m, 1H, H); 3.13 (bm, 1H; OH); 2.56 (m, 1H, H); 1.93 (s, 3H, N-CH$_3$); 0.83 (s, 3H, CH$_3$). **³¹P{¹H} NMR** (162 Hz, CDCl$_3$) δ (ppm) 41.72.[139]

5.4.4 Synthesis of (*S*)-(2-diphenylthiophsophinoferrocenyl)(acetoxy)-methane – (*S*)-5^Fe

1.5 g (3.45 mmol) of **(*S*)-4^Fe** was dissolved in 100 mL of acetic anhydride (1.06 mmol) under argon. The solution was stirred for 16 h at 120 °C. After cooling to room temperature, and *in vacuo* removal of the solvent, the crude products were filtered over silica gel with a 1:1 mixture of pentane/diethyl ether to yield 1.17g (2.47 mmol) of **(*S*)-5^Fe** as an orange solid. Yield 72 %.

¹H NMR (400 MHz, CDCl₃) δ (ppm) 7.82 (dd, $^3J_{HP}$ = 13.5, $^3J_{HH}$ = 6.9, 2H, *ortho* – PPh₂); 7.64 (dd, $^3J_{HP}$ = 13.5, $^3J_{HH}$ = 6.9, 2H, *ortho* – PPh₂); 7.48 (bm, 4H, *meta* – PPh₂); 7.39 (m, 2H, *para* – PPh₂); 5.55 (d, $^2J_{HH}$ = 11.6, 1H, CH₂-Cp); 5.05 (d, $^2J_{HH}$ = 11.6, 1H, CH₂-Cp); 4.63 (m, 1H, subst.-Cp); 4.41 (m, 1H, subst.-Cp); 4.38 (s, 5H, Cp); 3.84 (m, 1H, subst.-Cp); 1.56 (s, 3H, OC-CH₃). **¹³C NMR** (101 Hz, CDl₃) δ (ppm) 170.5 (s, C=O); 134.8 (d, $^1J_{CP}$ = 84.2, *ipso* – PPh₂); 133.4 (d, $^1J_{CP}$ = 84.2, *ipso* – PPh₂); 132.1 (d, $^2J_{CP}$ = 11.0, *ortho* – PPh₂); 132.1 (d, $^2J_{CP}$ = 11.0, *ortho* – PPh₂); 131.4 (d, $^4J_{CP}$ = 2.7, *para* – PPh₂); 131.1 (d, $^4J_{CP}$ = 2.7, *para* – PPh₂); 128.1 (d, $^3J_{CP}$ = 3.2, *meta* – PPh₂); 128.0 (d, $^3J_{CP}$ = 3.2, *meta* – PPh₂); 85.2 (d, $^2J_{CP}$ = 11.8, subst.-Cp); 75.8 (d, $^1J_{CP}$ = 80.0, P-Cp); 75.6 (d, $^2J_{CP}$ = 12.2, *ipso*–*C*p); 75.1 (d, $^3J_{CP}$ = 8.7, subst.-Cp); 70.7 (s, Cp); 69.6 (d, $^3J_{CP}$ = 9.8, subst.-Cp); 61.3 (s, CH₂); 20.7 (s, CH₃). **³¹P{¹H} NMR** (162 Hz, CDCl₃) δ (ppm) 41.26.[139]

5.4.5 Synthesis of (*S*)-2-diphenylthiophosphinoferrocenyl)methanol – (*S*)-6^Fe

A solution of 1 g (2.11 mmol) of **(*S*)-5^Fe** in 150 mL of methanol was slowly poured into a 75 mL NaOH solution in water (2 M). The reaction mixture was vigorously stirred overnight. After evaporation of methanol, the reaction mixture was extracted with dichloromethane, washed with brine, and dried on sodium sulphate. The crude product was then purified by flash chromatography on silica gel by using a 1:1 pentane/diethyl ether mixture to yield 0.8 g (1.85 mmol) of **(*S*)-6^Fe** as a brown-yellow solid. Yield 88%.

¹H NMR (400 MHz, CDCl₃) δ (ppm) 7.86 (dd, $^3J_{HP}$ = 13.9, $^3J_{HH}$ = 6.9, 2H, *ortho*-PPh₂); 7.62 – 7.44 (bm, 6H, PPh₂); 7.43 – 7.27 (bm, 2H, PPh₂); 4.71 (dd, $^2J_{HH}$ = 14.4, $^4J_{HH}$ = 6.7, 1H, CH₂); 4.61 (s, 1H, subst.-Cp); 4.33 (s, 5H, Cp); 4.33 – 4.30 (overlapped peaks, 2H, CH₂ & subst.-Cp); 3.80 (s, 1H, subst.-Cp); 1.42 (br, 1H, OH). **¹³C NMR** (101 Hz, CDl₃) δ (ppm) 135.0 (d, $^1J_{CP}$ = 85.7, *ipso*-PPh₂); 132.8 (d, $^1J_{CP}$ = 85.7, *ipso*-PPh₂); 132.2 (d, $^4J_{CP}$ = 10.7, *meta*-PPh₂); 131.6 (d, $^4J_{CP}$ = 11.0, *meta*-PPh₂); 131.6 (d, $^5J_{CP}$ = 3.3, *para*-PPh₂); 131.4 (d, $^5J_{CP}$ = 2.7, *para*-PPh₂); 128.6 (d, $^3J_{CP}$ = 12.5, *ortho*-PPh₂); 128.1 (d, $^3J_{CP}$ = 12.5, *ortho*-PPh₂); 93.5 (d, $^2J_{CP}$ = 11.9, *ipso*-subst.-Cp); 74.9 (d, $^4J_{CP}$ = 9.4, subst.-Cp); 74.5 (d, $^3J_{CP}$ = 12.4, subst.-Cp); 73.9 (d, $^1J_{CP}$ = 89.2, *ipso*-Cp); 70.5 (s, Cp); 69.0 (d, $^4J_{CP}$ = 10.3, subst.-Cp); 58.4 (s, CH₂). **³¹P{¹H} NMR** (162 Hz, CDCl₃) δ (ppm) 41.72.[140]

5.4.6 General procedure for the synthesis of ferrocenyl phosphino thioethers – (*S*)-7^Fe

The preparations of (*S*)-7^Fe followed a similar procedure outlined below:

100 mg (0.26 mmol) of (*S*)-6^Fe was dissolved in 2 mL of dry dichloromethane. 100 µL of fluoroboric acid (54 % in ether) was then added. After 1 minute of stirring, 6.4 mmol of the specified thiol was added. After a further 1 minute of stirring, the crude material was filtered on silica gel with ether as the eluent. After evaporation of the solvent, an oil was obtained, which was extracted into pentane to yield a solid product after evaporation.

Bright yellow solid. Mass = 130mg, yield 90%.

¹H NMR (400 MHz, CDCl₃) δ (ppm) 7.85 (ddd, $^3J_{HP}$ = 14.7, $^3J_{HH}$ = 7.1, $^4J_{HH}$ = 2.1, 2H, *ortho*-PPh₂); 7.69 (ddd, $^3J_{HP}$ = 14.7, $^3J_{HH}$ = 7.1, $^4J_{HH}$ = 2.1, 2H, *ortho*-PPh₂); 7.51 (m, 2H, *meta*-PPh₂); 7.48 (m, 2H, *ortho*-SPh); 7.42 (m, 2H, *meta* – PPh₂); 7.27 (m, 1H, *para* – PPh₂); 7.24 (m, 2H, *meta* – PPh₂); 7.21 (m, 1H, *para* – PPh₂); 7.17 (m, 1H, SPh); 4.53 (m, 1H, subst.-Cp); 4.43 (m, 1H, S-CH₂); 4.40 (m, 1H, S-CH₂); 4.35 (s, 5H, Cp); 4.29 (m, 1H, subst.-Cp); 3.81 (m, 1H, subst.-Cp). **¹³C NMR** (101 Hz, CDl₃) δ (ppm) 137.8 (s, *ipso*-S-Ph); 134.9 (d, $^1J_{CP}$ = 85.2, *ipso*-PPh₂); 132.2 (d, $^3J_{CP}$ = 11.1, *ortho*-PPh₂); 131.8 (d, $^4J_{CP}$ = 1.6, *meta*-PPh₂); 129.7 (s, *ortho*-S-Ph); 129.5 (s, *para*-PPh₂); 128.2 (s, *meta*-S-Ph); 125.9 (s, *para*-PPh₂); 88.9 (d, $^2J_{CP}$ = 11.8, subst.-Cp); 77.6* (P-Cp); 74.5 (d, $^2J_{CP}$ = 12.6); 73.6 (d, $^3J_{CP}$ = 9.2, subst.-Cp); 70.9 (s, Cp); 69.1 (d, $^3J_{CP}$ = 10.5, subst.-Cp); 33.2 (s, CH₂). **³¹P{¹H} NMR** (162 Hz, CDCl₃) δ (ppm) 41.5.[140]

Orange solid. Mass = 98 mg. Yield 68%.

¹H NMR (400 MHz, CDCl₃) *δ* (ppm) 7.83 (ddd, $^3J_{HP}$ = 13.9, $^3J_{HH}$ = 6.6, $^4J_{HH}$ = 1.6, 2H, *ortho*-PPh₂); 7.68 (ddd, $^3J_{HP}$ = 13.9, $^3J_{HH}$ = 6.6, $^4J_{HH}$ = 1.6, 2H, *ortho*-PPh₂); 7.55 – 7.45 (m, 4H, *meta*-PPh₂); 7.43 – 7.37 (m, 2H, *para*-PPh₂); 4.62 (dd, $^3J_{HP}$ = 5.6, $^3J_{HH}$ = 2.3, 1H, subst.-Cp); 4.35 (s, 5H, Cp); 4.31 (dt, $^4J_{HP}$ = 3.6, $^3J_{HH}$ = 1.5, 1H, subst.-Cp); 4.04 (d, $^2J_{HH}$ = 13.2, 1H, CH₂); 3.93 (d, $^2J_{HH}$ = 13.2, 1H, CH₂); 3.77 (dt, $^4J_{HP}$ = 3.6, $^3J_{HH}$ = 1.5); 2.49 (s, $^3J_{HH}$ = 4.3, 1H, S-CH); 1.86 – 1.61 (m, 6H, S-Cy); 1.47 – 1.31 (m, 4H, S-Cy). **³¹P{¹H} NMR** (162 Hz, CDCl₃) *δ* (ppm) 41.66

5.4.7 Deprotection of (*S*)-7^{Fe}

The preparations of **P,S^R** followed a similar procedure outlined below:

80 mg of the specified **(*S*)-7^{Fe}** was dissolved in 5 mL of toluene with 0.16 mL of tris-(dimethylamino)phosphine (5 equiv).The solution was kept at reflux overnight. The solution was then allowed to cool to room temperature, after which the solution was removed *in vacuo*. The crude material was purified under argon by flash chromatography on silica gel using dichloromethane as the eluent. The solution was concentrated to dryness *in vacuo*, and redissolved in pentane, to yield a solid precipitate. Yield 80 – 89 %.

Pale yellow solid. Yield 80 %.

¹H NMR (400 MHz, CDCl₃) *δ* (ppm) 7.6 – 7.5 (m, 2H, PPh₂); 7.42 – 7.34 (m, 3H, PPh₂); 7.28 – 7.15 (m, 10H, PPh₂); 4.35 (s, 1H, subst.-Cp); 4.29 (s, 1H, subst.-Cp); 4.15 (d, $^2J_{HH}$ = 11.9, 1H, S-CH₂); 4.10 (d, $^2J_{HH}$ = 11.9, 1H, S-CH₂); 4.05 (s, 5H, Cp); 3.83 (s, 1H, subst.-Cp). **¹³C NMR** (101 Hz, CDl₃) *δ* (ppm) 139.5 (d, $^3J_{CP}$ = 8.0, *ortho*-PPh₂); 137.4 (d, $^3J_{CP}$ = 8.0, *ortho*-PPh₂); 137.2 (s, *ipso*-SPh); 135.1 (d, $^1J_{CP}$ = 21.3, *ipso*-PPh₂); 132.5 (d, $^1J_{CP}$ = 18.0, *ipso*-PPh₂); 129.7 (s, *para*-PPh₂); 129.2 (s, *para*-PPh₂); 128.7 (s, *ortho*-SPh); 128.2 (d, $^3J_{CP}$ = 7.7, *meta*-PPh₂); 128.0 (d, $^4J_{CP}$ = 6.1, *meta*-PPh₂); 127.8 (s, *meta*-SPh); 126.0 (s, *para*-SPh); 89.9 (d, $^1J_{CP}$ = 25.4, Cp-P); 71.8 (d, $^3J_{CP}$ = 3.2, subst.-Cp); 71.5 (d, $^2J_{CP}$ = 2.8, subst.-Cp); 70.9 (s, subst.-Cp); 69.8 (s, Cp); 69.6 (s, subst.-Cp); 33.8 (s, CH₂). **³¹P{¹H} NMR** (162 Hz, CDCl₃) *δ* (ppm) -23.81.[140]

Deep orange solid. Yield 89%.

^{1}H NMR (400 MHz, CDCl$_3$) *δ* (ppm) 7.61 (bm, 2H, *ortho* – PPh$_2$); 7.59 (bm, 2H, *ortho* – PPh$_2$); 7.56 (bm, 2H, *meta* – PPh$_2$); 7.41 (m, 2H, *meta* – PPh$_2$); 7.24 (bm, 1H, *para* – PPh$_2$); 7.18 (bm, 1H, *para* – PPh$_2$); 4.53 (bs, 1H, subst.-Cp); 4.31 (bs, 1H, subst.-Cp); 4.02 (s, 5H, Cp); 3.79 (d, 1H, $^1J_{HH}$ = 14.3, S-CH$_2$); 3.69 (d, 1H, $^1J_{HH}$ = 14.3, S-CH$_2$); 2.47 (m, 1H, S-CH); 1.79 – 1.18 (m, 10H, S–Cy). **^{13}C NMR** (101 Hz, CDl$_3$) *δ* (ppm) 140.1 (d, $^2J_{CP}$ = 15.6, *ortho* – PPh$_2$); 135.2 (d, $^1J_{CP}$ = 25.1, *ipso* – PPh$_2$); 132.4 (d, $^1J_{CP}$ = 17.8, *ipso* – PPh$_2$); 129.4 (s, *para* – PPh$_2$); 128.1 (d, $^3J_{CP}$ = 8.1, *meta* – PPh$_2$); 127.9 (d, $^3J_{CP}$ = 6.1, *meta* – PPh$_2$); 127.8 (s, *para* – PPh$_2$); 91.9 (d, $^1J_{CP}$ = 31.6, Cp-PPh$_2$); 77.3* (d, subst.-Cp); 71.5 (d, $^2J_{CP}$ = 3.9, subst.-Cp); 71.3 (d, $^2J_{CP}$ = 4.2, subst.-Cp); 69.8 (s, Cp); 69.5 (s, subst.-Cp); 43.7 (s, S-C); 33.6 (s, Cy); 33.3 (s, Cy); 28.9 (s, Cy); 26.0 (s, Cy); 25.7 (s, Cy). **^{31}P{^{1}H} NMR** (162 Hz, CDCl$_3$) *δ* (ppm) -24.06.

5.4.8 Synthesis of [IrCl(P,S^R)(COD)] (1^{P,SR})

[IrCl(COD)]$_2$ (80 mg, 0.12 mmol) was added to the specified thioether ligand **(S)-P,S^R** (2 equiv.), dry dichloromethane (10 mL) was then added to the flask *via* cannula and set to stir at room temperature for 1 hr. At this point solution was concentrated to dryness *in vacuo*, and the solid product washed with pentane (2 x 10 mL) to yield a solid powder. Yield = 75 – 88 %. The NMR data for **1^{P,SCy}** and **1^{P,SPh}** are given in **Table 4-1** and **Table 5-7** respectively.

Table 5-7. NMR data of **1**[P,SPh] in dichloromethane-d_2 at 298 K.

Group	Chemical Shift ($δ$)
^{1}H, P-Ph	7.86 – 7.19*
S-Ph	7.86 – 7.19*
C_8H_{12} CH	3.69 (*a*); 3.79 (*b*); 3.85 (*e*); (*f*) 4.08
C_8H_{12} CH$_2$	2.17, 1.34 (*c*); 2.30, 1.70 (*d*); 2.58, 2.36 (*g*); 2.10,1.68 (*h*)
S – CH$_2$	4.54*, 3.81 (*j*)
Cp	4.55* (*k*); 4.21 (*l*); 4.73 (*n*); 4.55 (*q*)
^{13}C, P-Ph	134.2 – 127.9*
S-Ph	134.2 – 127.9*
C_8H_{12} CH	71.6* (*a*); 75.2 (*b*); 74.8 (*e*); (*f*) 71.2*
C_8H_{12} CH$_2$	32.3 (*c*); 31.9 (*d*); 33.7 (*g*); 28.7 (*h*)
S – CH$_2$	38.2 (d, $^3J_{CP}$ = 3.2, *j*)
Cp	73.3(d, $^3J_{CP}$ = 3.4, *k*); 70.3(*l*); 75.6 (*n*); 71.0 (*q*)
^{31}P, P,S^{Ph}	5.4

*Spectral assignment of each atom could not be deciphered due to overlap

5.4.9 General procedure for Asymmetric hydrogenation

Solutions of [IrCl(COD)(P,S^R)] (3.2 x 10^{-3} mmol) (R = Bz, Cy ^{i}Pr, Ph), KO^{t}Bu (1.6 x 10^{-2} mmol; 5 equiv), 0.37 mL of acetophenone (381 mg, 3.2 mmol) and 18-crown-6 (15 mg, 5.68 x 10^{-2} mmol) (where appropriate), in 2 mL of ^{i}PrOH were transferred to a glass vial with a stirrer bar. The glass vials were then placed into a stainless-steel autoclave.

The reaction vessel was pressurized to the required H$_2$ (30 bar) pressure and stirred for 4 hrs at 276 K. After 4 hrs the reaction was stopped by release of the H$_2$ pressure. The resultant solution was filtered on silica with dichloromethane into a vial with an external standard of *n*-decane (150 mg, 1.05 mmol). This solution was analysed by chiral GC.

5.4.10 Computational results

DFT calculations with the M06 functional[214] were carried out with the Gaussian 16 suite of programs[215] to analyse how the alkali cation influences the activity and enantioselectivity of the ketone hydrogenation in alcohol solvent. The actual $[Ir(H)_4(P,S^{Ph})]^-$, with no simplifications, was the catalyst used in the calculations, while acetone was modelled as the experimental substrate (acetophenone) to be hydrogenated and methanol modelled the experimental isopropanol solvent. As discussed in **Chapter 4**:, a proper description of the solvent is crucial to reproduce the experimental trends. There is increasing evidence that modelling catalytic processes in protic solvents, as alcohols, demands the inclusion of explicit solvent molecules to account for specific interactions.[216] For this reason, the solvent was described by means of a cluster-continuum approach, also referred as hybrid implicit-explicit solvation scheme. In addition to the SMD polarizable continuum model for methanol (ε = 35.688),[212] n explicit methanol molecules (n = 5) were introduced to describe the solvation sphere of the cation. The effect of the solvent was included both during geometry optimizations and single point calculations. Optimizations were performed using basis set BS1, which includes the 6-31G(d,p) basis set for the main-group atoms, [206,207] and the scalar relativistic Stuttgard-Dresden (SDD) effective core potential (ECP) and its associated double-ξ basis set,[208] complemented with a set of f polarization functions[209] for the Fe and Ir atoms. Frequency calculations were carried out for all the optimized geometries to characterize the stationary points as either minima or transition states. Connections between the transition states and the corresponding minima were checked by displacing in both directions, following the transition vector, the geometry of the transition states, and subsequent geometry optimization until a minimum was reached.

Energies in methanol were refined by means of single-point calculations at the optimized BS1 geometries using the same functional (M06), adding Grimme's D3 correction to account for long-range dispersion effects,[204] and an extended basis set (BS2). BS2 consists in the def2-TZVP basis set for the main group atoms, and the quadruple-ζ def2-QZVP basis set for transition metals, together with the Def2 ECP for Ir.[210,213] Gibbs energies in methanol were calculated adding to the BS2 energies in methanol the thermal and entropic corrections obtained with BS1. An additional correction of 1.9 Kcal mol^{-1} was applied to all Gibbs energies to change the standard state from the gas phase (1 atm) to the condensed phase (1 M) at 298.15K ($\Delta G^{1atm \rightarrow 1M}$).[211] In this way, all the energy values given in the article are Gibbs energies in methanol calculated using the formula:

$$G = E(BS2) + G(BS1) - E(BS1) + \Delta G^{1atm \rightarrow 1M}$$

Abbreviations

δ	chemical shift
atm	atmosphere
B3LYP	Becke, 3-parameter, Lee–Yang–Parr
BINAP	(2,2′-bis(diphenylphosphino)-1,1′-binaphthyl)
Bz	Benzyl, (-CH$_2$(C$_6$H$_5$))
COA	Cyclooctane
COD	Cyclooctadiene
COE	Cyclooctene
COSY	Correlated Spectroscopy
Cp	Cyclopentadienyl, η^5-C$_5$H$_5$
Cy	Cyclohexyl, (-CH(CH$_2$)$_5$
d	doublet
fac	facial
Dcpe	1,2-Bis(dicyclohexylphosphino)ethane
DEPT	Distortionless Enhancement by Polarization Transfer
dfepe	(C$_2$F$_5$)$_2$-PCH$_2$CH$_2$P-(C$_2$F$_5$)$_2$
DFT	Density Functional Theory
DIOP	*O*-Isopropylidene-2,3-dihydroxy-1,4 bis(diphenylphosphino)butane
DIPAMP	(Ethane-1,2-diyl)bis[(2-methoxyphenyl)(phenyl)phosphane]
DMSO	Dimethylsulfoxide
dpen	diphenylethylenediamine
dppb	1,4-Bis(diphenylphosphino)butane
dppe	1,2-Bis(diphenylphosphino)ethane
dppf	1,1'-Bis(diphenylphosphino)ferrocene
dppm	1,2-Bis(diphenylphosphino)methane
dppp	1,3-Bis(diphenylphosphino)propane
dtbpe	1,2-bis(di-*tert*-butylphosphino)ethane
ee	enantioselectivity
ESI-HRMS	Electrospray Ionization High Resolution Mass Spectroscopy
Et	Ethyl, (-C$_2$H$_5$)
equiv.	equivalents
h	hour
HMQC	Heteronuclear Multiple Bond Correlation

HSQC	Heteronuclear Single Quantum Coherence
Hz	Hertz
^{i}Pr	Isopropyl ($-CH(CH_3)_2$)
^{i}PrOH	Isopropanol
J	Coupling Constant
M06	Minnesota 06
MeOH	Methanol
mer	meridional
MPV	Meerwein-Ponndorf-Verley
NMR	Nuclear Magnetic Resonance
mL	Millilitre
Ph	Phenyl ($-C_6H_5$)
ppm	parts per million
P,S^R	$CpFe[1,2-C_5H_3(PPh_2)(CH_2S^R)$
s	seconds
t	triplet
^{t}Bu	*tert*-butyl
THF	tetrahydrofuran
TOF	Turnover frequency
TS	transition state

Bibliography

1   R. Schlögl, *Angewandte Chemie - International Edition*, 2015, 54, 3465–3520.

2   J. Ma, N. Sun, X. Zhang, N. Zhao, F. Xiao, W. Wei and Y. Sun, *Catal Today*, 2009, **148**, 221–231.

3   N. G. Gaylord, *J Chem Educ*, 1957, **34**, 367–374.

4   W. G. Dauben, G. J. Fonken and D. S. Noyce, *J Am Chem Soc*, 1956, **78**, 2579–2582.

5   E. C. Ashby and J. R. Boone, *J Am Chem Soc*, 1976, **98**, 5524–5531.

6   H. Aral and A. Vecchio-Sadus, *Ecotoxicol Environ Saf*, 2008, **70**, 349–356.

7   I. Vural Gürsel, T. Noël, Q. Wang and V. Hessel, *Green Chemistry*, 2015, **17**, 2012–2026.

8   S. Y. Pan, P. C. Chiang, W. Pan and H. Kim, *Crit Rev Environ Sci Technol*, 2018, **48**, 471–534.

9   M. Honda, S. Sonehara, H. Yasuda, Y. Nakagawa and K. Tomishige, *Green Chemistry*, 2011, **13**, 3406–3413.

10   G. W. Parshall and R. E. Putscher, *J Chem Educ*, 1986, **63**, 189.

11   D. Dylong, P. J. C. Hausoul, R. Palkovits and M. Eisenacher, *Flavour Fragr J*, 2022, 37, 195–209.

12   C. S. G. Seo and R. H. Morris, *Organometallics*, 2019, **38**, 47–65.

13   M. Peleg, M. D. Normand and M. G. Corradini, *Crit Rev Food Sci Nutr*, 2012, 52, 830–851.

14   S. Kozuch and S. Shaik, *Acc Chem Res*, 2011, **44**, 101–110.

15   S. Kozuch and J. M. L. Martin, *ACS Catal*, 2012, 2, 2787–2794.

16   R. Poli, *Comments on Inorganic Chemistry*, 2009, **30**, 177–228.

17   S. M. Lu and C. Bolm, in *Chemistry - A European Journal*, 2008, vol. 14, pp. 7513–7516.

18   H. Caner, E. Groner, L. Levy and I. Agranat, *Drug Discov Today*, 2004, **9**, 105–110.

19   H. U. Blaser, *Rendiconti Lincei*, 2013, **24**, 213–216.

20   J. C. Barreiro, M. E. Tiritan and Q. B. Cass, *TrAC - Trends in Analytical Chemistry*, 2021, 142.

21   S. J. Blanksby and G. B. Ellison, *Acc Chem Res*, 2003, **36**, 255–263.

22   C. Yin, Y. Pan, L. Zheng, B. Lin, J. Wen and X. Zhang, *Organic Chemistry Frontiers*, 2021, 0–3.

23   T. H. Hall, H. Adams, V. K. Vyas, K. L. Michael Chu and M. Wills, *Tetrahedron*, , DOI:10.1016/j.tet.2020.131771.

24   W. Hieber and F. Leutert, *Naturwissenschaften*, 1931, **19**, 360–361.

25   H. Dai and H. Guan, *Isr J Chem*, 2017, 57, 1170–1203.

26   G. Wilkinson and J. M. Birmingham, *J Am Chem Soc*, 1955, **77**, 3421–3422.

27   M. L. H. Green, L. Pratt and G. Wilkinson, *Journal of the Chemical Society (Resumed)*, 1958, 3916–3922.

28   S. J. LaPlaca and J. A. Ibers, *J Am Chem Soc*, 1963, **85**, 3501–3502.

29   K. A. Moltved and K. P. Kepp, *Journal of Physical Chemistry A*, 2019, **123**, 2888–2900.

30   L. Vaska and J. W. DiLuzio, *J Am Chem Soc*, 1961, **83**, 2784–2785.

31   L. Vaska and J. W. DiLuzio, *J Am Chem Soc*, 1962, **84**, 679–680.

32   G. J. Kubas, *J Organomet Chem*, 2014, **751**, 33–49.

33   G. J. Kubas, *Acc Chem Res*, 1988, **21**, 120–128.

34   R. H. Crabtree, *Acc Chem Res*, 1990, **23**, 95–101.

35   A. M. Kalsin, T. A. Peganova, I. S. Sinopalnikova, I. V. Fedyanin, N. V. Belkova, E. Deydier and R. Poli, *Dalton Transactions*, 2020, **49**, 1473–1484.

36   R. Malacea, J. C. Daran, S. B. Duckett, J. P. Dunne, C. Godard, E. Manoury, R. Poli and A. C. Whitwood, *Journal of the Chemical Society. Dalton Transactions*, 2006, 3350–3359.

37   E. M. Kozinets, M. Fekete, O. A. Filippov, N. V. Belkova, E. S. Shubina, R. Poli, S. B. Duckett and E. Manoury, *Dalton Transactions*, 2013, **42**, 11720–11730.

38   R. C. Schnabel, P. S. Carroll and D. M. Roddick, *Organometallics*, 1996, **15**, 655–662.

39   J. A. Osborn, F. H. Jardine, J. F. Young and G. Wilkinson, *J. Chem. Soc. A*, 1966, 1711–1732.

40   J. A. Labinger, *Organometallics*, 2015, 34, 4784–4795.

41   T. J. Hebden, K. I. Goldberg, M. D. Heinekey, X. Zhang, T. J. Emge, A. S. Goldman and K. Krogh-Jespersen, *Inorg Chem*, 2010, **49**, 1733–1742.

42   M. Yamakawa, H. Ito and R. Noyori, 2000, 1466–1478.

43   R. H. Morris, *Acc Chem Res*, 2015, **48**, 1494–1502.

44   M. Besora and F. Maseras, *Advances in Catalysis*, 2021, **68**, 385–426.

45   C. A. Sandoval, T. Ohkuma, K. Muñiz and R. Noyori, *J Am Chem Soc*, 2003, **125**, 13490–13503.

46   R. Poli, in *Advances in Organometallic Chemistry*, Academic Press Inc., 2023, vol. 79, pp. 87–133.

47   D. Wang and D. Astruc, *Chem Rev*, 2015, **115**, 6621–6686.

48   X. Li, X. Wu, W. Chen, F. E. Hancock, F. King, J. Xiao and C. V Ts, 2004, 2378–2381.

49   T. Ikariya and R. Noyori, 1995, 7562–7563.

50   J. Takehara, S. Hashiguchi, A. Fujii, S. Inoue, T. Ikariya and R. Noyori, 1996, **12**, 233–234.

51   P. A. Dub, N. J. Henson, R. L. Martin and J. C. Gordon, *J Am Chem Soc*, 2014, **136**, 3505–3521.

52   O. Eisenstein and R. H. Crabtree, *New Journal of Chemistry*, 2013, 37, 21–27.

53   R. M. Bullock, *Chemistry - A European Journal*, 2004, 10, 2366–2374.

54   R. J. Hamilton and S. H. Bergens, 2006, 13700–13701.

55   T. Imamoto, *Hydrogenation*, 2012, 3–30.

56   R. Noyori and S. Hashiguchi, 1997, **30**, 97–102.

57   Tkachenko V. Nikolay and Dub A. Pavel, *Journal of Physical Chemistry A*, 2021, **125**, 5726–5737.

58   F. Ling, S. Nian, J. Chen, W. Luo, Z. Wang, Y. Lv and W. Zhong, *Journal of Organic Chemistry*, 2018, **83**, 10749–10761.

59   R. Molina Betancourt, P. G. Echeverria, T. Ayad, P. Phansavath and V. Ratovelomanana-Vidal, *Synthesis (Germany)*, 2021, **53**, 30–50.

60   Y. Liu, X. Yue, C. Luo, L. Zhang and M. Lei, *Energy and Environmental Materials*, 2019, 2, 292–312.

61   R. H. Crabtree and M. W. Davis, *Organometallics*, 1983, **2**, 681–682.

62   A. Comas-Vives, G. Ujaque and A. Lledós, *Inner- and Outer-Sphere Hydrogenation Mechanisms: A Computational Perspective*, 2010, vol. 62.

63   J. S. M. Samec, J. E. Bäckvall, P. G. Andersson and P. Brandt, *Chem Soc Rev*, 2006, **35**, 237–248.

64   D. Evans, J. A. Osborn and G. Wilkinson, *Journal of the Chemical Society A: Inorganic, Physical, Theoretical*, 1968, 3133–3142.

65   M. Iglesias, M. P. Nicolás, P. J. S. Miguel, V. Polo, F. J. F. Alvarez, J. J. P. Torrente and L. A. Oro, *Chemical Communications*, 2012, **48**, 9480–9482.

66   N. García, E. A. Jaseer, J. Munarriz, P. J. Sanz Miguel, V. Polo, M. Iglesias and L. A. Oro, *Eur J Inorg Chem*, 2015, **2015**, 4388–4395.

67   A. Iturmendi, N. García, E. A. Jaseer, J. Munárriz, P. J. Sanz Miguel, V. Polo, M. Iglesias and L. A. Oro, *Dalton Transactions*, 2016, **45**, 12835–12845.

68   M. Iglesias and L. A. Oro, *Chem Soc Rev*, 2018, 47, 2772–2808.

69   S. B. Duckett, C. L. Newell and R. Eisenberg, *J Am Chem Soc*, 1997, **119**, 2068.

70   Y. R. S. Laxmi and J. E. Bäckvall, *Chemical Communications*, 2000, 611–612.

71   C. S. Yi, Z. He and I. A. Guzei, *Organometallics*, 2001, **20**, 3641–3643.

72   X. Guo, Y. Tang, X. Zhang and M. Lei, *Journal of Physical Chemistry A*, 2011, **115**, 12321–12330.

73   K. Flack, K. Kitagawa, P. Pollet, C. A. Eckert, K. Richman, J. Stringer, W. Dubay and C. L. Liotta, *Org Process Res Dev*, 2012, **16**, 1301–1306.

74   R. Cohen, C. R. Graves, S. B. T. Nguyen, J. M. L. Martin and M. A. Ratner, *J Am Chem Soc*, 2004, **126**, 14796–14803.

75   J. W. Handgraaf, J. N. H. Reek and E. J. Meijer, *Organometallics*, 2003, **22**, 3150–3157.

76   M. Yamakawa, H. Ito and R. Noyori, *J Am Chem Soc*, 2000, **122**, 1466–1478.

77   W. Wu, S. Liu, M. Duan, X. Tan, C. Chen, Y. Xie, Y. Lan, X. Q. Dong and X. Zhang, *Org Lett*, 2016, **18**, 2938–2941.

78   K. J. Haack, S. Hashiguchi, A. Fujii, T. Ikariya and R. Noyori, *Angewandte Chemie (International Edition in English)*, 1997, **36**, 285–288.

79   P. A. Dub and J. C. Gordon, *ACS Catal*, 2017, **7**, 6635–6655.

80   R. J. Hamilton and S. H. Bergens, 2006, 13700–13701.

81   P. A. Dub, N. J. Henson, R. L. Martin and J. C. Gordon, *J Am Chem Soc*, 2014, **136**, 3505–3521.

82   P. A. Dub, B. L. Scott and J. C. Gordon, *J Am Chem Soc*, 2017, **139**, 1245–1260.

83   J. M. Hayes, E. Deydier, G. Ujaque, A. Lledós, R. Malacea-Kabbara, E. Manoury, S. Vincendeau and R. Poli, *ACS Catal*, 2015, **5**, 4368–4376.

84   E. Le Roux, R. Malacea, E. Manoury, R. Poli, L. Gonsalvi and M. Peruzzini, *Adv Synth Catal*, 2007, **349**, 309–313.

85   G. E. Dobereiner, A. Nova, N. D. Schley, N. Hazari, S. J. Miller, O. Eisenstein and R. H. Crabtree, *J Am Chem Soc*, 2011, **133**, 7547–7562.

86   Z. Liang, T. Yang, G. Gu, L. Dang and X. Zhang, *Chin J Chem*, 2018, **36**, 851–856.

87   J. M. Hayes, E. Deydier, G. Ujaque, A. Lledós, R. Malacea-Kabbara, E. Manoury, S. Vincendeau and R. Poli, *ACS Catal*, 2015, **5**, 4368–4376.

88   S. M. W. Rahaman, J. C. Daran, E. Manoury and R. Poli, *J Organomet Chem*, 2017, **829**, 14–21.

89   E. M. Kozinets, M. Fekete, O. A. Filippov, N. V. Belkova, E. S. Shubina, R. Poli, S. B. Duckett and E. Manoury, *Dalton Transactions*, 2013, **42**, 11720–11730.

90   F. Ling, S. Nian, J. Chen, W. Luo, Z. Wang, Y. Lv and W. Zhong, *Journal of Organic Chemistry*, 2018, **83**, 10749–10761.

91   T. Ohkuma, H. Ooka, S. Hashiguchi, T. Ikariya and R. Noyori, *J Am Chem Soc*, 1995, **117**, 2675–2676.

92   E. Farnetti, J. Kašpar, R. Spogliarich and M. Graziani, *J. Chem. Soc., Dalton Trans.*, 1988, 947–952.

93   R. Noyori and T. Ohkuma, *Angewandte Chemie - International Edition*, 2001, 40, 40–73.

94   R. Hartmann and P. Chen, *Angewandte Chemie - International Edition*, 2001, **40**, 3581–3585.

95   A. Amgoune and D. Bourissou, *Chemical Communications*, 2011, **47**, 859–871.

96   O. M. Demchuk and R. Jasiński, *Phosphorus Sulfur Silicon Relat Elem*, 2016, **191**, 245–253.

97   S. E. Clapham, A. Hadzovic and R. H. Morris, *Coord Chem Rev*, 2004, 248, 2201–2237.

98   S. A. Popoola, E. A. Jaseer, A. A. Al-Saadi, V. Polo, M. A. Casado and L. A. Oro, *Inorganica Chim Acta*, 2015, **436**, 146–151.

99   S. M. W. Rahaman, J. C. Daran, E. Manoury and R. Poli, *J Organomet Chem*, 2017, **829**, 14–21.

100 D. G. I. Petra, P. C. J. Kamer, A. L. Spek, H. E. Schoemaker and P. W. N. M. Van Leeuwen, *Journal of Organic Chemistry*, 2000, **65**, 3010–3017.

101 P. Kvintovics, J. Bakos and B. Heil, *Journal of Molecular Catalysis*, 1985, 32, 111–114.

102 M. V. Jiménez, J. Fernández-Tornos, J. J. Pérez-Torrente, F. J. Modrego, P. García-Orduña and L. A. Oro, *Organometallics*, 2015, **34**, 926–940.

103 R. Spogliarich, J. Kašpar, M. Graziani and F. Morandini, *J Organomet Chem*, 1986, **306**, 407–412.

104 M. J. Fernandez, M. A. Esteruelas, M. Covarrubias and L. A. Oro, *J Organomet Chem*, 1986, **316**, 343–349.

105 M. Fabbian, N. Marsich and E. Farnetti, *Inorganica Chim Acta*, 2004, **357**, 2881–2888.

106 M. Martín, E. Sola, O. Torres, P. Plou and L. A. Oro, *Organometallics*, 2003, **22**, 5406–5417.

107 B. Raible, V. Gierz and D. Kunz, *Organometallics*, 2015, **34**, 2018–2027.

108 A. Togni, 1996, **50**, 86–93.

109 A. G. Orpen and N. G. Connelly, *Organometallics*, 1990, **9**, 1206–1210.

110 G. Schwarzenbach, *Helv Chim Acta*, 1952, **35**, 2344–2359.

111 E. G. Moschetta, K. M. Gans and R. M. Rioux, *J Catal*, 2014, **309**, 11–20.

112 W. S. Knowles and M. J. Sabacky, *Chemical Communications (London)*, 1968, 1445–1446.

113 T. P. Dang and H. B. Kagan, *Journal of the Chemical Society D: Chemical Communications*, 1971, **7**, 481.

114   A. Miyashita, H. Takaya, T. Souchi and R. Noyori, *Tetrahedron*, 1984, **40**, 1245–1253.

115   A. Togni, *Chimia (Aarau)*, 1996, **50**, 86.

116   / Am, K.-M. Chi, J.-C. Calabrese, W. M. Reiff, J. S. Miller, C. Zou, M. S. J. Wrighton, A. D. Am ; Ryabov, H. R. Allcock, J. A. Dodge, I. Manners, M. Parvez, G. H. Riding, K. B. Vissher, S. R. Marder, J. W. Perry, B. G. Tiemann, W. P. Schaefer, R. Isnin, A. E. Kaifer, J. C. Medina, C. Li, S. G. Bott, J. L. Atwood, G. W. Gokel, M. C. Grossel, M. R. Goldspink, J. A. Hrijac, S. C. Weston, A.-S. Carlstróm, T. Fredj, N. Motohashi, R. Meyer, S. R. Gollapudi, K. R. J. Bhattiprolu, T. Hayashi, M. Kumada, K. Isaki, T. Kiyoi, Y. Ito, K. Kanehira, T. Hagihara, A. Togni, S. D. Pastor, M. Sawamura, A. Yamauchi, T. Takegawa, T. P. E. Kenny, A. C. Knipe, W. E. Watts, E. Hungerbühler, D. Seebach, D. Wasmuth, J. Pawlak, K. Nakanishi, T. Iwashira, E. Borowski, K. Gokel, P. Hoffmann, H. Kleinmann, H. Klusacek, E. Negishi, N. Okukado, A. O. King, D. E. Van Horn, B. Spiegel, J. C. Chambron, C. Coudret and J. P. Sauvage, *A General Asymmetric Synthesis of Ferrocenes with Planar Chirality*, Chem. Soc, 1993, vol. 115.

117   H.-U. Blaser, W. Brieden, B. Pugin, F. Spindler, M. Studer and A. Togni, *Solvias Josiphos ligands: from discovery to technical applications*, 2002, vol. 19.

118   H. U. Blaser, B. Pugin and F. Spindler, *Helv Chim Acta*, 2021, 104.

119   L. X. Dai, T. Tu, S. L. You, W. P. Deng and X. L. Hou, *Acc Chem Res*, 2003, **36**, 659–667.

120   A. Miyashita, A. Yasuda, H. Takaya, K. Toriumi, T. Ito, T. Souchi and R. Noyori, *J Am Chem Soc*, 1980, **102**, 7932–7934.

121   O. Riant, O. Samuel and H. B. Kagan, *J Am Chem Soc*, 1993, **115**, 5835–5836.

122   M. Berthod, G. Mignani, G. Woodward and M. Lemaire, *Chem Rev*, 2005, 105, 1801–1836.

123   Y. Enomoto, H. Ichiryu, H. Hu, Y. Ura and M. Ogasawara, *Organometallics*, 2021, **40**, 1020–1024.

124   J. P. Genêt, P. Phansavath and V. Ratovelomanana-Vidal, *Isr J Chem*, 2021, 61, 409–426.

125   P. Meakin, J. P. Jesson and C. A. Tolman, *J Am Chem Soc*, 1972, **94**, 3240–3242.

126   D. S. Glueck, *Coord Chem Rev*, 2008, 252, 2171–2179.

127   T. MORIMOTO, N. NAKAJIMA and K. ACHIWA, *Chem Pharm Bull (Tokyo)*, 1994, **42**, 1951–1953.

128   F. Brüning, H. Nagae, D. Käch, K. Mashima and A. Togni, *Chemistry - A European Journal*, 2019, **25**, 10818–10822.

129   H. Nie, Y. Zhu, X. Hu, Z. Wei, L. Yao, G. Zhou, P. Wang, R. Jiang and S. Zhang, *Org Lett*, 2019, **21**, 8641–8645.

130   J. H. Xie, X. Y. Liu, J. B. Xie, L. X. Wang and Q. L. Zhou, *Angewandte Chemie - International Edition*, 2011, **50**, 7329–7332.

131   W. P. Liu, M. L. Yuan, X. H. Yang, K. Li, J. H. Xie and Q. L. Zhou, *Chemical Communications*, 2015, **51**, 6123–6125.

132   X. H. Yang, J. H. Xie and Q. L. Zhou, *Organic Chemistry Frontiers*, 2014, **1**, 190–193.

133   R. E. Rülke, V. E. Kaasjager, P. Wehman, C. J. Elsevier, P. W. N. M. van Leeuwen, K. Vrieze, J. Fraanje, K. Goubitz and A. L. Spek, *Organometallics*, 1996, **15**, 3022–3031.

134   A. Del Zotto, W. Baratta, M. Ballico, E. Herdtweck and P. Rigo, *Organometallics*, 2007, **26**, 5636–5642.

135   M. P. Carroll and P. J. Guiry, *Chem Soc Rev*, 2014, 43, 819–833.

136   T. Noël and J. Van Der Eycken, *Green Processing and Synthesis*, 2013, 2, 297–309.

137   J. Yu, J. Long, Y. Yang, W. Wu, P. Xue, L. W. Chung, X. Q. Dong and X. Zhang, *Org Lett*, 2017, **19**, 690–693.

138   J. Margalef, M. Biosca, P. de la Cruz Sánchez, J. Faiges, O. Pàmies and M. Diéguez, *Coord Chem Rev*, 2021, 446.

139   N. Mateus, L. Routaboul, J. C. Daran and E. Manoury, *J Organomet Chem*, 2006, **691**, 2297–2310.

140   L. Routaboul, S. Vincendeau, J. C. Daran and E. Manoury, *Tetrahedron Asymmetry*, 2005, **16**, 2685–2690.

141   L. Flores-Santos, E. Martin, A. Aghmiz, M. Diéguez, C. Claver, A. M. Masdeu-Bultó and M. Á. Muñoz-Hernández, *Eur J Inorg Chem*, 2005, 2315–2323.

142   A. M. Masdeu-Bultó, M. Diéguez, E. Martin and M. Gómez, *Coord Chem Rev*, 2003, 242, 159–201.

143   J. Margalef, M. Biosca, P. de la Cruz-Sánchez, X. Caldentey, C. Rodríguez-Escrich, O. Pàmies, M. A. Pericàs and M. Diéguez, *Adv Synth Catal*, 2021, **363**, 4561–4574.

144   M. Biosca, M. Coll, F. Lagarde, E. Brémond, L. Routaboul, E. Manoury, O. Pàmies, R. Poli and M. Diéguez, *Tetrahedron*, 2016, **72**, 2623–2631.

145   E. Le Roux, R. Malacea, E. Manoury, R. Poli, L. Gonsalvi and M. Peruzzini, *Adv Synth Catal*, 2007, **349**, 309–313.

146   R. Malacea, E. Manoury, L. Routaboul, J. C. Daran, R. Poli, J. P. Dunne, A. C. Withwood, C. Godard and S. B. Duckett, *Eur J Inorg Chem*, 2006, 1803–1816.

147   D. G. Gusev, A. J. Lough and R. H. Morris, *J Am Chem Soc*, 1998, **120**, 13138–13147.

148   S. E. Landau, K. E. Groh, A. J. Lough and R. H. Morris, *Inorg Chem*, 2002, **41**, 2995–3007.

149   R. Kusy, M. Lindner, J. Wagner and K. Grela, *Chem Catalysis*, 2022, **2**, 1346–1361.

150   A. Reyna-Madrigal, N. Ortiz-Pastrana and M. A. Paz-Sandoval, *J Organomet Chem*, 2019, **886**, 13–26.

151   M. C. and L. A. O. 1M. J. Fernandez, M. A. Esteruelas, 1986, **316**, 343–349.

152   P. Kisten, E. Manoury, A. Lledós, A. C. Whitwood, J. M. Lynam, J. M. Slattery, S. B. Duckett and R. Poli, *Dalton Transactions*, 2023, **52**, 2495–2505.

153   T. Makino, Y. Yamamoto and K. Itoh, *Organometallics*, 2004, **23**, 1730–1737.

154   M. Bikrani, L. Fidalgo and M. A. Garralda, *Polyhedron*, 1996, **15**, 83–89.

155   L. D. Field, B. A. Messerle, M. Rehr, L. P. Soler and T. W. Hambley, *Organometallics*, 2003, **22**, 2387–2395.

156   M. A. Esteruelas, L. A. Oro, M. C. Apreda, C. Foces-Foces, F. H. Cano, R. M. Claramunt, C. Lopez, J. Elguero and M. Begtrup, *J Organomet Chem*, 1988, **344**, 93–108.

157   C. Laborde, M. M. Wei, A. Van Der Lee, E. Deydier, J. C. Daran, J. N. Volle, R. Poli, J. L. Pirat, E. Manoury and D. Virieux, *Dalton Transactions*, 2015, **44**, 12539–12545.

158   R. C. Schnabel and D. M. Roddick, *Inorg Chem*, 1993, **32**, 1513–1518.

159   O. Tissot, M. Gouygou, F. Dallemer, J. C. Daran and G. G. A. Balavoine, *Eur J Inorg Chem*, 2001, 2385–2389.

160   R. A. Schunn, *Inorg Chem*, 1970, **9**, 2567–2572.

161   U. Casellato, B. Corain, R. Graziani, B. Longato and G. Pilloni, *Inorg Chem*, 1990, **29**, 1193–1198.

162   M. A. Esteruelas, M. Olivan, L. A. Oro, M. Schulz, E. Sola and H. Werner, *Organometallics*, 1992, **11**, 3659–3664.

163   I. Mena, P. García-Orduña, V. Polo, F. J. Lahoz, M. A. Casado and L. A. Oro, *Dalton Transactions*, 2017, **46**, 11459–11468.

164   R. P. Aggarwal, N. G. Connelly, B. J. Dunne, M. Gilbert and A. G. Orpen, *Journal of the Chemical Society, Dalton Transactions*, 1991, 1–9.

165   T. Suzuki, M. Shiotsuki, K. Wada, T. Kondo and T. Mitsudo, *Journal of the Chemical Society, Dalton Transactions*, 1999, 4231–4237.

166   A. M. Gull, P. E. Fanwick and C. P. Kubiak, 1993, 2121–2125.

167   N. Lease, E. M. Pelczar, T. Zhou, S. Malakar, T. J. Emge, F. Hasanayn, K. Krogh-Jespersen and A. S. Goldman, *Organometallics*, 2018, **37**, 314–326.

168   T. J. Hebden, K. I. Goldberg, M. D. Heinekey, X. Zhang, T. J. Emge, A. S. Goldman and K. Krogh-Jespersen, *Inorg Chem*, 2010, **49**, 1733–1742.

169   D. Decker, H. J. Drexler, W. Baumann, F. Reiß and T. Beweries, *New Journal of Chemistry*, 2022, **46**, 22314–22321.

170 F. M. Chadwick, N. Olliff and A. S. Weller, *J Organomet Chem*, 2016, **812**, 268–271.

171 R. C. Schnabel, P. S. Carroll and D. M. Roddick, *Organometallics*, 1996, **15**, 655–662.

172 R. C. Schnabel and D. M. Roddick, *Organometallics*, 1993, **12**, 704–711.

173 Q. Zhu, D. Shi, C. Xia and H. Huang, *Chemistry - A European Journal*, 2011, **17**, 7760–7763.

174 S. Subongkoj, S. Lange, W. Chen and J. Xiao, *J Mol Catal A Chem*, 2003, **196**, 125–129.

175 S. Akutagawa, *Appl Catal A Gen*, 1995, **128**, 171–207.

176 K. Mashima, K. Higashida, A. Iimuro, H. Nagae and Y. Kita, *Chemical Record*, 2016, **16**, 2585–2594.

177 R. Malacea, R. Poli and E. Manoury, *Coord Chem Rev*, 2010, **254**, 729–752.

178 R. M. Kissling and M. R. Gagné, *Journal of Organic Chemistry*, 1999, **64**, 1585–1590.

179 C. S. G. Seo and R. H. Morris, *Organometallics*, 2019, **38**, 47–65.

180 J. Wen, F. Wang and X. Zhang, *Chem Soc Rev*, 2021, 50, 3211–3237.

181 R. A. Grey, G. P. Pez, A. Wallo and J. Corsi, *Ann N Y Acad Sci*, 1983, **415**, 235–243.

182 G. P. Pez, R. A. Grey and J. Corsi, *J Am Chem Soc*, 1981, **103**, 7528–7535.

183 R. A. Grey, G. P. Pez and A. Wallo, *J Am Chem Soc*, 1980, **102**, 5948–5949.

184 R. A. Grey, G. P. Pez, A. Wallo and J. Corsi, *J Chem Soc Chem Commun*, 1980, 783–784.

185 W. A. Fordyce, R. Wilczynski and J. Halpern, *J Organomet Chem*, 1985, **296**, 115–125.

186 R. Wilczynski, W. A. Fordyce and J. Halpern, *J Am Chem Soc*, 1983, **105**, 2066–2068.

187 D. E. Linn Jr and J. Halpern, *J Am Chem Soc*, 1987, **109**, 2969–2974.

188 J. G. L. Cortes, O. Ramon, S. Vincendeau, D. Serra, F. Lamy, J. C. Daran, E. Manoury and M. Gouygou, *Eur J Inorg Chem*, 2006, 5148–5157.

189 V. Polo, A. A. Al-Saadi and L. A. Oro, *Organometallics*, 2014, **33**, 5156–5163.

190 S. P. Smidt, N. Zimmermann, M. Studer and A. Pfaltz, *Chemistry - A European Journal*, 2004, **10**, 4685–4693.

191 R. H. Crabtree, H. Felkin and G. E. Morris, *J Organomet Chem*, 1977, **141**, 205–215.

192 S. J. Roseblade and A. Pfaltz, *Comptes Rendus Chimie*, 2007, 10, 178–187.

193   S. M. Härling, S. Krieck, H. Görls and M. Westerhausen, *Inorg Chem*, 2017, **56**, 9255–9263.

194   D. J. Sam and H. E. Simmons, *J Am Chem Soc*, 1974, **96**, 2252–2253.

195   S. J. Park, I. S. Hwang, Y. J. Chang and C. E. Song, *J Am Chem Soc*, 2021, **143**, 2552–2557.

196   B. Cordero, V. Gómez, A. E. Platero-Prats, M. Revés, J. Echeverría, E. Cremades, F. Barragán and S. Alvarez, *Journal of the Chemical Society. Dalton Transactions*, 2008, 2832–2838.

197   C. Liu, R. van Putten, P. O. Kulyaev, G. A. Filonenko and E. A. Pidko, *J Catal*, 2018, **363**, 136–143.

198   W. Yang, T. Y. Kalavalapalli, A. M. Krieger, T. A. Khvorost, I. Y. Chernyshov, M. Weber, E. A. Uslamin, E. A. Pidko and G. A. Filonenko, *J Am Chem Soc*, , DOI:10.1021/jacs.2c00548.

199   J. Choudhury, S. Podder and S. Roy, *J Am Chem Soc*, 2005, **127**, 6162–6163.

200   M. J. Frisch, G. W. Trucks, H. B. Schlegel, G. E. Scuseria, M. A. Robb, J. R. Cheeseman, G. Scalmani, V. Barone, B. Mennucci, G. A. Petersson, H. Nakatsuji, M. Caricato, X. Li, H. P. Hratchian, J. V. Ortiz, A. F. Izmaylov, J. L. Sonnenberg, D. Williams-Young, F. Ding, F. Lipparini, F. Egidi, J. Goings, B. Peng, A. Petrone, T. Henderson, D. Ranasinghe, V. G. Zakrzewski, J. Gao, N. Rega, G. Zheng, W. Liang, M. Hada, M. Ehara, K. Toyota, R. Fukuda, J. Hasegawa, M. Ishida, T. Nakajima, Y. Honda, O. Kitao, H. Nakai, T. Vreven, K. Throssell, J. A. Montgomery Jr., J. E. Perala, F. Ogliaro, M. Bearpark, J. J. Heyd, E. Brothers, K. N. Kudin, V. N. Staroverov, T. Keith, R. Kobayashi, J. Normand, K. Raghavachari, A. Rendell, J. C. Burant, S. S. Iyengar, J. Tomasi, M. Cossi, J. M. Millam, M. Klene, C. Adamo, R. Cammi, J. W. Ochterski, R. L. Martin, K. Morokuma, O. Farkas, J. B. Foreseman and D. J. Fox, *Gaussian, Inc., Wallingford CT*.

201   C. Lee, W. Yang and R. G. Parr, *Phys Rev B*, 1988, **37**, 785–789.

202   B. Miehlich, A. Savin, H. Stoll and H. Preuss, *Chem Phys Lett*, 1989, **157**, 200–206.

203   A. D. Becke, *J Chem Phys*, 1993, **98**, 5648–5652.

204   S. Grimme, J. Antony, S. Ehrlich and H. Krieg, *Journal of Chemical Physics*, , DOI:10.1063/1.3382344.

205   A. V. Marenich, C. J. Cramer and D. G. Truhlar, *Journal of Physical Chemistry B*, 2009, **113**, 6378–6396.

206   W. J. Hehre, K. Ditchfield and J. A. Pople, *J Chem Phys*, 1972, **56**, 2257–2261.

207   M. M. Francl, W. J. Pietro, W. J. Hehre, J. S. Binkley, M. S. Gordon, D. J. DeFrees and J. A. Pople, *J Chem Phys*, 1982, **77**, 3654–3665.

208   D. Andrae, U. Haeussermann, M. Dolg, H. Stoll and H. Preuss, *Theor Chim Acta*, 1990, **77**, 123–141.

209   A. W. Ehlers, M. Böhme, S. Dapprich, A. Gobbi, A. Höllwarth, V. Jonas, K. F. Köhler, R. Stegmann, A. Veldkamp and G. Frenking, *Chem Phys Lett*, 1993, **208**, 111–114.

210   F. Weigend and R. Ahlrichs, *Physical Chemistry Chemical Physics*, 2005, **7**, 3297–3305.

211   V. S. Bryantsev, M. S. Diallo and W. A. Goddard, *Journal of Physical Chemistry B*, 2008, **112**, 9709–9719.

212   A. V. Marenich, C. J. Cramer and D. G. Truhlar, *Journal of Physical Chemistry B*, 2009, **113**, 6378–6396.

213   F. Weigend, *Physical Chemistry Chemical Physics*, 2006, **8**, 1057–1065.

214   Y. Zhao and D. G. Truhlar, *Theor Chem Acc*, 2008, **120**, 215–241.

215   M. J. Frisch, G. W. Trucks, H. B. Schlegel, G. E. Scuseria, M. A. Robb, J. R. Cheeseman, G. Scalmani, V. Barone, G. A. Petersson, H. Nakatsuji, X. Li, M. Caricato, A. V. Marenich, J. Bloino, B. G. Janesko, R. Gomperts, B. Mennucci, H. P. Hratchian, J. V. Ortiz, A. F. Izmaylov, J. L. Sonnenberg, D. Williams-Young, F. Ding, F. Lipparini, F. Egidi, J. Goings, B. Peng, A. Petrone, T. Henderson, D. Ranasinghe, V. G. Zakrzewski, J. Gao, N. Rega, G. Zheng, W. Liang, M. Hada, M. Ehara, K. Toyota, R. Fukuda, J. Hasegawa, M. Ishida, T. Nakajima, Y. Honda, O. Kitao, H. Nakai, T. Vreven, K. Throssell, J. A. , Jr. Montgomery, J. E. Peralta, F. Ogliaro, M. J. Bearpark, J. J. Heyd, E. N. Brothers, K. N. Kudin, V. N. Staroverov, T. A. Keith, R. Kobayashi, J. Normand, K. Raghavachari, A. P. Rendell, J. C. Burant, S. S. Iyengar, J. Tomasi, M. Cossi, J. M. Millam, M. Klene, C. Adamo, R. Cammi, J. W. Ochterski, R. L. Martin, K. Morokuma, O. Farkas, J. B. Foresman and D. J. Fox, *Gaussian, Inc., Wallingford CT, 2016.*

216   G. Norjmaa, G. Ujaque and A. Lledós, *Top Catal*, 2022, **65**, 118–140.